

**CFD MODELLING AND
MATHEMATICAL OPTIMISATION OF
A CONTINUOUS CASTER
SUBMERGED ENTRY NOZZLE**

submitted in partial fulfillment of the requirements for the degree of

Master of Engineering (Mechanical)
in the
Faculty of Engineering, Built Environment and
Information Technology
University of Pretoria

Compiled by: Gideon Jacobus de Wet
9701364-2

Study leader: Prof. K. J. Craig

Year: April 2005

SUMMARY

CFD Modelling and Mathematical Optimisation of a Continuous Caster Submerged Entry Nozzle

Author : Gideon Jacobus de Wet
Student number : 9701364-2
Study leader : Prof. K.J. Craig
Degree: : Master of Engineering (Mechanical)
Department : Department of Mechanical and Aeronautical Engineering

Abstract:

In the continuous casting of steel, the Submerged Entry Nozzle (SEN), in particular the SEN geometry, has a primary influence on the flow pattern: the SEN controls the speed, direction and other characteristics of the jet entering the mould. The SEN is however relatively inexpensive to change (in comparison with other continuous casting equipment). Thus; there is a feasible incentive to exactly understand and predict the flow of molten steel through the SEN and into the mould, in order to maximise the quality of the steel by altering the design of the SEN.

By changing the SEN geometry and SEN design, the flow pattern in the mould will also change: it is thus possible to obtain an optimum SEN design if (or when) the desired flow patterns and/or certain predetermined temperature distributions are achieved.

Expensive and risky plant trials were traditionally utilised to “perfect” continuous casting processes. As opposed to the plant trials, this dissertation is concerned with the Computational Fluid Dynamics (CFD) modelling of the SEN and mould, which, when used in conjunction with the Mathematical Optimiser LS-OPT, will enable the optimisation of the SEN design to achieve desired results. The CFD models are experimentally verified and validated using 40%-scaled (designed and built in-house) and full-scale water model tests.

This dissertation proves that the CFD modelling of the SEN and mould can be quite useful for optimisation and parametric studies, especially when automated model generation (geometry, mesh and solution procedures) is utilised. The importance of obtaining reliable and physically correct CFD results is also emphasised; hence the need for CFD model verification using water modelling.

Keywords: Submerged Entry Nozzle (SEN), mould, continuous casting, CFD modelling, scaled water model, CFD validation and verification with water modelling, mathematical optimisation, parametric studies.

OPSOMMING

Berekeningsvloeiemeganika-modellering en Wiskundige Optimering van ‘n Stringgietry se Ondergedompelde Spuitstuk

Skrywer : Gideon Jacobus de Wet
Studentenommer : 9701364-2
Studieleier : Prof. K.J. Craig
Graadbenaming : Magister in Ingenieurswese (Meganies)
Departement : Departement Meganiese en Lugvaartkundige Ingenieurswese

Opsomming:

Die ondergedompelde spuitstuk (OS voortaan) in die staal-stringgietryproses het ‘n primêre invloed op die vloeipatrone binne-in die gietstukvolume: die OS beheer die spoed, rigting en ander karakteristieke van die spuitstraal wat die gietstukvolume binnestroom vanuit die OS se poorte. Tog is die OS relatief goedkoop om te verander in vergelyking met ander toerusting in die stringgietryproses. Gevolglik is daar ‘n dryfveer om presies die vloei deur die OS tot in die gietstukvolume te voorspel, ten einde die kwaliteit van die vervaardigde staal te maksimeer, deur slegs die ontwerp van OS stelselmatig te verander.

Deur die OS geometrie en ontwerp te wysig, sal die vloeipatrone ook verander: gevolglik sal dit moontlik wees om ‘n optimum OS te ontwerp sodra die verlangde vloeipatrone en/of temperatuurverspreidings verkry word.

Duur en riskante aanlegtoetse (van onder andere nuwe OS ontwerpe) was die tradisionele metode om ontwikkelingswerk vir die stringgietryproses te verrig. Hierteenoor, besig hierdie verhandeling hom met die berekeningsvloeiemeganika (alombekend as CFD) modellering van die OS en gietstukvolume. Tesame met die Wiskundige Optimeringspakket, LS-OPT, kan ‘n OS ontwerp die resultaat wees van ‘n optimeringsoefening – waar sekere voorafbepaalde resultate aan voldoen sal word deur die optimum OS ontwerp. Die CFD modelle wat gebruik is tydens die

optimering, word eksperimenteel bevestig met behulp van watermodeltoetse (40%-skaal watermodel wat intern ontwerp en opgerig is), asook eksterne volskaal watermodeltoetse.

Hierdie verhandeling bevestig dat CFD modellering baie handig te pas kan wees vir die optimering en parametriese studies van die OS ontwerp, veral wanneer outomatiese modelgenerasie (geometrie, maas en CFD oplossingsprosedure) gebruik word. Die belangrikheid om betroubare en korrekte CFD resultate te gebruik vir optimeringsdoeleindes word ook beaam; daarom die behoefte aan gereelde CFD model eksperimentele bevestiging (met behulp van watermodeltoetse).

Sleutelwoorde: Ondergedompelde spuitstuk, kontinue staalgietproses (oftewel stringgietproses), berekeningsvloeimeganika (CFD) modellering, eksperimentele bevestiging van CFD modelle, watermodeltoetse, geskaalde watermodeltoetse, Wiskundige optimering, parametriese studies.

ACKNOWLEDGEMENTS

EXPRESSION OF THANKS

The following persons are thanked for their individual efforts and assistance in order to realise this dissertation:

Professor Ken Craig, for his leadership, patience, and moral guidance throughout the duration of study. Apart from his excellent abilities and expertise as a technical study leader, his overall modesty made an everlasting impression on the author.

Johan Haarhoff, for his dedicated assistance enabling the author to make sense of the UNIX / Linux powered network. He is also thanked for his contribution in perfecting the parameterised 3D model, which was used in Chapter 5 (as opposed to the author's parameterised model which was not appropriate as it does not support a welded SEN design).

Danie de Kock, for his expertise concerning FLUENT and GAMBIT, and his willingness and dedication to assist users in the Department¹ at the most inconvenient of times (for him, of course).

Thomas Kingsley, for help, advice and assistance in a wide variety of (mostly electronic) tasks at hand.

Chris Pretorius, for his knowledge of C programming and his contribution in extracting information from FLUENT during automated optimisation exercises.

Johan Ackerman (from Columbus Stainless), for his persistent nagging (seen in a positive spirit) during the period to complete the 40%-scaled water model, in an effort not to miss the window of opportunity to find an optimum SEN design. He was also a key role player responsible for the commencement of the entire THRIP² project, of which this dissertation is a part.

Katlego Makgata, a fellow- post graduate student in the cfd-labs, MDOG, University of Pretoria, for mutual support during the more dreary times, especially when full-time studies were halted, and many computer problems persisted.

¹ Department of Mechanical and Aeronautical Engineering, School of Engineering, University of Pretoria, South Africa.

² THRIP: The Technology and Human Resources for Industry Programme (of South Africa)

Marius Botha, for his unique ideas and competently executed modifications (towards the end of the period) to enhance the usefulness of the 40%-scaled water model.

Petrus Mojela, for his dedicated assistance during the construction phase of the initial 40%-scaled water model, which was used for preliminary validation purposes.

FORMAL ACKNOWLEDGEMENTS

The Technology and Human Resources for Industry Programme (THRIP) of South Africa; a partnership programme funded by the Department of Trade and Industry (DTI) and managed by the National Research Foundation (NRF), supported this work. Columbus Stainless is acknowledged as the main industry partner of this THRIP project. LTM Technologies is also acknowledged as an active partner in this research.

TABLE OF CONTENTS

<u>LIST OF TABLES</u>	<u>xiii</u>
<u>LIST OF FIGURES</u>	<u>xv</u>
<u>1. INTRODUCTION</u>	<u>1</u>
<u>2. LITERATURE SURVEY</u>	<u>7</u>
<u>2.1 Historical Development of Continuous Casting</u>	<u>7</u>
2.1.1 Historical Background	7
2.1.2 Evolution of Continuous Casting Machine Design	9
2.1.3 Vertical Continuous Casting versus Horizontal Continuous Casting	11
<u>2.2 Submerged Entry Nozzle Literature</u>	<u>14</u>
2.2.1 Current continuous casting: background	14
2.2.2 SEN influence on steel	14
2.2.3 Classification of Literature	16
2.2.4 Previous work on Submerged Entry Nozzle design	18
2.2.4.1 Plant trials	18
2.2.4.2 Water modelling	19
2.2.4.3 Numerical modelling of SEN and mould design	20
<u>2.3 CFD background</u>	<u>24</u>
2.3.1 General: Numerical modelling and CFD	24
2.3.1.1 Introduction: basic equations	24
2.3.1.2 Boundary conditions: general	27
2.3.1.3 Discretisation of equations: the CFD approach	28
2.3.2 Pre-processing: geometry and grid generation	30
2.3.3 Models in commercial CFD-codes	30
2.3.4 Performance and monitoring criteria (for CFD modelling)	31
2.3.4.1 Residuals	31
2.3.4.2 Solution monitoring	32
<u>2.4 Design Optimisation</u>	<u>33</u>
2.4.1 Base case evaluation and model perfection	34

2.4.2	Parameter and objective function identification	35
2.4.3	Parametrisation of CFD-model	36
2.4.4	Design optimisation [general description]	36
2.4.5	Experimental validation	37
<u>2.5</u>	<u>Conclusion of Literature Survey</u>	<u>38</u>
<u>3.</u>	<u>EXPERIMENTAL VERIFICATION: 40%-SCALED WATER MODEL AND RESULTS</u>	<u>40</u>
<u>3.1</u>	<u>40%-Scaled water model of SEN and mould</u>	<u>40</u>
3.1.1	Concept design	40
3.1.2	Design	42
3.1.3	Construction	51
3.1.4	Commissioning	51
3.1.5	Further improvements after commissioning	53
<u>3.2</u>	<u>Similarity issues</u>	<u>56</u>
3.2.1	General	56
3.2.2	Fr-number	57
3.2.3	Re-number	59
3.2.4	Wb-number	62
<u>3.3</u>	<u>Validation Results and Other Results</u>	<u>63</u>
3.3.1	Validation of 40%-scaled model with full-scale water model	63
3.3.1.1	Widest width (1575mm) validation	63
3.3.1.2	Smallest width (1060mm) validation	65
3.3.1.3	Medium width (1250mm) validation	66
3.3.2	Other Water Model Results	67
<u>4.</u>	<u>CFD MODELLING AND VERIFICATION OF BASE CASE</u>	<u>70</u>
<u>4.1</u>	<u>Approach: CFD modelling of base case design</u>	<u>70</u>
4.1.1	General approach to modelling the base case	71
4.1.2	Verifying base case CFD model	72
4.1.3	Summary: approach to base case CFD modelling	73
<u>4.2</u>	<u>Description of base case SEN design</u>	<u>75</u>
4.2.1	SEN description	75

4.2.2	Mould description	76
4.2.3	Momentum only vs. momentum and energy combined	77
4.2.4	Simultaneous SEN and mould modelling	77
4.2.5	2D and 3D CFD modelling	79
<u>4.3</u>	<u>CFD-set-up</u>	<u>80</u>
4.3.1	Geometry and gridding strategy (pre-processing)	80
4.3.2	Boundary conditions	84
4.3.3	CFD options and assumptions	86
4.3.4	Solution Procedure	92
<u>4.4</u>	<u>CFD model: Verification Results</u>	<u>96</u>
4.4.1	CFD model verification: mimic water model	96
4.4.1.1	Case 1: Base case (Old SEN of Columbus Stainless)	97
4.4.1.2	Case 2: New SEN of Columbus Stainless	99
4.4.2	2D versus 3D verification results	100
4.4.2.1	3D verification results	100
4.4.2.2	Differences between 2D and 3D CFD models of SEN and mould	102
<u>4.5</u>	<u>CFD model of steel plant</u>	<u>103</u>
4.5.1	Geometry and gridding strategy	104
4.5.2	Boundary conditions	104
4.5.3	CFD options and assumptions	105
4.5.4	Solution procedure	106
4.5.5	CFD Results and discussion	106
<u>4.6</u>	<u>CFD SEN and mould model: reduced widths</u>	<u>116</u>
<u>4.7</u>	<u>Conclusion of base case CFD modelling</u>	<u>119</u>
<u>5.</u>	<u>DESIGN OPTIMISATION OF SEN</u>	<u>120</u>
<u>5.1</u>	<u>Automation of Optimisation process</u>	<u>121</u>
5.1.1	Parameterising: Automation of grid generation	121
5.1.2	Automation of CFD-Optimiser interface	124
<u>5.2</u>	<u>Candidate objective functions and constraint functions</u>	<u>127</u>
<u>5.3</u>	<u>Design variables x</u>	<u>130</u>
<u>5.4</u>	<u>Optimisation process</u>	<u>132</u>

5.4.1	Response Surface Methodology	133
5.4.2	Optimisation algorithm: LFOPC	137
5.4.3	Variable screening (ANOVA)	138
<u>5.5 2D Optimisation: An example of the design optimisation process</u>		<u>139</u>
5.5.1	Identification: Objective and constraint functions	139
5.5.2	Design variables x	140
5.5.3	Formulation of Optimisation problem	141
5.5.4	Base case and first perturbation set: discussion and results	143
5.5.4.1	Geometry and Mesh for 2D	144
5.5.4.2	SEN nozzle height in optimisation study: 3D vs. 2D	145
5.5.4.3	Boundary conditions	146
5.5.4.4	Solver solution procedure	146
5.5.5	Automation for design optimisation	146
5.5.5.1	GAMBIT parameterised script file	146
5.5.5.2	FLUENT script files	147
5.5.5.3	LS-OPT command file	147
5.5.6	Results and discussion of subsequent design iterations	148
5.5.6.1	Flow and Meniscus Turbulent Kinetic Energy Results: base case	148
5.5.6.2	Optimisation History	148
5.5.7	Optimum design with design variables x^*	151
<u>5.6 3D SEN design space exploration</u>		<u>154</u>
5.6.1	Computational expensive 3D models	154
5.6.2	Design space exploration	156
5.6.2.1	General and design variables	156
5.6.2.2	Formulation of multi-objective function	157
5.6.2.3	Geometry and mesh (parameterisation of mesh)	158
5.6.2.4	Boundary conditions and other settings	160
5.6.2.5	Experimental design	161
5.6.3	Results: Design space exploration	163
5.6.4	Design space exploration: geometry of chosen design	166
5.6.5	Validation of chosen design with 40%-scaled water model	167
5.6.6	CFD comparison between chosen design and base case model	169

<u>6. FUTURE WORK AND CONCLUSION</u>	<u>172</u>	
<u>6.1 Future 3D Optimisation</u>	<u>174</u>	
6.1.1 CFD model: further refinements and comments	174	
6.1.1.1 Symmetry assumption	174	
6.1.1.2 Steady / unsteady behaviour of SEN-mould solutions	174	
6.1.1.3 More refined CFD models (especially on wide moulds)	176	
6.1.1.4 Temperature	176	
6.1.1.5 Complexity of flow: natural frequency in SEN design and mould widths	178	
6.1.1.6 Volume of Fluid (VOF) methods for meniscus modelling	178	
6.1.2 Parameterisation: full 3D optimisation	180	
<u>6.2 Robustness studies on optimum designs</u>	<u>181</u>	
<u>6.3 Other global approximation techniques</u>	<u>182</u>	
6.3.1 Kriging and optimisation with CFD	182	
6.3.2 Neural network approximations	183	
<u>6.4 Conclusion</u>	<u>183</u>	
 <u>REFERENCES</u>	 <u>184</u>	
 <u>APPENDICES</u>	 <u>190</u>	
Appendix	Description	p.
<u>Appendix A</u>	Related literature on continuous casting (tundish and ladle work)	<u>190</u>
<u>Appendix B</u>	Water model design: Detail drawings of bottom tank: Unfolded sheet metal drawings together with folding instructions	<u>194</u>
<u>Appendix C</u>	Water model design: Frame design hand calculations confirming choice of steel sections	<u>199</u>
<u>Appendix D</u>	Water model design: Detail hand drawings of 3-part Aluminium SEN	<u>205</u>
<u>Appendix E</u>	Water model construction: More information and Gantt-chart for water model construction	<u>211</u>

Appendix	Description	p.
<u>Appendix F</u>	Water model results	<u>215</u>
<u>Appendix G</u>	Drawing of existing Columbus Stainless SEN (old SEN)	<u>220</u>
<u>Appendix H</u>	Drawing of new Columbus Stainless SEN (new SEN)	<u>222</u>
<u>Appendix I</u>	Comparison of 2D CFD results: VOF free surface as meniscus boundary vs. slip wall as meniscus boundary	<u>225</u>
<u>Appendix J</u>	Optimisation automation: GAMBIT script file for 2D SEN and mould half model	<u>228</u>
<u>Appendix K</u>	Optimisation automation: Combined FLUENT script file for 2D SEN and mould half model (set-up file and run file)	<u>237</u>
<u>Appendix L</u>	Optimisation automation: LS-Opt command file (com) for 2D SEN and mould half model	<u>241</u>
<u>Appendix M</u>	GAMBIT 3D script file for generating 3D quarter model meshes (Parameterised for 5 parameters or variables)	<u>244</u>
<u>Appendix N</u>	3D design exploration: Results: contours of velocity magnitude	<u>250</u>
<u>Appendix O</u>	3D design exploration: Results: best 4 designs symmetry plane comparisons	<u>264</u>
<u>Appendix P</u>	3D design exploration: Results: best 4 designs iso-surfaces	<u>282</u>
<u>Appendix Q</u>	3D design exploration: Validation of chosen or optimum SEN design with 40%-scaled water model	<u>286</u>

LIST OF TABLES

1. CHAPTER 1: INTRODUCTION	p.	1
2. CHAPTER 2: LITERATURE SURVEY		7
3. CHAPTER 3: EXPERIMENTAL VERIFICATION: 40%-SCALED WATER MODEL AND RESULTS		40
Table 3.1: Summary of Fr-similarity and Re-similarity calculations		62
Table 3.2: Preliminary validation of 40%-scaled water model: comparison with full-scale model		64
4. CHAPTER 4: CFD MODELLING AND VERIFICATION OF BASE CASE		70
Table 4.1: Comparison between different turbulence models [10]		88
Table 4.2: Comparison between different near-wall treatments [10]		90
Table 4.3: Verification of 2D CFD model (slip wall and free surface meniscus boundary condition) with 40%-scaled water model. CFD results displayed using contours of velocity magnitude		98
Table 4.4: Verification of 2D CFD model (slip wall and free surface meniscus boundary condition) with 40%-scaled water model. CFD results displayed using contours of velocity magnitude		100
Table 4.5: Verification of base case 3D CFD model (comparing RSM and k- ω (standard) as turbulence models) with 40%-scaled water model; 1575mm full-scale width. CFD results on quarter model centre plane displayed using contours of velocity magnitude		102
5. CHAPTER 5: DESIGN OPTIMISATION OF SEN		120
Table 5.1: Constant parameters used in optimisation study: geometrical and steel properties		141
Table 5.2: Constant parameters used in optimisation study: energy/temperature considerations		141
Table 5.3: Ranges (or bounds) of SEN design variables and initial design for optimisation study		141
Table 5.4: Summary of design optimisation results		152
Table 5.5: Constant parameters used in 3D design space exploration optimisation study: geometrical and steel properties		157
Table 5.6: Experiments in central-composite design, including base case (experiment 1.0) and linear and quadratic optima fits by LS-OPT		162
Table 5.7: Chosen design following 3D design space exploration		166
Table 5.8: Values: comparison between base case and chosen design from 3D exploration study		170

6. CHAPTER 6: FUTURE WORK AND CONCLUSION	172
REFERENCES	184
APPENDICES	190
Appendix C	199
Table C.1: Steel sections for water model frame	199
Appendix F	215
Table F.1: List of water model experiments and reference Figure number	216
Appendix I	225
Table I.1: Details of comparison between the two boundary condition options (slip wall vs. free surface)	225
Appendix N	250
Table N.1: Experiments in central-composite design, including base case (experiment 1.0) and linear and quadratic optima fits by LS-OPT	251
Table N.2: Summary Results data: maximum TKE and maximum velocity on meniscus of each SEN design for both widths (1060 and 1250mm)	252

LIST OF FIGURES

	p.
1. CHAPTER 1: INTRODUCTION	1
Figure 1.1: Continuous Casting process [7]	2
2. CHAPTER 2: LITERATURE SURVEY	7
Figure 2.1: Principle types of continuous casting machines [8]	10
Figure 2.2: Evolution of continuous casting machine design [8]	11
Figure 2.3: Horizontal caster with stationary mould and movable tundish in casting position	13
Figure 2.4: Connection mode between tundish and mould, through a refractory nozzle	13
Figure 2.5: SEN in the current continuous casting process and typical influential parameters [7]	15
Diagram 2.1: Continuous casting Literature classification	17
3. CHAPTER 3: EXPERIMENTAL VERIFICATION: 40%-SCALED WATER MODEL AND RESULTS	40
Figure 3.1: Design concept: open tank with Δh as flow velocity source	41
Figure 3.2: Schematic representation of SEN/mould water model and layout	42
Figure 3.3: General layout of water model (top tank, frame and bottom tank – perspex mould not shown)	43
Figure 3.4: Isometric view of upper cylindrical tank and detachable lid	45
Figure 3.5: Stopper inside the upper cylindrical tank	46
Figure 3.6: Application of dye through the stopper – hole drilled through stopper	46
Figure 3.7: Isometric view of bottom rectangular tank (baffles inside not shown)	48
Figure 3.8: Aluminium SEN (3 different parts) shown in exploded view	50
Figure 3.9: Water model being filled up: SEN nozzles exhausting in the air	52
Figure 3.10: Upgraded flow control and flow rate measurement section at the mould model outlet	54
Figure 3.11: Improved modular SEN bottom insert compared with previous insert	55
Figure 3.12: Comparison between full-scale ADVENT water model [32] and the 40%-scaled model, satisfying the Fr-similarity in the latter case	64
Figure 3.13: Comparison between full-scale ADVENT water model [32] and the 40%-scaled model, satisfying Fr-similarity in the latter case: 1060mm mould width	66
Figure 3.14: Comparison between full-scale ADVENT water model [32] and the 40%-scaled model, satisfying Fr-similarity in the latter case: 1250mm mould width	67
4. CHAPTER 4: CFD MODELLING AND VERIFICATION OF BASE CASE	70
Figure 4.1: Diagram: Summary of the development of the base case CFD model	74

Figure 4.2: Basic geometry of base case SEN	76
Figure 4.3: Location of SEN outlet port / mould inlet port (quarter model)	78
Figure 4.4: Static and Dynamic pressure distribution in 3D SEN port face (quarter model)	79
Figure 4.5: Typical boundary conditions for momentum-only CFD model validation (quarter model)	81
Figure 4.6: Unstructured grid in area where complex jet flow occurs: incorrect solutions often result (quarter model, 3D)	82
Figure 4.7: Structured grid (hexahedral cells) in complex flow area results in more repeatable solutions (quarter model, 3D)	83
Figure 4.8: Residuals during solution procedure ('recipe')	96
Figure 4.9: Comparison of 2D and 3D velocity predictions on centre plane of mould for 3D (base case SEN design)	103
Figure 4.10: Residuals history (as a function of iteration number)	108
Figure 4.11: Physical property (maximum TKE on meniscus) as a function of iteration number	108
Figure 4.12: Base case velocity magnitude contours on symmetry plane: range 0 – 1 m/s	111
Figure 4.13: Base case vorticity magnitude contours on symmetry plane: range 0 – 25 1/s	111
Figure 4.14: Base case helicity magnitude contours on symmetry plane: range -0.5 – 0.5 m/s ²	112
Figure 4.15: Base case turbulent kinetic energy contours on symmetry plane: range 0 – 0.1 m ² /s ²	112
Figure 4.16: Base case wall shear stress contours on wide mould face: range 0 – 10 Pa	113
Figure 4.17: Base case temperature contours on symmetry plane: range 1723 – 1758 K	113
Figure 4.18: Base case path lines coloured by vorticity magnitude: range 0 – 25 1/s (isometric view)	114
Figure 4.19: Base case iso-surface of velocity magnitude (v=0.25m/s) coloured by turbulent kinetic energy: range 0 – 0.1 m ² /s ²	114
Figure 4.20: Base case velocity vectors coloured by velocity magnitude: range 0 – 1 m/s (isometric view)	115
Figure 4.21: Base case turbulent kinetic energy contours on meniscus surface: range 0 – 0.001 m ² /s ² (top view)	116
Figure 4.22: Comparison: Old SEN 40%-scaled water model with 3D CFD model (contours of velocity) on centre plane	117
Figure 4.23: Submergence depth does not influence jet angle significantly at Fr-similarity flow rate	118
5. CHAPTER 5: DESIGN OPTIMISATION OF SEN	120
Figure 5.1: Design optimisation: parameterisation of 2D SEN	122
Figure 5.2: Diagram depicting the tasks (including coordinating tasks) performed by LS-OPT during the design optimisation process	127
Figure 5.3: Design space terminology (design space, region of interest and experimental design points): response surface methodology [57]	135

Figure 5.4: Example of response surface approximated over experimental design points [57]	135
Figure 5.5: Successive sub-region reduction scheme [57]	136
Figure 5.6: Successive sub-region reductions combined with optimisation of response surfaces (not shown) converges to an optimum [57]	137
Figure 5.7: Structured mesh of SEN and mould 2D half-model	144
Figure 5.8: Side view of the 3D SEN nozzle and subsequent reduction of port height for average height (2D height)	145
Figure 5.9: Flow pattern (velocity vectors) and point of impingement of initial design	148
Figure 5.10: Optimisation history: Objective function (max TKE) and maximum velocity on meniscus	150
Figure 5.11: Optimisation history: Constraint functions g_1 (geometrical constraint) and g_3 (jet direction constraint)	150
Figure 5.12: Optimisation history: Design variables	151
Figure 5.13: Comparison of turbulent kinetic energy on meniscus surface between initial design and optimum design (2D half model)	153
Figure 5.14: Turbulent kinetic energy [m^2/s^2] contours in flow field of optimum design compared with initial design	154
Figure 5.15: Typical boundary conditions for quarter model of 3D CFD SEN and mould model	161
Figure 5.16: Central-composite design experimental points	163
Figure 5.17: Multi-objective values of the experiments listed in Table 5.6	164
Figure 5.18: Geometry of chosen design (port angle = 20° downwards, port height = 80mm, no well)	167
Figure 5.19: Validation of optimum SEN design at mould width 1250mm and 200mm submergence depth, using contours of velocity (scale 0 – 1 m/s)	168
Figure 5.20: Validation of optimum SEN design at mould width 1250mm and 200mm submergence depth, using path lines coloured by velocity magnitude (scale 0 – 1 m/s)	169
Figure 5.21: Comparison between TKE on the meniscus of the base case and chosen design from 3D exploration study for casting conditions indicated in Table 5.8	170
6. CHAPTER 6: FUTURE WORK AND CONCLUSION	172
Figure 6.1: Top view of 3D model of SEN and mould, indicating heat flux boundary conditions causing areas of too low temperature	177
REFERENCES	184

APPENDICES	190
Appendix A	190
Diagram A.1: Tundish classification of literature	191
Appendix B	194
Figure B.1: Detail folded open drawing extracted from Solid Edge: Belly or base	196
Figure B.2: Detail folded open drawing extracted from Solid Edge: Top	196
Figure B.3: Detail folded open drawing extracted from Solid Edge: Side, left	197
Figure B.4: Detail folded open drawing extracted from Solid Edge: Side, right	197
Figure B.5: Detail folded open drawing extracted from Solid Edge: Support and baffle, right	198
Figure B.6: Detail folded open drawing extracted from Solid Edge: Support and baffle, middle and left	198
Appendix C	199
Figure C.1: Water model frame, front view: Detail hand drawing	201
Figure C.2: Water model frame, side view: Detail hand drawing	202
Figure C.3: Water model frame, top view and detail: Detail hand drawing	203
Figure C.4: Water model frame: detail of hanging sections: Detail hand drawing	204
Appendix D	205
Figure D.1: Aluminium SEN: Assembly drawing: full section	206
Figure D.2: Aluminium SEN: Assembly drawing: side view	207
Figure D.3: Aluminium SEN: Auxiliary sections and views	208
Figure D.4: Mandrel for manufacture of Aluminium SEN inside	209
Figure D.5: Assembly drawing of 40%-scaled stopper and SEN upper part	210
Appendix F	215
Figure F.1: Old SEN (1060mm width, 150mm submergence depth, 1.1 m/min full-scale cast speed) snapshots	217
Figure F.2: Old SEN (1060mm width, 150mm submergence depth, 1.0 m/min full-scale cast speed) snapshots	217
Figure F.3: New SEN (1060mm width, 150mm submergence depth, 1.0 m/min full-scale cast speed) snapshots	217
Figure F.4: Old SEN (1060mm width, 80mm submergence depth, 1.0 m/min full-scale cast speed) snapshots	218
Figure F.5: New SEN (1060mm width, 80mm submergence depth, 1.0 m/min full-scale cast speed) snapshots	218
Figure F.6: Old SEN (1250mm width, 150mm submergence depth, 1.0 m/min full-scale cast speed) snapshots	218

Figure F.7: New SEN (1250mm width, 150mm submergence depth, 1.0 m/min full-scale cast speed) snapshots	219
Figure F.8: Old SEN (1250mm width, 80mm submergence depth, 1.0 m/min full-scale cast speed) snapshots	219
Figure F.9: New SEN (1250mm width, 80mm submergence depth, 1.0 m/min full-scale cast speed) snapshots	219
Appendix G	220
Figure G.1: Old SEN Columbus Stainless: Official Drawings (copyright Vesuvius)	221
Appendix H	222
Figure H.1: New SEN Columbus Stainless: Official Drawings (copyright Vesuvius)	224
Appendix I	225
Figure I.1: 2D CFD-model meniscus boundary condition comparison: base case (Old SEN) (comparing velocity contours of magnitude)	226
Figure I.2: CFD-model (2D) meniscus boundary condition comparison: base case (New SEN) (comparing velocity contours of magnitude)	226
Appendix L	241
Figure L.1: Diagram depicting the tasks (including coordinating tasks) performed by LS-OPT during the design optimisation process	242
Appendix N	250
Figure N.1: Graphical display of data in Table N.2	253
Figure N.2: Experiment 1.0 contours of velocity magnitude on centre plane (range 0 – 1 m/s)	254
Figure N.3: Experiment 1.1 contours of velocity magnitude on centre plane (range 0 – 1 m/s)	254
Figure N.4: Experiment 1.2 contours of velocity magnitude on centre plane (range 0 – 1 m/s)	255
Figure N.5: Experiment 1.3 contours of velocity magnitude on centre plane (range 0 – 1 m/s)	255
Figure N.6: Experiment 1.4 contours of velocity magnitude on centre plane (range 0 – 1 m/s)	256
Figure N.7: Experiment 1.5 contours of velocity magnitude on centre plane (range 0 – 1 m/s)	256
Figure N.8: Experiment 1.6 contours of velocity magnitude on centre plane (range 0 – 1 m/s)	257
Figure N.9: Experiment 1.7 contours of velocity magnitude on centre plane (range 0 – 1 m/s)	257
Figure N.10: Experiment 1.8 contours of velocity magnitude on centre plane (range 0 – 1 m/s)	258
Figure N.11: Experiment 1.9 contours of velocity magnitude on centre plane (range 0 – 1 m/s)	258
Figure N.12: Experiment 1.10 contours of velocity magnitude on centre plane (range 0 – 1 m/s)	259
Figure N.13: Experiment 1.11 contours of velocity magnitude on centre plane (range 0 – 1 m/s)	259
Figure N.14: Experiment 1.12 contours of velocity magnitude on centre plane (range 0 – 1 m/s)	260
Figure N.15: Experiment 1.13 contours of velocity magnitude on centre plane (range 0 – 1 m/s)	260

Figure N.16: Experiment 1.14 contours of velocity magnitude on centre plane (range 0 – 1 m/s)	261
Figure N.17: Experiment 1.15 contours of velocity magnitude on centre plane (range 0 – 1 m/s)	261
Figure N.18: Experiment 1.16 contours of velocity magnitude on centre plane (range 0 – 1 m/s)	262
Figure N.19: Experiment 2.0_linear contours of velocity magnitude on centre plane (range 0 – 1 m/s)	262
Figure N.20: Experiment 2.0_quadratic contours of velocity magnitude on centre plane (range 0 – 1 m/s)	263
 Appendix O	 264
Figure O.1: Contours of velocity magnitude on the symmetry plane (range 0 – 1 m/s)	266
Figure O.2: Contours of helicity on the symmetry plane (range –0.5 – 0.5 m/s ²)	266
Figure O.3: Contours of turbulent kinetic energy on symmetry plane (range 0 – 0.1 m ² /s ²)	267
Figure O.4: Contours of vorticity on the symmetry plane (range 0 – 25 s ⁻¹)	267
Figure O.5: Contours of shear stress on the wide mould walls (range 0 – 10 Pa)	268
Figure O.6: Contours of temperature on the symmetry plane (range 1723 – 1758 K)	268
Figure O.7: Path lines originating from the SEN inlet, coloured by vorticity magnitude (range of vorticity 0 – 25 s ⁻¹)	269
Figure O.8: Contours of velocity magnitude on the symmetry plane (range 0 – 1 m/s)	270
Figure O.9: Contours of helicity on the symmetry plane (range –0.5 – 0.5 m/s ²)	270
Figure O.10: Contours of turbulent kinetic energy on symmetry plane (range 0 – 0.1 m ² /s ²)	271
Figure O.11: Contours of vorticity on the symmetry plane (range 0 – 25 s ⁻¹)	271
Figure O.12: Contours of shear stress on the wide mould walls (range 0 – 10 Pa)	272
Figure O.13: Contours of temperature on the symmetry plane (range 1723 – 1758 K)	272
Figure O.14: Path lines originating from the SEN inlet, coloured by vorticity magnitude (range of vorticity 0 – 25 s ⁻¹)	273
Figure O.15: Contours of velocity magnitude on the symmetry plane (range 0 – 1 m/s)	274
Figure O.16: Contours of helicity on the symmetry plane (range –0.5 – 0.5 m/s ²)	274
Figure O.17: Contours of turbulent kinetic energy on symmetry plane (range 0 – 0.1 m ² /s ²)	275
Figure O.18: Contours of vorticity on the symmetry plane (range 0 – 25 s ⁻¹)	275
Figure O.19: Contours of shear stress on the wide mould walls (range 0 – 10 Pa)	276
Figure O.20: Contours of temperature on the symmetry plane (range 1723 – 1758 K)	276
Figure O.21: Path lines originating from the SEN inlet, coloured by vorticity magnitude (range of vorticity 0 – 25 s ⁻¹)	277
Figure O.22: Contours of velocity magnitude on the symmetry plane (range 0 – 1 m/s)	278
Figure O.23: Contours of helicity on the symmetry plane (range –0.5 – 0.5 m/s ²)	278
Figure O.24: Contours of turbulent kinetic energy on symmetry plane (range 0 – 0.1 m ² /s ²)	279
Figure O.25: Contours of vorticity on the symmetry plane (range 0 – 25 s ⁻¹)	279
Figure O.26: Contours of shear stress on the wide mould walls (range 0 – 10 Pa)	280
Figure O.27: Contours of temperature on the symmetry plane (range 1723 – 1758 K)	280

Figure O.28: Path lines originating from the SEN inlet, coloured by vorticity magnitude (range of vorticity $0 - 25 \text{ s}^{-1}$)	281
Appendix P	282
Figure P.1: Iso-surface of velocity coloured by turbulent kinetic energy (range $0 - 0.1 \text{ m}^2/\text{s}^2$)	284
Figure P.2: Iso-surface of velocity coloured by turbulent kinetic energy (range $0 - 0.1 \text{ m}^2/\text{s}^2$)	284
Figure P.3: Iso-surface of velocity coloured by turbulent kinetic energy (range $0 - 0.1 \text{ m}^2/\text{s}^2$)	285
Figure P.4: Contours of turbulent kinetic energy on symmetry plane (range $0 - 0.1 \text{ m}^2/\text{s}^2$)	285
Appendix Q	286
Figure Q.1: Validation of optimum SEN design at 80mm submergence depth, using contours of velocity (scale $0 - 1 \text{ m/s}$)	287
Figure Q.2: Validation of optimum SEN design at 80mm submergence depth, using path lines coloured by velocity magnitude (scale $0 - 1 \text{ m/s}$)	287
Figure Q.3: Validation of optimum SEN design at 150mm submergence depth, using contours of velocity (scale $0 - 1 \text{ m/s}$)	288
Figure Q.4: Validation of optimum SEN design at 150mm submergence depth, using path lines coloured by velocity magnitude (scale $0 - 1 \text{ m/s}$)	288

CHAPTER 1: INTRODUCTION

Steel (whether it is low or high carbon steel, any alloy or a stainless steel alloy) is still the most reliable, appropriate and inexpensive building material for automobiles, trains, ocean liners, industrial vehicles, household appliances, industrial appliances and computer cases to name but a few. Even in a time where alternative materials (especially composites and plastics) are increasingly utilised, steel still seems to be irreplaceable owing to its availability, strength and price advantage above non-metallic materials that are equivalent in strength. Moreover, the recycling of steel is certainly an added advantage above composites and plastics from an environmental viewpoint.

Flat steel products in the form of rolled coils are mostly utilised for aforementioned applications. These coils are the result of a reduction process (hot or direct rolling) of billets, blooms or slabs¹ directly after casting (ingot casting² or continuous casting³). Since the quite recent commercial adoption of continuous casting (after World War II but only as a significant production process in the early 1960's) [1], it has practically replaced all ingot casting processes due to the increase in yield and reduced production costs. The energy savings (reduced production costs) are achieved primarily by elimination of the soaking pits and slabbing mill, and the possibility for direct rolling (no or much less reheating required).

¹ Definitions of billet, bloom and slab according to cross-section measurements: [8]

billet: square sections up to 150mm square or round sections up to 150mm diameter;

bloom: square or rectangular cross sections greater than 150mm square up to 800 x 400mm, also rounds with a diameter of more than 150mm diameter;

slab: anything larger than blooms; usually with an aspect ratio of more than 2.

² Ingot Casting: The cast of liquid steel into a stationary mould or ingot mould. Each mould consists of cast iron forming a thick walled container open at the top and set up before casting on large cast iron *bottom plates* or *stools*. After solidification, the ingot mould is removed with a *stripping crane* and the ingot is then charged into a soaking pit and slabbing mill, after which it is reheated and transported on rollers towards the final reduction process (rolling). [1][8]

³ Continuous Casting: The cast of liquid steel into an open-ended mould, directly extracting the solidifying slab from the mould, eliminating the soaking pits and slabbing mill. Slabs are cut whilst moving at casting speed, directly transporting the cut slabs towards the hot reduction process resulting in a usable flat steel product.

The Submerged Entry Nozzle (SEN) plays a major part in the continuous casting process as indicated in other studies [2][3][4][5][6]: (Refer to Figure 1.1 [7] for diagrammatic presentation of the continuous casting process.)

The SEN introduces the molten steel emanating from the tundish into the mould, where the final particle removal process takes place in the continuous casting process. As the SEN introduces the flow to the mould, it has an effect on the flow pattern in the mould; consequently the SEN has an impact on the quality of the steel. The SEN, in particular the SEN geometry, has a primary influence on the flow pattern: the SEN controls the speed, direction and other characteristics⁴ of the jet entering the mould.

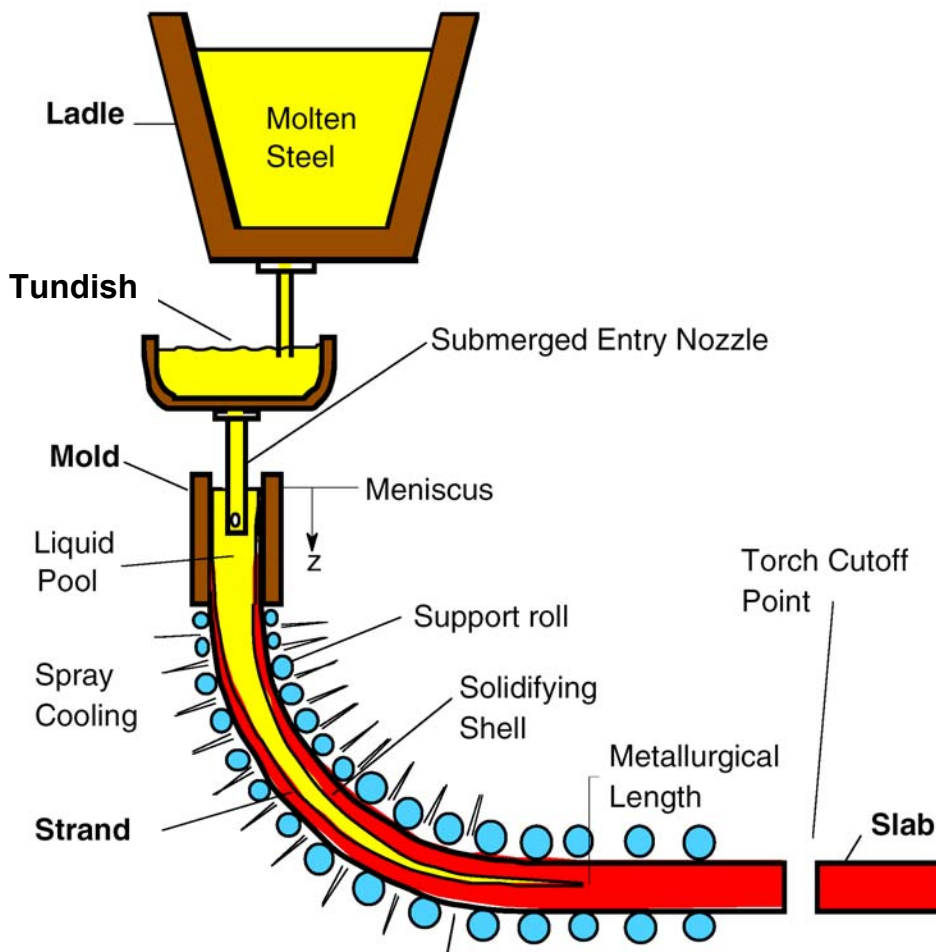


Figure 1.1: Continuous Casting process [7]

⁴ Other characteristics of the jet emanating from the SEN may include turbulence effects, the occurrence of vortices, jet angle as it exits from the SEN, impingement point onto the narrow mould wall, impingement angle, etc.

The SEN geometry is however relatively inexpensive to change [5]. Thus; there is a feasible incentive to exactly understand and predict the flow of molten steel through the SEN and into the mould, in order to maximise the quality of the steel by altering the design of the SEN.

It is conceivable that by changing the SEN geometry and SEN design, the flow pattern in the mould will also change. It is thus possible to obtain an optimum SEN design if (or when) the desired flow patterns and/or certain predetermined temperature distributions are achieved. Expensive plant trials (downtime for set-up of experiments, tons of scrapped steel should the experiment fail, to name a few possibilities) can be eliminated if accurate and believable⁵ mathematical and/or physical models are developed for the SEN and mould flow domain. The most common and reliable mathematical modelling technique is the use of Computational Fluid Dynamics (CFD)⁶, especially when the flow path is quite difficult to define analytically and whenever the flow is turbulent (high Reynolds number), rendering classical analytical mathematical modelling almost impossible to solve [9].

Both cases stated above are true when modelling the SEN and mould:

- The geometry is complicated and it is thus difficult to describe the latter and subsequently difficult applying an analytical modelling technique.
- The flow (especially of the jets emanating from the SEN) is highly turbulent; the equations of viscous flow (Navier-Stokes equations – refer to Chapter 2) are thus impossible to solve analytically, because the boundary conditions become randomly time-dependent [9].

Consequently CFD techniques (also known as numerical modelling) will be applied in this study as an inexpensive alternative to genuine plant trials, in order to find an optimum SEN design by applying mathematical optimisation.

⁵ The mathematical or physical model of the plant situation should be accurate and obviously predict the genuine flow situation; otherwise the use of mathematical modelling is obsolete.

⁶ CFD: Computational Fluid Dynamics. These techniques comprise: Discretising the flow path into finite elements, and solving the Navier-Stokes Momentum Equations as well as mass and energy conservation equations (refer to Chapter 2 for more details concerning these equations) for each element (or cell), taking into account the boundary conditions enclosing the flow path. Energy conservation equations are especially important for heat transfer modelling.

Using journal or scripting capabilities of the commercial CFD-package FLUENT's [10] pre-processor GAMBIT [11], the CFD grid generation process can be automated with respect to certain predetermined variables (mathematically stated as the vector \mathbf{x}) in the SEN design. Examples of candidate variables are the SEN nozzle height, SEN nozzle angle as design variables; and submergence depth of the SEN nozzle as an example of an operational parameter that may also influence the solution. A fully automated set-up thus comprises automatic grid generation for any (predetermined) variable value and any (predetermined) boundary condition variation; and subsequently an optimiser can be linked to this automated CFD parameterisation set-up.

Mathematical optimisation can be applied to real problems (as the optimisation of the SEN design), by identifying a suitable objective function (or combination of objective functions or rather a multi-objective function). As a rule of thumb, the objective function is chosen in such a manner that an optimum solution (thus an optimum combination of variables) will be obtained if the objective function is minimised.

The mathematical optimisation technique applied in this project, is the response surface methodology as implemented in LS-OPT [12][13], which briefly involves the following:

Design response surfaces of the objective and constraint functions are fitted through points in the design space (the full range of all the variables \mathbf{x}) to form approximate optimisation problems on a sub-design region (a smaller region within the ranges of the variables \mathbf{x}). These response surfaces are approximated using a linear (or quadratic) approximation for this study. The size of the sub-design region is heuristically adjusted with each design iteration to counteract oscillations due to numerical noise in the optimisation process [13].

The successive response surface of the objective function is minimised using the adapted dynamic trajectory method of Snyman (LFOPC), which uses appropriate penalty function formulations in order to handle constrained optimisation sub problems [14].

An example of an objective function applicable to this problem is to minimise the turbulent kinetic energy on the meniscus surface. Various studies (*e.g.* Refs. [2][4][5]) have linked excessive turbulence on the meniscus (where the slag powder and liquid are found) to quality problems due to the entrainment of slag into the molten steel. For 2D cases in this study, minimising the maximum turbulent kinetic energy on the meniscus is selected as a candidate objective function to evaluate the combined effect of typical SEN design parameters when linked to a mathematical optimiser. The author is aware that an “optimum” SEN design that results from an optimisation study using the minimisation of the maximum turbulent kinetic energy (TKE) on the meniscus surface, may not be an optimum solution. By minimising the maximum TKE on the surface, the focus is on minimising slag entrainment from the meniscus surface, neglecting the possible effect of meniscus freezing **caused** by too low a TKE value. However, for the first 2D study (in Chapter 5, Section 5.2), temperature effects are neglected, which renders meniscus freezing impossible to be determined numerically. Furthermore, in an effort to prevent obvious meniscus freezing in the 2D optimisation study, constraint functions are incorporated to limit minimum meniscus velocity (magnitude) and to prevent an excessively deep jet impingement. Refer to Chapter 5, Sections 5.2 and 5.5 for detail.

Two optimisation approaches or studies are performed in this study: a 2D case (fully automated optimisation) as well as a 3D design exploration case. At first, it was assumed that the numerical CFD solutions are correct and the optimisation study was valid without experimental verification. However, when evaluating the base case (firstly in 3D modelling), it was found that the solution is very dependent on the mesh quality – especially in the high vorticity zones near the jet exits at the SEN ports. In order to validate the CFD solution procedure to be used with all separate CFD evaluations, a 40%-scale mould water model was designed and built by the author. Two base cases were validated with experimental water model results and compared satisfactorily.

The main objective of this study is to design a SEN that will cause desirable flow situations and thus result in good quality steel, by using CFD linked with mathematical optimisation. The design will be achieved by starting off with a base design, which is currently in use at Columbus Stainless, Middelburg, South Africa,

and optimising this design by minimising pre-selected multi-objective functions (that represent the selected desirable flow situations and/or boundary conditions). Further objectives include validating CFD results as well as the effectiveness of mathematical optimisation by comparing CFD results (2D and 3D) with 40%-scale water model experimental results. Another objective is to prove that CFD linked with mathematical optimisers (especially parametric CFD-optimisation studies) can be a very valuable and usable tool to achieve significant results (optimal SEN designs). These techniques can be applied by steel plants to design a SEN to suit their needs (different flow situations, plant circumstances and steel grades will necessarily require different SEN designs) without significant production losses due to unsuccessful and costly plant trials.

In the following Chapter, some background is presented to acquaint the reader with the history of steel making and the ultimate development of continuous casting, as well as the importance and influence of the SEN in the continuous casting process.

The design and construction of the 40%-scaled water model is then presented, as well as the verification of the scaled water model with a full-scale water model. Water model results are presented for later comparisons.

Thereafter, it is shown that base case design is the obvious first step in the optimisation process, which is followed by the official formulation of the optimisation problem for this study. The solution of the optimisation problem follows, using 2D and 3D models, where optimum SEN designs are obtained by linking CFD with mathematical optimisation. The base case design as well as an optimum SEN design (from the 3D design exploration case) are validated experimentally using the specifically designed and built 40%-scaled SEN and mould water model.

This dissertation is concluded with a brief conclusion and a description of future work and related topics that arose from this study.

CHAPTER 2: LITERATURE SURVEY

2.1 Historical Development of Continuous Casting

2.1.1 Historical Background

For well over a century the traditional method for the conversion of liquid steel to solid steel was by use of ingot moulds. Each mould consists of cast iron forming a thick-walled container open at the top and set up before casting on large cast iron *bottom plates* or *stools*. Each ingot was cast independently from a single ladle of liquid steel. There were a number of different ingot mould designs which were mainly divided into the big-end-down moulds and big-end-up moulds [8]. After the liquid steel had solidified in the ingot mould, the mould was removed from the ingot and the ingot was charged into soaking pits (for reheating) for later processing into semi-finished or finished products.

As early as the 19th century, the attraction of solidifying steel in a more continuous fashion was recognised by pioneers as G E Sellars (1840), J Laing (1843) and H Bessemer (1846) [1][8]. These pioneering continuous casting methods were mainly applied to non-ferrous materials with low melting points: it was used for the production of lead tubings and the production of glass [1]. Continuous casting was not applied to steel yet owing to the many technical problems associated with high temperatures involved and the low thermal conductivity of steel.

However, R M Daelen pursued the possibility of solidifying steel using a water-cooled mould, open at the top and bottom in 1887. He patented¹ and envisaged a process comprising:

A stream of liquid steel was poured vertically into an open-ended mould and then passed into a secondary cooling system and withdrawn by pinch rolls prior to being cut by a torch device. This process would be started by the use of a

¹ German Patent No. 51217 of 30 July 1889 (R.M. Daelen).

retractable *dummy bar*.² These features are in essence similar to continuous casting machines still in operation today.

Meanwhile, considerable problems occurred due to the sticking of the solidified shell to the water-cooled mould wall until Siegfried Junghans laid the foundations for modern continuous casting. He suggested (and patented) a non-harmonic mould oscillation, which would not influence the heat transfer between strand and mould [1]. In 1933, the first plant for industrial continuous casting of brass, according to the vertical open-ended mould, was built in Germany by S Junghans.

It was not until the Second World War that semi-industrial pilot plants began to emerge for the continuous casting of steel.

The first pilot plants for the continuous casting of steel were built at Babcock and Wilcocks (USA), Low Moor (Great Britain) and Steel Tube Works, Amagasaki (Japan) in 1946 and 1947.

From 1950 onwards the development of the continuous casting of steel on a large scale developed rapidly. Technological advances, which are applicable to this study, will briefly be mentioned: (More detailed information on the advances (and corresponding dates) can be viewed in References [1] and [8].)

- 1952: German patent by O. Schaeber describing the casting of a bent vertical strand instead of a straight vertical strand
- 1952: The first electromagnetic stirrer designed for continuous casting at Mannesmann by Junghans and Schaeber
- 1956: At Barrow (Great Britain) vertical cutting of the billet strand was replaced by horizontal cutting which implied that the withdrawn strand was bent before cutting

² The start-up of the continuous casting process requires a bar head (*dummy bar*), which is marginally smaller in cross section than the mould, to be driven in to the bottom of the mould by steering it up from the bottom of the machine using a dummy bar chain. When liquid steel enters the mould, it solidifies around the claw shaped dummy bar. As soon as the mould is filled with molten steel, the dummy bar is withdrawn and the continuous casting process commences. The dummy bar is then removed from the solidifying strand and parked away from the strand.

- 1963: At Dillinger Steelworks (Germany) the first vertical type slab machine made use of horizontal discharge by bending the slab strand
- 1970 – 1983:
 - Rapid ladle and tundish changing equipment to improve productivity and yield
 - Variable width adjusting moulds to minimise mould changing and thus improve yield
 - Mist cooling using air atomised water to improve cooling efficiency and homogeneity
 - Total shrouding of metal streams from ladle to tundish and from tundish to mould to avoid contact with air (oxygen) in order to improve quality. Shrouding from the tundish to the mould is in the form of a refractory tube and generally known as the Submerged Entry Nozzle (SEN). With the casting of billets, an inert gas shrouding is used (as opposed to a refractory tube) due to the small cross sectional area of the mould opening.
 - Integrated computer control of the complete casting process

2.1.2 Evolution of Continuous Casting Machine Design

The basic principle of the continuous casting process for steel (as envisaged by R M Daelen in 1887) is based on the pouring of liquid steel vertically into a water-cooled copper mould, which is open at the bottom. Heat transfer to the copper mould immediately solidifies the liquid steel and a solid skin (commonly known as the *shell*) is formed which increases in thickness down the length of the copper mould. To avoid sticking of the shell to the copper mould, the mould is reciprocated sinusoidally and a lubricant has to be provided to be an interface between the shell and the copper mould. This lubricant is usually introduced as a casting or mould powder, which melts to form a slag. The slag infiltrates the gaps between the steel shell and copper at the meniscus to provide lubrication [15][16].

The early continuous casting machines were totally vertical: they required considerable height to achieve reasonable production rates per strand. Moreover, the support rolls and pinch rolls beneath the mould were under severe stress due to the ferrostatic forces in the strand. Since approximately 1965, continuous casting machines evolved from totally vertical to the curved type. Refer to Figure 2.1 for the diagrammatic depiction of the principle types of (vertical) continuous caster machines. In recent years the curved mould machine (curved mould with straightening or CS as depicted in Figure 2.1) has been widely used. Multi-radius machines (or rather curved mould with progressive straightening or CPS) are also in use currently, which enable an even further reduction in height and thus ferrostatic forces.

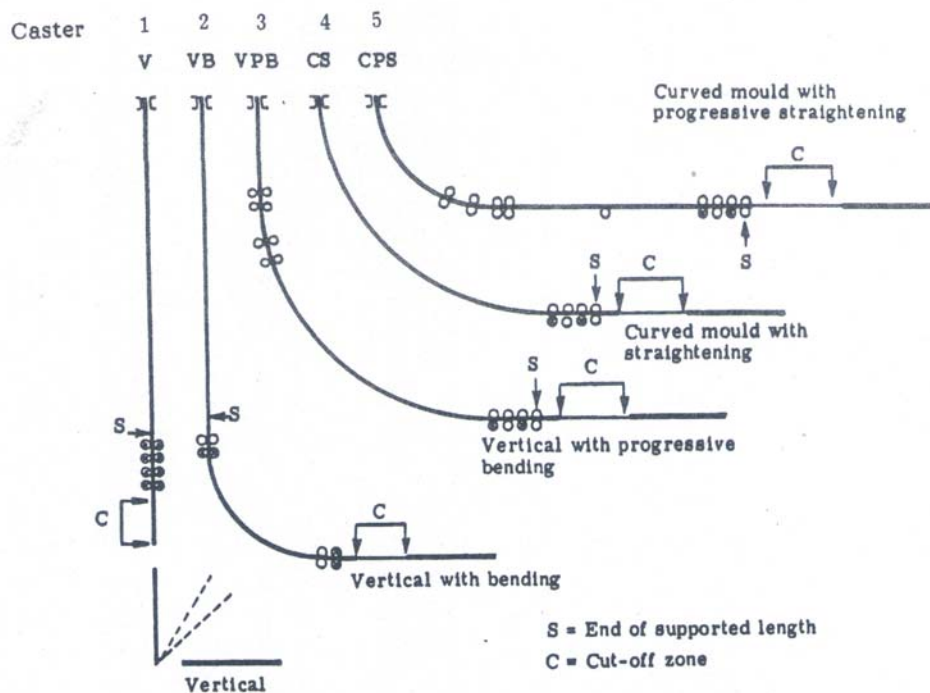


Figure 2.1: Principle types of continuous casting machines [8]

The main advantage of the curved vertical continuous casters is the reduction of machine height with the following benefits:

- reduced costs for plant buildings (lower buildings);
- reduced crane costs (crane height reduced);
- less maintenance (roller gap geometries and roller alignments) for roller support system due to lower ferrostatic forces; and

- no mechanism required to turn the cut off vertical slab horizontally.

The evolution of machine design for slab, bloom and billet casters is depicted in Figure 2.2, where the systematic switch to curved vertical continuous casting machines is emphasised.

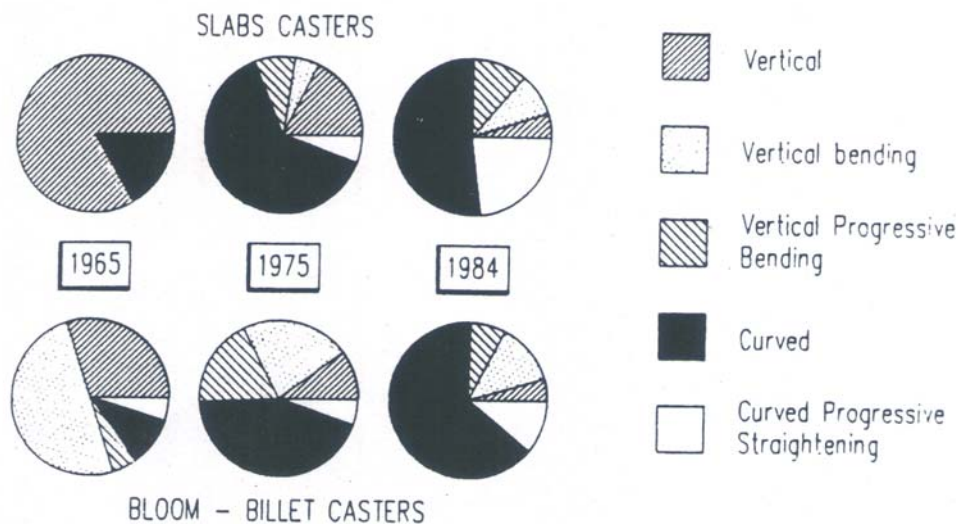


Figure 2.2: Evolution of continuous casting machine design [8]

However, multi-radius machines (Caster 5 (CPS) in Figure 2.1) are limited to a minimum height due to quality difficulties and mould teeming difficulties.

Moreover, by striving to reduce the height of continuous casting machines, in the limit the strand could become totally horizontal. However, considerable difficulties occur with the liquid steel feed arrangement in a horizontal set-up.

2.1.3 Vertical Continuous Casting versus Horizontal Continuous Casting

In the limit where the strand becomes horizontal in order to minimise the machine height, the process is no longer vertical continuous casting, but horizontal continuous casting. As mentioned in the previous section, although the reduction in height implies much less ferrostatic forces and thus simplifying strand support

requirements, the steel feed arrangement becomes involved and proves to be difficult. Considerable work has been carried out over the years to further develop total horizontal casting. There are several horizontal continuous casting machines that exist today; however, these machines are mainly limited to billet casters (castings of small cross sectional area – refer to Chapter 1).

As indicated in the previous section, conventional continuous casting can be regarded as vertical casting, which progressed from total vertical casting (maximum height) to the low head / multipoint straightening design (minimum height for conventional casting). Refer to Figure 2.1 in the previous section for the diagrammatical difference between these conventional casting extremities.

However, horizontal casting requires a horizontal tundish-mould joint and special conditions to reduce mould friction owing to the fact that the mould is rigidly fixed to the tundish by means of the feeding link. The mould-tundish link or connection is made of refractory material, which is called the break ring [1][8][17].

During casting, the mould-tundish connection (henceforth break ring) remains fixed and the solidification process is controlled by the withdrawal machine with phases of pull and pause.

Figure 2.3 shows a typical horizontal caster with stationary mould and moveable tundish in casting position. The connection between the tundish and mould (which has a similar function as the SEN) is schematically shown in Figure 2.4. The typical withdrawal cycle of a slab of horizontally casted steel comprises equal phases of pull and pause.

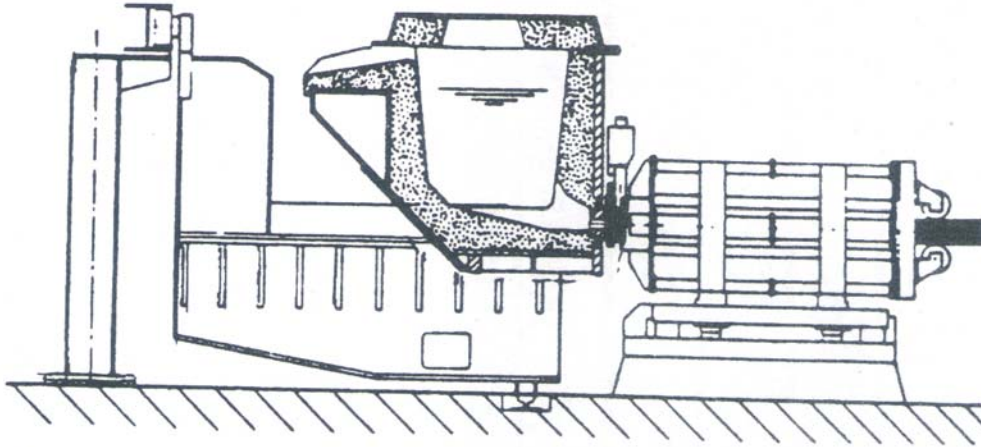


Figure 2.3: Horizontal caster with stationary mould and movable tundish in casting position

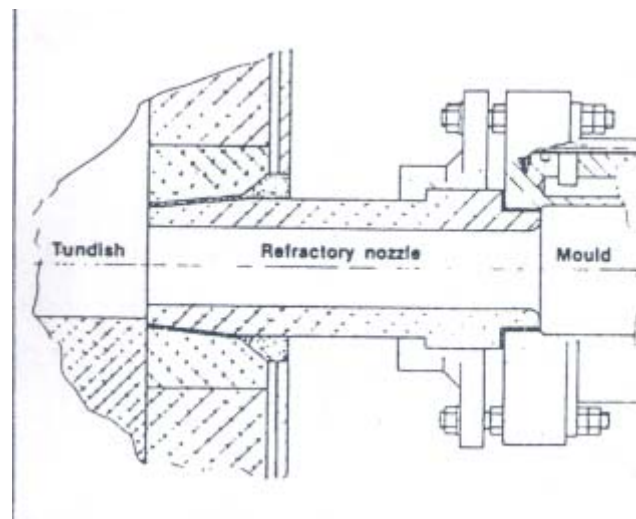


Figure 2.4: Connection mode between tundish and mould, through a refractory nozzle

However, this study involves the mathematical optimisation of the Submerged Entry Nozzle (SEN) in the continuous casting process. Although not stated in the title, this study refers to the optimisation of the SEN in the **conventional** continuous casting process. Quite obviously, due to the absence of the SEN (and the influence of the SEN on the flow pattern inside the mould) in the horizontal casting process, this study is not applicable to the horizontal continuous casting process(es).

2.2 Submerged Entry Nozzle (SEN) Literature

2.2.1 Current continuous casting: background

The current continuous casting process is very similar to that developed by the pioneers in the nineteenth century described in Section 2.1 of this chapter. After the steel has been “mixed” (ingredients or supplements added to molten iron), it is poured into the ladle (Refer to Figure 2.5(a)). The molten steel is then transferred to the tundish, which was traditionally only applied as a reservoir to sustain continuous casting while changing ladles. However, later it was realised that the tundish can also be utilised as a steel purifying vessel. This is achieved by forcing certain flow patterns in the tundish to help extract inclusions and other unwanted particles by entraining the latter in the slag layer on the tundish meniscus [18][19][20][21][22].

The SEN and mould can be regarded as the last casting equipment in the continuous casting process. All other processes afterwards are mainly concerned with extracting the quasi-solidified slab from the mould for further cooling and ultimately to be cut up in slabs for milling (for example).

The direct influence of the SEN on the flow field in the mould will be elaborated on next.

2.2.2 SEN influence on steel

As indicated in previous studies [2][3][4][5][6], the SEN has a primary influence on the flow pattern in the mould and the resultant steel quality: it controls the speed, direction and other characteristics of the steel jet entering the mould. The

SEN also has a major influence on the meniscus behaviour, which has a direct influence on the steel quality.

Figure 2.5 (a) depicts the SEN in the continuous casting process. Figure 2.5 (b) shows (schematically using a 2 dimensional half model of a SEN) the typical parameters that can have an influence on the steel jet exiting into the mould cavity.

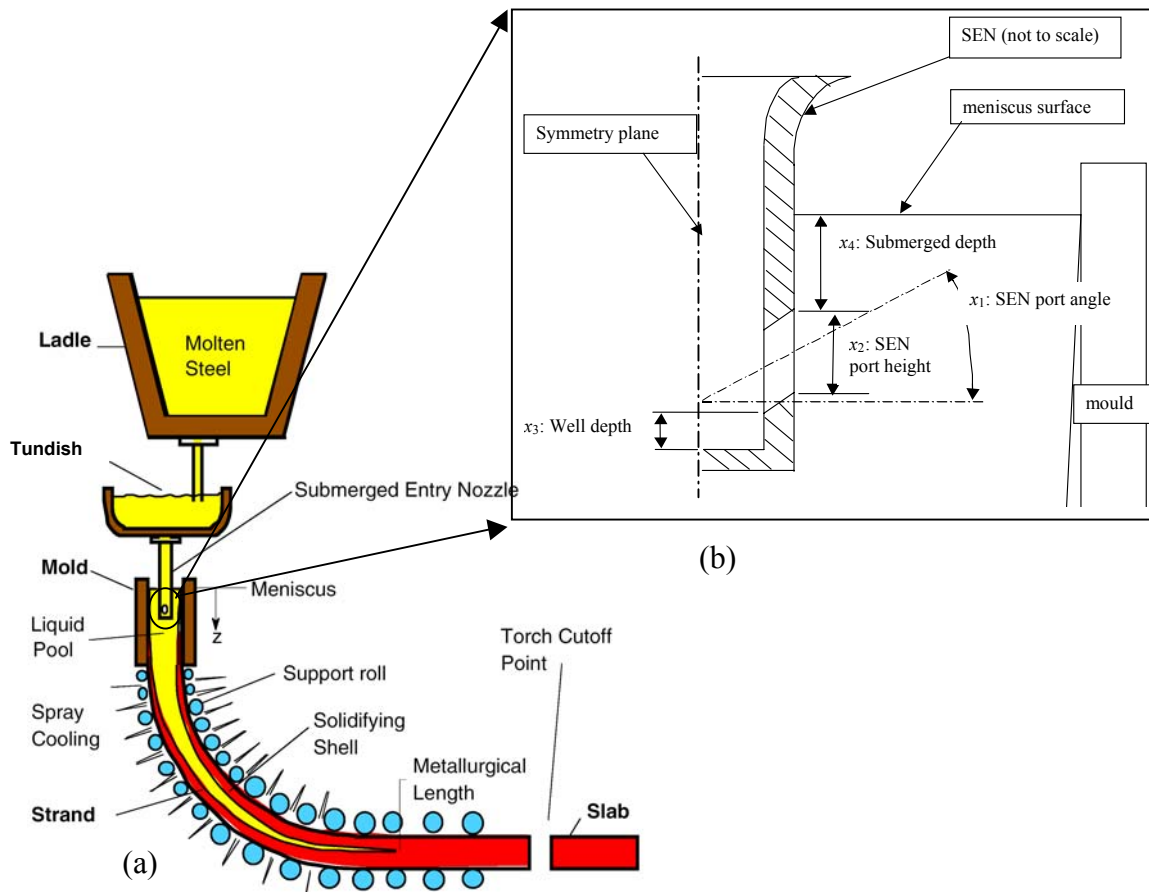


Figure 2.5: SEN in the current continuous casting process and typical influential parameters [7]

Moreover, the SEN is, compared to the complexity of the rest of the continuous casting machinery, rather simple and thus a relatively inexpensive part to change or alter after an optimisation exercise. Consequently, the SEN is an attractive optimisation topic, which will be exploited in this dissertation.

2.2.3 Classification of Literature

The literature referred to in this dissertation have been classified into certain groups. As this dissertation is part of a bigger and ongoing continuous casting research enterprise, the classification of all the references used by the University of Pretoria during the last 4 years will be shown for completeness. Diagram 2.1 depicts most references used during the past four years. Most SEN and mould references are also the references for this dissertation. (The references for the tundish, ladle and inclusion work will be shown in [Appendix A](#) for the sake of completeness.)

Diagram 2.1 provides a way of classifying continuous casting literature in major and minor categories. For the references, suffixes are used corresponding to the broad categories:

[] = Mould³, T = Tundish, I = Inclusions, L = Ladle.

Acronyms used in the diagram:

PIV = Particle Image Velocimetry

LDV = Laser Doppler Velocimetry

LES = Large Eddy Simulation

RTD = Residence Time Distribution.

³ Mould and SEN related references are mostly references for this dissertation.

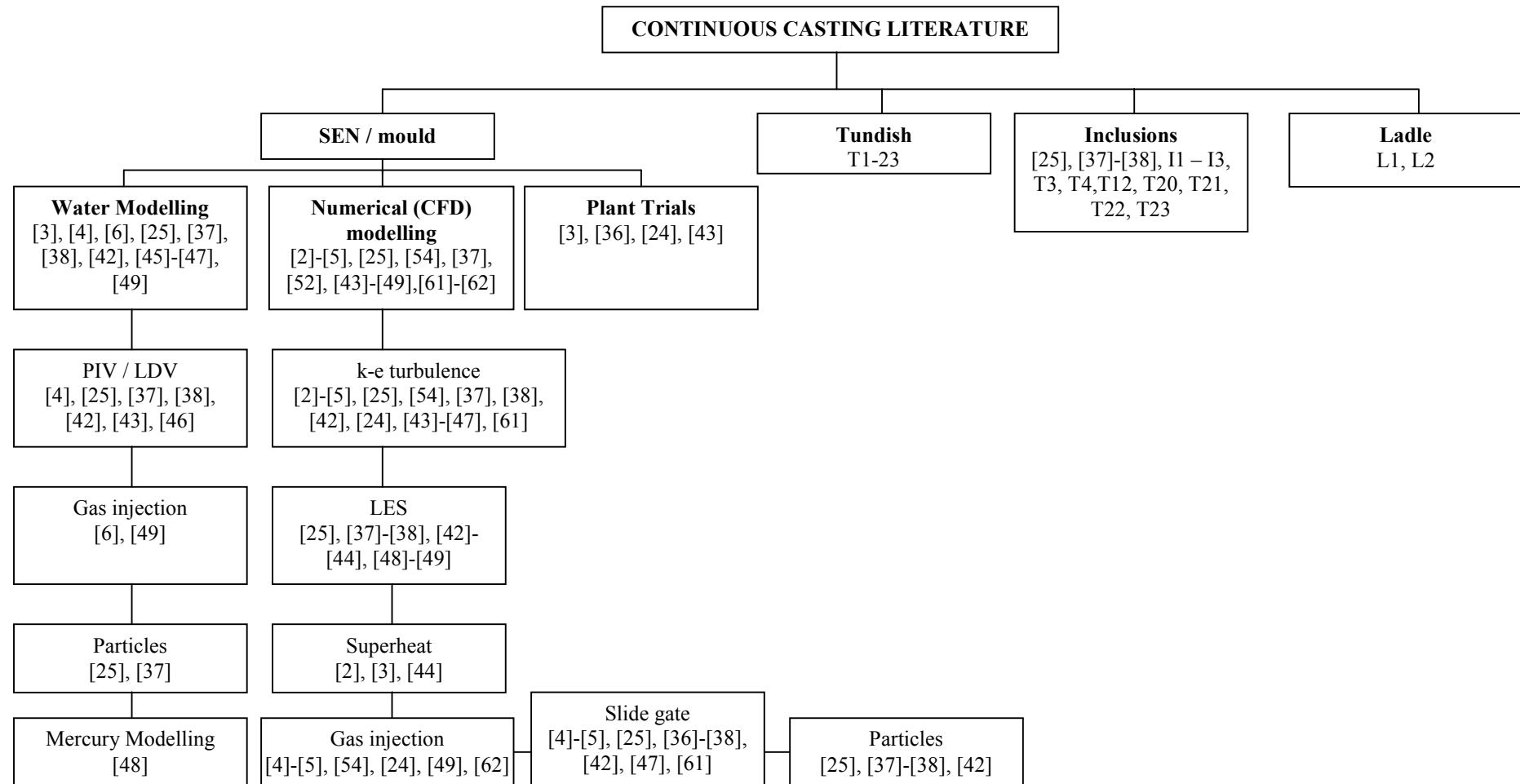


Diagram 2.1: Continuous casting Literature classification

As indicated in Diagram 2.1, the literature on specifically the SEN and mould in continuous casting can be subdivided into three categories:

- Water modelling
- Numerical modelling
- Plant trials

A number of tundish references proved to be quite contributing owing to the similarities in typical problem approaches. CFD⁴ models are also validated using water modelling, instead of using traditional plant trial methods. The very similar classification of typical tundish references is shown in [Appendix A](#).

More detail on literature will be discussed in the next section, where previous work on the SEN (and mould) will be mentioned and discussed.

2.2.4 Previous work on Submerged Entry Nozzle design

2.2.4.1 Plant trials

Most plant trials were performed if circumstances were impractical to perform water model tests: e.g., the effects of temperature and surface tension needed to be established. Plant trials were thus very common until approximately a decade ago, where computational models could replace costly plant trials. [23][24].

Plant trials can be very costly, especially if a desired result is not achieved. Moreover, using trial and error plant trial methods, a few unsuccessful iterations can be quite devastating to any steel plant.

Recently, with the global steel price being set by major steel manufacturers, the ever-continuous improvement (or rather cost saving) programmes at steel plants worldwide, prohibits plant trials to take place. Furthermore, high-risk

⁴ “CFD” is the acronym for Computational Fluid Dynamics and encompasses the entire study field of Fluid Mechanics using computational or numerical methods.

plant trials influence the efficiency of a steel plant, let alone the possible losses associated with failed (or partially failed) plant trials.

The same trend is followed with tundish design work, where different tundish designs and furniture arrangements are increasingly experimented using CFD modelling and water model verification exclusively. Refer to [Appendix A](#) for some tundish references, where striking similarities with SEN design research were identified.

2.2.4.2 Water modelling

Where possible, water model tests were and are mostly performed on full-scale water models of the SEN and mould layout. Owing to the approximate dynamic similarity between water and liquid steel, water models are mostly utilised in an effort to optimise SEN and mould set-ups by acquiring certain desired flow situations for various applications [23]. Water models can however not accurately predict the effect of Ar-bubbles on steel flow, as the relative difference in density is quite marked. The surface tension of liquid steel also differs significantly from the full-scale water model counterparts; subsequently plant trials were a necessity in some cases.

However, since the possibility of numerically solving similar flow situations using CFD techniques (refer to sections 2.2.4.3 and 2.3) with the arrival of powerful enough computers, plant trials are not a necessity during the initial development of continuous casting components.

Although complex numerical models can accurately predict the flow of liquid steel in the SEN and mould with more information available than physical plant trials, water modelling is definitely not obsolete. Water modelling is currently used to verify numerical and/or CFD models, to ensure that subsequent solutions of flow fields are believable and a representation of physical flow. Most previous studies utilised water models (full-scale and smaller scale) to verify CFD models before the CFD solutions are accepted as true and accurate [3][6][18][19][25][26].

Tundish work in water modelling was quite in abundance in the literature. A number of visualisation techniques employed in the water modelling of tundishes can be applied directly to SEN and mould work: PIV (particle image velocimetry) and LDV (laser Doppler velocimetry). The concept of residence time distribution can also be used with SEN and mould water modelling to determine the efficiency of the SEN to remove potential particles with recirculation zones. Refer to [Appendix A](#) for further tundish and inclusion references.

2.2.4.3 Numerical modelling of SEN and mould design

Early numerical work

Early numerical modelling of the SEN and mould is distinguished from CFD modelling: early numerical modelling employed analytical differential equations with macro boundary conditions applicable to very specific SEN and mould problems.

These equations are then solved using numerical computational methods⁵ developed in the 1970's [9]. These methods were extremely tedious and the complex flow of a jet exiting into a bigger cavity proved to be practically impossible to solve using these early methods.

Specific mathematical modelling (to be solved numerically) of the SEN and mould have been applied in the 1970s and 1980s [9] (as an example) to predict the temperature field and shell profile in the solidifying steel strand as a function of variables such as section size, casting speed and external cooling conditions. These pioneering methods were very toiling as the models had to be set up for a specific case (geometry, flow situation, flow assumptions, amongst others). However, these early numerical models are based on exactly

⁵Example of different numerical methods used to solve differential equations for simple problem specific flows (**laminar** boundary flow in this case): Crank Nicolson (1947) method, implemented for boundary layers by Blottner (1970); and the “finite volume” method pioneered by Patankar and Spalding (1970) – implemented in the computer code GENMIX by Spalding (1977).

the same flow equations (more detail in Section 2.3) as that of current CFD codes, and the results of early work certainly paved the way for later (i.e., current) computational work.

CFD modelling work

Current commercially available CFD techniques can be applied to any geometry and any flow situation. Although much more computing power is required than problem specific computer solutions, the solution of complex flow phenomena are now available to the general engineering public, and not only restricted to mathematicians who are able to manipulate problem specific differential equations for numerical solutions. Section 2.3 that follows shortly will briefly explain Computational Fluid Dynamic techniques.

Much work has been done regarding SEN design using numerical modelling methods. Refer to Diagram 2.1 in this Chapter for all SEN/mould work references. These references, especially Refs. [2], [4], [5], [61] and [62], laid the foundation for this dissertation, pointing out the effects of nozzle design (e.g. port angle, port size, port geometries, nozzle bottom) and operational parameters (e.g. casting speed, Argon gas injection rate⁶, clogging) on the resultant steel quality.

Most work was performed on SEN-mould models using slide-gate valves (between the tundish and SEN) to control the flow rate for a specific casting speed. The slide-gate orientation invariably causes uneven flow distribution through the bifurcated nozzles [5], resulting in asymmetry in the mould with associated quality problems. However, the work in this dissertation is based on a continuous casting set-up making use of a stopper (rod), actuated from above the tundish. Accordingly, the implicit assumption that flow is uniform in the SEN as the flow enters through the annular inlet, holds throughout this dissertation. This assumption (and reality of a stopper-type flow control system) is therefore a simplification of slide-gate continuous casting plants.

⁶ Using Ar-gas during continuous casting is beyond the scope of this dissertation.

Regarding SEN design in an effort to obtain quality continuous cast steel, the following information from Refs. [5], [60] and [61] (amongst others) laid the foundation for the optimisation work in this dissertation. The effects of different SEN designs (summarised below) guided the author in selecting meaningful design variables, objective functions, constraint functions as well as sensible design variable bounds.

*Summary of typical numerical SEN design work:*⁷

Port angle:

The port angle has a major influence on the mean jet angle, which is critical for flow inside the mould. It is interesting to note that the mean jet angle is always more downward than the port angle [61], which was unexpected by the author, but obvious if one considers the downward momentum of the molten steel inside the SEN shaft (before exiting the nozzle ports). It is also noteworthy the turbulent intensity of the mean jet increases with increased angle (positive or negative), implicating that certain bounds should be specified for optimisation work.

Port height:

Increasing the height of a nozzle port (keeping the width constant), implicates the increase of the port area. Defining a *port-to-bore ratio* based on the areas of the two ports and SEN bore respectively, Honeyands *et al.* (Reference ^[16] in [61]) correlated the area fraction β ([61]) to be 1 with a port-to-bore ratio of 1 (*i.e.*, no recirculation area at the top of the port). By increasing the height of the ports, β is decreased (implicating a larger recirculation area, that may be vulnerable to detrimental inclusion build-up and clogging of the nozzle ports).

Port thickness:

Thicker ports (thus longer ports) tend to shape the mean jet angle more closely to the port walls, increasing the effect of the SEN design on the resulting molten steel jet.

⁷ Based on work done in these references: [2][3][4][5][7][24][36][45][46][61][62]

Port width:

A narrower port will also increase the effect of the port angle and shape, provided that the bore-to-port ratio is larger than 1. If this ratio is smaller than 1, the effect (on the characteristics of the jet) of the width is less than that of the port height.

For this reason the width has been kept constant for optimisation work in this dissertation.

Port shape:

Round ports increase the swirling component of the jet relative to square ports. This may lead to increased spread angles, increased turbulence intensity and higher ineffective area fractions.

Bottom design:

The bottom design (which may be either flat, recessed or in-line with the bottom port angle) seems to have influences on the meniscus behaviour and general turbulence intensity in the mean jet area.

Influences of varying casting speed:

By increasing the casting speed, the jet speed and turbulence levels merely increase. Strangely, it does not affect the jet angle or other characteristics (recirculating area, spread, amongst others) of the jet.

Other insights:

The flow through the nozzles and into the mould cavity was regarded as steady turbulent flow in mostly all references. This assumption is also incorporated in all work in this dissertation study.

CFD work on other related casting equipment

Not surprisingly, more coinciding CFD techniques exist between the tundish and SEN/mould work. However, a major difference between the two continuous casting subjects is the fact that the flow can be assumed to be

laminar in a tundish, as opposed to fully turbulent flow through the SEN and as the jet exits into the mould cavity. Of course this fact has implications on the choice of turbulence models during the CFD modelling process. Refer to [Appendix A](#) for these references.

2.3 CFD background

2.3.1 General: Numerical modelling and CFD

2.3.1.1 Introduction: basic equations

Currently, the mention of “CFD” is synonymous with commercial CFD packages such as FLUENT [10], CFX, STAR-CD and MSC Flow to mention but a few.

However, as already defined in footnote 4, “CFD” is the acronym for Computational Fluid Dynamics and encompasses the entire study field of Fluid Mechanics using computational or numerical methods.

It is however interesting to note that all these commercially available CFD packages are built upon the past 5 decades of research in numerical flow modelling [27]. As CFD researchers discover new applications and as computational power increases, commercial CFD packages include these new methods in their programmes in the form of more options.

The basic differential equations on which all CFD packages are built will be briefly presented in this section and the use of computers to solve these equations will be made relevant.

The basic equations are based on the three laws of conservation for a physical system: [9]

1. Conservation of mass (continuity)

2. Conservation of momentum (Newton's second law)
3. Conservation of energy (first law of thermodynamics)

The three unknowns, which must be simultaneously derived from these three basic equations, are the velocity \mathbf{v} , the thermodynamic pressure p , and the absolute temperature T . The final forms of conservation equations (which will be presented shortly) contain four other thermodynamic properties or variables: density ρ , enthalpy h , and the two transport properties μ (viscosity) and k (conduction). However, these four additional variables are assumed (following the assumption of local thermodynamic equilibrium) to be determined by the only independent variables p and T .

In order to specify a particular problem completely, the conditions (of various types) for \mathbf{v} , p and T must be known at every point of the boundary of the flow regime. The preceding considerations however apply only to a fluid of uniform, homogeneous composition: *i.e.*, diffusion and chemical reactions are not considered. Multi-component reacting fluids must consider at least two additional basic relations:

4. Conservation of species
5. Laws of chemical reactions

plus additional auxiliary relations such as knowledge of the diffusion coefficients $D = D(p, T)$, chemical-equilibrium constants, reaction rates, and heats of formation.

However, for the purposes of this introduction and basic background to CFD methods, only the differential equations⁸ derived from the basic three laws for physical flow will be presented.

⁸ To be more precise, partial differential equations (PDEs) are derived from these three basic laws. As it is not the purpose of this dissertation to derive the basic partial differential equations on which the CFD methods are based, these basic equations will only be shown (in basic form). However, whenever these basic equations are "modified" [28] in this dissertation using the FLUENT code [10] to enhance the numerical approximations of the analytical equations, it will be mentioned in the text and indicated accordingly.

In the event that the reader may require the derivations of these basic equations, refer to the following CFD sources in the references: [9][28][29]

The following partial differential equations were derived for general control volumes, expressed in Cartesian coordinates⁹:

1. Conservation of mass: the equation of continuity

$$\frac{D\rho}{Dt} + \rho \cdot \text{div}V = 0 \quad \text{with} \quad \frac{D}{Dt} = \frac{\partial}{\partial t} + (V \cdot \nabla)$$

$$\text{and } \text{div}V = \nabla \cdot V = \frac{\partial u}{\partial x} + \frac{\partial v}{\partial y} + \frac{\partial w}{\partial z} \quad \text{[eqs 2-1]}$$

where: V = velocity vector (column)

ρ = density

x, y, z = space coordinates in 3D

u, v, w = velocity components

t = time

2. Conservation of momentum: the Navier-Stokes¹⁰ equations

In scalar form, the Navier-Stokes equations, with the assumption of a general linear (Newtonian) viscous fluid, are presented as follows:

$$\rho \frac{Du}{Dt} = \rho g_x - \frac{\partial p}{\partial x} + \frac{\partial}{\partial x} \left(2\mu \frac{\partial u}{\partial x} + \lambda \text{div}V \right) + \frac{\partial}{\partial y} \left[\mu \left(\frac{\partial u}{\partial y} + \frac{\partial v}{\partial x} \right) \right] + \frac{\partial}{\partial z} \left[\mu \left(\frac{\partial w}{\partial x} + \frac{\partial u}{\partial z} \right) \right]$$

[eq 2-2-1]

$$\rho \frac{Dv}{Dt} = \rho g_y - \frac{\partial p}{\partial y} + \frac{\partial}{\partial x} \left[\mu \left(\frac{\partial v}{\partial x} + \frac{\partial u}{\partial y} \right) \right] + \frac{\partial}{\partial y} \left(2\mu \frac{\partial v}{\partial y} + \lambda \text{div}V \right) + \frac{\partial}{\partial z} \left[\mu \left(\frac{\partial v}{\partial z} + \frac{\partial w}{\partial y} \right) \right]$$

[eq 2-2-2]

$$\rho \frac{Dw}{Dt} = \rho g_z - \frac{\partial p}{\partial z} + \frac{\partial}{\partial x} \left[\mu \left(\frac{\partial w}{\partial x} + \frac{\partial u}{\partial z} \right) \right] + \frac{\partial}{\partial y} \left[\mu \left(\frac{\partial v}{\partial z} + \frac{\partial w}{\partial y} \right) \right] + \frac{\partial}{\partial z} \left(2\mu \frac{\partial w}{\partial z} + \lambda \text{div}V \right)$$

[eq 2-2-3]

where: in addition to the variables defined in equations 2-1 (above),

⁹ These equations can also be expressed in Polar coordinates or Cylindrical coordinates to suit these specific geometries. Refer to [9].

¹⁰ Although the momentum equations are derived from Newton's second law ($F=ma$), these equations are known as the Navier-Stokes equations owing to the fact that these equations were only derived following important and necessary assumptions made by Navier (1823) and Stokes (1845). [9]

$$\frac{D}{Dt} = \frac{\partial}{\partial t} + (V \cdot \nabla)$$

μ = viscosity for a Newtonian fluid

3. Conservation of energy: the energy equation (first law of thermodynamics)

With the assumption that the heat transfer to the element volume is governed by Fourier's law¹¹, the energy takes the final form of:

$$\rho \frac{Dh}{Dt} = \frac{Dp}{Dt} + \text{div}(k\nabla T) + \Phi \quad [\text{eq 2-3-1}]$$

where: in addition to the variables defined in equations 2-1 to 2-2 (above),

Φ = dissipation function or deformation heating¹²

k = conduction of continuum

h = enthalpy

p = pressure

The preceding basic equations (eqs 2-1 through 2-3) form the fundamental building blocks for all CFD codes.

2.3.1.2 Boundary conditions: general

In order to solve the flow (V , p , T) of a specified problem, an appropriate set of governing equations and boundary conditions must be selected. It is always prudent to consider solving simplified forms of the Navier-Stokes equations when the simplifications retain the physics, which are essential to the goals of the simulation.

¹¹ Fourier's law: $q = -k\nabla T$

where: q = the vector heat flow per unit area; k = conduction of the continuum; T = absolute temperature

¹² The dissipation function Φ involves the viscous stresses. It is always positive definite, in accordance with the second law of thermodynamics, since viscosity cannot add energy to the system [9].

Examples of simplified governing equations include steady flows ($d/dt = 0$) or incompressible flows ($\rho = \text{constant}$). Boundary types may include solid walls, inflow and outflow boundaries, periodic boundaries, and symmetry boundaries amongst others.

If necessary, physical models must be used for processes, which cannot be simulated within specified constraints (boundary conditions, assumptions). Turbulence is an example of a physical process that is not simulated but rather modelled using empirical information and modifications to the Navier-Stokes equations due to constraints in the Navier-Stokes equations [28].

Furthermore, the success of a simulation depends much on the engineering insight involved in selecting the governing equations, boundary conditions and physical models based on the problem specification. This fact will be elaborated on in the base case formulation in Chapter 4.

2.3.1.3 Discretisation of equations: the CFD approach

Solving the partial differential equations of a flow problem involving complex geometries requires a numerical approach: the complex flow domain needs to be divided into cells or elements. Such a numerical approach requires the tessellation of the flow domain, which is known as a mesh or a grid (in 2 dimensions (2D) or 3 dimensions (3D)). The sum of these cells (in 3D) or areas/elements (in 2D) will equal the flow domain.

Each of these cells can be regarded as a control volume. In order to solve for the flow (for example) in the calculation domain, the differential equations need to be discretised.

A numerical solution of a differential equation consists of a set of numbers from which the distribution of the dependent variables (for example p , T) can be constructed. This is different from the analytical solution that describes the

continuous values of p and T throughout the domain (for example x, y in 2D) – thus an infinite amount of values of the dependent variables.

Discretisation is thus a method that replaces the continuous information contained in the exact solution of the differential equation with discrete values of T and p (following the example) at a finite number of given points in the domain [29]. Employing a suitable discretisation method, the continuum calculation domain can be discretised: the discretisation of space and of the dependent variables makes it possible to replace the governing (partial) differential equations with simple algebraic equations, which can be solved with relative ease.

The discretisation method followed by most CFD codes is the control volume formulation: The calculation domain is divided into a number of non-overlapping control volumes such that there is one finite control volume surrounding one grid point. The differential equations are then integrated over each control volume.

Suppose (as a vehicle for explanation) that there is only one dependent variable ϕ described by a differential equation. Piecewise profiles expressing the variation of ϕ between the grid points are used to evaluate the required integrals: the result is a discretisation equation containing the values of ϕ for a group of grid points. The discretisation equation obtained in this manner expresses the conservation principle for ϕ for the finite control volume, just as the differential equation expresses it for an infinitesimal control volume [29].

The control volume discretisation formulation ensures the integral conservation such as mass, momentum and energy over any group of volumes, and thus over the entire calculation domain.

For more information on developing or deriving control volume discretisation equations for CFD codes, refer to references [28][29][30][31].

2.3.2 Pre-processing: geometry and grid generation

Pre-processing for any CFD flow problem to be solved comprises the preparation of the geometry, as well as dividing of the flow domain or geometry into cells or elements, called the mesh or grid. Pre-processing can thus be summarised as being the process of geometry and (initial)¹³ grid generation.

Most commercial CFD packages employ their own pre-processor¹⁴ to generate the geometry and grid. In the event of a design study (or optimisation design), most pre-processors enable users to make use of a parametric grid description, which can be automatically altered by merely adjusting parameters.

Different gridding strategies exist: structured (mostly hexagonal), unstructured (triagonal and pyramids), hybrids, composite and overlapping grids. The choices of numerical methods (discretisation equations) and models (especially turbulence models) to be used, and gridding strategies, are strongly interdependent. The success of a simulation can depend on appropriate choices (gridding strategies and models) for a certain class of problems.

2.3.3 Models in commercial CFD codes

Instead of using the complete set of partial differential equations (based on the complete compressible equations shown in section 2.3.1), “model” equations are used which isolate certain aspects of physics contained in the complete set of equations.

¹³ Pre-processing creates an initial grid before the CFD solution process is initiated and started. Most CFD codes include an option to alter the grid based on the solution in progress, also known as solution-adaptive gridding. These grid changes (grid refinement or grid coarsening for example) take place during the solution procedure and are obviously not part of pre-processing in CFD models.

¹⁴ The pre-processor used in this dissertation is GAMBIT [11], which is the pre-processor for FLUENT [10]

In order to save computational time, model equations (simplification assumptions on the flow) can be carefully selected to be representative of the solution of the complete set of equations.

The selection of turbulence models is especially important, as the direct numerical simulation of turbulence is extremely computationally expensive and thus not currently an option. Therefore, different turbulence models are used by CFD codes to “model” the expected influence of turbulence on the flow domain. Accompanying wall functions also need to be defined by the user when a turbulence model is chosen, to assume the boundary layer appearance (as the boundary layer will differ from that of a laminar flow domain).

More detail will be devoted on the choice of turbulence models and other settings in Chapter 4.

In conclusion on CFD simulations (sections 2.3.1 – 2.3.3): the success of the simulation depends almost entirely on engineering insight into the problem:

- intelligent choice of domain boundary conditions and grid strategy is essential;
- choice of CFD turbulence models is essential for representative solution of the class of problem;
- solution-adaptive gridding and convergence selection criteria¹⁵ are essential to ensure physically correct results.

2.3.4 Performance and monitoring criteria (for CFD modelling)

2.3.4.1 Residuals

When evaluating a flow problem using CFD techniques, it is important to constantly monitor the residuals of the solution procedure. The residuals are

¹⁵ More detail will be devoted on the choice of turbulence models and other settings in Chapter 4.

(briefly) the difference between the values of the solution field (velocity, temperature, continuity, and turbulence) for the preceding iteration and the current iteration. Low residuals suggest a solution that converged and can be considered as stable if the residuals keep lowering.

A typical criterion for a converged solution field is residual threshold values required for variables during the iteration process. Mostly, the energy required residual value is below 10^{-6} , and for momentum or continuity at least 10^{-3} . More detail on this matter will be discussed in Chapters to follow, especially Chapter 4.

In most CFD codes, it is possible to accelerate or slow down the changes from iteration to iteration. These methods are called over-relaxation and under-relaxation respectively. Under-relaxation (slowing down changes) is a very useful device for non-linear problems (especially the Navier-Stokes equations). It is often employed to avoid divergence in the iterative solution of strongly non-linear problems [29]. This method will be discussed at a later stage as a very important and useful tool to enforce convergence.

2.3.4.2 Solution monitoring

Low residuals are not a guarantee that the solution is correct. The solution might converge to an incorrect or non-physical¹⁶ flow field answer. It is therefore implorable that other performance criteria are monitored to ensure answers that, in the event of sufficient residual convergence, can be accepted and trusted as physically correct.

It is therefore customary and recommended by CFD coders that a physical quality or variable of the solution flow field is monitored to ensure a true converged solution:

¹⁶ The term non-physical is used to describe a flow field or heat distribution (for example) that is not possible or does not reflect physical reality. The concept of answers that are non-physical is common with CFD analyses and care must be taken to identify when a solution is diverging from reality.

For example, the velocity magnitude on the meniscus-surface (at a specific point) in a model of the continuous casting mould can be monitored. During the initial stages of the numerical computation, the residuals and the variables (physical qualities) will vary with each iteration. If the values of the residuals are sufficiently low, the answer may still not be converged: the velocity magnitude of a certain point on the meniscus surface may still be oscillating or still be asymptotically nearing its final value, indicating a solution that is not sufficiently converged. If the velocity magnitude remained constant for a sufficient¹⁷ number of iterations, and the residuals reached the pre-determined criteria, the answer (flow field) can be assumed to be converged and to consequently represent physical reality.

It is emphasised that a physical property must be monitored to ensure true solution convergence, especially since excessive under-relaxation (by the CFD user) can easily reduce residuals to unrealistically low values without true solution convergence.

2.4 Design Optimisation

The following section offers a general background on design optimisation to the reader who is unfamiliar with this process. More detail information on the specific mathematical optimisation technique used in this dissertation will be presented in Chapter 5.

Design optimisation using CFD modelling encompasses the following processes (in chronological order):

- Base case evaluation

¹⁷ This term is also quite commonly used with CFD calculations, as the sufficient criteria for convergence depends on the type of problem, type of assumptions, type of equations used, type of grid and solution convergence strategy, *inter alia*. In this dissertation, the term “sufficient” will be defined properly in the text whenever used.

- CFD model perfection
- Parameter / variable identification
- Objective function(s) and constraint function(s) identification
- Parameterisation of geometry to be designed
- Optimisation begins:
 - Evaluate perturbations around base case
 - Optimiser¹⁸ predicts new optimum set of points (one design iteration)
 - New perturbations are chosen (by the Optimiser) around optimum set of points – new optimum is predicted after all perturbations (of variables) are evaluated
 - Optimisation continues until objective function is minimised and constraint functions are satisfied sufficiently (more design iterations)
- Experimental evaluation of optimum or final design (if necessary)
- Evaluation of off-design performance of optimum design – robustness of optimum (as in the case with manufacturing tolerances, for example)
- Trade-off studies with regards to certain parameters and variables to obtain true optimum

2.4.1 Base case evaluation and model perfection

Most design optimisation problems involve an existing physical process to be optimised. This existing process is called the base case in the optimisation design process. The logical first step is to evaluate the base case in the CFD code and to compare the results with the real physical process. All the relevant gridding strategies, assumptions made and models chosen in the CFD code can be experimented with to perfect (or to at least closely resemble the physical process) the CFD model of the base case.

¹⁸ The Optimiser refers to a software package (based on a mathematical optimising algorithm) utilised to predict the combination of variables that will minimise the chosen objective function, using the base case information and a set of perturbed base case designs (set of parameters). The Optimiser used in this dissertation is LS-OPT [12]

Evaluating the base case usually gives the user insight into the problem and can lead the user to identify suitable parameters or variables that have a marked influence on the solution flow field.

2.4.2 Parameter and objective and constraint functions identification

The goal of optimisation is to alter certain design variables (selected from process parameters) of an existing process (the base case) in such a way that the “best” combination of parameters (thus design) is found. The “best” design must be quantified: this is achieved by choosing (or developing) an objective function (a function of the parameters or variables). Usually, the objective function is chosen in such a way that the latter must be minimised for the best or optimum solution. Simultaneously, constraint functions are chosen for obvious constraints (e.g., minimum temperature cannot be lower than the solidus temperature) and other design-related constraints as a certain maximum SEN nozzle angle, for example. These constraint functions must be satisfied while minimising the objective function.

For example, if the maximum turbulent kinetic energy on the meniscus surface of a mould in the continuous casting process is to be minimised while limiting the minimum meniscus temperature to prevent freezing, the combination of variables (e.g., nozzle angle with horizontal, submergence depth of nozzle, nozzle port height) that causes the lowest turbulent kinetic energy, is the optimum (and constrained) design.

Further examples of constraint functions are typical bounds (minimum and maximum) for all design parameters, along with other physical constraints as manufacturing tolerances, for example. Monitored quantities such as velocities, temperatures and pressures, or integrals of them on surfaces or in volumes, may also be used as constraints to be satisfied during optimisation.

2.4.3 Parameterisation of CFD model

The more variables to be optimised, the more perturbations are necessary for the optimiser to predict the next optimum design in each design iteration. In this dissertation the amount of variables (and thus number of CFD evaluations needed) forced the author to make use of the scripting capability of the pre-processor GAMBIT [11]: the geometry and mesh generation were parameterised. The Optimiser can now specify a set of variables for a new and unique geometry to be generated by GAMBIT with the parameters as the only input.

Linking the Optimiser, CFD code and pre-processor, the design optimisation process can be started.

2.4.4 Design optimisation [general description]

The first design iteration comprises the evaluation of the base case and the perturbations (of designs) “around” the base case. The objective function value is now known for all these cases. The Optimiser fits a curve or rather hyper surface¹⁹ or approximation through the points (values of objective function as a function of the design variables), and predicts the new combination of variables (thus a design) where the lowest objective function value occurs (according to the curve or approximation fitted through the known points).

For the second design iteration, the optimum achieved in the preceding iteration serves as the new “base case”. The same procedure is followed to obtain an optimum design for the second design iteration.

¹⁹ This is a very general description and only applicable to one and two variable optimisation problems: obviously, if there are more than two variables, this “curve” cannot be visualised (in which case it will be a hyper surface).

This process is continued until the objective function converges to a constrained minimum, corresponding to the optimum combination of design variables, also known as the optimum design.

2.4.5 Experimental validation

The optimum design is usually validated by the physical process. For example, if a new design for a Submerged Entry Nozzle (SEN) is suggested, the SEN will typically be built and the CFD results can be validated if compared to the measurements in the real physical continuous casting process.

In the event of a process that will have immense environmental and/or financial implications (as a nuclear reactor design change), other experimental validations of the CFD models can be considered. In this dissertation, the CFD models are validated and compared with full scale and 40%-scaled water models of the continuous casting mould. The validation of the CFD models with water modelling will be discussed in detail in the appropriate Chapter.

2.5 Conclusion of Literature Survey

The brief history of continuous casting of steel was firstly presented to show the progress of this process over the years. Initially, the SEN was not focused on at all due to the many other technical problems that had to be eliminated to enable continuous casting. In an ongoing historical effort to reduce the height of continuous casting machines (consequently lowering the ferrostatic forces and therefore plant costs), a horizontal casting machine is acquired in the limit. However, with the latter set-up, a SEN is substituted for a horizontal refractory nozzle, and therefore falls beyond the scope of this dissertation.

More recently, as indicated by the vertical continuous casting literature, the SEN is recognised as the last component in the continuous casting process, which may have a marked influence on the ultimate quality of the steel. It is therefore an attractive subject for design optimisation.

The continuous casting literature consulted was classified in different categories, namely SEN/mould, tundish, inclusions and ladle literature. The SEN/mould literature (as well as the tundish literature) can be subdivided into the following categories: water modelling, numerical modelling and plant trials. This dissertation will mostly be involved with water modelling and numerical modelling.

Necessary background on numerical modelling and CFD modelling illustrated the basic principles of using computers to model real engineering flow problems. Furthermore, the importance of engineering insight into any CFD modelling exercise was highlighted.

Lastly, a very brief description of general mathematical optimisation was presented as general background to the reader unfamiliar with optimisation techniques.

This concludes the literature survey and should place the dissertation topic (CFD model generation and validation, in an effort to obtain an optimum SEN design using mathematical optimisation techniques) into perspective for the reader.

CHAPTER 3: EXPERIMENTAL VERIFICATION: SCALED WATER MODEL AND RESULTS

The importance of a correct CFD model is immeasurable, as an incorrect model (non-repeatable solutions) will render the entire design optimisation process useless. At first, this study was based on the assumption that the CFD models are physically correct and that repeatable results will easily be obtained. However, it was soon discovered that the specific flow situation (jet flowing into a bigger cavity) is complicated and that experimental verification is essential to ensure correct CFD models. Thus, it was decided that a water model should be built to verify the CFD models of the base case Submerged Entry Nozzle (SEN) design (and obviously later designs as well).

A full-scale water model simplifies the comparison of results with the plant circumstances due to the similar kinematic viscosities¹ of water and steel. However, the water model is a 40%-scaled model due to height constraints in the university laboratory. An equivalent full-scale height of 3 to 4 metres is achieved with the 40%-scaled model, which the author deems as a necessity to prevent effects of the bottom on the flow field (which would have been the case with a shallower full-scale water model).

3.1 40%-Scaled water model of SEN and mould

3.1.1 Concept design

A few design criteria were laid down before conceptual designs for the 40%-scaled water model were conceived:

- Maximum (laboratory) height restriction of approximately 2 metres

¹ Kinematic viscosity $\nu = \frac{\mu}{\rho}$; μ = dynamic viscosity; ρ = density

- SEN bottom part (nozzle area) must be interchangeable (to easily allow the test of other SEN designs)
- Design should accommodate different widths, ranging from a full-scale 900mm to approximately 1575mm
- Design must share the water source currently used for the existing Columbus tundish water model² in the laboratory of the University of Pretoria
- Entire water SEN and mould model must be bolted together, to facilitate easy dismantling in the event of the possible relocation of the water model

The first concept was to use an open tank mounted on top of the SEN/mould to simulate the tundish in the real plant circumstances. According to preliminary calculations, Re-similarity velocities would not be reached (refer to section 3.2 for detailed explanations) owing to the too low Δh due to the height restriction (see Figure 3.1 below).

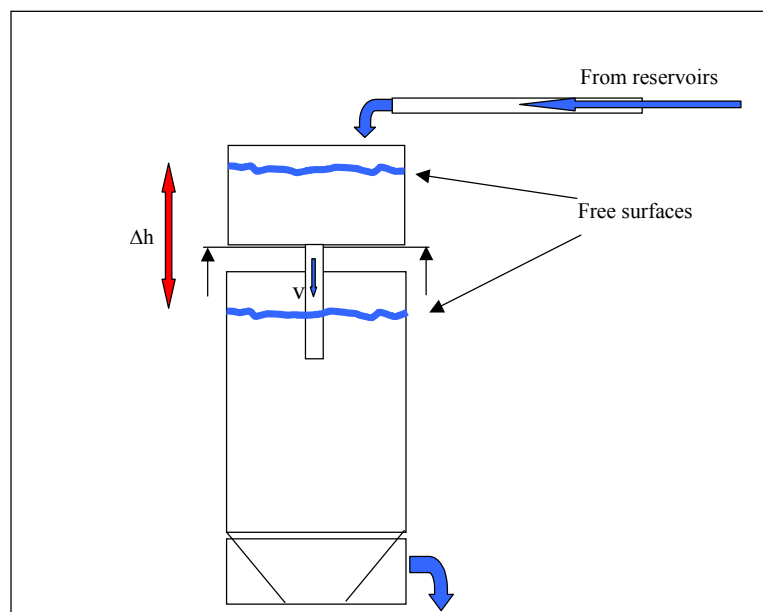


Figure 3.1: Design concept: open tank with Δh as flow velocity source

Calculations proved that a closed top tank would be needed, together with the water reservoirs on the laboratory's roof (currently used for the tundish water

² Joint venture by Columbus Stainless, Middelburg, and the cfdlab of the Multi-Disciplinary and Optimisation Group (MDOG), University of Pretoria

model). An additional pump would also be necessary for extra pressure to obtain the correct exit velocity from the SEN ports. Refer to Figure 3.2 for the schematic representation of the final concept and layout of the 40%-scaled water model.

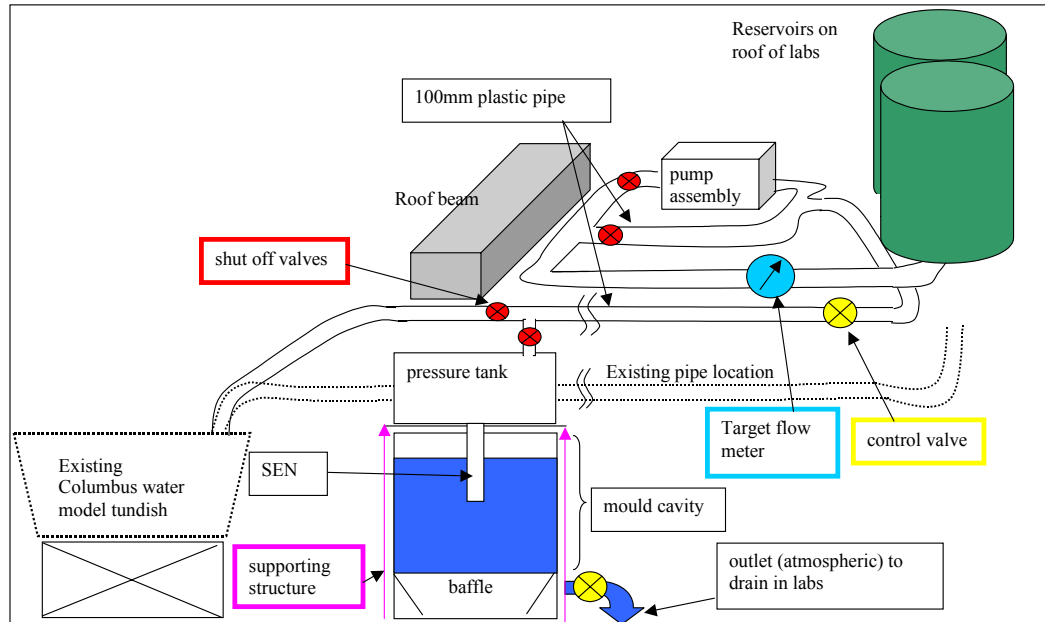


Figure 3.2: Schematic representation of SEN/mould water model and layout

3.1.2 Design

The water model mainly consists of five parts: (Refer to Figure 3.3 for the general water model layout)

1. Top tank with stopper to simulate a tundish. The tank can either be kept open to control the water height, or be closed off to be pressurised for very high flow rates.
2. Perspex mould (not shown in Figure 3.3), which can be varied in width from 360mm to 630mm (a full-scale 900mm to 1575mm). The thickness is a constant 80mm (full-scale 200mm). The thickness can easily be varied at a later stage by installing different narrow Perspex walls.
3. Bottom tank with holes and baffles to slow down and evenly distribute the water flow, together with a gate valve to throttle down the flow towards the drain.

4. Frame that supports the top tank, Perspex mould, as well as the bottom tank.
5. Aluminium SEN consisting of three parts:
 - the upper part connected to the top tank;
 - a middle section which screws onto the upper part;
 - and an insert at the bottom, which contains the bifurcated ports.The insert will typically be the only part that will be altered during SEN design optimisation; consequently costs will be kept low when new optimum designs need to be validated with the water model.



Figure 3.3: General layout of water model (top tank, frame and bottom tank – Perspex mould not shown)

The remaining parts or components mainly consist of pipes, reducers, shut-off valves, elbows, T-sections and other water piping accessories and equipment. These ‘off the shelf’ components are only applicable to the construction phase (section 3.1.3).

More detail on the design of the five (5) different parts of the water model will follow. Detail design calculations are included in Appendices where deemed necessary.

1. Top tank

Description:

The top tank is constructed from stainless steel and is cylindrically shaped. An inner baffle inside the cylindrical tank, as indicated in Figure 3.4, ensures that the flow simulates the annular flow that typically takes place at the outlet of a tundish. The tank is designed to operate with an open top (for low SEN velocities) or a closed top – where a pressure of at least 6m of water (59kPa gauge) can be accommodated.

As the top tank is not constrained by the rectangular shape of the frame (unlike the bottom tank), the more convenient cylindrical shape saves cost and increases volume.

The thickness of the stainless steel plate used for the tank circumference, inner ring, base and (detachable) lid is 2.5 mm. Calculations showed that 2.5mm thick plate is sufficient to hold the mass of the water, as well as the additional pressure should the faster flow rate be required. Figure 3.4 below shows an isometric view of the upper tank and its detachable lid.

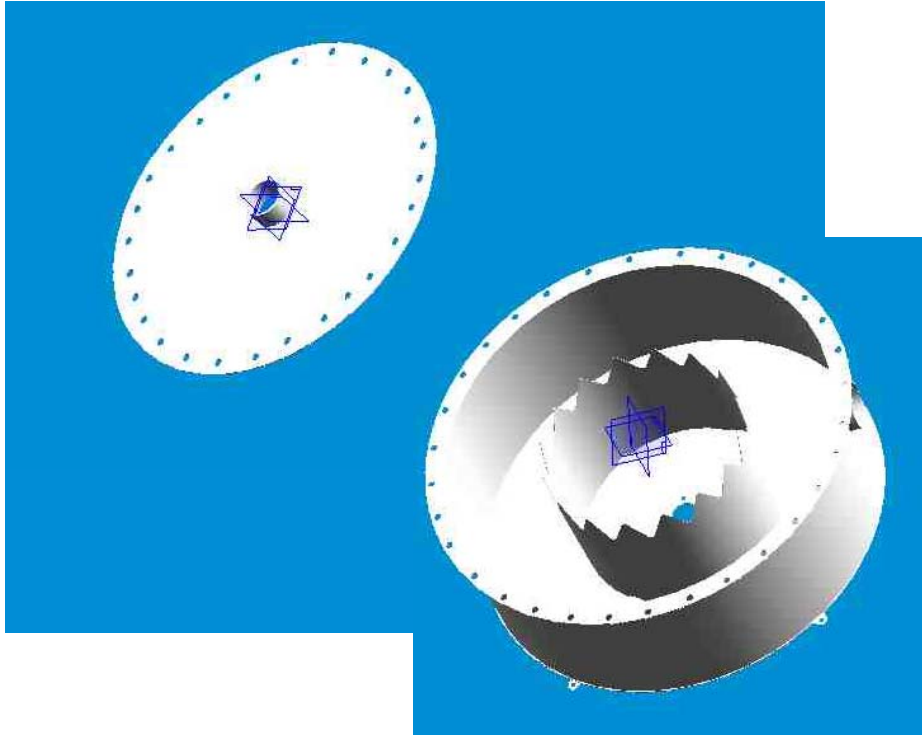


Figure 3.4: Isometric view of upper cylindrical tank and detachable lid

The stopper inside the upper tank can be adjusted to simulate the stopper of a real tundish. Figure 3.5 shows that the stopper can even be adjusted if the lid is fastened, using the extended lead screw. The 40%-scaled stopper has a small hole drilled in its centre, which is connected with a flexible tube to a dye injector (refer to Figure 3.6). A hand drawing (assembly drawing with Aluminium SEN) indicating the dimensions of the 40%-scaled stopper is shown in [Appendix D](#), Figure D.5.

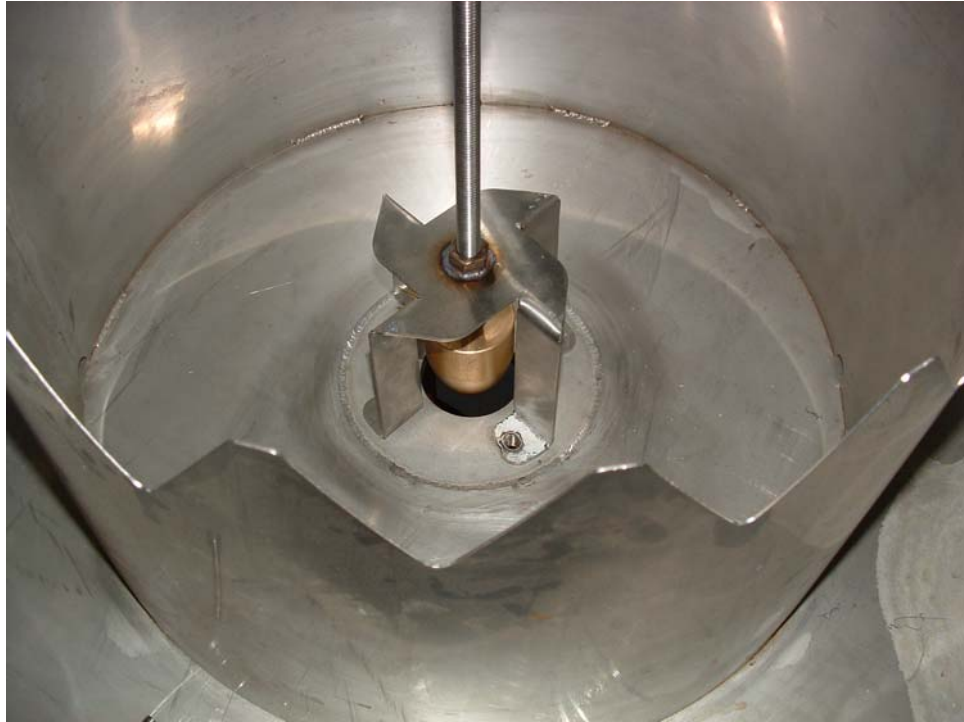


Figure 3.5: Stopper inside the upper cylindrical tank



Figure 3.6: Application of dye through the stopper – hole drilled through stopper

2. *Perspex mould*

The Perspex mould is the most important part of the water model, as the flow visualisation will take place here. In order to maximise visibility, the upper parts of the Perspex mould should not be obscured by steel supports or the frame.

The design is simple, yet different widths (and even slab thicknesses if desired at a later stage) can easily be modelled. Two thick³ Perspex (Plexiglas) narrow walls are clamped between two Perspex sheets along the length (vertical direction) of the mould cavity using the specifically designed adjustable frame. The four walls (narrow walls and wide walls) are sealed on the bottom tank, also using the frame.

Calculations proved that Perspex with a thickness of 10mm is sufficient to support the worst-case scenario (deepest submergence and largest width), provided the sides are supported throughout the depth, as well as supported in the width at predetermined depths to prevent bulging as the water pressure increases towards the bottom tank.

3. *Bottom tank*

The bottom tank shape is rectangular in order to be accommodated inside the frame. It is designed from 2.5mm thick stainless steel: the entire tank is designed to be laser-cut, folded and TIG⁴ welded. Furthermore, the tank is a sealed unit and cannot be opened. The bottom tank is designed to safely accommodate the pressure exerted by a brim-full mould, as well as sustaining the load of the Perspex mould full of water.

The lid is provided with 16 holes where the Perspex mould is sealed to the bottom tank, to simultaneously slow down the flow. Inside the sealed tank, another three baffles are present in an effort to uniformly slow down the flow towards the exit valve at the bottom of the bottom tank. Refer to Figure 3.7 below for an isometric view of the bottom tank. The baffles inside the tank are not shown, but can be viewed in [Appendix B](#). Also refer to [Appendix B](#) for the detail drawings of the bottom tank (open folded sheet metal).

³ Thick Perspex narrow mould walls: three or four layers of Perspex are bonded or glued together

⁴ TIG welding: Tungsten Inert Gas welding. Tungsten tip welding machines are used with an inert gas (mostly CO₂) to weld stainless steel, as high temperatures are required.

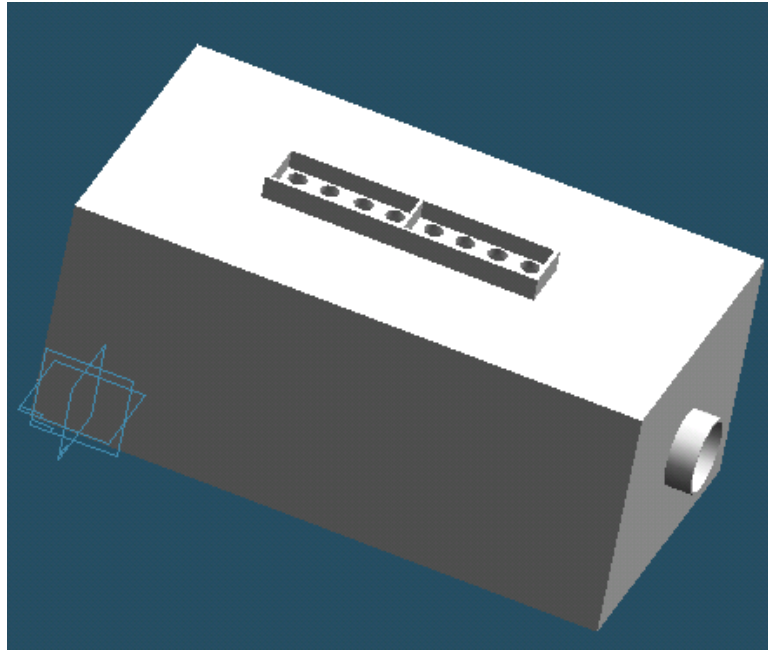


Figure 3.7: Isometric view of bottom rectangular tank (baffles inside not shown)

4. Frame

The fact that the water model must be “portable”, implicated that the frame must be able to support itself on a base plate or its own “feet”. This ruled out the possibility of erecting a frame that is concreted into the laboratory floor.

The frame concept can be described as four angle iron “legs” bolted onto two similar angle iron feet, separated by quite large section square tubing. (Refer to Figure 3.3 above for clarification). Hanging from the top square tubing separators, four similar square tubing sections ensure that the Perspex walls are pressed firmly against the thin walls, using long bolts and aluminium strips (to distribute the bolt pressure uniformly). These four hanging sections are automatically locked into position due to the outward pressure of the opposing bolts, pressing the Perspex sheets (wide mould walls) against the narrow mould walls.

The steel sections used to construct the frame were chosen after taking into account the mass of the (filled) top water tank, mass of the water inside the Perspex mould, as well as the forces exerted by the hanging sections onto the frame to counter the effect of the water pressure inside the Perspex mould.

Refer to [Appendix C](#) for the steel sections chosen ([Table C.1](#)). The choice of steel sections was based on not exceeding design stresses (taking into account a Safety Factor of at least 2) caused by bending moments on the sections in question.

[Appendix C](#) also shows the final detailed (hand) drawings of the frame and structure, showing where all the sections are utilised.

Mark-off die

During the design phase, the author anticipated potential accuracy problems regarding the connecting holes of the angled sections: a one millimetre mark-off error at the feet or base sections can cause a deviation of more than 200mm at the top of the frame. A special mark-off die was devised to assist in the mark-off procedure, to ensure repeatable and accurate holes in the angled sections.

5. Aluminium SEN

The Aluminium SEN is a 40%-scaled replica of the base case SEN design⁵ of Columbus Stainless. The Aluminium SEN consists of three parts.

The insert (bottom part) will typically be the only part that will be altered during SEN design optimisation; consequently costs will be kept low if new optimum designs need to be validated with the water model. Another more inexpensive method of altering the bottom part would be to insert small pieces into a generic bottom part, sealing the bifurcated ports with silicon or something similar.

In order to save time, the Aluminium SEN was manufactured from detail hand drawings. These drawings can be viewed in [Appendix D](#).

⁵ Base case SEN design: Refer to Chapter 4 for detail information concerning the current SEN design of the company Columbus Stainless, Middelburg, South Africa. This base case will be the starting design for the optimisation work later in this dissertation, and further work to follow.

The middle section is the most interesting part, which morphs from a circular cross section to a rectangular cross section (including the inside downward ports). A spark erosion technique was used to form the inside ports: a copper mandrel (machined to represent the negative of the inside or downward ports) is connected to large electrical current, causing high-energy sparks (arcing) to the earthed Aluminium SEN. The mandrel slides into the melting Aluminium, forming the desired ports. The manufacturing of these parts was outsourced, as such facilities are not available at the university.

Refer to Figure 3.8 below, which shows the 3 exploded parts of the Aluminium SEN.

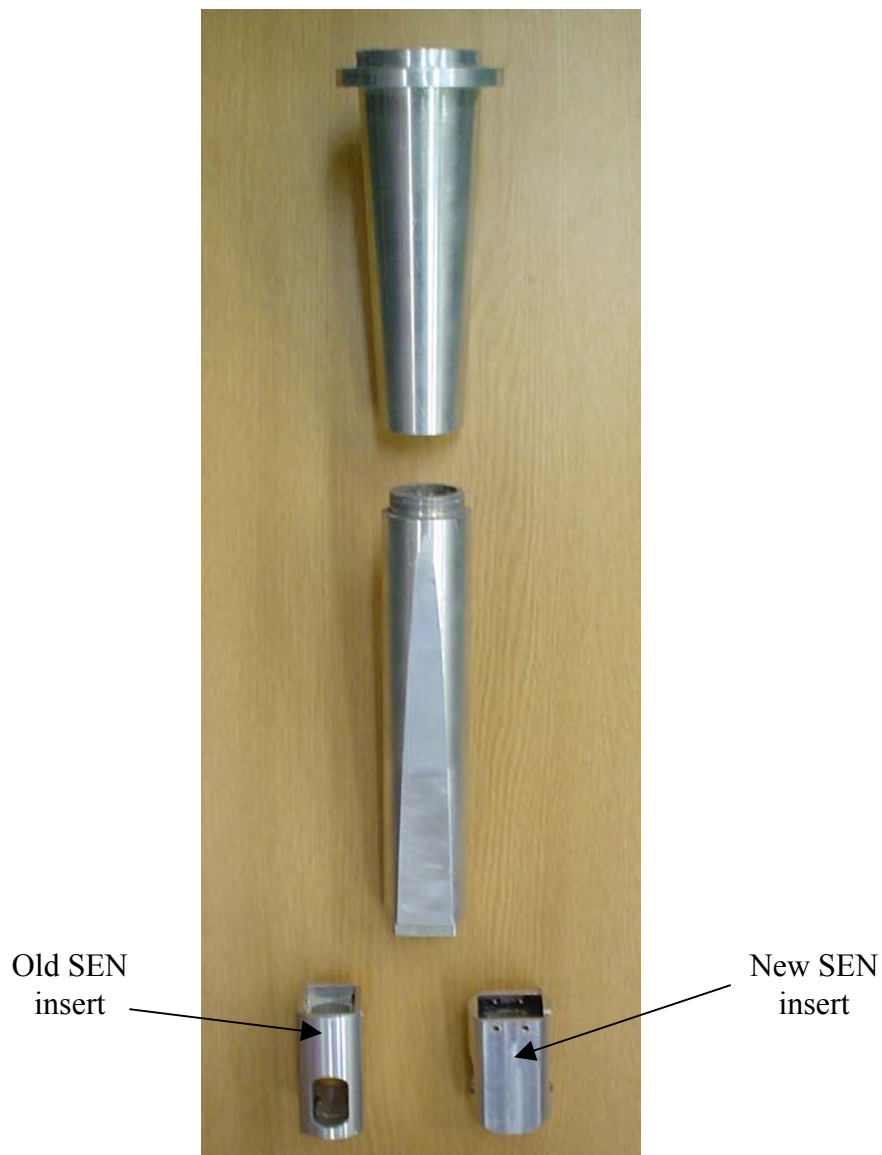


Figure 3.8: Aluminium SEN (3 different parts) shown in exploded view

3.1.3 Construction

In order to avoid elaborate and chronological explanations of the exact progress with regard to the construction of the SEN and mould water model, the construction progress is presented in [Appendix E](#). A Gantt-chart of the progress of the water model construction is also shown for the sake of completeness. Note that the author was involved part-time from January 2003.

3.1.4 Commissioning

Official commissioning took place on 15 September 2003 at the Mechanical Engineering laboratory of the University of Pretoria.

The commissioning could only take place after all pipes, valves and elbows were connected to the water model. The commissioning was performed with an open top tank to enable better view for fault finding, and as only the lower test speeds were to be used.

Figure 3.9 below shows one of the first steps during commissioning, showing water from the nozzle jets exhausting in the air as the Perspex mould is being filled up (by keeping the outlet gate valve at the bottom tank closed).



Figure 3.9: Water model being filled up: SEN nozzles exhausting in the air

The commissioning involved the following tests and actions:

- Fill up the top tank to check for leaks
- Open the stopper in the top tank (refer to Figure 3.5) to enable flow through the SEN
- Keep bottom valve closed until water level is at desired height (thus desired submergence depth for the SEN).
- Check the effectiveness of the seals:
 - between the Perspex mould and bottom tank
 - between the wide mould walls (single Perspex sheet) and the narrow mould walls
- Check for any bulging of the wide walls of the Perspex mould – which will indicate the lack of sufficient support
- Inject dye into the stopper to view the flow patterns. Evaluate the effectiveness of the dye and injection method

The following conclusions were reached after the commissioning, which will be addressed before final and official testing can take place:

- Sealing between Perspex mould and bottom tank inadequate. The use of additional silicon should resolve the matter.
- Sealing between narrow and wide Perspex walls inadequate due to lack of uniform distribution of opposite bolt forces. More aluminium blocks to be used in-between current bolt locations, to distribute sealing forces more uniformly.
- Better flow rate measurements are needed, especially if an open top tank will be used. A rotary flow meter in the outlet of the bottom tank will be installed. If the mould depth is kept constant, the outlet flow meter will accurately represent the flow rate through the SEN.

3.1.5 Further improvements after commissioning

Additional improvements took place since the commissioning of the water model, with the help of an under-graduate student for his fourth year project⁶.

The most significant improvements concerned the installation of a rotameter flow meter at the outlet, as well as the replacement of the front Perspex panel with a much stiffer carbon-Perspex sheet. Figure 3.10 shows the upgraded flow control section at the outlet of the mould model.

⁶ *Computational and experimental modelling of continuous caster mould and submerged entry nozzle*, Marius Botha, October 2004. Undergraduate thesis, Department Mechanical and Aeronautical Engineering, University of Pretoria.

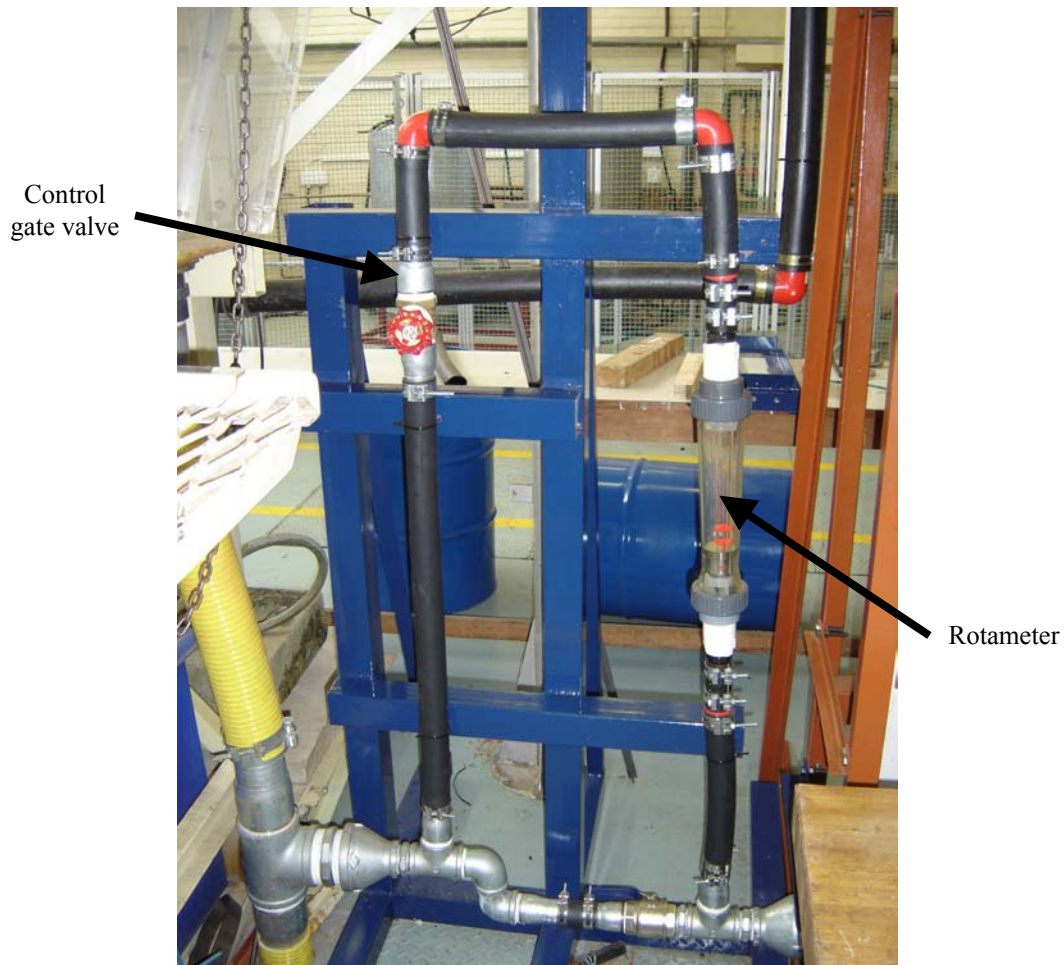


Figure 3.10: Upgraded flow control and flow rate measurement section at the mould model outlet

A modular bottom section of the Aluminium SEN was also devised, consisting of a main body where only small parts or inserts need to be machined. This modular bottom insert is compared with the previous base case bottom insert in Figure 3.11. This is a significant improvement, as the manufacturing of a typical previous bottom section required expensive machining techniques (*i.e.*, spark erosion). The small inserts can be manufactured using conventional milling machines. However, the boxy outside dimensions of the modular bottom section does not correspond exactly to the actual SEN dimensions. However, the effect of these differing outside dimensions on the subsequent flow is assumed to be negligible.

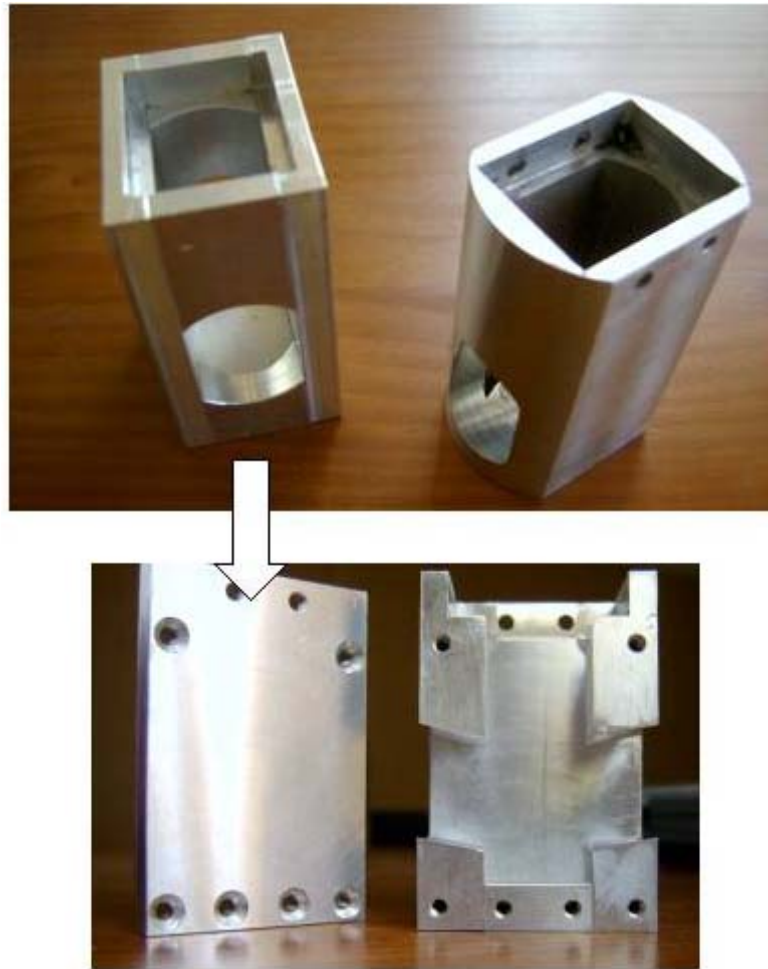


Figure 3.11: Improved modular SEN bottom insert compared with previous insert

Other improvements included:

- General stiffening of the frame (mostly the four hanging pillars exerting pressure onto the Perspex mould)
- Different sealing method: double seal system employing O-rings to seal narrow walls to the wide Perspex walls
- Fixed bolts on hanging pillars to ease set-up of mould during width changes.

3.2 Similarity issues

3.2.1 General

Before comparing results (during and shortly after commissioning) of the 40%-scaled water model with an ADVENT full-scale model [32], some similarity issues need to be elaborated on.

Froude, Reynolds and Weber similarity in scaled modelling

A full-scale water model requires no velocity scaling due to the dynamic similarity between liquid steel and water, as they share approximately the same kinematic viscosity. However, the 40%-scaled model in this dissertation requires a velocity scaling according to Froude, Reynolds or Weber similarity.

Depending on the flow situation, different similarity tests need to be performed:

- If the meniscus motion of the water model needs to be dynamically similar to that of the steel caster, Froude (Fr) similarity needs to be satisfied. The Fr-number relates inertial forces to gravitational forces and is the dominant effect in wave motion of free-surface flows and is totally unimportant if there is no free surface [33].
- If the SEN jet needs to be captured with water modelling tests, Reynolds (Re) similarity should be satisfied. The Re-number is always important, with or without a free surface, as it relates inertial forces to viscous forces, and can be neglected only in flow regions away from high velocity gradients as solid surfaces, jets or wakes.
- Another free-surface parameter is the Weber (Wb^7) number. It relates inertia to surface tension. The Wb-number is important only if it is of order unity or less, which typically occurs when the surface curvature is comparable in size to the liquid depth, e.g., in droplets, ripple waves and very small hydraulic systems [33].

⁷ Some references [9] also make use of the abbreviation We-number when referring to the Weber number.

However, with the assumption that the flow is fully turbulent at a high flow rate, the jet behaviour will be independent of the Re-number and the SEN jet will be dynamically similar at the lower velocity of the Fr-similarity as at the higher flow rate. Refer to section 3.2.3 for detail explanation [33].

3.2.2 Fr-number

The Froude number (Fr-number) is proportional to the ratio of inertial forces to gravitational forces in a flow field or situation. Mathematically, it can be expressed as:

$$Fr = \frac{V^2}{Dg}$$

where: V = velocity
 D = diameter or length
 g = gravitational constant

As explained above, Fr-similarity needs to be satisfied whenever wave phenomena and meniscus behaviour are modelled. If Fr-similarity is satisfied, the meniscus motion will be dynamically similar to that of the full-scale water model (and therefore the full-scale caster).

In order to compare the 40%-scaled water model meaningfully with a full-scale water model, the flow rate must be calculated to satisfy Fr-similarity.

A typical casting speed is 0.9m/min for a 1575mm-width mould, with a thickness of 200mm.

The plant flow rate (Q_p) will thus be:

$$Q_p = 1.575 \times 0.2 \times \frac{0.9}{60} m^3 / s$$

$$\text{or } Q_p = 17m^3 / h$$

The flow rate for the 40%-scaled model (Q_m) will differ from that of the plant caster. In order to satisfy Fr-similarity, the Fr-numbers must be equal:

$$\frac{V_m^2}{D_m g} = \frac{V_p^2}{D_p g} \quad [\text{eq 3-1}]$$

where: V_m = velocity inside 40%-scaled model SEN
 D_m = diameter or length of 40%-scaled model SEN
 g = gravitational constant (9.81 m/s²)
 V_p = velocity inside full-scale SEN
 D_p = diameter or length of full-scale SEN

Solving equation 3-1, the necessary velocity of the 40%-scaled model (V_m) can be computed:

$$V_m = \sqrt{\frac{D_m}{D_p}} \times V_p \quad [\text{eq 3-2}]$$

By substituting $D_m/D_p = 0.4$ ([eq 3-3]) into equation 3-2, V_m is now expressed in terms of V_p : namely $V_m = 0.632455 V_p$

Subsequently, the flow rate for the 40%-scaled model, satisfying Fr-similarity, can be expressed as (equation 3-4):

$$Q_m = A_m \times V_m \quad [\text{eq 3-4}]$$

where: Q_m = 40%-scaled model flow rate required
 A_m = cross sectional area inside 40%-scaled model SEN
 V_m = velocity inside 40%-scaled model SEN

$$\text{or } Q_m = \frac{\pi}{4} (D_m^2) \times V_m \quad [\text{eq 3-5}]$$

By substituting equation 3-3 into equation 3-5, the following results:

$$Q_m = \frac{\pi}{4} (D_p^2 \times (0.4)^2) \times 0.632455 V_p \quad [\text{eq 3-6}]$$

Thus, by rearranging equation 3-6,

$$Q_m = \frac{\pi}{4}(D_p^2) \times V_p \times (0.4)^2 \times 0.632455$$

$$Q_m = A_p \times V_p \times 0.1012$$

$$\text{Thus: } Q_m = 0.1012Q_p = 1.72 \text{ m}^3/\text{h} \quad [\text{eq 3-7}]$$

In order to satisfy Fr-similarity with a 40%-scaled model, a flow rate through the 40%-scaled SEN of approximately 10% of that of the full-scale model or plant caster, is required. Refer to section 3.3 in this chapter to view the results, where the 40%-scaled model is compared with the full-scale model, whilst satisfying Fr-similarity.

3.2.3 Re-number

Re-similarity is regarded as the most important similarity to be adhered to during fluid dynamical scale modelling. The Re-number is proportional to the ratio of inertial forces to viscous forces, and is expressed as

$$\text{Re} = \frac{\rho VD}{\mu}$$

where: ρ = density of fluid
 V = velocity
 D = diameter or length
 μ = dynamic viscosity

Following the same process as in section 3.2.2 above, the required flow rate will be calculated in order to satisfy Re-similarity:

Assume that the plant casting speed or flow rate is $Q_p = 17 \text{ m}^3/\text{h}$ again.

In order to satisfy Re-similarity, the corresponding velocity in the 40%-scaled SEN (V_m) must be isolated from equation 3-8 below:

$$\left(\frac{\rho VD}{\mu} \right)_m = \left(\frac{\rho VD}{\mu} \right)_p \quad [\text{eq 3-8}]$$

where: V_m = velocity inside 40%-scaled model SEN
 D_m = diameter or length of 40%-scaled model SEN
 μ_m = dynamic viscosity of water [1.0x10⁻³ kg/(m.s)]
 ρ_m = density of water (for water model) [998 kg/m³]
 ρ_p = density of steel (for caster) [6975 kg/m³]
 μ_p = dynamic viscosity of liquid steel [6.4x10⁻³ kg/(m.s)]
 V_p = velocity inside full-scale SEN
 D_p = diameter or length of full-scale SEN

Thus;

$$V_m = \left(\frac{\rho_p \mu_m}{\rho_m \mu_p} \right) \left(\frac{D_p}{D_m} \right) V_p \quad \text{[eq 3-9]}$$

And by substituting the values given in equation 3-8 into equation 3-9, the following is obtained:

$$\begin{aligned} V_m &= (1.092)(2.5)V_p \\ &= 2.73 V_p \end{aligned}$$

The required flow rate is thus:

$$Q_m = \frac{\pi}{4} (D_m^2) \times V_m, \text{ and following the same process as in section 3.2.2, it}$$

follows that

$$Q_m = 0.4368 Q_p \quad \text{[eq 3-10]}$$

which is approximately 4 times larger than the required flow rate when Fr-similarity is satisfied.

Assumption:

However, as briefly mentioned in the general description above (section 3.2.1), the author assumes that the flow is already fully turbulent at the flow rate corresponding to the Fr-similarity, which renders the jet behaviour independent of the Re-number.

The assumption is vindicated by the following explanation:

Recalling the typical Darcy friction factor⁸, f , as a function of the Re-number inside a pipe [33], note that as soon as the flow becomes fully turbulent, f remains constant, independent of the Re-number.

The same principle applies for the flow inside the 40%-scaled SEN and as the jets exit the nozzles: the flow is already fully turbulent when the Fr-similarity is satisfied, as equations 3-11 to 3-12 verifies below.

In order to satisfy Fr-similarity, (from equation 3-7)

$$Q_m = 0.1012 Q_p = 0.1012(17.01/3600) = 4.7817 \times 10^{-4} \text{ m}^3/\text{s}$$

The diameter inside the SEN is $\phi 24\text{mm}$ (40% of the full-scale $\phi 60\text{mm}$), thus the velocity inside the model is

$$V_m = \frac{Q_m}{A_m} = \frac{4.7817 \times 10^{-4}}{\frac{\pi}{4}(0.024)^2} = 1.057 \text{ m/s} \quad \text{[eq 3-11]}$$

Using the definition for Re, the Re-number for the 40%-scaled model is calculated:

$$\text{Re} = \frac{\rho V D}{\mu} = \frac{(998)(1.057)(0.024)}{(1 \times 10^{-3})} \approx 25300 \quad \text{[eq 3-12]}$$

For internal flow, fully turbulent flow is assumed at $\text{Re} \geq 2300$ [9]. The assumption that the flow is already fully turbulent (and thus independent of Re-number) when Fr-similarity is satisfied, is thus plausible.

Table 3.1 below summarises above calculations:

⁸ Darcy friction factor: f . [33]

This dimensionless parameter is named after Henry Darcy (1803 – 1858), a French engineer renowned for his pipe-flow experiments. f is a measure of resistance in a pipe, and is a function of the Re-number and roughness of (the inside of) the pipe. This dimensionless parameter is used for finding primary pipe head loss due to friction using the following equation:

$$h_f = f \frac{L}{D} \frac{V^2}{2g}; L = \text{length of pipe}; D = \text{diameter of pipe}; V = \text{velocity in pipe}; g = 9.81 \text{ m/s}^2$$

Table 3.1: Summary of Fr-similarity and Re-similarity calculations

	Q_p	Q_m (Fr-similarity)	Q_m (Re-similarity)
Symbols	Q_p	$0.1012Q_p$	$0.4368Q_p$
Base case (0.9m/s cast speed)	$17 \text{ m}^3/\text{h}$	$1.72 \text{ m}^3/\text{h}$	$7.4256 \text{ m}^3/\text{h}$ (not applicable due to assumption)

3.2.4 Wb-number

The Wb-number is an important free-surface parameter if it is order unity or less:

$$Wb = \frac{\rho V^2 D}{Y}$$

where: ρ = density of fluid
 V = velocity
 D = diameter or length
 Y = surface tension [water at 20°C: 0.0728N/m]

In order to verify the influence or sensitivity of the Wb-number, it is evaluated at the flow rate, which satisfies Fr-similarity ($V_m=1.057\text{m/s}$):

$$Wb = \frac{\rho V_m^2 D}{Y} = \frac{(998)(1.057)^2(0.024)}{0.0728} = 367.58 \gg 1 \quad \text{[eq 3-13]}$$

In order to investigate the influence of the Wb-number with the (base case) steel caster at a casting speed of 0.9 m/min (corresponding to a flow rate of $Q_p = 17 \text{ m}^3/\text{h}$), the Wb-number is evaluated using the properties of steel⁹:

$$Wb = \frac{\rho V_m^2 D}{Y} = \frac{(6975)(1.670)^2(0.060)}{0.450} = 2594 \gg 1 \quad \text{[eq 3-14]}$$

The Wb-number is sufficiently large for both the 40%-scaled water model and the real steel caster (much larger than unity [33]), and will be neglected for the

⁹ The exact surface tension of liquid steel depends on the sulfur content [34]. A value of 450 mN/m proved to be a good average value for typical cast steel.

validation of the 40%-scaled water model. The W_b -similarity will also be neglected in later validations of CFD models (refer to Chapter 4).

3.3 Validation Results and Other Results

For the validation results of the water model verification, there will only be focused on a comparison between the 40%-scaled water model and a full-scale water model.

More detail comparisons between the 40%-scaled water model tests and CFD models, will be expounded on in Chapters 4 and 5. These comparisons will simultaneously *serve* as CFD model verifications. The verification of CFD simulations was and is the main objective of designing and constructing a SEN and mould water model.

3.3.1 Validation of 40%-scaled model with full-scale¹⁰ water model

3.3.1.1 Widest width (1575mm) validation

Figure 3.12 shows the favourable comparison between the 40%-scaled water model with that of the full-scale ADVENT water model [44]. Both water simulations had similar (scaled) submergence depths, identical (scaled) widths, and made use of exactly the same base SEN designs (Columbus Stainless's old design). The flow pattern is made visible by injecting a suitable dye at the top of the SEN (as explained in section 3.1; not shown in Figure 3.12) as soon as the flow is stable and steady (also performed by references [35]). The acceptable correlations prove that the Froude similarity assumption indeed ensures dynamically similar flow fields.

¹⁰ Full-scale model test: performed by ADVENT in 1999. [32]

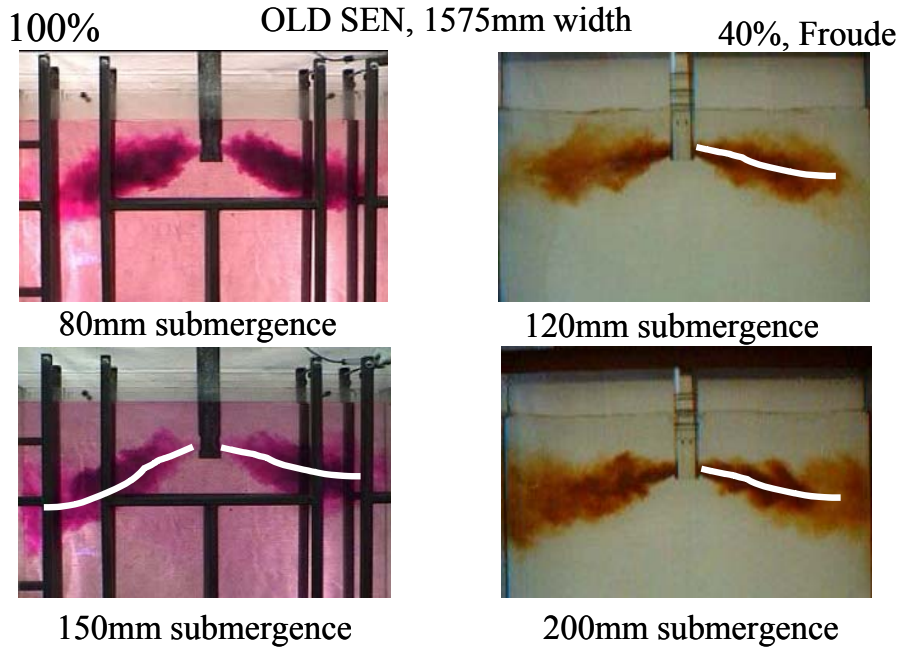


Figure 3.12: Comparison between full-scale ADVENT water model [32] and the 40%-scaled model, satisfying the Fr-similarity in the latter case

The submergence depths, indicated in Figure 3.12, are scaled to the full-scale values. The submergence depth (scaled) values for the two different experiments are not identical, but are regarded to be adequate for preliminary comparison. Refer to Table 3.2 for more detail regarding the two tests.

Table 3.2: Preliminary validation of 40%-scaled water model: comparison with full-scale model

Description	Full-scale (ADVENT [44])	40%-scaled (Preliminary, during commissioning)
SEN design	Replica of old Columbus SEN	Geometrical identical 40%-scaled
Width of mould	1575mm	630mm (equivalent 1575mm)
Thickness of mould	200mm	80mm (equivalent 200mm)
Flow rate (both experiments)	$Q_p = 17 \text{ m}^3/\text{h}$	$Q_m = 1.72 \text{ m}^3/\text{h}$ est. ¹¹ . (satisfying Fr-similarity – refer to section 3.2)

¹¹ This value is estimated as the flow meter during commissioning was not 100% operational

Discussion:

This preliminary comparison enables the reader to just compare the flow patterns made visible by injecting dye. In Chapter 4, with the help of CFD results, more detail on the flow situation will be expounded on.

It is also interesting to note that, especially for the full-scale model, that the flow field is not exactly symmetrical. There can be a number of causes:

- Flow in SEN shaft not uniform. This can result if the water supply is not equivalent to the real plant circumstances.
- SEN ports not exact due to a tolerance issue
- Mould cavity too shallow, which causes unwanted backflow in the upper mould volume, which is not representative of plant circumstances. The full-scale model mould depth is only approximately 1.5 m (which is regarded as too shallow by some references [2]). The 40%-scaled water model has an equivalent full-scale depth in excess of 3m, which is more than sufficient to prevent unwanted backflow interference in the upper mould volume [2].

Furthermore, the relative good correspondence between the 40%-scaled model and the full-scale model confirms that the assumption that the flow is already turbulent at Froude similarity flow velocity (velocity is 40% of full-scale velocity) is correct.

(In order to avoid repetition of explanations, the detail of the flow patterns, differences and similarities will be expounded on in Chapter 4, sections 4.4 to 4.6).

3.3.1.2 Small width (1060mm) validation

Further water model validation tests were also performed on other widths to ensure that the assumption that satisfying Fr-similarity ensures correct jet angles and flow patterns, is correct.

Refer to Figure 3.13 for the validation of the 40%-scaled water model at a (full-scale) submerged depth of 150mm and mould width of 1060mm, satisfying Fr-similarity.

UP 40%-scaled water model

Advent full-scale water model



Figure 3.13: Comparison between full-scale ADVENT water model [32] and the 40%-scaled model, satisfying Fr-similarity in the latter case: 1060mm mould width

3.3.1.3 Medium width (1250mm) validation

Refer to Figure 3.14 for the validation of the 40%-scaled water model at a (full-scale) submerged depth of 80mm and mould width of 1250mm, satisfying Fr-similarity.

UP 40%-scaled water model

Advent full-scale water model

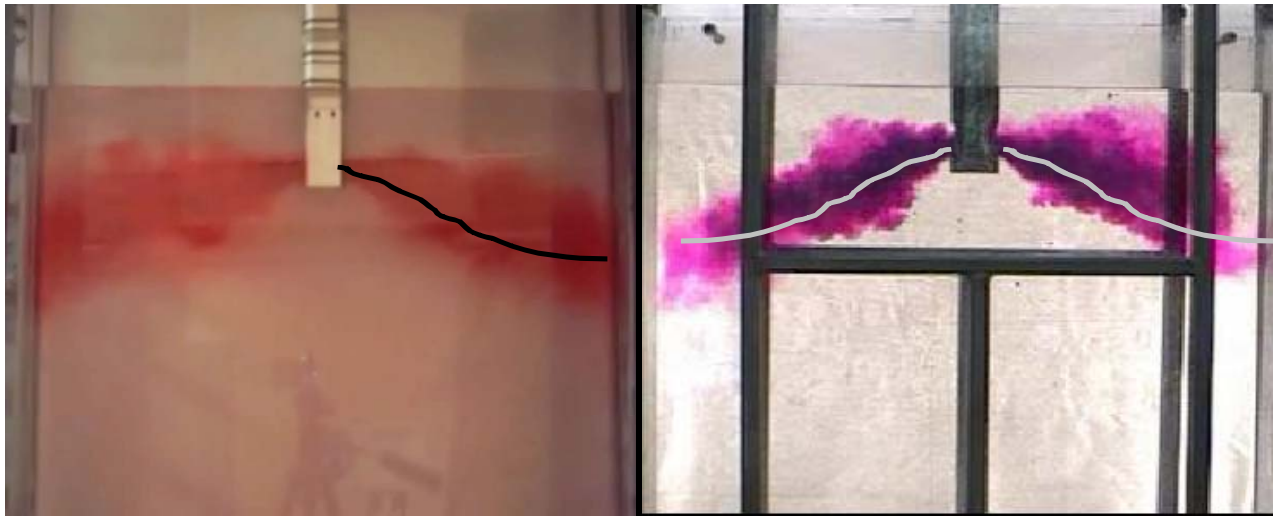


Figure 3.14: Comparison between full-scale ADVENT water model [32] and the 40%-scaled model, satisfying Fr-similarity in the latter case: 1250mm mould width

3.3.2 Other Water Model Results

A number of 40%-scaled water model tests were performed with the two different SEN designs (“old” and “new”¹²) for validation purposes: ultimately, these tests can be used to validate CFD models (in Chapter 4), to ensure physical correctness of these models.

With the water model testing, only the bottom insert of the Aluminium SEN needs to be replaced. (As explained in the design section (section 3.1.2)). Moreover, the new modular SEN bottom section will also be used to perform validation tests of the optimum design achieved in Chapter 5.

All the water model results are displayed in [Appendix F](#).

¹² The old SEN is the original base case SEN design as used by Columbus Stainless. The new SEN design is another case also used in this study for comparison purposes. The exact specifications of the SEN designs are described in Chapter 4. The drawings of the old and new SENs can also be viewed in [Appendices G](#) and [H](#) respectively.

Two widths will be tested for both SEN designs, each at two different flow speeds (equivalent to casting speeds) and two different submergence depths:

- Widths: 1060mm and 1250mm
- Submergence depths: 80mm and 150mm
- Flow rates
 - 1.28 m³/h (satisfying Fr-similarity for a casting speed of 1.0 m/min) for 1060mm width
 - 1.52 m³/h (satisfying Fr-similarity for a casting speed of 1.0 m/min) for 1250mm width

Visualisation:

Although the flow field is assumed to be steady (does not change with passing time), a dye injected into the top of the SEN will highlight the steady flow patterns. However, as the jet mixes with the water in the mould cavity, the jet becomes less visible until the entire mould cavity is the same colour. The double barrel and upward swirling of the jets can also be visualised.

In order to illustrate the three-dimensional flow field, the results will be shown as “snapshots”, exactly as the water model test would unfold before an observer.

Discussion:

With reference to [Appendix F](#), the following conclusions are made following the water model results:

Firstly, when similar SEN designs and casting speeds are compared, the jet angle corresponds closely. Consequently, it appears that the submergence depth does not have such a major impact on the jet angle and flow pattern than the SEN design and mould width.

Secondly, a noticeable difference between the old SEN and new SEN is noticed:

The flow pattern of all comparable tests of the old SEN seems much more stable, as opposed to the very fluttering and erratic jet angle (and consequent turning

pattern) of the new SEN. This can be attributed to the design of the new SEN, specifically due to the presence of the well. Refer to [Appendix H](#) for the drawings of the new SEN and description of the design. Although the new SEN is not the base case which forms a basic departure point for this study, it is however included for additional information.

Thirdly, the effect of the slightly faster casting speed on each case is quite noticeable. It seems as if the faster jet speed causes a more turbulent (or rather erratic) jet appearance. This fact is theoretically expected, but the visual difference observed was quite unexpected.

The next step towards optimisation of the SEN and mould using CFD techniques is generating CFD models of the base case (or base cases). The 40%-scaled water model, specifically designed and built as described in this chapter, must be used to ensure that the CFD models are physically correct and reliable. As soon as a CFD model can be regarded as trustworthy, optimisation can commence (described extensively in Chapter 5).

CHAPTER 4: CFD MODELLING AND BASE CASE VERIFICATION

The objective of this dissertation is to ultimately perform design optimisation of the SEN using CFD modelling, in order to achieve an optimum SEN in the continuous casting process. This will involve the set-up and solution of multiple CFD models. The first step towards this goal is to model the base case (starting point of the optimisation exercise), which is usually a current SEN design. As soon as confidence in the CFD modelling process is achieved (by the end of this chapter), different SEN designs can be evaluated for optimisation purposes (Chapter 5).

By the end of this chapter, the reader will be convinced that the methods followed to model a typical SEN and mould set-up is reliable and will ensure correct CFD solution flow fields, as these solutions are validated with water model experiments.

4.1 Approach: CFD modelling of base case design

A CFD model of any engineering flow application involves a number of inputs by the user to be physically representative of the real flow situation. These inputs involve a wide range of issues from grid generation (type of grid-elements, and geometric simplifications, *inter alia*) to turbulence modelling (choice of models to use to simulate physical turbulence) [28]. All these choices necessarily alter the simplified forms of the Navier-Stokes equations and will have a large impact on the validity of the solutions of the CFD model.

The CFD modelling of the flow (and heat transfer) in the SEN and mould of the continuous casting process is no different: the author had to make a number of choices, assumptions and geometric adjustments and/or simplifications that can have (and had) an impact on the ultimate solution.

Modelling the base case SEN and mould in the continuous casting process using CFD techniques, involves some trial and error work and a survey of the available literature¹ to determine which options in the CFD code suit the flow situation in question best. Obtaining a solution for the base case that is not only physical correct, but also robust, is crucial for a design optimisation exercise.

The approach followed to develop a robust method (from geometry and mesh generation to modelling options and assumptions) for this dissertation, is briefly described in the sections to follow.

4.1.1 General approach to modelling the base case

As already stated in the previous chapters, when confronted with the problem to model the SEN and mould with CFD techniques, the obvious first step is the generation of the physical geometry. The next step is to divide the geometry in elements or volumes (meshing the geometry). Thereafter, the boundaries of the geometry must be defined in the pre-processor (GAMBIT [11] in this dissertation) to be recognised by the CFD code (FLUENT [10] in this dissertation).

After importing the geometry and mesh into FLUENT, the user has to define, amongst other smaller issues too many to mention:

- the boundary conditions (for the already selected boundary types in the pre-processor, GAMBIT);
- the use of the energy equation;
- the operating conditions (e.g., gravity, atmospheric pressure and temperature);
- the viscous model – laminar or turbulent, after which a suitable turbulence model must be chosen for the latter.

¹ The following references made use of typical CFD approaches to flow situations similar to that with the SEN and mould in the continuous casting process. Much of these references were a source of ideas and a guide to approaching the CFD modelling problem(s):
[2][3][4][5][6][25][36][37][38][39][40][41][42][43][44][45][46][47][48][49]

All aspects, options and definitions must be carefully considered and specified by the user; otherwise default values will be used by FLUENT, possibly resulting in incorrect solutions if the flow requires specific value changes.

Initially, the author had no prior experience in modelling the very complex flow situation of the molten steel jet that enters the mould cavity. For a first iteration in an effort to obtain a first solution, default options for the flow of jets were chosen. As can be expected, a number of changes were necessary to obtain solutions that were representative of the real flow situation.

4.1.2 Verifying base case CFD model

Any CFD solution (usually required to make a design decision or some engineering judgement) should be verified in some way to ensure the solution is physically correct; otherwise the entire exercise will be meaningless. As mentioned in the Literature Survey, the most common verification method is a comparison with plant trials and/or water models. A model can be verified by only comparing certain significant measurements (key indicators), for example the impact point of the SEN jet(s) on the wall of the mould in this case. If these key indicators correspond closely, the CFD solution can be assumed to be correct, and other meaningful information can be extracted from the solution using post-processing² tools. E.g., the downward force on the SEN can be accurately computed using the CFD solution.

Most base cases in design optimisation exercises are based on the existing technology and/or application in the industry – several real ‘plant trials’ (or rather plant information) are thus available to the CFD modeller to validate the base case CFD model. However, in the case of the modelling in the SEN and mould, most

² Post-processing tools are usually included in the CFD code. In this dissertation, FLUENT has various tools, where forces, velocities, temperature distributions (to name but a few) can be computed from the solutions of the (adapted) Navier-Stokes equations and presented in the form of plots and/or contours (colour coded) on the desired geometries.

plant information only consists of mould temperatures and eventual defects in the processed product, e.g., hot rolled plate.

As anticipated, the first few solutions either did not converge towards a solution, or the solution was incorrect when compared to the literature and a full-scale water model. The process followed by the author to obtain a correct solution is best described in the diagram (Figure 4.1) in the section that follows. The process, as can be seen in Figure 4.1, involves a number of iterations to individually change settings in FLUENT and/or model geometry and gridding strategies (in GAMBIT) until a physically correct and converged solution is obtained.

4.1.3 Summary: approach to base case CFD modelling

Refer to Figure 4.1 for a summary of the approach followed by the author to obtain a satisfactory CFD solution for the base case.

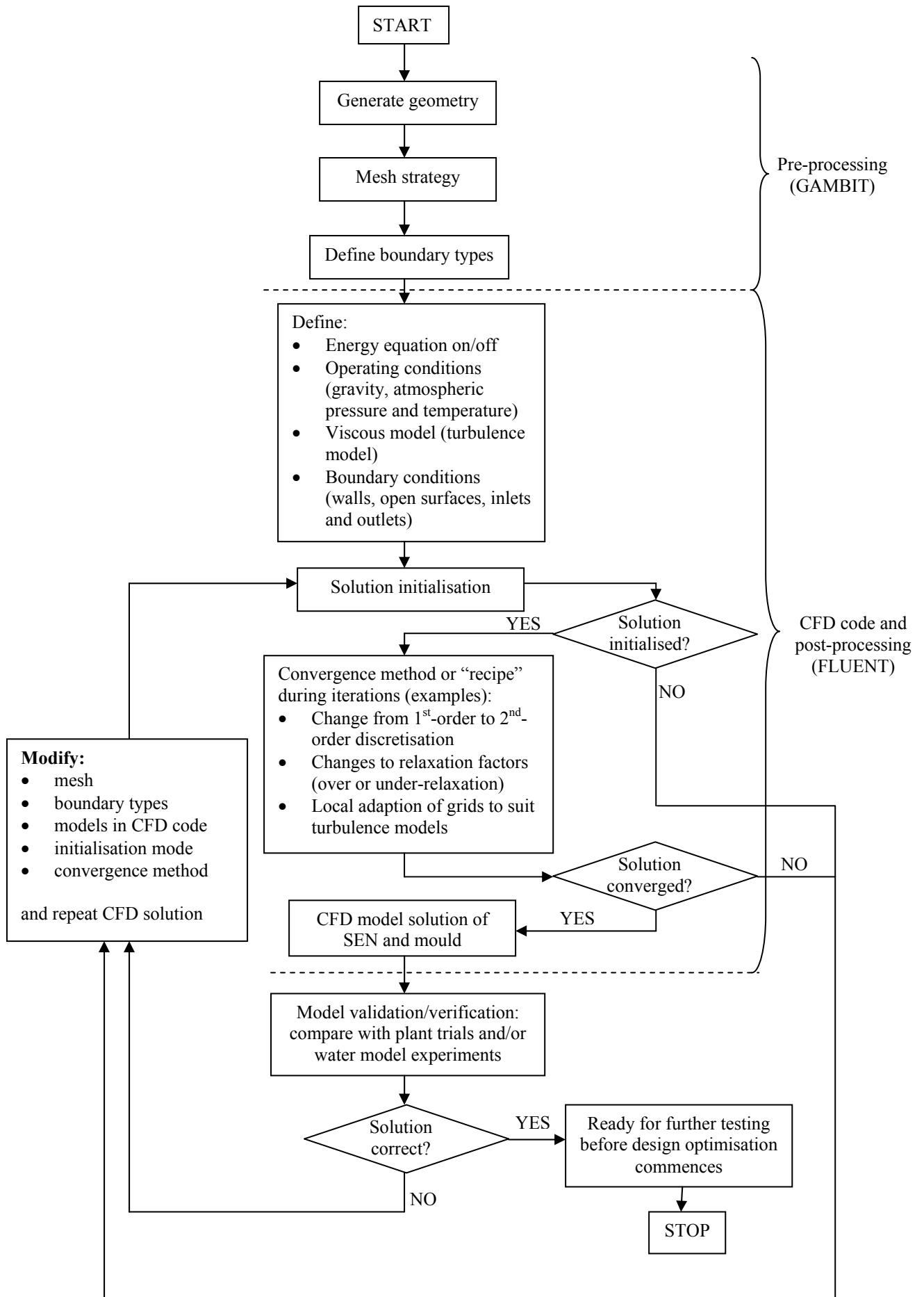


Figure 4.1: Diagram: Summary of the development of the base case CFD model

In the sections that follow, the specific gridding strategies used, choices made for turbulence models and boundary conditions will be discussed, and the reasons why they are preferred above other models and options will be stated accordingly. These choices of turbulence models, strategies, “recipes” and other options, will be repeated for other arbitrary SEN and mould designs for subsequent design optimisation exercises.

4.2 Description of base case

4.2.1 SEN description

The base case of this design optimisation exercise is the SEN currently³ used at Columbus Stainless in Middelburg, South Africa.

The geometry of the base case SEN is shown in Figure 4.2. The Vesuvius[®] SEN has a bifurcated configuration, without a well, and the angle of the SEN ports are 15° upwards from the horizontal. The heights of the SEN ports are 70mm. The total length of the SEN is approximately 1.1m, and it tapers down from the top towards the nozzles, simultaneously morphing from a round cross sectional area to an almost rectangular cross sectional area. The submerged depth of the base case is 120mm, measured from the top of the nozzle port to the meniscus surface. However, during continuous casting, the submerged depth is varied from 80mm to approximately 200mm.

An extract of the drawings for the base case SEN design can be viewed in [Appendix G](#).⁴

³ Currently refers to 2001/2002. Another SEN design, which comprises a well-type configuration, is to replace the current type without the well. Refer to [Appendix H](#) for the details and drawings.

⁴ [Appendix G](#): Copyright: Vesuvius, South Africa.

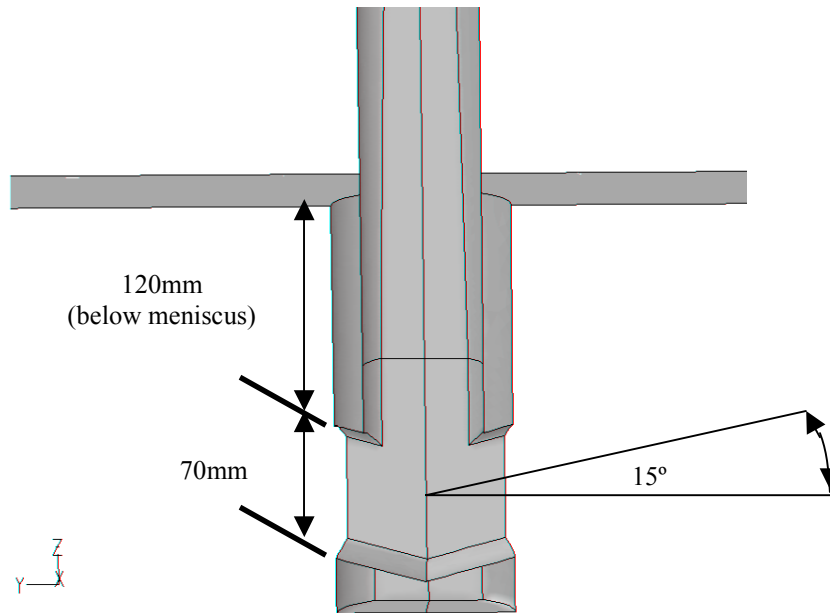


Figure 4.2: Basic geometry of base case SEN

4.2.2 Mould description

For the base case, the width of the full-scale mould (and thus the slab width) is 1575mm. This is the width at which Columbus Stainless is experiencing the most quality problems. The thickness of the mould is 200mm. The mould is assumed to be rectangular, and the exact detail of the mould walls is thus neglected. Refer to section 4.3 in this chapter for more graphical information.

In the steel plant, the copper mould is approximately 800mm long, after which the solidified shell is extracted from the mould with water-cooled rollers. The slab (with shell that is solidified as it is cooled down) is then bent from a vertical orientation to a horizontal orientation through a curvature radius of approximately 9m, as explained in the Historical Development of Continuous Casting (Chapter 2). However, trial and error methods in previous work [2] have shown that if the curvature is neglected, and a total mould length of at least 3m is modelled, accurate and comparable results are obtained.

In this dissertation, the CFD modelling and the water model experimental set-up make use of this assumption, where a total mould length (includes roller-supported curvature in real steel plants) of 3 m (or more, where possible) is used.

4.2.3 Momentum only vs. momentum and energy combined

In an effort to validate the CFD model with water model experiments, the energy equation will be neglected, as cold water is used as the fluid in the CFD modelling. The effect of temperatures on the buoyancy of water is negligible in any event (the effect on liquid steel flow patterns is deemed to be not that influential [2]). However, after validation of the CFD model, the modelling fluid can easily be changed to liquid steel with associated temperature boundary conditions and energy equation modelling using FLUENT.

4.2.4 Simultaneous SEN and mould modelling

Unlike some other similar CFD work on SEN and moulds [2][3][4][5][6], the CFD model in this dissertation comprises the simultaneous solution of the SEN and mould, as the submergence of the SEN into the mould influences the resultant solution field.

In this dissertation (and optimisation work to follow), the SEN and mould will be simulated together in one CFD model for better correspondence with plant circumstances (and the water model). This complicates the flow field, especially at the nozzle ports as the flow exits into the mould. The importance of mesh quality at the nozzle exit ports will be discussed in more detail later in section 4.3.

When separating the SEN from the mould, solutions seem to be more stable and converge quickly to predetermined criteria. However, when evaluating the SEN

separately, a pressure outlet boundary condition is applied to the SEN where it exits into the mould cavity. The pressure will typically be assumed to be the ferrostatic pressure due to the submergence depth of the SEN below the meniscus. The flow is then solved and the velocity profile of the SEN exit nozzle is applied as a velocity inlet boundary for the mould in a separate simulation. Refer to Figure 4.3 for the location of the SEN outlet / mould inlet.

However, when measuring (in a SEN and mould combined CFD model after convergence) the pressure distribution on the SEN port face, a non-constant pressure distribution is observed. The static and dynamic pressure distributions are illustrated in Figure 4.4, and show that the pressure distribution is not constant or a linear pressure distribution. The dynamic pressure distribution in Figure 4.4(b) includes the effect of the jet kinetic energy (observed as a high total pressure in the region of high jet velocity). This proves the importance of evaluating the SEN and mould together in one CFD model, in an effort to capture the real physical flow situation.

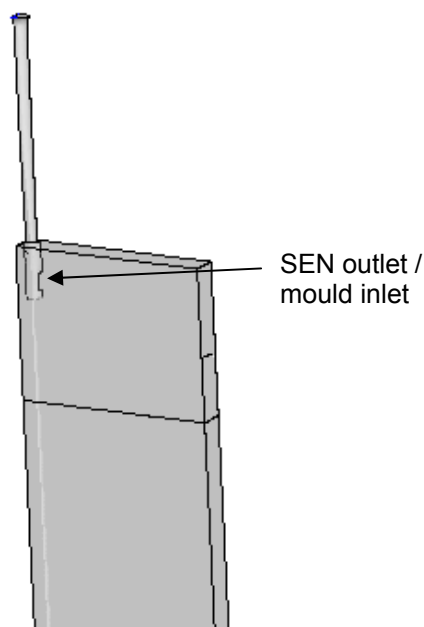


Figure 4.3: Location of SEN outlet port / mould inlet port (quarter model)

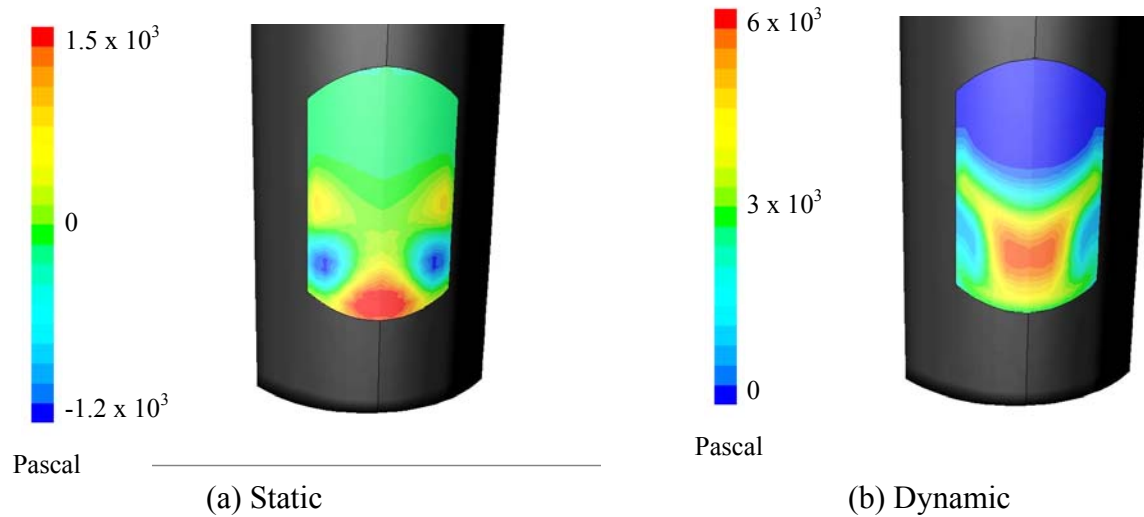


Figure 4.4: Static and Dynamic pressure distribution in 3D SEN port face (quarter model) in Pascal

4.2.5 2D and 3D modelling

Although 3D CFD modelling will be much more representative of the physical flow situation in the SEN and mould, 2D models are also developed alongside the 3D models. The main reason is the fact that 3D CFD models are much more computationally expensive than 2D models. If the 2D CFD model solutions are similar to that of 3D (and there are many similarities – refer to section 4.4.2), it would be much more sensible to perform design optimisation with 2D models.

Thus, throughout this dissertation, there will be made use of both 2D and 3D CFD models and, when compared, differences will be pointed out and explained.

4.3 CFD set-up

4.3.1 Geometry and gridding strategy (pre-processing)

Symmetry assumed:

In this dissertation, the flow is assumed to be symmetrical. A half model is therefore used for the 2D model, and a quarter model for the 3D model. However, due to small flow differences experienced in continuous casting plants and the water model, the flow will never be completely symmetrical in practice. The water model results proved this fact (refer to Chapter 3, section 3.3 where the asymmetrical flow field is shown in Figure 3.12). The overall geometry (flow area) can be seen in Figure 4.5, where the 3D quarter model is shown without the mesh to indicate boundary conditions.

Importance of element types:

Trial and error methods have proven that the element types chosen have a significant effect on the solution: not only the end result, but also the manner (stability, numerical errors amongst others) in which the solution approaches convergence.

Initially, in order to accommodate later optimisation parameterisation, the volume around the nozzle area was meshed using an unstructured grid (tetrahedral elements or volumes). The author used this method as the mentioned volume (refer to Figure 4.6) will change if the typical nozzle parameters (port height, port angle for example) change, and unstructured (tetrahedral) grids are automatically generated by the pre-processor GAMBIT for rather complicated volumes. However, the most complex flow is found at the SEN nozzles, where the jets exit into the mould cavity. Subsequently, incorrect flow patterns regularly (but not always) were observed using unstructured grids at the critical and unstable jet orifices.

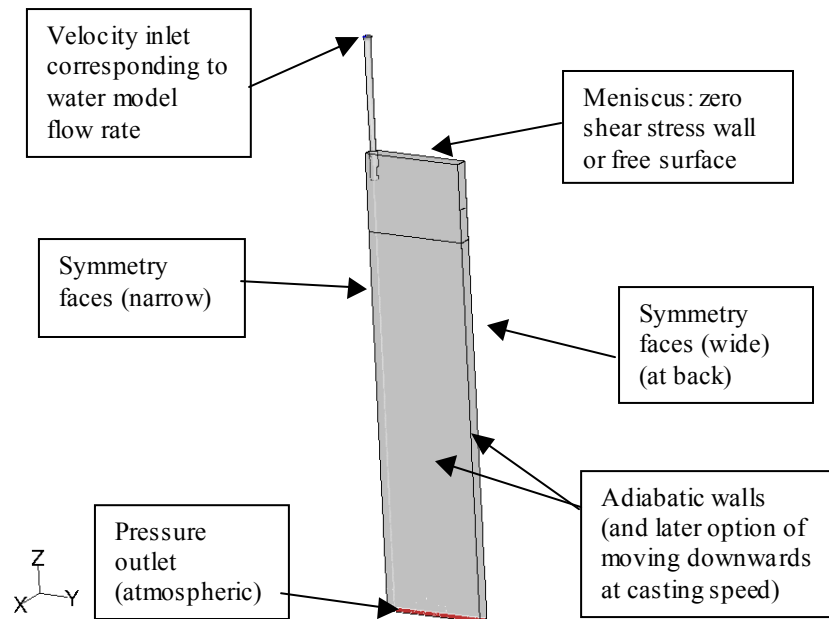


Figure 4.5: Typical boundary conditions for momentum-only CFD model validation (quarter model)

In collaboration with another university⁵ also modelling different flow situations in continuous casting using CFD, it was found that hexahedral cells proved to deliver much more reliable and repeatable solutions. Accordingly, the volume shown in Figure 4.6 has to be divided into smaller volumes that can be meshed with hexahedral cells or elements.

⁵ University of Illinois at Urbana-Champaign

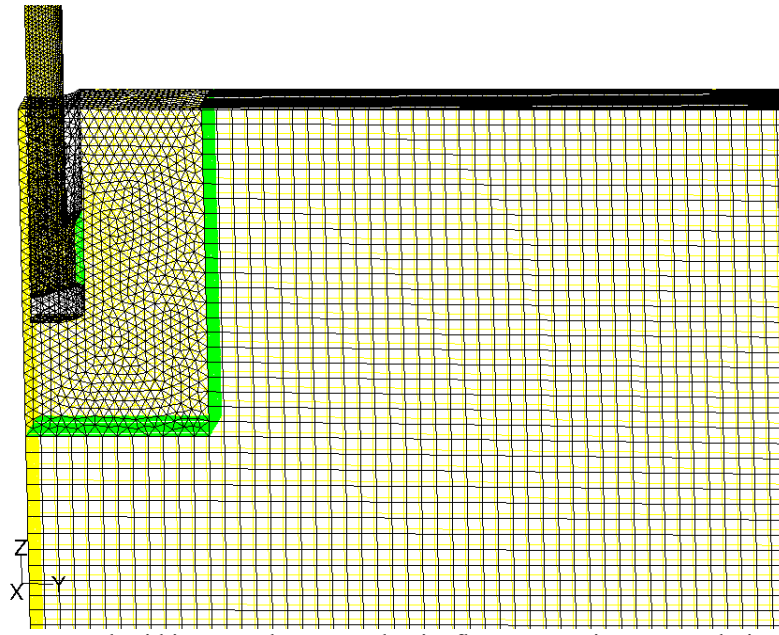


Figure 4.6: Unstructured grid in area where complex jet flow occurs: incorrect solutions often result (quarter model, 3D)

Figure 4.7 shows a zoomed-in view (from the back) of the same volume that is divided into simpler volumes, which can be meshed using hexahedral cells. The nozzle volumes (inside the lower part of the SEN) also needed to be divided into simpler volumes to enable exclusive hexahedral cells meshing.

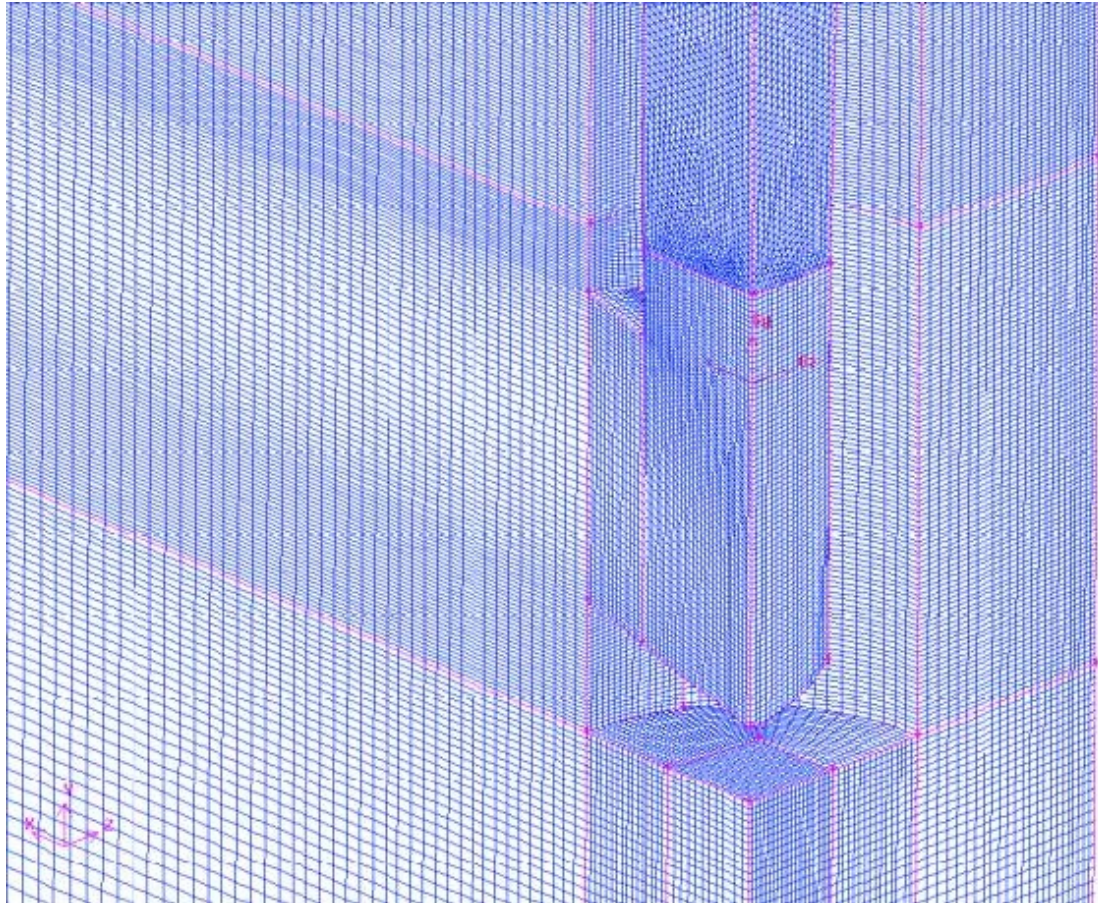


Figure 4.7: Structured grid (hexahedral cells) in complex flow area results in more repeatable solutions (quarter model, 3D)

The SEN shaft morphs from a circular cross section to a partly rectangular cross section. This fact causes a sharp edge in the quarter model of the geometry, forcing one to make use of tetrahedral cells in a small volume about this sharp edge. Unfortunately, these tetrahedral cells have a detrimental effect on the flow field, upsetting the uniform flow inside the SEN shaft just before being directed by the SEN nozzles into the mould cavity.

Virtual geometry enables exclusive hexahedral meshing

The solution to this mesh problem was to make use of FLUENT's virtual geometry and meshing capabilities [10]. Before meshing the volume about the sharp edge, a virtual⁶ modification is made to the geometry. Virtual hexahedral

⁶ "Virtual" suggests that the modification is not made to the real volume or geometry. The pre-processor (GAMBIT) performs a superficial modification to enable a more stable mesh, without altering the basic geometry.

cells are then generated within the virtual geometry. Subsequently, the entire 3D model of the SEN and mould can be meshed with the exclusive use of hexahedral cells, which, as trial and error has proven, is essential for correct and repeatable CFD results.

The use of virtual volumes and virtual hexahedral cells was also incorporated in the GAMBIT script file (for automatic geometry and mesh generation) in Chapter 5, during the design space exploration as an optimisation exercise to find an optimum 3D SEN design.

Similar problems also occurred in 2D modelling: subsequently quadrilateral elements are used instead of unstructured pave elements. This was achieved by dividing all areas with 5 or more sides (polygons) into quadrilateral areas or cells, before attempting to mesh the geometry.

4.3.2 Boundary conditions

The typical boundary conditions specified in the CFD model for the base case are shown in Figure 4.5 above. The 2D boundary conditions are similar to that of the 3D model.

Meniscus boundary condition:

The meniscus boundary condition (see Figure 4.5 above) can either be a zero shear stress wall, or a free surface with a volume air generated above the latter. Using the Volume of Flow (VOF) method in FLUENT, the behaviour of the free surface (meniscus) and the influence on the flow solution inside the mould was evaluated. The VOF-method required very expensive unsteady solvers: thus only a 2D simulation was evaluated. The mould flow fields compared favourably (refer to [Appendix I](#)); consequently the less expensive boundary condition (zero shear stress wall or slip wall which simulates a free surface) will be used for later optimisation studies and for the base case CFD model validations in this chapter. Moreover, it is currently much easier to extract heat from the meniscus by simply

specifying a heat flux boundary condition. However, in possible future work when the exact behaviour of the meniscus becomes important, the use of the VOF-method (or something similar) will be a necessity.

Velocity inlet:

The velocity inlet, specified as perpendicular to the inlet boundary, corresponds to the water model flow rate. Later, it can easily be correlated with the steel mass flow rate taking into account the density of the steel to be cast. The stopper of the tundish (which is also modelled in the water model – refer to Chapter 3), which controls the flow to the mould, is taken into account in the CFD model by modelling the inlet boundary as an annular inlet.

Symmetry faces:

The assumption of symmetry in the width and thickness of the mould allows one to only model a quarter of the SEN and mould (3D model). The solution is thus assumed to be identical in all four quarters. By defining two symmetry planes, FLUENT can solve the entire mould model – by only solving a quarter model.

Mould walls:

Adiabatic walls (only for model verification purposes):

For the purpose of the base case CFD model validation, the walls will be considered to be adiabatic and stationary. However, the model can easily be altered to move the walls at casting speed and with a liquidus temperature imposed, to more closely simulate plant conditions for later optimisation evaluations.

Walls at liquidus temperature: (for model of steel plant):

As soon as the CFD model of the base case is verified using the water model results, it is easy to alter the boundary conditions of the walls in FLUENT. The boundary conditions on the mould walls will include the following settings:

- walls at liquidus temperature (1450 °C)
- walls moving downwards at casting speed (1.0 m/min for base case)

- heat flux from the flow field in the copper mould contact area and from meniscus (approximately $300\,000\text{W/m}^2$, which must be converted for 2D models)

Owing to the fact that only thick slab casting is considered in this work, it is assumed that the shape of the solidifying shell does not influence the fluid flow, as the walls are assumed to be straight. However, the author is aware that shell forming may have a profound influence on the flow patterns with thin slab casting, which is beyond the scope of this work.

Subsequently, only single-phase flow will be evaluated in the mould volume, as it is assumed that solidification does not take place.

Pressure outlet (atmospheric):

Trial and error methods have proven that the use of an atmospheric pressure outlet results in more physically correct solutions, than using an outflow (zero gradient) outlet. As the steel solidifies in the strand, the correct choice of boundary conditions is difficult. Rather, this boundary location is chosen to be far enough away, in such a way not to influence the flow patterns around the SEN. At first, a mould length of 3m was used and deemed to be far enough away; however, with later 3D design exploration models (refer to Chapter 5, section 5.6), a mould or rather strand length of 4.3m was used, with much success⁷.

4.3.3 CFD options and assumptions

Steady-state:

The steady-state solution for the CFD flow field is required in order to compare with the water model – it is assumed that the water model has reached a steady flow field as soon as the meniscus level is stable (when the dye is injected – refer to Chapter 3 for more information).

⁷ Solutions were more stable and converged faster due to lack of excessive backflow through the mould exit.

However, some SEN designs caused a very unstable simulated flow field, where the jets never really stabilised, but rather fluctuated around an average jet position. This unsteady behaviour was mostly noticed on 3D CFD models with wide widths (1575mm), and thus did not severely influence the optimisation studies in Chapter 5. Some recommendations for future work concerning unsteady flow fields are discussed in Chapter 6.

Operating conditions:

Operating conditions include specifying the

- atmospheric pressure (which can of course be lower than 101.3 kPa depending on height above sea level);
- surrounding atmospheric temperature; and the
- gravity vectors (depending on orientation of model).

Turbulence model:

A jet exiting into a larger cavity (such as the SEN nozzle exiting into the mould) definitely suggests turbulent flow [9]. FLUENT offers a number of viscous and turbulence models to suit most flow problem types. Whenever a turbulent flow situation is anticipated, the k- ϵ turbulence model is usually implemented because of its adequate accuracy (in most circumstances) as opposed to relative little computing time.

Whenever more accurate turbulent models are implemented, such as Large Eddy Simulation (LES) or the Reynolds Stress Model (RSM), a considerable increase in computing time is required. With LES, an extremely fine mesh is necessary to successfully use this sub-grid scale turbulence model [38]. With RSM, on the other hand, 7 equations must be solved for each cell every iteration for 3D (as opposed to the k- ϵ model's 2 equations).

FLUENT compares the relevant turbulence models as follows (Table 4.1):

Table 4.1: Comparison between different turbulence models [10]

Model	Strengths	Weaknesses
Standard k-ϵ	Robust, economical, reasonably accurate; long accumulated performance data	Mediocre results for complex flows involving severe pressure gradients, strong streamline curvature, swirl and rotation
RNG⁸ k-ϵ	Good for moderately complex behaviour like jet impingement, separating flows, swirling flows, and secondary flows	Subjected to limitations due to isotropic eddy viscosity assumption
Realisable k-ϵ	Offers largely the same benefits as RNG; resolves round jet anomaly however	Subjected to limitations due to isotropic eddy viscosity assumption
Reynolds Stress Model (RSM)	Physically most complete model of large and small-scale turbulence (history, transport, and anisotropy of turbulent stresses all accounted for); isotropy not assumed	Requires more CPU effort (2 to 3 times more than k- ϵ methods); tightly coupled momentum and turbulence equations
Standard k-ω⁹	Apart from similar strengths as Standard k- ϵ model, it incorporates low Re-number effects and shear flow spreading. Applicable to wall-bounded flows and free shear flows.	Subjected to limitations due to isotropic eddy viscosity assumption. Also marginally more expensive due to more built-in models and sophistication for specific flow circumstances.
SST k-ω	Blend robust and accurate formulation of k- ω model in near-wall regions with free stream independence of k- ϵ in far field. More accurate and reliable for wider class of flows, <i>i.e.</i> , adverse pressure gradient flows (e.g., airfoils), transonic shockwaves, etc.	Subjected to limitations due to isotropic eddy viscosity assumption
Large Eddy Simulation (LES)	Models small-scale turbulence directly; no assumptions on flow	Requires extremely fine mesh and (mostly) exclusive hexagonal

⁸ RNG: Renormalisation Group Method. This k- ϵ method encompasses the standard k- ϵ equations, with the addition of applying a rigorous statistical technique [10].

⁹ Addition to turbulence models available in FLUENT since 2003

	conditions	(structured) grids. Subsequently ridiculously computationally expensive and not suited for optimisation work.
--	------------	---

Trial and error methods proved that the choice of a turbulence model has a radical effect on this particular flow field. The flow field is sensitive to the combination of turbulence model, mesh quality and solution procedure followed. For this dissertation, the RSM model was selected for some 3D simulations owing to its better grid independence (as opposed to the $k-\epsilon$ model). The RSM model is further more accurate in predicting real turbulent 3D flow fields, as turbulent velocity fluctuations around a time-averaged mean velocity is computed by solving transport equations for each of the terms in the Reynolds stress tensor [10]. The family of $k-\epsilon$ and $k-\omega$ models assume turbulent fluctuations to be the same in all directions (isotropic turbulence – also see Table 4.1). The anisotropic nature of turbulence in highly swirling flows and stress-driven secondary flows has a dominant effect on the mean flow situation – therefore RSM is clearly the superior model for the SEN and mould model [10].

The cost of RSM however disqualified it for use in an optimisation environment, where many simulations need to be performed. The base case SEN design (with a submergence depth of 200mm, however) was modelled using the RSM turbulence model. The mesh consisted of approximately 3 million cells. In order to ensure convergence, the CFD model iterated for several months on a 3 GHz Intel Pentium 4, reaching approximately 44 000 iterations. This proves that the RSM turbulence model is not suitable for general optimisation use with current computational power.

However, since the addition of the $k-\omega$ turbulence model to FLUENT in 2003 [10], this much less expensive 2-equation model proved to be well suited for jet-like flows. The Standard $k-\omega$ model is based on the Wilcox $k-\omega$ model [50]. Both $k-\omega$ turbulence models (Standard (STD) and Shear Stress Transport (SST)) [51] incorporate modifications for low Re-number effects, compressibility, and shear flow spreading. Wilcox's model predicts shear flow spreading rates that are in close agreement with

measurements for far wakes, mixing layers, as well as plane, round and radial jets. These models are thus applicable to wall-bounded flows and free shear flows.

The Standard $k-\omega$ model proved to be most suited for 3D CFD models of the SEN and mould. This turbulence model was also used successfully in Chapter 5, section 5.6, during a design space exploration optimisation exercise for specifically 3D SEN and mould models.

On the other hand, 2D modelling proved to be accurate with the $k-\varepsilon$ Realisable model [39]. Although this model also assumes isotropic turbulence, the effect on the mean flow is negligible in 2D modelling. The $k-\varepsilon$ Realisable model (as opposed to the Standard $k-\varepsilon$ model) is more suited for flow features that include strong streamline curvature, vortices, rotation and complex secondary flow features (see Table 4.1).

Near-wall treatments:

Most $k-\varepsilon$, $k-\omega$, and RSM turbulence models will not predict correct near-wall behaviour if integrated down to the wall. For this reason, so-called wall functions need to be used in conjunction with these turbulence models to empirically predict the correct transition from the fully turbulent region to the laminar viscous sub layer. FLUENT compares three near-wall treatments to be used in conjunction with any of the turbulence models discussed above (Table 4.2):

Table 4.2: Comparison between different near-wall treatments [10]

Wall functions	Strengths	Weaknesses
Standard wall functions	Robust, economical, reasonably accurate	Empirically based on simple high Re-number flows; poor for low Re-number effects, ∇p , strong body forces, highly 3D flows
Non-equilibrium wall functions	Accounts for ∇p effects, allows non-equilibrium for: separation, re-attachment and impingement	Poor for low Re-number effects, massive transpiration, severe ∇p , strong body forces, highly 3D flows

Wall functions	Strengths	Weaknesses
Two-layer zonal model	Does not rely on law-of-the-wall, good for complex flows, especially applicable to low Re-number flows	Requires finer mesh resolution and therefore larger CPU and memory resources

Although Table 4.2 suggests that non-equilibrium wall functions should be superior to standard wall functions, trial and error methods proved that no significant advantage was obtained using the former. Either of the wall function treatments can thus be used for the current application. Note that the two-layer zonal model was not even considered, as it is more appropriately used with low Re-number flow fields.

The use of quadrilateral elements (2D) and hexahedral cells (3D) is advised at the boundaries for more accurate results using wall functions. In order to ensure that the wall functions predict correct near-wall flow, the cell (or element) size needs to be chosen correctly: this is checked periodically during the solution procedure – refer to section 4.3.4 below for more detail.

Other settings:

Depending on the software used, different settings are required for highly swirling flows and jets. Constants in the models and equations were tuned specifically for this flow field as suggested by the CFD software and trial and error methods to stabilise the flow. Noteworthy areas not mentioned in the discussion above include:

- pressure discretisation scheme settings (PRESTO! and body weighted schemes proved to be the most suited for the SEN and mould modelling [10])
- solution criteria monitor settings
- solution procedures (*i.e.*, under-relaxation factors, ‘recipe’ of changing from first-order discretisation to second-order discretisation – see section 4.3.4 in this chapter).

4.3.4 Solution Procedure

Initialisation:

During the iteration process, certain milestones must be reached before switching to more accurate solver algorithms. For example, before the iteration process can commence, an initial solution must be guessed. This initial estimate of a flow field can thus be seen as a first milestone before the iteration process can begin.

1st-order and 2nd-order discretisation schemes:

Due to the nature of the numerical solution of the discretised Navier-Stokes equations, the solution needs to “propagate” from the inlet boundary through the SEN into the mould cavity. In order to speed up this process, the first few hundred iterations (may differ immensely depending on type of grid, 2D or 3D, type of turbulence model, etc.) are performed with first-order discretisation.

As the first-order solution approaches convergence, the second-order discretisation scheme is enabled, using the solution of the first-order scheme as an initial solution from which to iterate. When the second-order solution has converged, it is assumed to be the solution to the initial CFD problem.

Under- and over-relaxation factors:

As explained in the Literature Survey (Chapter 2, section 2.3.4.2), it is often necessary to adjust the over-relaxation factors to prevent the non-linear Navier-Stokes equations from diverging. Under-relaxation comprises the slowing down of changes from iteration to iteration. Over-relaxation (accelerating these changes) is often used to test whether a “converged” solution is indeed converged and stable.

However, trial and error methods have indicated that a certain ‘recipe’ or rather procedure is required to ensure convergence of SEN and mould CFD problems. It is necessary to adjust the under-relaxation factors every few hundred iterations (see below for solution procedure and Figure 4.8) to ensure that the residuals converge sufficiently. As soon as the solution seems to be nearing convergence (also comparing real flow indicators monitored during the iteration procedure), the

relaxation factors can be adjusted upwards (towards over-relaxation) to ensure a true converged solution.

Wall functions – grid adaption necessary:

In order for the wall functions (described in section 4.3.3) to predict the near-wall flow correctly, the grid cells adjacent to the wall need to be sized correctly. The size is determined by the y^+ -value of that cell: the y^+ -value of a cell is a function of the velocity of and the properties (density, viscosity *inter alia*) of the fluid in that cell, and is in fact a local Reynolds number based on the friction velocity and the normal spacing of the first cell. For the k - ϵ and k - ω turbulence models, the wall function approach requires the y^+ -value to be between 50 and 500 [dimensionless].

Whenever reverse flow is experienced over any boundaries in a CFD model, the situation may arise that mass imbalances occur. The SEN and mould CFD model is an example where mass imbalances occur: due to a recirculation zone in the mould, reverse flow is experienced over the pressure outlet boundary. These mass imbalances must be periodically rectified during the solution procedure using grid adaption (refer to the solution procedure below).

Grid adaption and virtual meshes:

Whenever virtual meshes are required and used (for 3D mesh of SEN and mould), normal grid adaption during solution iterations is not possible. Consequently, grid adaption due to mass-imbalances is also not possible.

Dynamic grid adaption:

However, a new feature added to FLUENT (FLUENT 6.1.1. [10]) enables the user to dynamically adapt the virtual grid during the solution procedure. Starting (since initialisation) from an initial mesh size (typically 500 000 cells for this 3D case), the mesh is refined and coarsened as the solution proceeds, based on velocity gradients (other criteria can also be used). This is an attempt to follow the formation of the SEN jet with grid clustering. A maximum cell count of approximately 850 000 is reached in this process depending on the complexity of

the flow field and the SEN geometry used (part size, number of design parameters, etc.). The dynamic mesh adaption option is chosen and configured before the solution iteration process is started, and dynamically adapts the mesh as the solution proceeds until sufficient convergence is achieved.

Other solution procedure settings:

Different functions and schemes can be switched on and off during the solution procedure to aid the solution to meet the convergence criteria as soon as possible. Obviously, these setting changes can only be performed when the iteration procedure has been interrupted. Over-zealous interruptions and setting changes can have a negative impact on the convergence and subsequent correctness of the CFD solution.

The (typical) solution procedure used to obtain the results displayed in section 4.4 is shown below. Refer to Figure 4.8 for the graphical presentation of the solution procedure, using the residuals.

The **solution method** or **procedure** comprises:

First-order solution

1. Run 300 iterations
2. Adapt (refine) grid as follows:
 - y^+ values at walls: ensure that $50 < y^+ < 200$
 - mass-imbalance: ensure that $-10^{-5} < mi < 10^{-5}$
3. Run 300 iterations
4. Adjust under-relaxation as follows:
 - pressure correction equation:

p	=	0.2	(from default 0.3)
---	---	-----	--------------------
 - momentum equation:

mom	=	0.5	(from default 0.6)
-----	---	-----	--------------------
 - turbulence kinetic energy equation:

k	=	0.6	(from default 0.8)
---	---	-----	--------------------
 - ε equation (from k- ε)

ε	=	0.6	(from default 0.8)
---------------	---	-----	--------------------
5. Run 100 iterations

6. Adapt grid for mass-imbalance
7. Run 250 iterations
8. Under-relaxation as follows:

momentum:	mom	=	0.4	(from 0.5)
-----------	-----	---	-----	------------
9. Run 400 iterations

Second-order solution

10. Change all settings to second-order, except pressure discretisation method (set this to body weighted or PRESTO!)
11. Run 150 iterations
12. Unrelax in order to ensure correct solution as follows:

pressure correction:	p	=	0.3	(from 0.2)
momentum:	mom	=	0.6	(from 0.4)
13. Run 400 iterations
14. Adapt grid for mass-imbalance
15. Run 150 iterations
16. Under-relax as follows:

momentum:	mom	=	0.5	(from 0.6)
-----------	-----	---	-----	------------
17. Run 350 iterations
18. Tighten the convergence criteria for momentum to 0.00075 (from 0.001)
19. Under-relax as follows:

momentum:	mom	=	0.4	(from 0.5)
-----------	-----	---	-----	------------
20. Run 300 iterations
21. Under-relax as follows:

momentum:	mom	=	0.375	(from 0.4)
-----------	-----	---	-------	------------
22. Run 1000 iterations (until convergence which mostly occurred before 700 iterations)

(Total number of iterations = 2250 to 2850, depending on convergence occurrence in step 22)

Note that whenever an adjustment to any of the CFD code settings is made (relaxation factor adjustment to discretisation scheme adjustment), the residuals spike momentarily (refer to Figure 4.8).

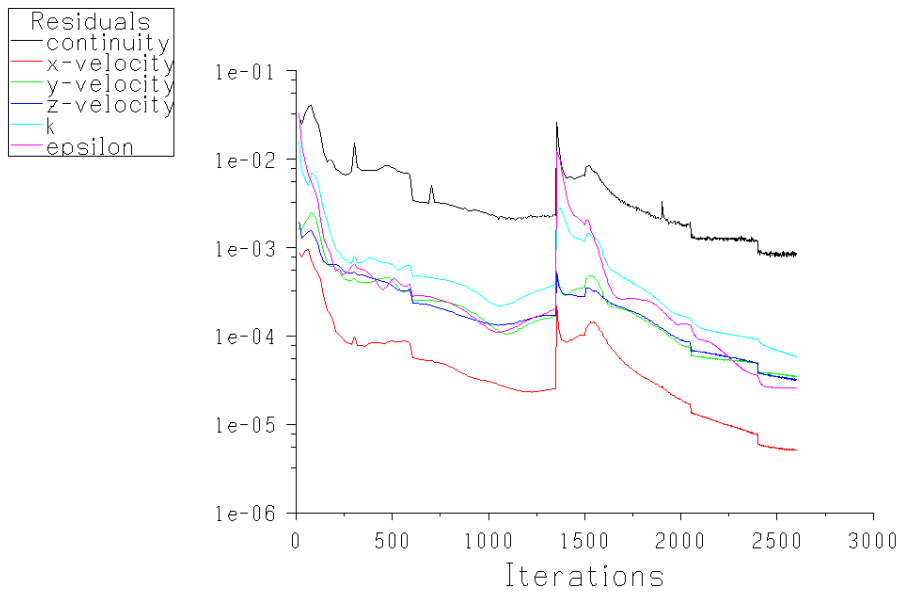


Figure 4.8: Residuals during solution procedure ('recipe')

4.4 CFD model: Verification Results

4.4.1 CFD model verification: mimic water model

The reason as to why a water model was designed and built by the University of Pretoria (the author) was to validate the CFD model of the SEN and mould before any design optimisation is attempted.

The first step to validate the model is to concentrate on the flow patterns only (momentum only), by exactly imitating the 40%-scaled water model. If the CFD momentum model closely matches the flow patterns of the 40%-scaled water model, the model¹⁰ can be assumed to be acceptable.

From here, it is rather a straightforward exercise to extend the model to imitate real plant circumstances, by scaling the geometry to full-scale, enabling the

¹⁰ The CFD "model" includes all aspects covered in Figure 4.1, and briefly includes geometry and gridding strategy, flow assumptions, CFD options and CFD assumptions, boundary conditions, and finally the solution procedure.

energy equation (and therefore allow temperature and buoyancy effects), and adjusting and supplementing the boundary conditions. Refer to section 4.5 for these actions. It should however be stressed that a high-fidelity modelling of the plant situation (e.g., modelling of mould oscillation, solidification, conglomeration of inclusions, etc.) falls outside the scope of this dissertation.

4.4.1.1 Case 1: Base case (Old SEN of Columbus Stainless)

In summary, the following operating parameters and/or settings were selected for this CFD simulation:

- Base case SEN design as described in section 4.2, scaled to 40% in FLUENT to match the water model
- Energy equation disabled: only momentum equations considered
- CFD options:
 - k- ϵ realisable turbulence model for 2D
 - standard wall function
 - symmetry assumed (half model for 2D and quarter model for 3D)
- Boundary conditions: (refer to Figure 4.5)
 - Casting speed: inlet SEN velocity scaled to exactly match Fr-similarity flow rate of 1.72 m³/h (refer to Chapter 3 for details)
 - Meniscus: zero shear stress wall
 - Mould walls: adiabatic (by default) and stationary
 - Outlet at atmospheric pressure
- Material properties:
 - Water at 998 kg/m³
 - Other properties of water at Standard Temperature and Pressure

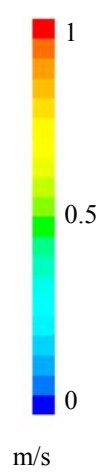
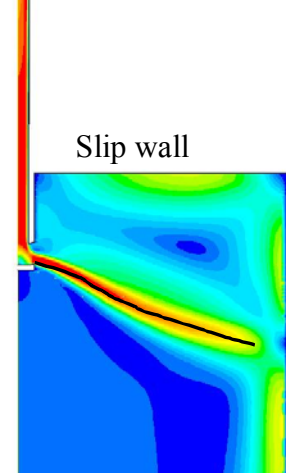
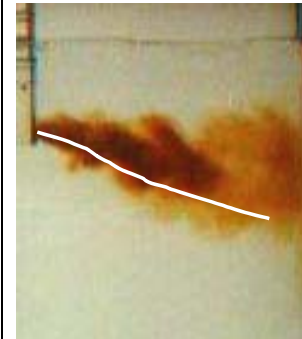
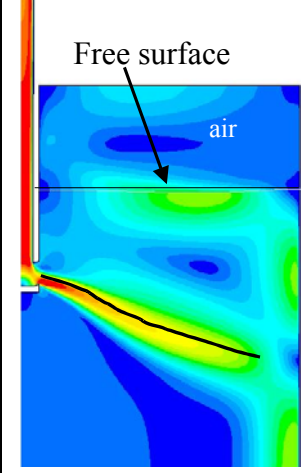
For the validation purposes of the CFD model, the submergence depth was modelled at 200mm (as opposed to the 120mm in the original base case), as several water model tests had already been performed at 200mm submergence.

Refer to Table 4.3 for the comparison of the 2D CFD model with the water model results. For the sake of completeness, the 2D results (Table 4.3) where the meniscus boundary was evaluated as a free surface (as opposed to a less expensive slip wall) are also shown to demonstrate the favourable comparison (also see Appendix I).

It can be seen that the 2D CFD model predicts a jet that penetrates deeper than observed in the water model. The intensity of the 2D simulated jet seems to be higher than that of the water model, *i.e.*, higher velocities are concentrated on the centreline of the simulated jet, as opposed to the more dissipated nature of the water model jet. The same trend is also observed when comparing simulated 2D and 3D results, with the 3D results being more representative of the water model observations.

The CFD results in Table 4.3 are displayed in the form of contours of velocity magnitude, just to highlight the flow pattern (momentum only) for validation purposes.

Table 4.3: Verification of 2D CFD model (slip wall and free surface meniscus boundary condition) with 40%-scaled water model. CFD results displayed using contours of velocity magnitude

CFD Scale	2D: zero shear stress (slip) wall meniscus	UP 40% Water model	2D: free surface meniscus
 <p>1 0.5 0 m/s</p>	 <p>Slip wall</p>		 <p>Free surface air</p>
<p>Base case (Old SEN): Submergence 80mm (200mm full-scale); Fr-similarity 1.72m³/h</p>			

4.4.1.2 Case 2: New SEN of Columbus Stainless

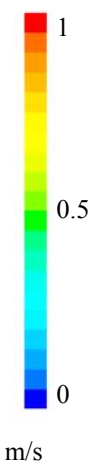
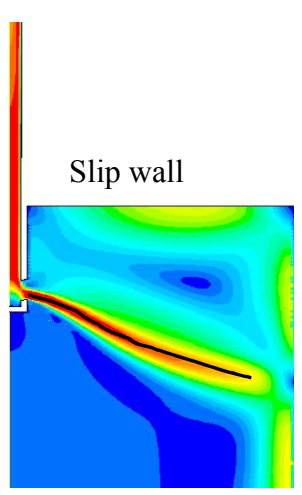
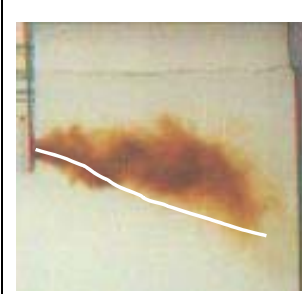
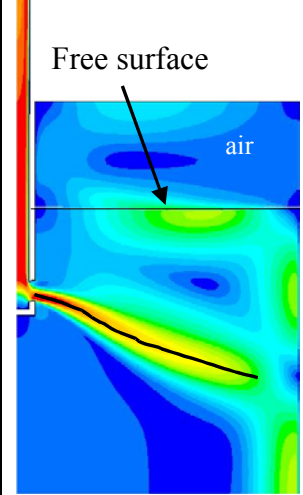
Columbus Stainless also requested water model testing of their more recent SEN design. Subsequently, the author was in possession of another case (physical SEN insert for the water model experimental set-up) to verify the CFD model of the SEN and mould.

The parameters and/or settings were identical to that of the base case (Old SEN), except for the different SEN design. The new design has the following parameters: (refer to [Appendix H](#) for drawings of new SEN design)

- port angle: 15° upward
- port height: 60 mm
- port width and radii: 45mm and 35mm (similar to base case design)
- well depth: 15mm
- well angle: flat

Refer to Table 4.4 (below) for the comparison of the 2D CFD model of the New SEN with the 40%-scaled water model results.

Table 4.4: Verification of 2D CFD model (slip wall and free surface meniscus boundary condition) with 40%-scaled water model. CFD results displayed using contours of velocity magnitude

CFD Scale	2D: zero shear stress (slip) wall meniscus	UP 40% Water model	2D: free surface meniscus
 <p>1 0.5 0 m/s</p>	 <p>Slip wall</p>		 <p>Free surface air</p>
<p>New SEN: Submergence 80mm (200mm full-scale); Fr-similarity 1.72m³/h</p>			

Again, it can be seen that the 2D CFD model predicts a jet that penetrates deeper than that observed in the water model. The line drawn inside the jet (all three figures in Table 4.4) corresponds closely to the concentrated jet of the 2D CFD solutions, indicating the more dissipative jet of the water model.

4.4.2 2D vs. 3D verification results

4.4.2.1 3D verification results

Settings:

Apart from extending the 2D CFD model settings and parameters to 3 dimensions, the turbulence model choice had to be altered:

As trial and error methods have proven, the k-ε turbulence models are not suited for 3D modelling. Consequently, as explained in section 4.3.3, the rather expensive RSM turbulence model was selected for this validation study. However, it was soon realised that the RSM turbulence model is too

computational expensive for general optimisation purposes, as it also demands a fine mesh (in excess of 2 million cells), apart from the fact that it requires 7 equations to be solved per iteration (as opposed to only 2 of the k - ϵ models). The result displayed in Table 4.5 has run for 52000 iterations, taking several months on a 3GHz Pentium IV with 2GB RAM computer to complete.

The less expensive Standard k - ω turbulence model (also only 2 equations per iteration) was selected as the turbulence model for the 3D model of the steel plant (section 4.5), which proved to be a good assumption, especially for smaller width moulds.

Refer to the Table 4.5 for the comparison between the 3D models of both turbulence models (k - ω and RSM) on the base case SEN design, and the 40%-scaled water model. The contours of velocity magnitude on the symmetry plane (*i.e.*, centre plane of the mould) of the CFD models are displayed. Note that both CFD models were configured to exactly imitate the 40%-scaled water model test.

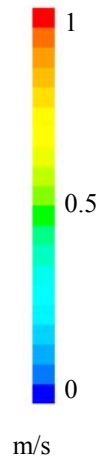
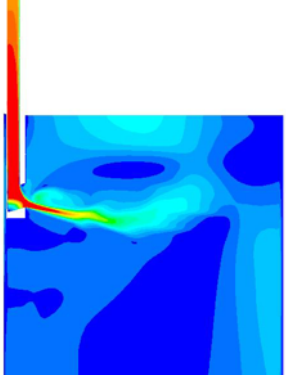
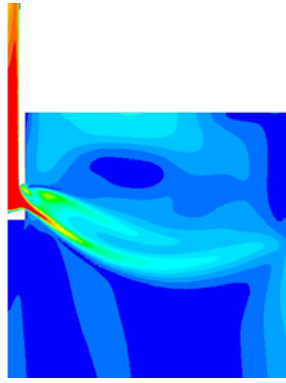

Note on Table 4.5: differences between 3D CFD models and water model results

There is a noticeable difference between the 3D CFD models (k - ω and RSM turbulence closure) and the 40%-scaled water model. As more experience in SEN 3D modelling was gained during this study, it was noticed that the wider widths presented problems for most CFD methods. For example, the residuals struggled to fall below 3rd-order convergence. Moreover, the flow field seem unstable and pseudo-transient, although otherwise suggested by water model experiments. Furthermore, the pseudo-transient nature of the results seems to worsen as soon as 2nd-order upwinding is introduced.

Nevertheless, later 3D optimisation work in Chapter 5 was conducted on narrower slab widths (range 1000 – 1300mm), and the 3D CFD models

employing k- ω (standard) turbulence closure proved to closely simulate water model verification experiments (refer to Chapter 5, Figure 5.19).

Table 4.5: Verification of base case 3D CFD model (comparing RSM and k- ω (standard) as turbulence models) with 40%-scaled water model; 1575mm full-scale width. CFD results on quarter model centre plane displayed using contours of velocity magnitude

CFD Scale	3D centre plane RSM turbulence model, 2 nd -order accuracy	3D centre plane k- ω (standard) turbulence model, 2 nd -order accuracy	UP 40% Water model
 1 0.5 0 m/s			
Base case (Old SEN): Submergence 80mm (200mm full-scale); Fr-similarity 1.72m³/h			

4.4.2.2 Differences between 2D and 3D CFD models of SEN and mould

Comparing the CFD results in Tables 4.3, 4.4 and 4.5, the 3D flow pattern of the vertical section through the mould centre parallel to the wide face (*i.e.*, centre plane) can be reasonably approximated with the 2D model, also as pointed out by Thomas [2]. The only significant difference between the two flow patterns is the increased upward curvature of the jet in the bulk of the mould in the 3D results, clearly pointed out in Figure 4.9. The result is a higher impingement point on the narrow face of the mould with the 3D model (note that this is mostly on the centre plane).

According to Thomas (and agreed to by the author), this curvature in the 3D model is caused by the upward lifting force on the broadening 3D jet due to

the reduced pressure in the upper recirculating zone [2]. As Figure 4.9 illustrates, the 2D (flat) jet broadens less, consequently retaining more momentum (than the 3D jet) in order to resist this upward bending.

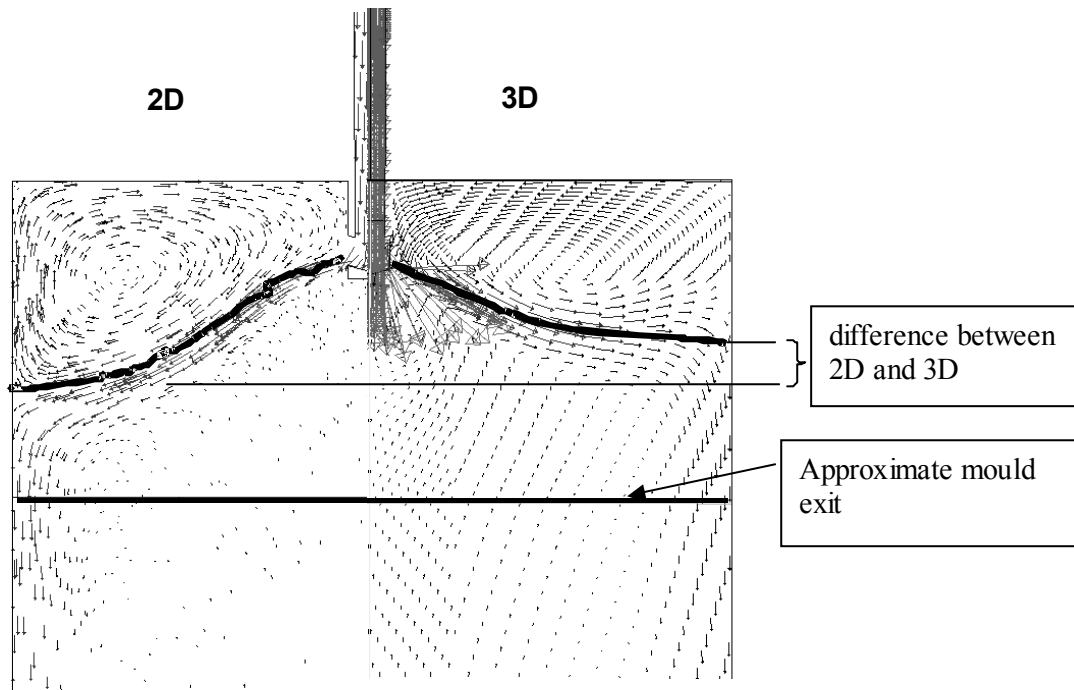


Figure 4.9: Comparison of 2D and 3D velocity predictions on centre plane of mould for 3D (base case SEN design)

Nevertheless, the true 3D nature of the jet flow will be illustrated in the following section, collaborating the above explanation.

4.5 CFD model of steel plant

As depicted in the diagram in Figure 4.1, firstly the momentum CFD models were developed for CFD model verification.

The next step, now that the author is quite confident in the accuracy of the CFD modelling process, is to extend the model to be able to imitate the real steel plant circumstances.

All the preceding information in this chapter serves the purpose of a stepping-stone for the final 3D CFD model of the base case SEN design.

4.5.1 Geometry and gridding strategy

A 3D quarter model geometry and mesh were constructed using approximately 500 000 exclusive hexahedral cells. As described earlier in this chapter, a special function in GAMBIT [11] had to be employed to eliminate tetrahedral cells: a virtual geometry and accompanying virtual hex-mesh were created before exporting the mesh to FLUENT to set up all CFD parameters.

4.5.2 Boundary conditions

All the adiabatic walls (indicated in Figure 4.5) are replaced with walls with predetermined heat fluxes and temperatures, amongst others. The heat fluxes are estimated from 1D heat transfer simulations of the shell and mould. (Based on work of BG Thomas [2] and [52] (300kW/m^2 becomes 60kW/m for 0.2m wide 2D case)).

The meniscus surface was modelled as a slip wall with a predetermined heat flux towards the surroundings. The walls of the mould cavity were modelled with downward moving walls (at casting speed of 1.0 m/min), while the walls were kept at the liquidus temperature ($1450\text{ }^\circ\text{C}$) of the molten steel.

The mould cavity outlet was modelled as a pressure outlet at atmospheric pressure. Choosing this boundary condition far enough away from the SEN, the influence on the flow patterns surrounding the SEN will be small.

The inlet face at the top of the SEN was modelled as a velocity inlet, matching the mass flow rate of the steel corresponding to a casting speed of 1.0 m/min.

Owing to the assumption of full symmetry, the centre planes (wide and narrow) are defined as symmetry faces or boundaries.

4.5.3 CFD options and assumptions

Firstly, full symmetry was assumed due to the fact that a quarter model mesh was used¹¹, as already stated in section 4.5.2 above.

The flow was assumed to be steady-state. Although the author did encounter some SEN and mould cases (verified by water model test) where the jet seemed to be oscillating about an average position, most SEN designs demonstrated a steady jet angle and flow pattern.

Operating conditions were specified as being standard atmospheric pressure (101.3 kPa) and temperature of 20 °C. Gravity was switched on at 9.81 m/s², which will of course have a buoyancy influence on the hotter emerging jet (albeit practically negligible [2]).

The turbulence model chosen for 3D CFD modelling is the k- ω turbulence model of Wilcox [10][50]. Although the RSM turbulence model is clearly the superior model for 3D due to its anisotropic evaluation of turbulence (as opposed to k- ϵ and k- ω -models' assumption of isotropic turbulence), it is far too expensive for optimising purposes. The Standard k- ω turbulence model is however “tweaked”¹²

¹¹ Refer to Chapter 6 where complete SEN and mould models are discussed for potential future work. Robustness and reliability studies should be performed on SEN design for the event that one port may be smaller than the other due to manufacturing tolerances, for example.

¹² Refer to section 4.3.3 for all the detail and comparisons between the turbulence models available in FLUENT.

to predict high shear flows and especially jet flow very accurately for 3D models as well.

The standard near-wall function was selected for this model (to predict flow accurately close to walls, by modelling turbulent boundary layers).

More complex phenomena like solidification and oscillating mould were not modelled.

4.5.4 Solution procedure

In essence, the same solution procedure was followed as described in section 4.3.4. However, due to the use of a virtual mesh, normal grid adaption (for mass imbalances and y^+ adaption for near-wall functions) is not possible.

However, dynamic grid adaption is used instead, where the mesh is refined and/or coarsened as the solution proceeds (hence “dynamic”) based on velocity gradients (chosen for this case). This is an attempt to follow the formation of the SEN jet with grid clustering, and to keep the number of cells as low as possible.

4.5.5 CFD Results and discussion

Following the solution procedure, after approximately 30000 iterations, the solution was considered to be converged sufficiently.

The history of residuals (only the first 10000 are shown) in Figure 4.10 below shows the typical convergence history when dynamic grid adaption is employed. Each spike indicates when dynamic adaption occurred. Again, the switch to 2nd-order accuracy influenced the convergence stability, as the residuals seem to become unstable from that moment.

To ensure that the solution has truly converged, the maximum turbulent kinetic energy (TKE)¹³ on the meniscus is displayed in Figure 4.11 as a function of each iteration. The convergence of a physical property of the CFD model towards a steady value, coinciding with sufficient and significant residual drops, constitutes a converged solution. The failure of the maximum meniscus TKE to reach a steady value (Figure 4.11) provides an indication of the possible unsteady nature of the solution. A time accurate transient simulation is required to verify this, although the water modelling experiments tend to indicate that the flow field is steady.

Admittedly, the residuals for the 3D CFD model of the base case (presented in Figure 4.10) suggest that the solution might not be converged. However, the following reasons might be blamed:

- The flow seems to be pseudo-transient, as also reflected by Figure 4.11. Pseudo-transient flow has been experienced to be more pronounced with wider mould widths, as the history of residuals is much more stable and convergent with narrower width moulds (3D exploration study in Chapter 5).
- The dynamic mesh adaption methods used (in an effort to control mesh sizes) seem to prohibit the residuals from stabilising. As soon as the solution starts to converge, the grid changes and the residuals are simultaneously enlarged. More work on dynamic adaption methods is necessary in future work.

The mesh quality is outstanding (100% hexahedral cells), and is thus not suspected as being the main culprit, although this possibility cannot be ruled out completely.

¹³ In Chapter 5, this measurement will play a significant role in the objective function during the optimisation of the SEN.

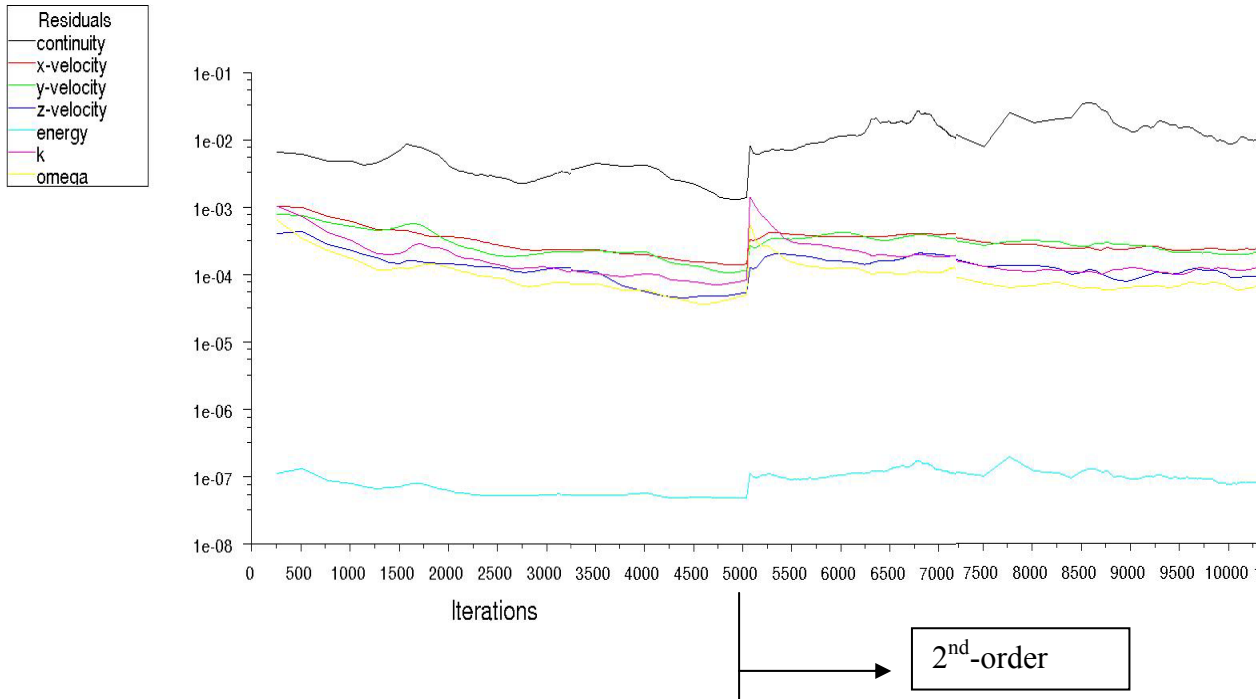


Figure 4.10: Residuals history (as a function of iteration number)

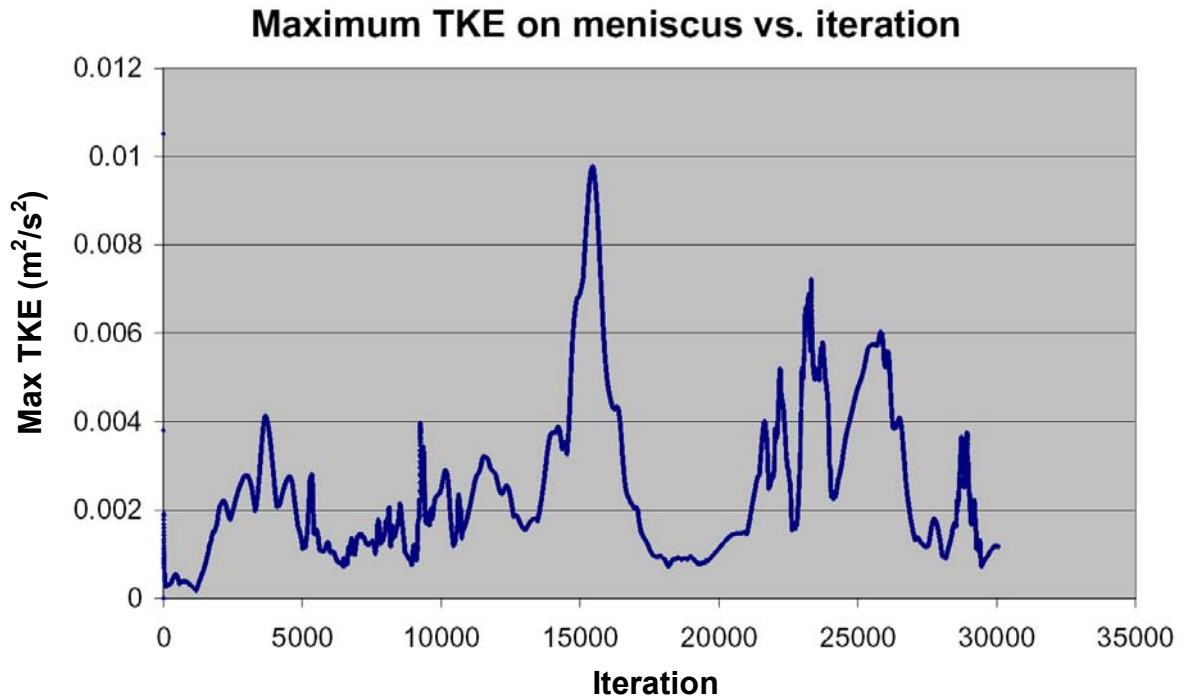


Figure 4.11: Physical property (maximum TKE on meniscus) as a function of iteration number

It is noticeable in Figure 4.11 that there is noise in the physical measured property (maximum TKE on meniscus in this case) as the solution progresses. If a certain

property were to be used as part of the objective function for optimisation purposes (Chapter 5), the specific property would need to be averaged in order to obtain a more representative value.

The results of the 3D CFD half model are displayed symmetrically in Figures 4.12 to 4.20, in the form of:

- contours of velocity and vorticity magnitude on the symmetry plane (*i.e.*, centre plane) (Figures 4.12 and 4.13)
- contours of helicity¹⁴ on the symmetry plane (Figure 4.14)
- contours of turbulent kinetic energy (TKE) on symmetry plane (Figure 4.15)
- contours of shear stress on the wide mould walls (Figure 4.16)
- contours of temperature on the symmetry plane (Figure 4.17)
- path lines originating from the SEN inlet, coloured by vorticity magnitude (Figure 4.18)
- iso-surfaces of velocity magnitude coloured by turbulent kinetic energy (Figure 4.19), and
- velocity vectors scaled and coloured by its magnitude (Figure 4.20).

The turbulent kinetic energy on the meniscus surface (plan view) is displayed in Figure 21.

Different features of the jet and its three-dimensional shear layers can be discerned when comparing these results. E.g., path lines (Figure 4.18) and velocity vectors (Figure 4.20) illustrate recirculating behaviour, whereas vorticity magnitude (Figure 4.13) shows the extent of the jet shear layer. The impingement location (important to prevent breakouts if this location is below the mould exit) is most clearly depicted using path lines and helicity contours (Figure 4.14).

¹⁴ Helicity identifies the core of streamwise longitudinal vortices. By definition, normalised helicity represents the cosine of the angle between velocity and the vorticity vectors. The sign of helicity is dependent on the orientation of the local velocity vector relative to the vorticity vector. Thus the core of a streamwise vortex can be identified as the region of high helicity. Boundary layers are regions of high vorticity and low helicity [10].

The turbulent kinetic energy contours (Figure 4.15) show that the kinetic energy is mostly concentrated inside the jet, as expected.

Figure 4.12, displaying contours of velocity magnitude on the centre plane of the 3D model, does not illustrate the true 3D nature of the flow, and the flow appears to be purely 2-dimensional.

However, the wall shear stress contours (Figure 4.16) clearly indicate the 3D nature of the flow that takes place inside the mould: the yellow areas on the mould wall indicate that the jet dissipates (and lifts) as it propagates along the wall towards the narrow mould wall. This corresponds to the initial water model experiments discussed in section 4.4.1.

The path lines (Figure 4.18) further illustrate the 3D flow patterns, as well as the complexity of the flow (secondary recirculating zones above jet exits). The iso-surface of velocity magnitude contour (Figure 4.19) confirms the strange jet behaviour highlighted by the path lines and shear stress walls figures: the “ends” of the jet lift up as the jet moves through the mould towards the narrow wall. It is evident from this figure that the jet centre line (on the centre plane of the mould) is lower than the sides or ends of the jet.

Figure 4.17, displaying contours of temperature magnitude on the centre plane, clearly shows that the boundary condition on the mould walls is satisfied, where the mould walls are at the lowest temperature (in the accompanying temperature scale), corresponding to the steel liquidus temperature (1723 K or 1450 °C). As expected, the (high) temperature of the jet is rapidly dissipated into the mould cavity. The double recirculation zones (upper and lower) are also easily spotted in this figure.

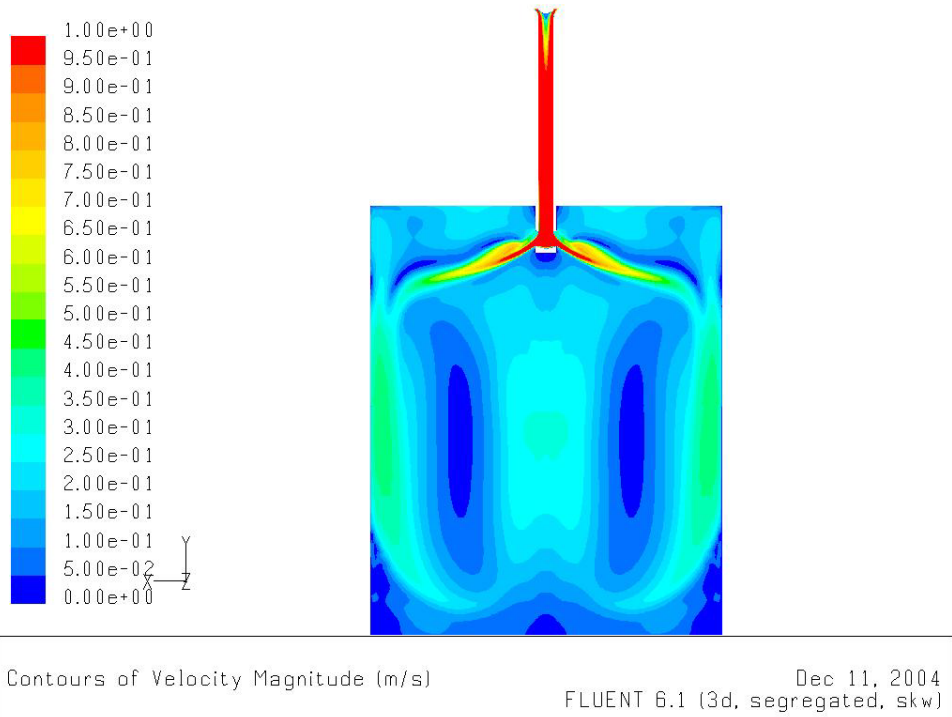


Figure 4.12: Base case velocity magnitude contours on symmetry plane: range 0 – 1 m/s

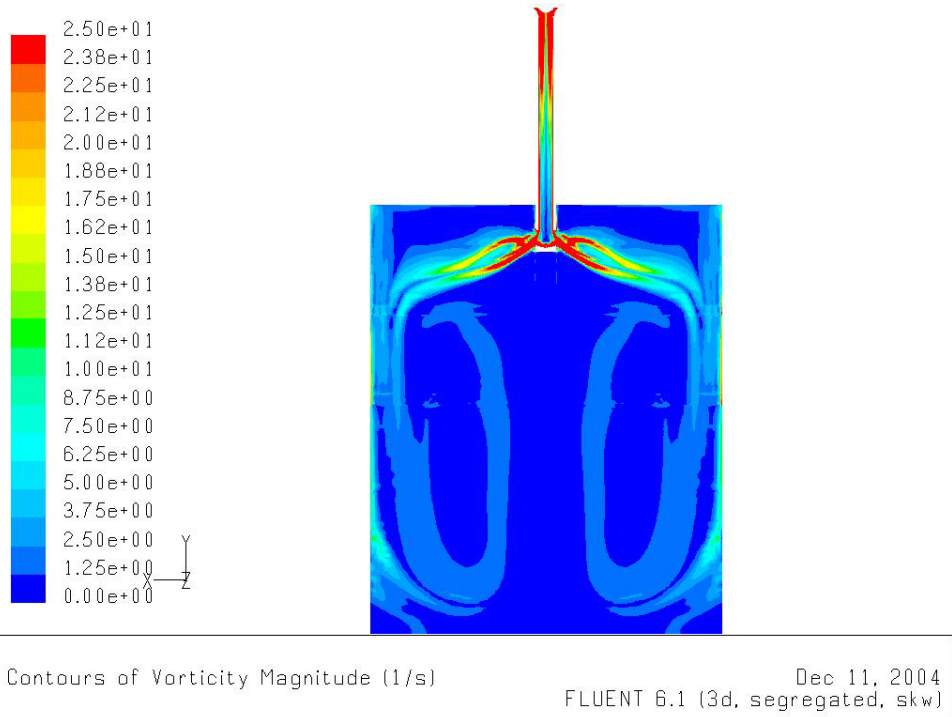


Figure 4.13: Base case vorticity magnitude contours on symmetry plane: range 0 – 25 1/s

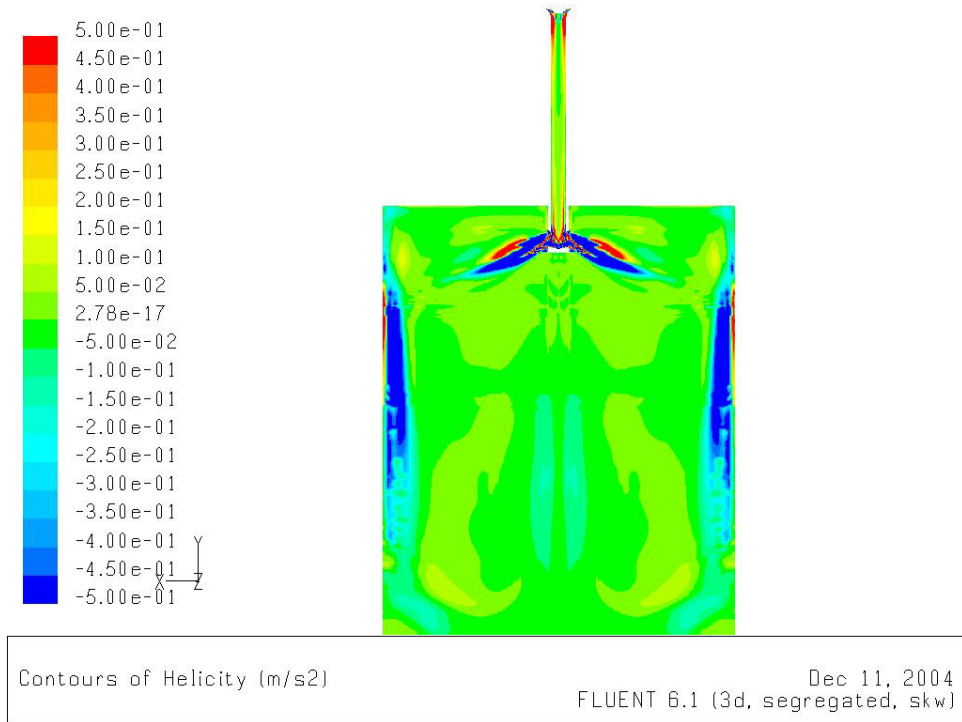


Figure 4.14: Base case helicity magnitude contours on symmetry plane: range -0.5 – 0.5 m/s²

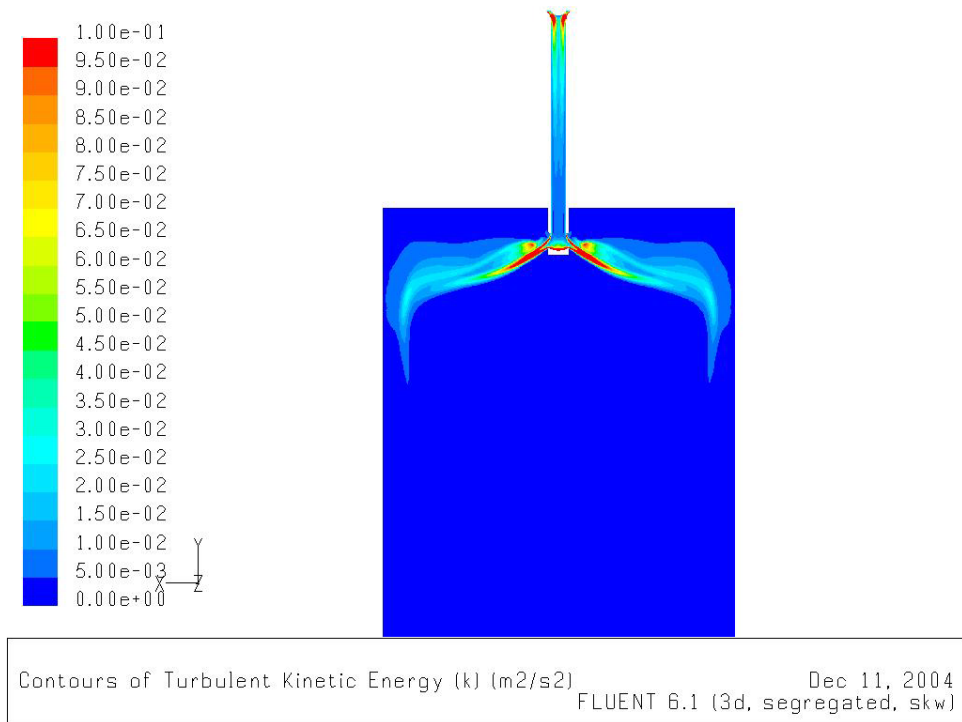


Figure 4.15: Base case turbulent kinetic energy contours on symmetry plane: range 0 – 0.1 m²/s²

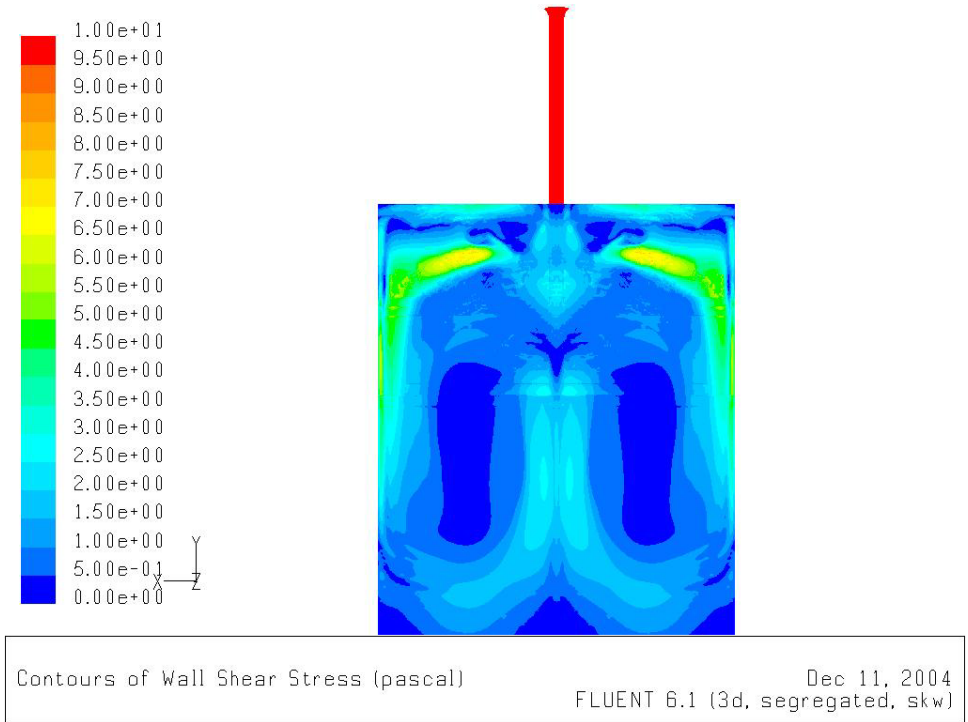


Figure 4.16: Base case wall shear stress contours on wide mould face: range 0 – 10 Pa

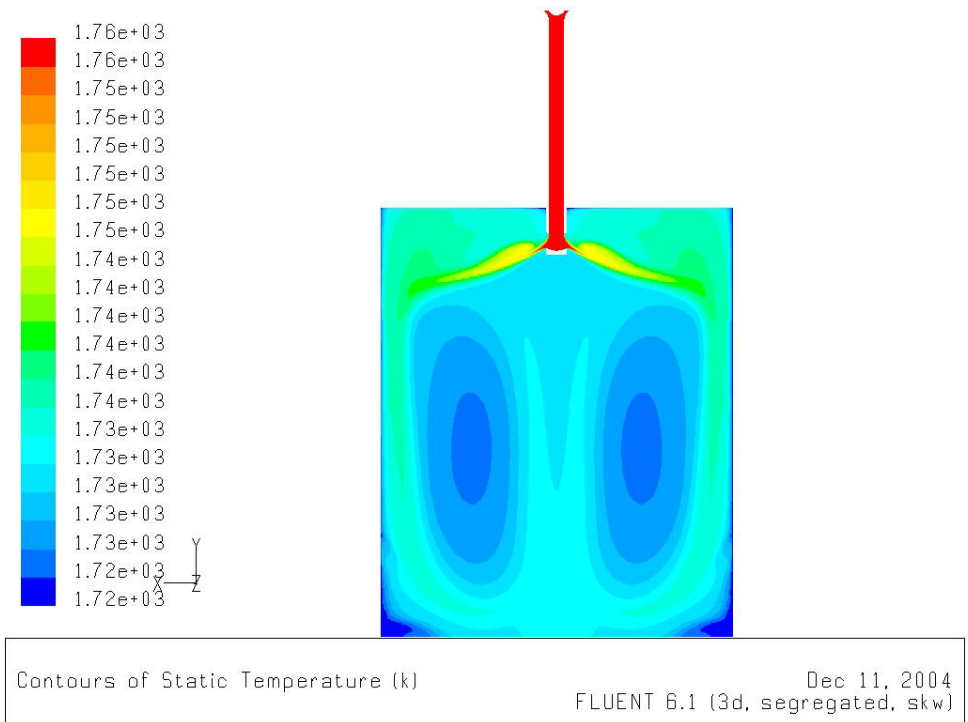


Figure 4.17: Base case temperature contours on symmetry plane: range 1723 – 1758 K

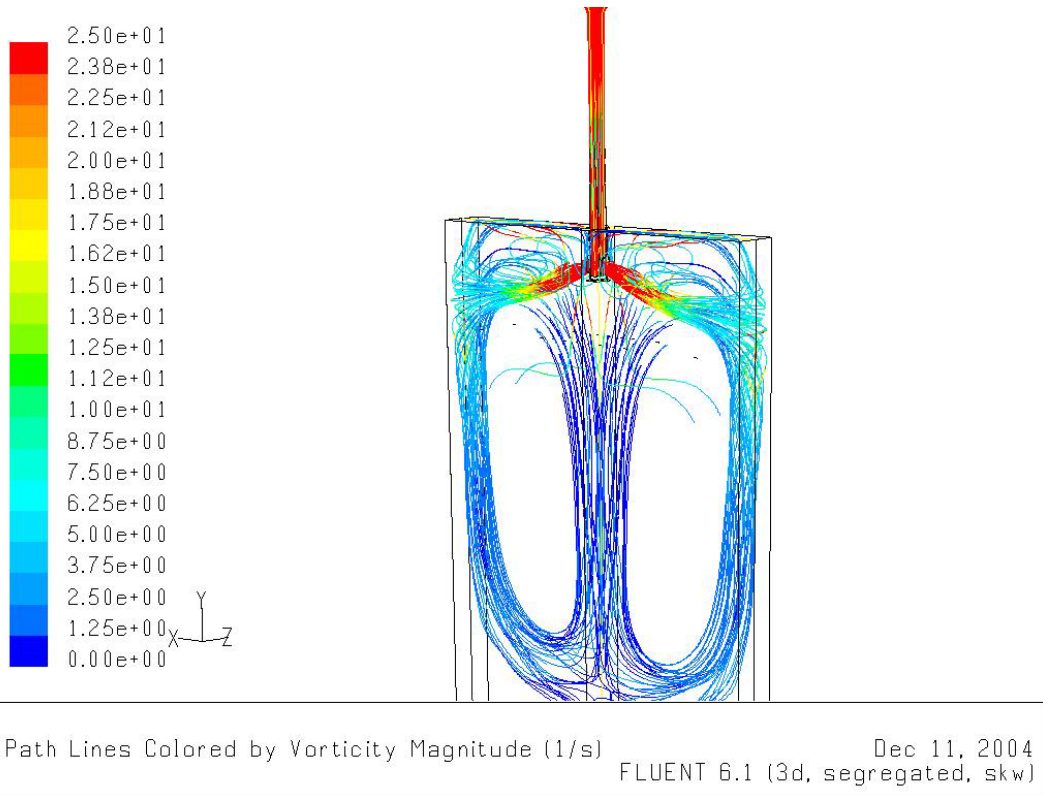


Figure 4.18: Base case path lines coloured by vorticity magnitude: range 0 – 25 1/s (isometric view)

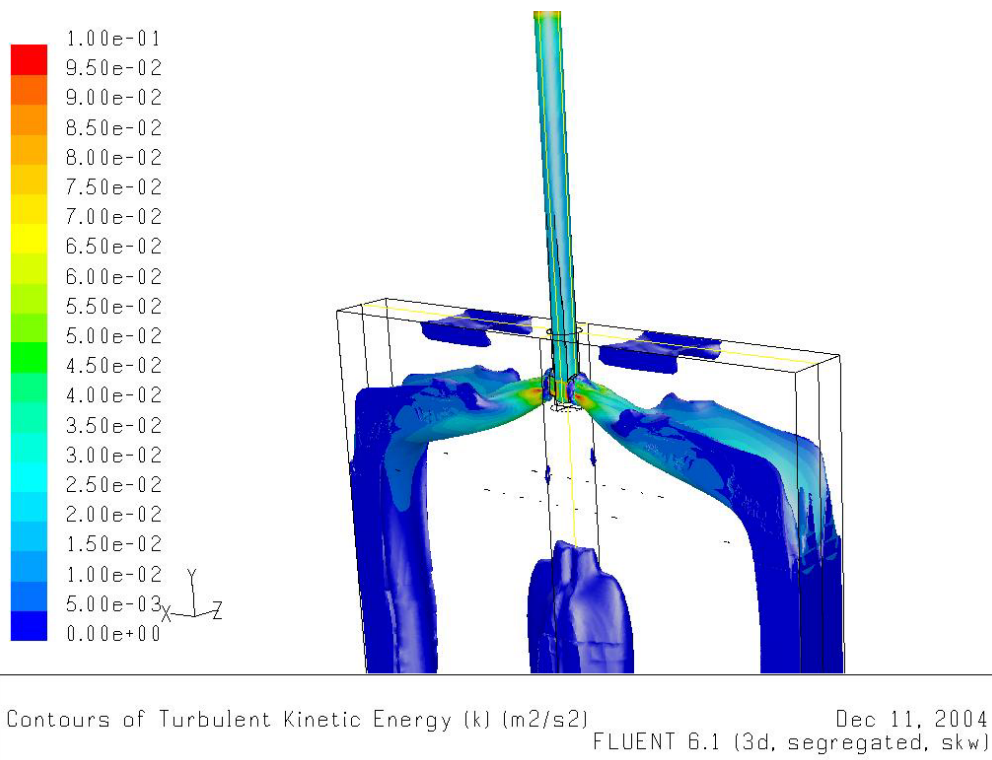


Figure 4.19: Base case iso-surface of velocity magnitude ($v=0.25\text{m/s}$) coloured by turbulent kinetic energy: range 0 – $0.1\text{ m}^2/\text{s}^2$

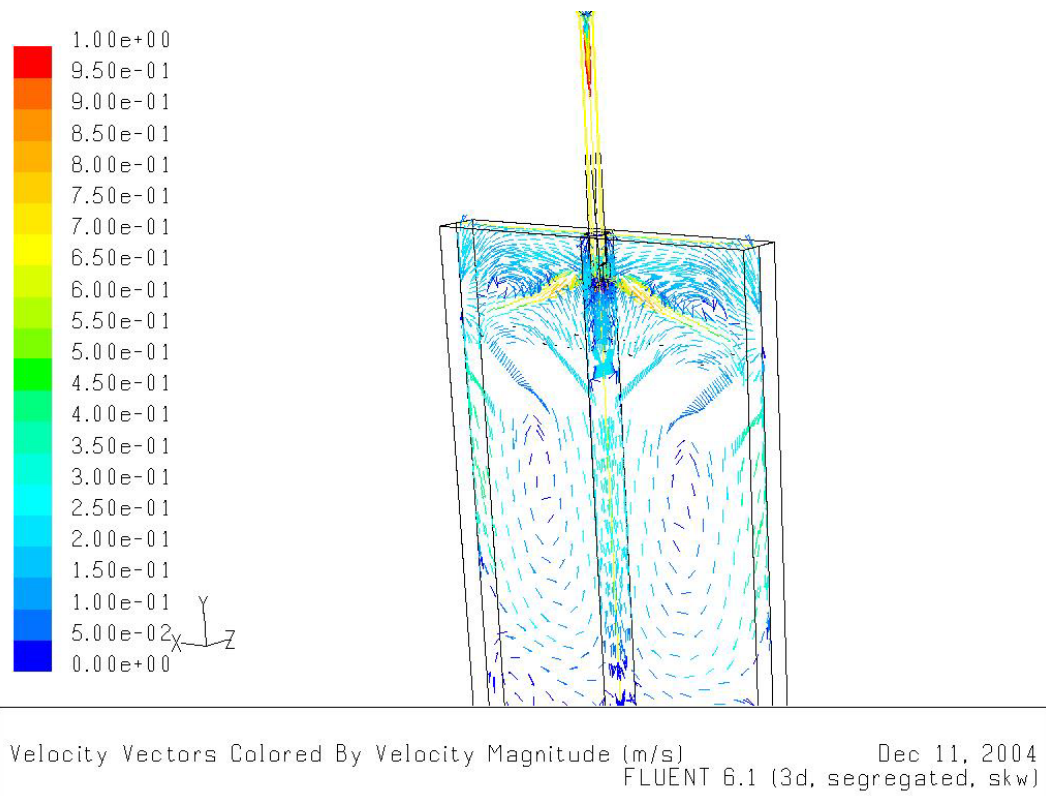


Figure 4.20: Base case velocity vectors coloured by velocity magnitude: range 0 – 1 m/s (isometric view)

The turbulent kinetic energy on the meniscus surface is shown in Figure 4.21, illustrating the approximate positions where the maximum TKE occurs on the meniscus. The figure is of a specific iteration and changes with each iteration (refer to Figure 4.11), and appears to be transient in nature. In Chapter 5, the maximum TKE on the meniscus surface will play a significant role in the optimisation process of the SEN and mould.

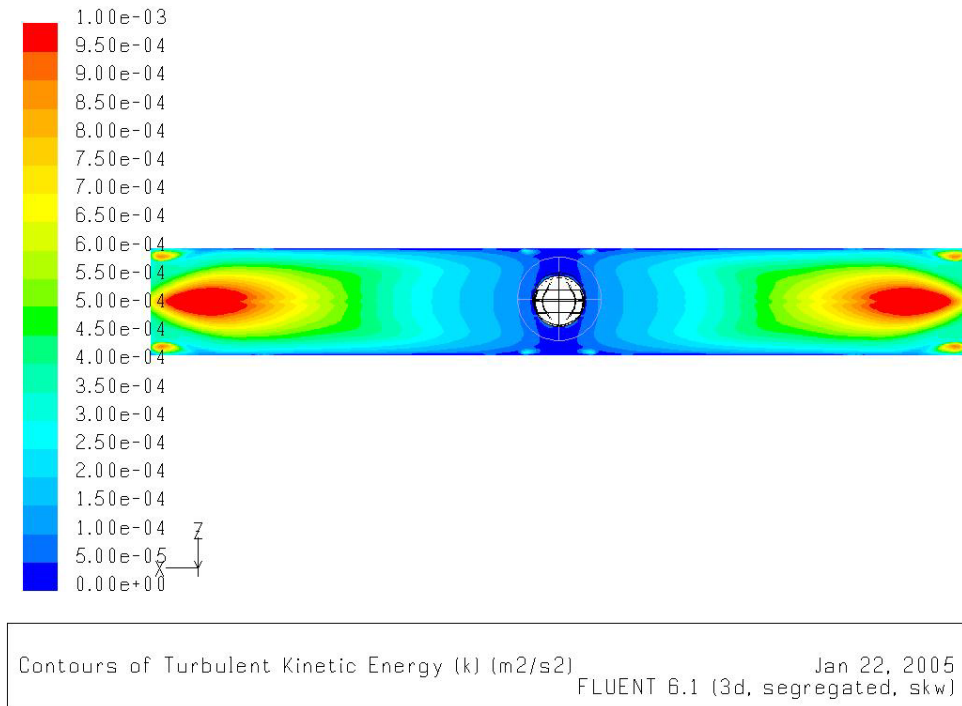


Figure 4.21: Base case turbulent kinetic energy contours on meniscus surface: range 0 – 0.001 m²/s² (top view)

4.6 CFD SEN and mould model: reduced widths

The initial base case and starting point of this study involved the 1575mm width slabs, as Columbus Stainless (a major initiator of the study topic) experienced the most quality problems on this width (their maximum width). As mentioned earlier in this chapter, a number of problems regarding the CFD modelling resulted in so-called unphysical flow solutions. Some inconsistencies still exist with models of the widest width.

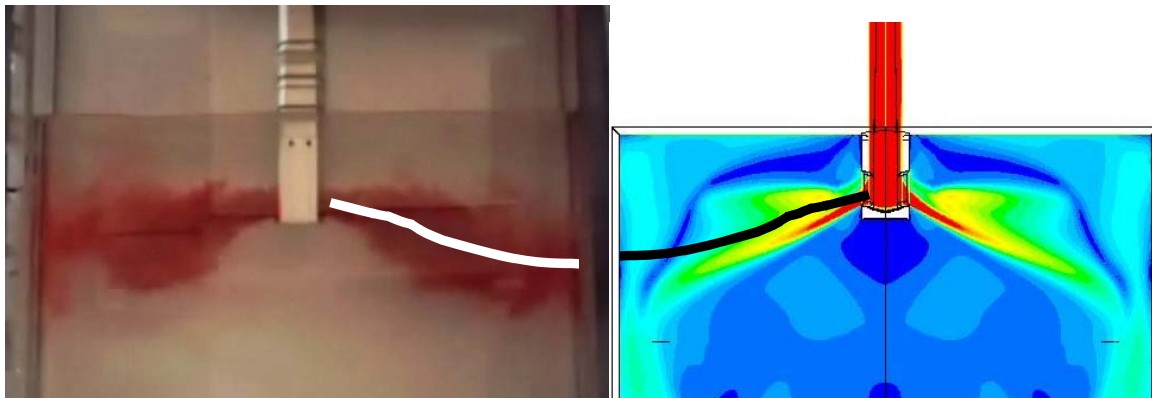
However, recently Columbus Stainless requested an optimum SEN design specifically for narrower slab widths (range 1000mm – 1300mm)¹⁵. Naturally, CFD models of these narrower widths were carried out, with surprising results:

¹⁵ Owing to availability of ADVENT full-scale water model results (also verified with UP 40%-scaled water model results), the widths 1060mm and 1250mm were chosen as representative for the 1000 – 1300mm range.

The 1060mm and 1250mm width results corresponded closely to water model validation (full-scale and 40%-scaled) results.

Refer to Figure 4.22 showing the good correspondence between the 3D CFD model velocity magnitude contours with the 40% water model test.

1060mm width; 80mm submergence depth; 1.1m/min casting



UP 40% water model

CFD $k-\omega$ turb model

Figure 4.22: Comparison: Old SEN 40%-scaled water model with 3D CFD model (contours of velocity) on centre plane

An interesting observation was that the submergence depth does not have a major influence on the jet angle – it is mostly determined by the SEN design (port height, angle, amongst others). Figure 4.23 clearly illustrates this point: the CFD model at a (full-scale) submergence of 80mm, visualised using path lines, corresponds accurately to the jet pattern of the 40%-scaled water model, at a much deeper submergence depth of 150mm (full-scale). The SEN design used in Figure 4.23 is the base case (old SEN) as described in section 4.2 of this chapter.

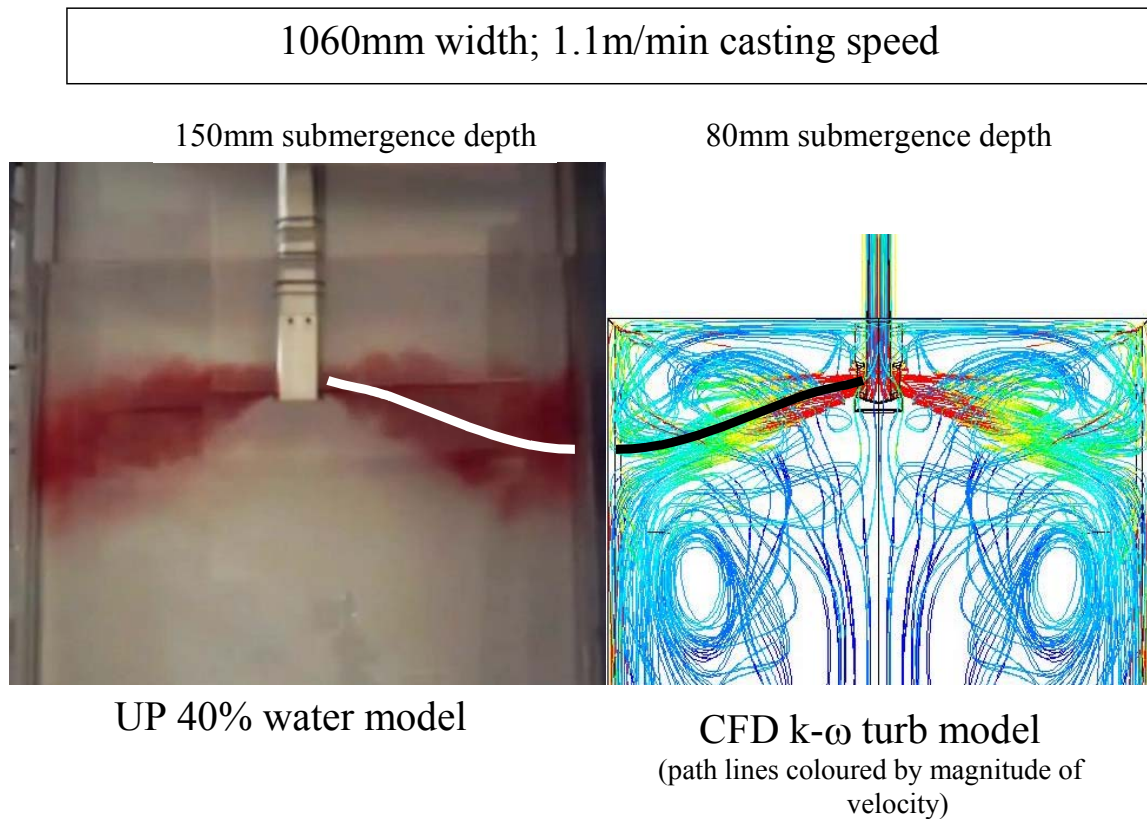


Figure 4.23: Submergence depth does not influence jet angle significantly at Fr-similarity flow rate

The improved correspondence of the CFD models of the narrower widths with water modelling can be attributed to the more stable solution procedure (as opposed to the somewhat erratic residuals history of the 1575mm wide CFD models). Not only are more cells necessary for the wide widths, but also the effect of the isotropic turbulence assumption model seems to influence the jet characteristics in the larger mould cavity. Usually, the jet seems to rise or “pick up” as it nears the mould wall, presumably as it runs out of momentum due to the spread-out of the jet in the mould cavity. The author believes that this can be partly attributed to the (incorrect) assumption of isotropic turbulence.

In Chapter 6, some suggestions are made with respect to CFD options to eliminate the deviations from the real (water modelled) flow, especially for the widest and coincidentally the most problematic widths.

4.7 Conclusion of base case CFD modelling

This chapter has illustrated CFD modelling of the SEN and mould base case as the stepping-stone towards SEN optimisation with CFD.

A typical approach to any CFD simulation problem was illustrated using a diagram. This approach was applied to the base case for this dissertation, which is the SEN currently used by Columbus Stainless, Middelburg, South Africa:

Firstly, the base case was described in detail and certain assumptions were motivated (e.g., simultaneous SEN and mould modelling, 2D vs. 3D modelling, etc.). Thereafter, the CFD set-up was described, including choice of mesh elements, boundary condition assumptions, choice of turbulence model, the solution procedure, to name but a few. A momentum-only model was created to mimic water model conditions for initial water model validation purposes.

After being confident that the CFD modelling of the water model was accurate, the next step was to extend the CFD model to be able to imitate the real steel plant circumstances. The solution of the full-scale CFD model of the real plant base case was illustrated using a number of visualisation techniques. The (possible) transient nature of the flow was also highlighted, which should be taken into account for optimisation purposes (by averaging the properties that will be used for the objective function/s). Furthermore, it was shown that reduced mould widths resulted in a more stable flow field (of the CFD solution), which also confirms the fact that Columbus Stainless experiences the most quality problems with their largest slabs with a width of 1575mm.

In conclusion: the CFD modelling approach (including CFD set-up and solution procedure) to typical SEN and mould applications was perfected and optimised for the base case and other similar cases. These methods were verified by validating the CFD solutions with water model experiments. Optimisation using these CFD modelling techniques follows in the next chapter.

CHAPTER 5: DESIGN OPTIMISATION OF SEN

All preceding work described in this dissertation constitute the stepping-stones towards the ultimate design optimisation of the SEN.

Design optimisation in the current field of application involves a few disciplines, woven into one composite process:

- CFD analysis
- Fluid mechanics (intervention of user required as explained in Literature Survey)
- Experimental Analysis
- Mathematical Optimisation
 - Engineering insight to:
 - identify candidate objective functions and constraint functions to ultimately obtain an “optimum” SEN design
 - identify all parameters, and select optimisation variables from these parameters to meaningfully express the objective and constraint functions
 - Classical formulation of optimisation problem [53]
 - Selection of optimisation algorithm
- Automation procedures of all of the above

Firstly, the automation procedures used in this dissertation will be expounded on, followed by formulating the classical design optimisation problem. Finally, the entire optimisation process will be illustrated using an example of a 2D SEN design optimisation exercise. Finally, due to computational limitations, an initial 3D SEN design space exploration will be conducted.

5.1 Automation of Optimisation process

As a meaningful design optimisation exercise may require at least three (3) design iterations (each consisting of a number of perturbations, depending on the number of design variables), it is crucial that the design optimisation process is automated.

5.1.1 Parameterisation: Automation of grid generation

The first step in any CFD model is the creation of geometry, and the discretisation of this geometry into cells (small volumes (3D) or areas (2D)), which is called meshing.

With design optimisation, it is desirable to create meshed geometries by just specifying a pre-programmed parameter. This idea (called parameterisation) will be described using a 2D SEN as an example.

Figure 5.1 shows a 2D SEN design with a number of possible parameters. Only 4 of these parameters were chosen as design variables:

- x_1 = SEN port angle
- x_2 = SEN port height
- x_3 = well depth
- x_4 = submergence depth

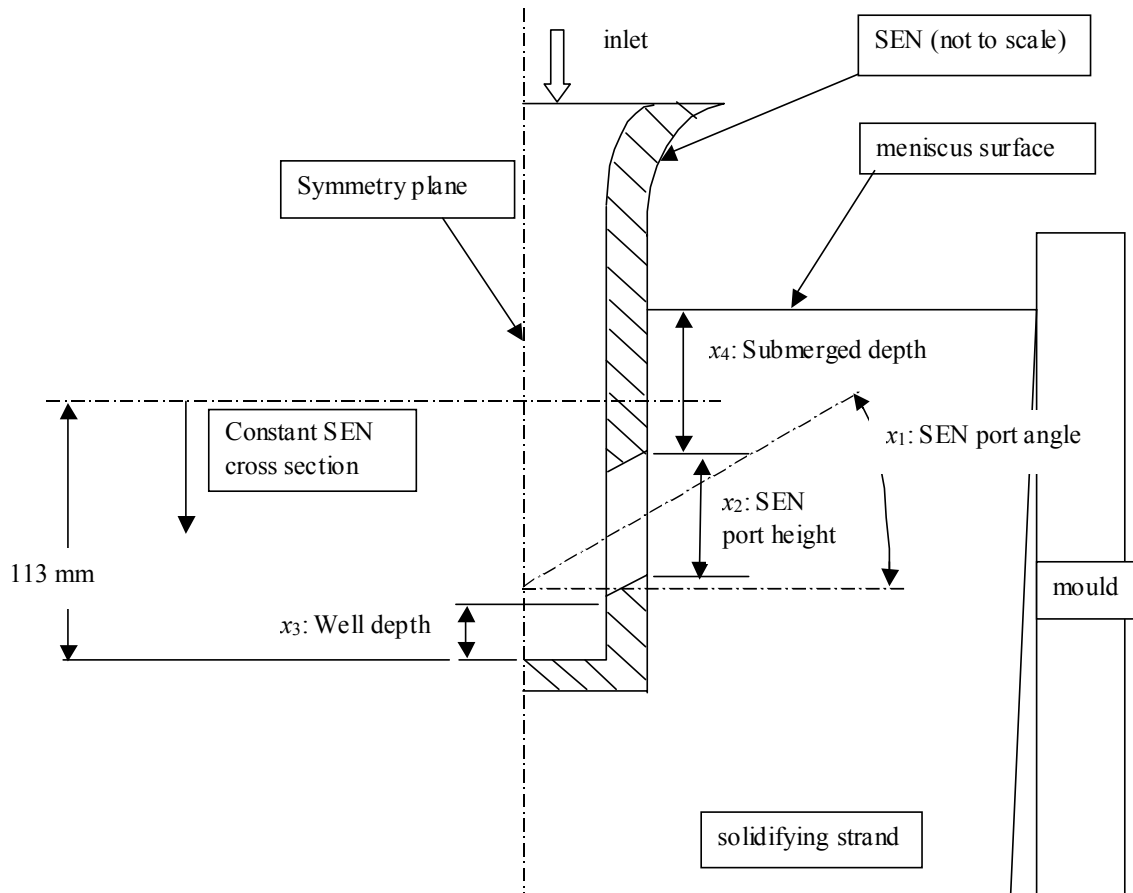


Figure 5.1: Design optimisation: parameterisation of 2D SEN

Suppose the base SEN design is similar to that of the new SEN of Columbus Steel with the base values for x_1 , x_2 , x_3 , x_4 or $\mathbf{x}^{(1,0)}$. The superscript (1,0) indicates the base case (0) of the first design iteration (1).¹

Scripting capability

The pre-processor, GAMBIT [11], has a scripting capability that enables a user to parameterise a geometry and mesh. Instead of using the GUI (Graphical User Interface) of GAMBIT, the user can enter command lines one at a time, or a number of commands using a text file (~.txt). This text file is commonly known as the script file, and the pre-processor simply interprets these commands consecutively and sequentially.

It is thus conceivable that with the generation of the 2D SEN geometry in Figure 5.1, the specific angle of the SEN port (for example) is specified during the

¹ Another explanatory example: The second (2nd) perturbation of the third (3rd) design iteration would be expressed as $\mathbf{x}^{(3,2)} = [x_1 \ x_2 \ x_3 \ x_4]^{(3,2)}$

rendering process. GAMBIT enables the user to use a variable in such a case. For example: Instead of specifying the command:²

```
“create vertex from vertex (0,0) at distance 20mm at angle 15°”
```

the following command is given:

```
“create vertex from vertex (0,0) at distance 20mm at angle %x1”
```

The variable %x1 (thus x_1) can now be specified in the beginning of the script file, e.g.

```
“%x1 = 15”.
```

Extrapolating this idea to the other variables, the geometry is considered to be parameterised. Consequently the following scenario is achievable:

By only specifying the variables %x1 (thus x_1), %x2, %x3 and %x4 at the beginning of the script file, the pre-processor will “automatically” render the geometry according to these specified parameters.

As briefly explained in the Literary Survey, the Optimiser suggests certain perturbations of the design (*i.e.*, other values for x_1 , x_2 , x_3 , x_4) during each design iteration. It is however possible to automatically update the values in the script files using the optimiser LS-OPT. This fact already hints in a direction of total automatic optimisation. However, the entire automatic linking process (that also involves the CFD code) will be discussed in sections 5.1.2 and 5.4.

Apart from rendering the geometry (according to the specified or suggested design parameters) and meshing the geometry, the boundary types must be specified and named in the pre-processor GAMBIT to ensure correct interpretation by the CFD code FLUENT [10].

To summarise: in GAMBIT, all the necessary GUI inputs required for a meshed geometry can also be performed using a parameterised script file (or journal file), which can be edited automatically by the Optimiser.

² Note: Pseudo code is used here only to illustrate a point. The correct scripting code can be viewed in [Appendix J](#).

For an example of such a script file, refer to [Appendix J](#). This script file generates a 2D SEN geometry and mesh, similar to that in Figure 5.1.

5.1.2 Automation of CFD code - Optimiser interface

As explained in detail in Chapter 4, the geometry and mesh imported from GAMBIT, needs to be defined and configured before the CFD solution can be initialised. All the definitions and configurations for any CFD model are performed using the GUI of FLUENT.

FLUENT has the same scripting capability as GAMBIT (explained above in section 5.1.1): script commands are interpreted sequentially and consecutively from these text files by FLUENT. As the geometry changes during the design optimisation, the boundary types remain the same; subsequently the FLUENT script files remain unchanged in essence during an optimisation exercise. However, if a flow parameter is included in the optimisation as a design variable, the FLUENT script file would change.

There are two script files applicable to a CFD model evaluation in FLUENT:

- Set-up script file (as explained above)
- Run (monitoring data etc.) or convergence procedure script file

The run script file ensures that the solution procedure, as developed in Chapter 4 by trial and error methods, is followed with each CFD evaluation, to ensure repeatable convergence of each model and accompanying physical correctness.

Optimiser as interface and coordinator

The CFD code “package” (GAMBIT and FLUENT) cannot perform optimisation without an optimising code (henceforth referred to as the Optimiser).

The Optimiser, using the classically formulated optimisation problem, and starting from a base case design, uses the CFD code package to ultimately find an optimum design (set of optimised variables) that satisfies the original optimisation problem.

LS-OPT, the optimiser used in this dissertation, can be viewed as being mainly an optimisation algorithm, but with coordinating (scheduling) and interfacing capabilities.

The tasks of LS-OPT during a design iteration are best described in the company of a diagram. Refer to Figure 5.2 for the diagram that depicts the coordinating tasks performed during each iteration.

Description (to be read in conjunction with the diagram in Figure 5.2):

The heart of LS-OPT can be described as the optimisation algorithm that endeavours to minimise the objective function $f(\mathbf{x})$, satisfying the constraints $g(\mathbf{x})$ and $h(\mathbf{x})$.

Starting from a base case design, $\mathbf{x}^{(1,0)} = [x_1 \ x_2 \ x_3 \ \dots \ x_n]$, LS-OPT needs to evaluate the base case (*i.e.*, run a CFD model and extract the relevant information) to

- establish the value of the objective function;
- establish whether the constraints are violated, or in what degree they are violated.

Firstly, LS-OPT updates the GAMBIT parameterised script file to contain the base case design $\mathbf{x}^{(1,0)}$, and execute GAMBIT with this script file as input. The GAMBIT output file is imported into FLUENT, simultaneously running the set-up script file. The desired geometry is now set up in FLUENT; consequently the run script file is executed. As soon as the CFD solution is converged, LS-OPT uses a similar script file to extract flow field data from the CFD solution (data was written to text files during solution convergence – as specified by the run script file). The data extracted from the converged solutions are also called responses. A

response can be a combination of information extracted from the converged CFD solution that LS-OPT uses to evaluate the objective and constraint functions.

LS-OPT now uses the flow field data to calculate the values of $f(\mathbf{x}^{(1,0)})$, $g(\mathbf{x}^{(1,0)})$ and $h(\mathbf{x}^{(1,0)})$.³

LS-OPT then chooses a first perturbation design ($\mathbf{x}^{(1,1)} = [x_1 \ x_2 \ x_3 \ \dots \ x_n]$), with reference to the values calculated for the objective and constraint functions from the flow field data.

LS-OPT repeats the procedure described above for the first perturbation, until the required number of perturbations are evaluated. Suppose 8 perturbations are required by LS-OPT per design iteration: After evaluating perturbation design $\mathbf{x}^{(1,8)}$, LS-OPT uses its optimising algorithm to predict the optimum design $\mathbf{x}^{(1,*)}$ for the first design iteration, taking into account designs $\mathbf{x}^{(1,1)}$ to $\mathbf{x}^{(1,8)}$.

The optimum design of design iteration 1 ($\mathbf{x}^{(1,*)}$), doubles as the base case design for design iteration 2 ($\mathbf{x}^{(2,0)}$), and the entire process repeats itself until the optimisation problem has converged sufficiently.

³ Traditionally in Mathematical Optimisation, $f(x)$ refers to the objective function, $g(x)$ to the inequality constraint function(s) and $h(x)$ to the equality constraint function(s).

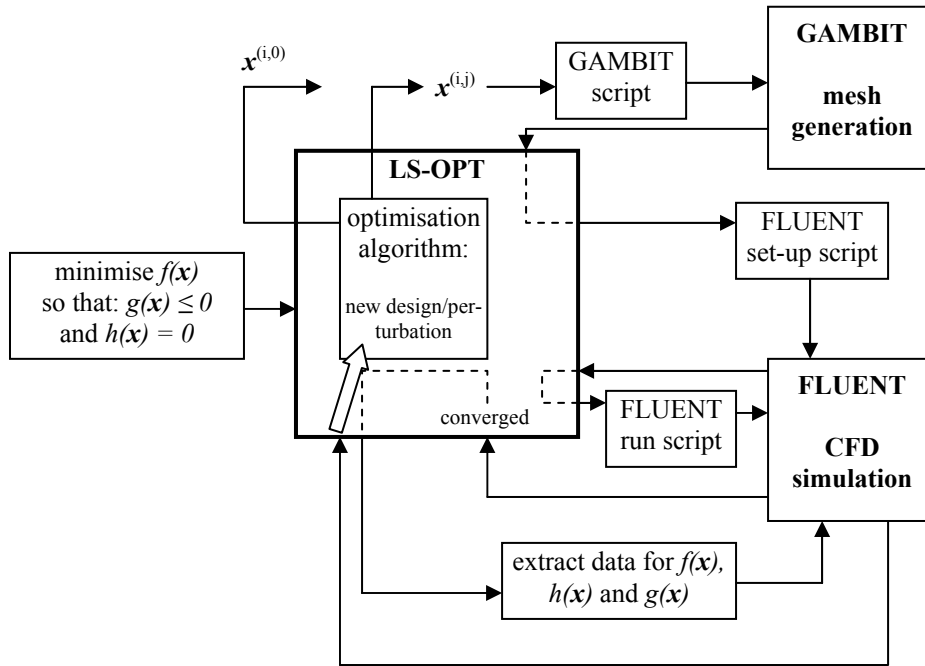


Figure 5.2: Diagram depicting the tasks (including coordinating tasks) performed by LS-OPT during the design optimisation process

LS-OPT is set-up beforehand by the user to carry out the coordinating tasks depicted in Figure 5.2 and explained above. The user sets up a command file (which is similar to a script file) that is interpreted by LS-OPT at each design iteration, orchestrating all the necessary run-commands. The operating system used in these command files is UNIX or more specifically Linux.

Refer to section 5.5 for an example of such a command file.

5.2 Candidate objective and constraint functions

The standard mathematical optimisation problem concerns the minimisation of an objective function with respect to design variables subject to certain constraints. When defining a mathematical optimisation design problem, the choice of objective function and constraint function(s) is crucial to the success of the design optimisation

process. The selection of design variables also requires some insight into the possible sensitivity of parameters defining the design. Some of these parameters become variables in the design if they are deemed to influence the quality parameter or objective function significantly, in other words, if their variation would improve the design. Improving the design means that the value of the chosen objective function improves (thus becomes less, owing to the fact that the objective function is chosen in such a way that it needs to be minimised).

The SEN plays a major part in the continuous casting process explained in Chapters 2 and 4. As the SEN introduces the flow to the mould, it has an effect on the flow pattern in the mould; consequently **the SEN has an impact on the quality of the steel**. The SEN, in particular the SEN geometry, has a primary influence on the flow pattern: the SEN controls the speed, direction and other characteristics⁴ of the jet entering the mould.

However, in the continuous casting steel making industry, the definition of quality is not straightforward, mainly because it depends largely on the type of product being cast and the manufacturing practices being followed. Consequently, defining parameters and/or flow situations (objective functions) that are desirable, is a difficult task. For the purpose of this study, quality is defined as the “internal cleanliness” of the steel, implicating that a stable meniscus surface is required for a constant casting speed. The stability of the meniscus surface becomes critical, especially when high casting speeds are considered.

In fact, previous studies [54] investigated the effect of static magnetic-field application on the mould in order to suppress the fluctuations of molten steel at the meniscus, and to provide uniformity of downward flow in the lower part of the mould. Too much fluctuation (instability) of the meniscus enhances slag powder entrainment. Entrained slag (or slag powder) is detrimental to the quality of the steel, as it solidifies within the slab and results in defects within and even on the surface of the final

⁴ Other characteristics of the jet emanating from the SEN may include turbulence effects, the occurrence of vortices, jet angle as it exits from the SEN, impingement point onto the narrow mould wall, impingement angle, etc.

product. Thus, minimising the maximum turbulent kinetic energy on the meniscus surface is a good initial objective function in order to ensure meniscus stability.

There is, however, a contradictory constraint on the relative intensity of meniscus activity (resulting from upward and downward flows within the mould). The advantages of a very stable meniscus were discussed above; however, meniscus freezing may occur with possible catastrophic consequences [54]. Kubota *et al.* [55][56] proposed an optimum range of surface velocities (between 0.15 and 0.25 m/s) to minimise surface defects on sheet metals while preventing meniscus freezing. The possible existence of this optimum flow will be explored and investigated when the effect of temperature is linked to this optimisation process later in this Chapter. However, for the purposes of this study, the author assumes that meniscus freezing will not occur.

From the premise that “good quality” refers to the internal cleanliness of cast steel, other objective functions to consider for later optimisation studies include:

- minimising path lines that exit at the bottom of the mould
- maximising particle entrapment by the slag layer on the meniscus
- minimising the exit of the particles at the mould exit
- maximising the magnitude of the vortices or the barrel-roll effect of the steel jet as it impinges the mould wall, to ensure Ar-bubbles are drifted upwards, simultaneously limiting excessive meniscus movement (for the case where Argon is injected to manipulate the SEN jet and to prevent SEN port clogging).

Inter-relatedness of objective and constraint functions

The above paragraph (especially the last objective (and constraint) functions) illustrates the inter-dependency of the choice of objective and constraint functions. Practical design optimisation studies seldom produce meaningful results without cleverly chosen constraint functions.

For example: Suppose the objective function is to minimise the maximum kinetic turbulent energy on the meniscus. With no constraint functions, the mathematical

optimiser would obviously suggest a SEN design with a downward angle, a substantial submergence depth and large nozzles, until the objective function is practically zero. Moreover, without any constraints, the “optimum” SEN design’s downward angles and oversize nozzles may be unmanufacturable (due to lacking material properties).

Thus; in order to extract some value from the optimum design, meaningful and carefully considered constraint functions must be chosen. In this example, the first obvious constraints will be physical constraints on the design to ensure that the optimum SEN can be manufactured. Secondary constraints necessary to achieve a meaningful practical design will probably be to limit the meniscus velocity, to prevent meniscus freezing, and to limit stationary spots on the meniscus surface, amongst others.

Refer to section 5.5 where the objective functions and constraint functions are formulated for the 2D design optimisation.

5.3 Design variables x

The importance of correctly chosen design variables cannot be over-emphasized. The selection of design variables also requires some insight into the possible sensitivity of parameters defining the design. Moreover, the choice of design variables is also influenced by the objective and constraint functions, as certain parameters are more dependent and linked to certain flow phenomena – represented by the functions in question.

During the parameterisation of the SEN geometry and mesh necessary for automation (section 5.1), a number of parameters (that can easily be altered) were identified. However, some parameters are operational parameters (and subsequently do not alter

the SEN design), and other design parameters might have an insignificant effect on the flow field.

Thus; the user needs to select design variables from the available parameters in a design optimisation study that will deliver the most effective improvement (depending on objective function) results.

As explained in section 5.1, the design variables \mathbf{x} , can be expressed as:

$$\mathbf{x} = \begin{bmatrix} x_1 \\ x_2 \\ \dots \\ x_n \end{bmatrix}; \text{ with } n \text{ design variables}$$

The values of the design variables \mathbf{x} describe the design. Using the example in section 5.1 (refer to Figure 5.1), the design variables describe the SEN design (2D) with respect to the SEN port angles, SEN port heights, inherent well depth inside the SEN, and submergence depth of the SEN below the meniscus.

The optimum design, will be the values of $\mathbf{x}^* = [x_1^* \ x_2^* \ x_3^* \dots \ x_n^*]$, which should be the optimum design of at least the 3rd design iteration⁵ (equivalent to $\mathbf{x}^{(4,0)}$ or the ‘base case’ of the fourth design iteration according to definitions in section 5.1).

Scaling of design variables and constraints

In the event that the values of design variables differ in three orders of magnitude or more, it is advisable that the formal optimisation problem be set up in such a way that the values of the variables are scaled to similar orders of magnitude. LS-OPT scales design variables automatically in the event of optimisation variables differing in orders of magnitude. On the other hand, constraint functions are not scaled automatically. It is therefore recommended that different constraint functions are of similar orders of magnitude to ensure equal weight during the optimisation process, especially in the treatment of multiple violated constraints.

⁵ A meaningful optimum design will not necessarily be reached after three design iterations: past experience only indicates that at least three design iterations were necessary for a meaningful improvement in the design.

5.4 Optimisation process

Apart from the coordinating ability of LS-OPT (to enable automated design optimisation as described in section 5.1.2), the “heart”/essence of LS-OPT is obviously its mathematical algorithms to predict the optimum design from the results of a number of CFD model evaluations.

LS-OPT uses a Response Surface Methodology together with a mathematical optimising algorithm (Snyman’s LFOPC), and has certain advantages above other approximation methods⁶: [57]

- Design rules based on global approximations
- Does not require analytical sensitivity analyses
- Smooths design response and stabilises numerical sensitivities
- Less function evaluations required due to accurate design surfaces in sub-regions, and trade-off curves and variable screening developed interactively

Existing and classical gradient-based optimisation algorithms do not perform satisfactory with real-world problems. This is particularly applicable to the field of engineering, where unique difficulties prevent the general application of general optimisation techniques. These optimisation difficulties that arise typically are:

- The functions are very expensive to evaluate (especially time-consuming with CFD simulations)
- The existence of noise (numerical or experimental) in the functions
- The presence of discontinuities in these functions
- Multiple local minima in these functions exist, requiring a global optimisation technique – as the response surface methodology
- The existence of regions in the design space where the functions are not defined

⁶ An approximation is regression in essence, where a suitable mathematical function (curve in 2D or surface in 3D) is approximated over a pre-determined number of design points (values of objective function in terms of design variables \mathbf{x}).

- The occurrence of a large number of design variables, disqualifying certain classical optimisation methods (as sequential quadratic problems, for example)

LS-OPT therefore employs the successive region scheme (or successive response surface methodology) combined with an optimisation algorithm of Snyman to find the global minimum of the chosen objective functions, simultaneously satisfying the constraint functions.

5.4.1 Response Surface Methodology

In essence, response surfaces can be described as the approximations of experimental design points in smaller design spaces (also called regions of interest or sub-regions). Their (initial) sizes are determined by the ranges of variables chosen beforehand. Linear (or quadratic, depending on the accuracy required) approximations (called response surfaces) are fitted in these sub-regions. With each successive design iteration, these sub-regions are adjusted (reduced or moved) until the optimum design is found. Any optimisation algorithm can be used to evaluate these response surface approximations. As already mentioned, LS-OPT uses Snyman's Leapfrog and penalty function method (LFOPC) [14] to determine the optimum design on each response surface. The latter is called the optimisation algorithm.

Firstly, the most important terminology associated with the response surface methodology will be explained. Refer also to Figures 5.3 to 5.6 for visual representation (only 2 design variables) of these terminologies.

- *design space*: global ranges of design variables. With two design variables a design space can be illustrated as an area.
- *response surface*: mathematical approximation (linear or quadratic in LS-OPT) of experimental design points in region of interest or sub-region
- *design point*: value of objective function, where the objective function is expressed in terms of the design variables

- *regions of interest or sub-regions*: ranges of variables in which response surfaces are approximated. With 2 variables, it can be illustrated as smaller areas inside the total design space area.

Figure 5.3 represents the design space with the initial region of interest (with pre-determined variable ranges) inside it. The “baseline design” (Figure 5.3) is equivalent to the base case design as explained previously. The experimental design points are the chosen perturbations within the pre-determined and chosen ranges of design variables.

Figure 5.4 illustrates (example with only 2 design variables) how a response surface is approximated through the base case and experimental (perturbations) design points. The least squares method of approximating response surfaces is employed by LS-OPT. The LS-OPT user has three (3) options of basis functions for the response surface approximations:

- First-order approximation: linear
The cost of first-order approximations is approximately n (using n design variables)
- Second-order approximations:
 - Full quadratic: cost $\approx n^2$
 - Elliptical approximation: cost $\approx 2n$

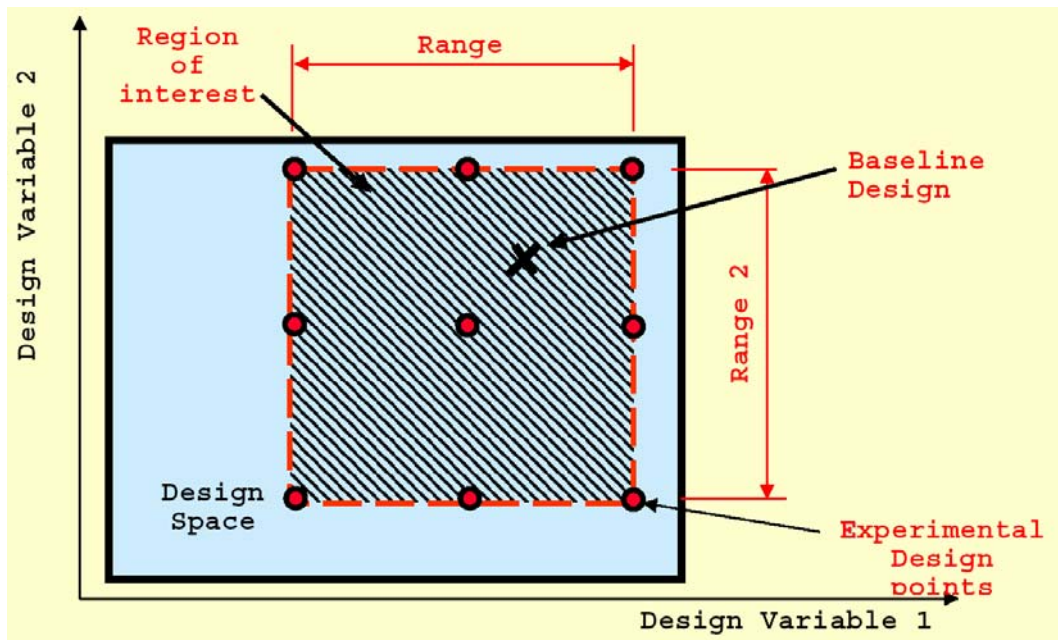


Figure 5.3: Design space terminology (design space, region of interest and experimental design points): response surface methodology [57]

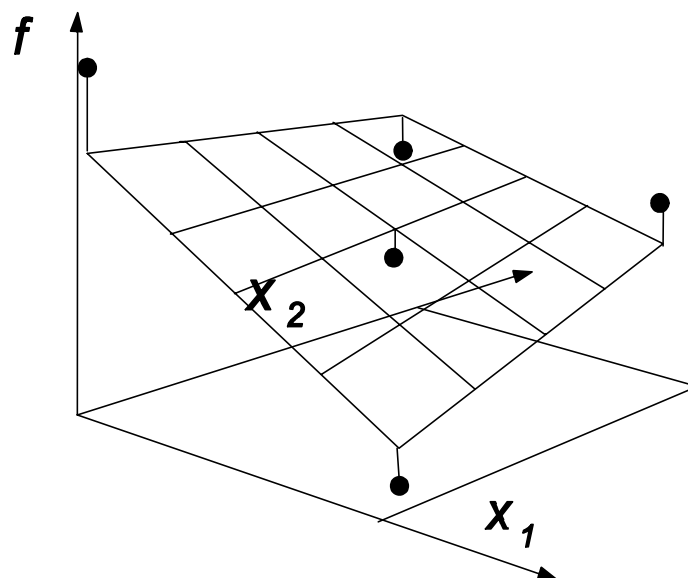


Figure 5.4: Example of response surface approximated over experimental design points [57]

The successive response surface approximation takes place on different (or rather adjusted) sub-regions, depending on the predicted optimum design point of the previous design iteration. The sub-regions (or successive regions of interest) can either “pan” (move) or “zoom” (reduce), or simultaneously pan and zoom. These adjustments are best described referring to Figure 5.5:

- pan: previous optimum predicted on the boundary of the region of interest of the previous design iteration
- zoom: previous optimum predicted close to the base case design point of the region of interest of the previous design iteration
- simultaneous pan and zoom: previous optimum predicted inside the boundary of the region of interest of the previous design iteration

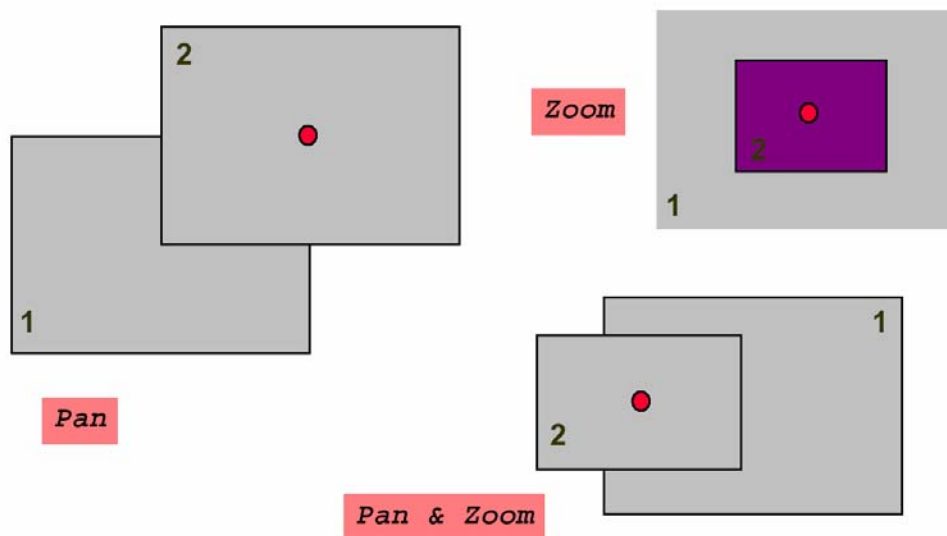


Figure 5.5: Successive sub-region reduction scheme [57]

Finally, Figure 5.6 illustrates the entire successive response surface methodology: The first region of interest is chosen (ranges of design variables pre-determined) around the starting design point (base case design). The second region of interest (that of the second design iteration) is panned, while that of the third and fourth design iterations are panned and zoomed – until an optimum design is found.

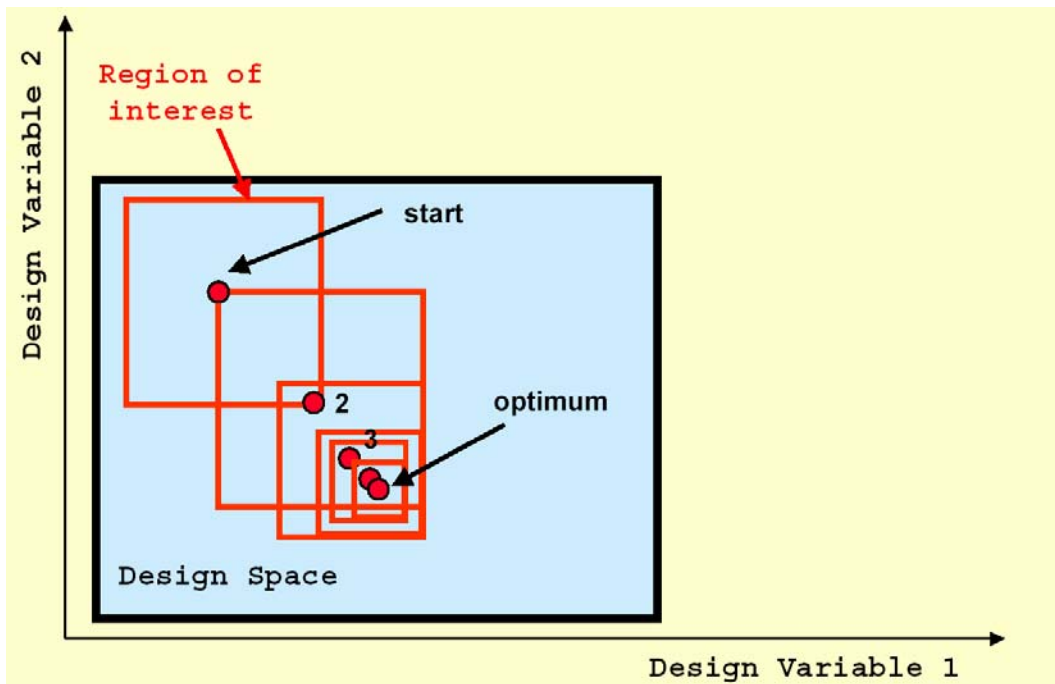


Figure 5.6: Successive sub-region reductions combined with optimisation of response surfaces (not shown) converges to an optimum [57]

5.4.2 LS-OPT Optimisation algorithm: LFOPC

The Leap-frog Method for Constrained Optimisation (LFOPC of Snyman) [14] is also known as the dynamic trajectory optimisation method, which is based on a physical model of a unit mass (ball) in a gravitational force field with a certain starting potential energy. After fitting an approximation or response surface to the experimental points inside each successive sub-region, the LFOPC algorithm is used to predict the optimum on the response surface in question.

The LFOPC algorithm is gradient-based, and also boasts the following characteristics:

- it uses only objective function *gradient* information or ∇f ;
- no explicit line searches are performed;
- it is robust, handling steep valleys, discontinuities and noise in the objective function and its gradient vector with relative ease;

- it seeks relative low minima and is thus suitable for global optimisation (although not a necessity with cleverly chosen starting regions of interest);
- it solves constrained optimisation problems using a penalty function formulation.

Penalty function formulations of a constrained optimisation problem forces the minimum of the unconstrained problem to also satisfy the inequality and equality constraint functions. More detail regarding the exact formulations and stages of penalty function applications can be viewed in Reference [14].

5.4.3 Variable screening (ANOVA)

After each design iteration, LS-OPT performs an analysis of variance (or ANOVA) on all responses to determine the significance of each response with respect to each variable. Significance of variables is a measure of their contribution towards change (improvement or deterioration) of each response.

Other measures of significance:

Variables with small gradients are designated as less significant. Noisy variables that display large scatter also reduce their significance.

The measure of significance used by LS-OPT is the lower bound of the 90% confidence interval of the regression coefficient b_j , or rather $b_j - \frac{\Delta b_j}{2}$. If this

lower bound is close to or smaller than zero (0), the regression coefficient is regarded as insignificant. In a linear approximation, a variable can be removed if its coefficient is insignificant.

For more information on obtaining the regression coefficient b_j , and the type of distribution functions used to determine the confidence intervals, please refer to the LS-OPT manual and theory references [12][57].

Usually, before attempting an optimisation exercise, it is advisable to firstly only run the base case and a few perturbations to allow LS-OPT to evaluate the significance of the design variables. The obvious result of an ANOVA analysis is the reduction of variables without influencing the optimum value of the objective function. In other words, the optimum value of the objective function using only significant design variables compares favourably with the optimum of the objective function using all the variables [58].

5.5 2D Optimisation: An example of the design optimisation process

5.5.1 Objective and constraint functions

Following the explanations in section 5.2 concerning typical objective functions for a 2D SEN design optimisation, the objective function is formulated as follows: In an effort to improve the internal cleanliness of the cast steel in the mould, the meniscus activity will be limited to prevent the entrainment of slag. This will be achieved by minimising the maximum turbulent kinetic energy on the mould meniscus.

Typical constraint functions will be limiting the design parameters to be physical possible (manufacturable) SEN designs, as well as ensuring that the impact point is above the mould outlet (to prevent obvious break-outs). Another geometrical constraint is the linking of the SEN port angle to the submergence depth, thus prohibiting the occurrence of a jet impinging directly into the meniscus.

In an effort to prevent slag entrainment due to excessive velocity on the meniscus, the maximum average velocity on the meniscus is constrained to a maximum of 0.6m/s, as proposed by Kubota *et al* [56].

On the other hand, in an attempt to prevent meniscus freezing, the minimum meniscus temperature will be monitored and constrained to remain above the solidus temperature of the steel used in this optimisation study (1728K or 1414°C).

5.5.2 Design variables x

Amongst the many design parameters in SEN design, the following parameters were selected as design variables for this optimisation study owing to their dominant effect on the flow pattern and their relevance to the current 2D application; *i.e.*, nozzle port angle, nozzle port height, and well depth. Although the submergence depth of the SEN was chosen as a variable in a previous optimisation study, it was decided to choose a constant 200mm submergence depth, mainly because it is regarded as an operational parameter rather than a design parameter. The submergence of the SEN is altered in any event during casting conditions as the SEN wall is eroded at the meniscus surface. Thus; a specified submerged depth below the meniscus will thus be of little use to a steel plant. Refer to Figure 5.1 (in section 5.1) for the definitions of these optimisation variables, with the exception of the submergence depth as a design variable.

Other typical SEN design parameters (not used in this study as variables) include: total length of SEN, amount of nozzle ports, geometrical shape of nozzle ports, radii of nozzle port corners, inner wall roughness of SEN, Argon gas injection rate (if present in order to counter clogging), to name a few.

Other operational parameters are kept constant for this optimisation study, and are listed in Tables 5.1 and 5.2 below.

Table 5.1: Constant parameters used in optimisation study: geometrical and steel properties

Description	Casting speed [mm/min]	Slab width [mm]	Submergence depth [mm]	Steel dynamic viscosity [kg/(ms)]	Steel solidus temperature [K]/[°C]	Liquid steel density [kg/m ³]
Constant value	1000	1575	200	0.0064	1725/1440	6975

Table 5.2: Constant parameters used in optimisation study: energy/temperature considerations

Description	Mould walls temperature [°C]	Heat flux from mould walls [W/m ²]	Inlet temperature [°C]	Outlet temperature [°C]	Heat flux from meniscus [W/m ²]
Constant value	1450	-300 000	1485	1410	-60 000

The ranges (or bounds) of the design variables were chosen by the author to represent possible physical SEN designs. These bounds (shown in Table 5.3) are represented by the inequality constraints in the formal optimisation problem formulation. The initial design was the base case or starting “point”.

The minimum well depth was limited to 0.1mm (as opposed to an obvious 0mm) due to problems encountered in the automatic grid generation process in GAMBIT.

Table 5.3: Ranges (or bounds) of SEN design variables and initial design for optimisation study

Optimisation variable	Minimum	Maximum	Initial design
x_1 : SEN port angle [°]	-25	25	15
x_2 : SEN port height [mm]	30	80	70
x_3 : Well depth [mm]	0.1	50	0.1

5.5.3 Formulation of Optimisation problem

The complete mathematical formulation of the optimisation problem, in which the inequality constraints are written in the standard form $g_j(\mathbf{x}) \leq 0$, where \mathbf{x} denotes the vector of the design variables $(x_1, x_2, x_3)^T$, or rather (nozzle port angle, nozzle port height, well depth)^T, is as follows:

minimise $f(\mathbf{x})$ = maximum turbulent kinetic energy on meniscus surface

subject to:

$$g_1(\mathbf{x}) = x_2 + x_3 - 113 \leq 0$$

$$g_2(\mathbf{x}) = \text{point of impingement under meniscus} - 675\text{mm} \leq 0$$

$$g_3(\mathbf{x}) = x_1 - 15/70 * \text{submergence} - 75/7 \leq 0$$

$$g_4(\mathbf{x}) = \text{average maximum velocity} - 0.6\text{m/s} \leq 0$$

$$g_5(\mathbf{x}) = \text{average minimum meniscus temperature} + 1725^\circ\text{C} \leq 0$$

$$g_6(\mathbf{x}) = -x_1 - 25 \leq 0$$

$$g_7(\mathbf{x}) = x_1 - 25 \leq 0$$

$$g_8(\mathbf{x}) = -x_2 + 30 \leq 0$$

$$g_9(\mathbf{x}) = x_2 - 80 \leq 0$$

$$g_{10}(\mathbf{x}) = -x_3 + 0.1 \leq 0$$

$$g_{11}(\mathbf{x}) = x_3 - 50 \leq 0$$

} bounds of design variables

where:

- The ranges (or limits) of the design variables (see Table 5.3 and g_6 to g_{11}) are chosen in order to constrain the optimisation process to ensure a physically possible optimum.
- The inequality constraint g_1 is required to ensure a physically or geometrically possible SEN design (due to manufacturing constraints). Refer to Figure 5.1 to note that the sum of the SEN port height (x_2) and the well depth (x_3) may not exceed 113 mm.
- The constraint g_2 prohibits the impingement point to be more than 675 mm below the meniscus surface. Most continuous caster moulds currently used at Columbus Stainless are 800 mm in length; however, at most only 700mm of the mould is in contact with the molten steel. If the impingement point is too low, *i.e.*, under the mould exit, where the unsupported shell (especially the narrow shell) is at its thinnest and weakest, the likelihood of bulging and breakouts will increase. A maximum value of 675 mm is chosen in order to compensate for different meniscus levels and still ensure that the impingement point remains above the mould exit.

- The constraint g_3 ensures that the jet never impinges the meniscus directly (with a large positive angle and the constant submergence depth), which will only result in the violation of the constraint g_4 that endeavours to limit the maximum meniscus velocity to 0.6 m/s. If a geometrical SEN design that will surely result in a violation of a constraint function (*i.e.*, g_4) can be avoided from the first instance, a precious (and computational expensive) CFD evaluation can be saved. The Optimiser is thus much more effective with the assistance of this constraint function.
- The constraint g_4 endeavours to limit the maximum meniscus velocity to 0.6 m/s in an effort to prevent slag entrainment.
- Constraint g_5 monitors the minimum meniscus temperature to ensure that this temperature remains above the solidus temperature of the steel. This will hopefully prevent meniscus freezing, which is also a serious cause of breakouts.

Note that constraints g_1 to g_5 were scaled using LS-OPT to ensure that all the violations of the constraint functions are of the same order. This will prevent constraint functions with larger violations from dominating the Optimiser's choice of perturbations during the optimisation exercise.

5.5.4 Base case: discussion

As described in previous chapters in this dissertation, the base case design needs to be set up and confirmed or validated before commencing with the optimisation study.

The 2D base case was developed and validated in Chapter 4. For the sake of completeness, the basic CFD modelling is repeated:

5.5.4.1 Geometry and Mesh for 2D

Due to symmetry, only half of the SEN and mould is modelled by applying a symmetry plane (or edge for 2D) on the centre plane of the mould. It is known that the flow is non-symmetrical when a slide gate valve is used upstream of the SEN in order to control the meniscus height and casting speed [4][5]. However, when using a stopper as a control valve (which is the case at Columbus Stainless), the flow is generally more symmetrical and thus assumed to be symmetrical for the purposes of this design study.

The grid for the 2D half-model SEN and mould geometry is generated automatically for all the design iterations and perturbations using GAMBIT as described in section 5.1. A fine (high density), fully-structured grid is generated using quadrilateral (commonly known as “hex”) cells. The mesh of the starting design configuration is shown in Figure 5.7 and consists of approximately 75 000 cells. Grid adaption was employed during each CFD evaluation; however, only in the jet regions and not throughout the entire mould.

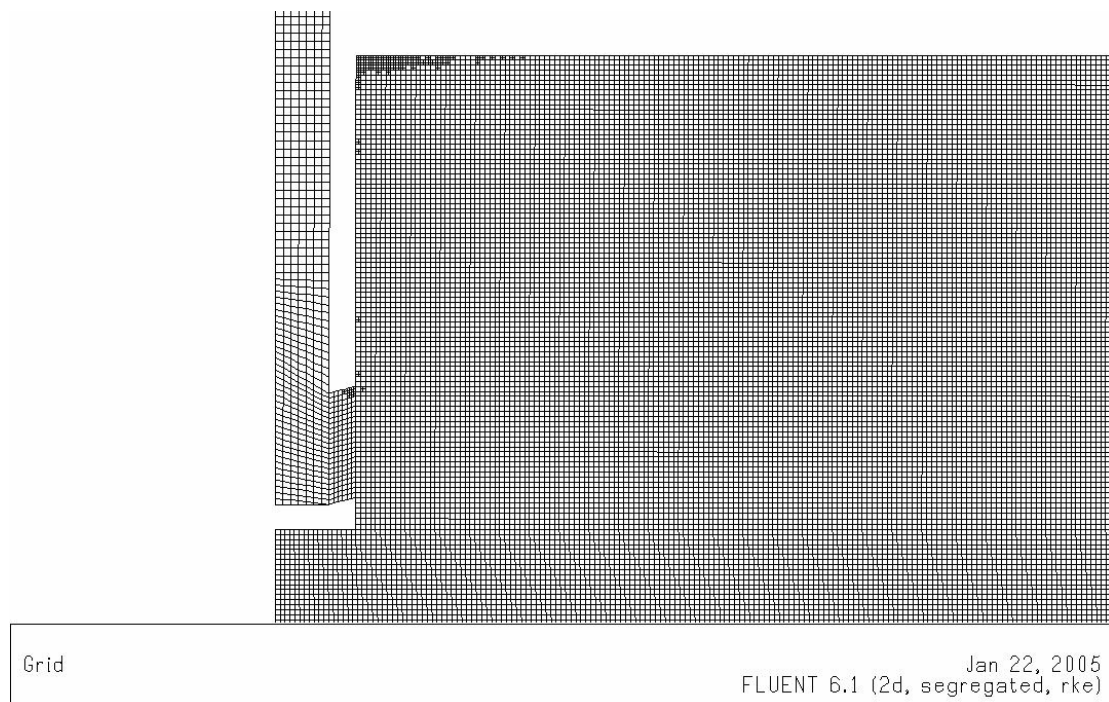


Figure 5.7: Structured mesh of SEN and mould 2D half-model

5.5.4.2 SEN nozzle height in optimisation study: 3D vs. 2D

The SEN port height shown in Figure 5.1 is the actual height of the 3D SEN port on the centre plane. However, when modelling a 2D SEN and mould, the jet is no longer modelled to be emanating from a hole, but rather from an indefinitely long slot. Observing the shape of the 3D nozzle (from the side) in Figure 5.8, it is clear that the height of the slot must be reduced to be compared to the 3D nozzle. Taking into account the radius of the upper and lower curve and the width of the nozzle hole (which was coincidentally held constant for this study), the average height is computed analytically (integrated along the radius) for each grid generated during each design iteration, as shown in Figure 5.8. The average height of the 3D nozzle therefore becomes the 2D nozzle (or rather slot) height, in order to achieve more accurate 2D results, which will hopefully be more comparable with the results of similar 3D CFD models.

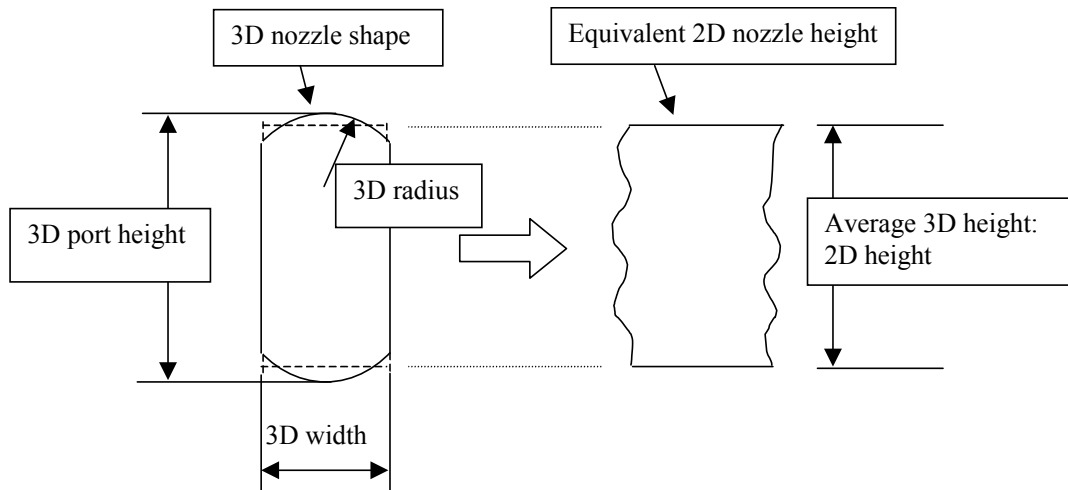


Figure 5.8: Side view of the 3D SEN nozzle and subsequent reduction of port height for average height (2D height)

5.5.4.3 Boundary conditions

A slip surface (zero shear stress) is used on the upper boundary of the steel (*i.e.*, the meniscus surface) to model the slag layer as indicated in Figure 5.7. The narrow mould wall is modelled as a moving wall, moving downwards at the casting speed as indicated in Table 5.1. The bottom of the mould is modelled as a pressure outlet boundary condition at atmospheric pressure. The length of the mould is modelled as approximately 4.1 meters, which is more than is required (approximately 3m [2]) to model both recirculating zones.

5.5.4.4 Solver solution procedure

A similar solution procedure as described in Chapter 4 was used to achieve converged results. The only difference is that when grid adaption takes place, it only takes place in the jet region, and not throughout the entire mould as implicated in Chapter 4. Sufficient convergence is assumed when at least a four-order drop in all normalised residuals are achieved.

5.5.5 Automation for design optimisation

As explained in section 5.1 above, the following script files were developed as soon as the base case design CFD model were validated and trustworthy, in order to automate the design optimisation process:

- GAMBIT script file
- FLUENT script files
 - Set-up file
 - Run file
- LS-OPT command file

5.5.5.1 GAMBIT parameterised script file

Refer to [Appendix J](#) for the GAMBIT script file for the generation of all possible designs within the bounds of the design variables of this optimisation

study. Section 5.1 explains the fundamental concepts behind parameterised geometries and how to create any geometry using script files.

5.5.5.2 FLUENT script files

- a) Set-up file
- b) Run file

Usually these two script files are combined into one FLUENT script file, as the second set of tasks (run file) naturally follows the set-up procedure. Refer to [Appendix K](#) for the combined FLUENT script file as used in this optimisation study:

- set-up section,
- followed by the run section.

Section 5.1 explains the fundamentals behind the automatic manipulation of the CFD solver FLUENT using script files.

5.5.5.3 LS-OPT command file

The command file has all the information concerning the optimisation exercise, including the variables and their respective bounds, as well as all the run commands for GAMBIT and FLUENT.

Refer to [Appendix L](#) for the command file (com-file) used for this optimisation exercise.

5.5.6 Results and discussion of design iterations

5.5.6.1 Flow and Meniscus Turbulent Kinetic Energy Results: base case

The flow pattern of the initial design (or base case design) is shown in Figure 5.9. The constraint g_2 is also shown in Figure 5.9, as well as the approximate mould exit. The velocity magnitude of the vectors is indicated by their relative lengths with respect to the 1 m/s vector shown in the same figure, as well as the colour scale.

Note that the impingement point for the base case is well above the lowest allowable point; however, there is believed to be still much room for improvement for the maximum Turbulent Kinetic Energy (henceforth TKE) on the meniscus surface.

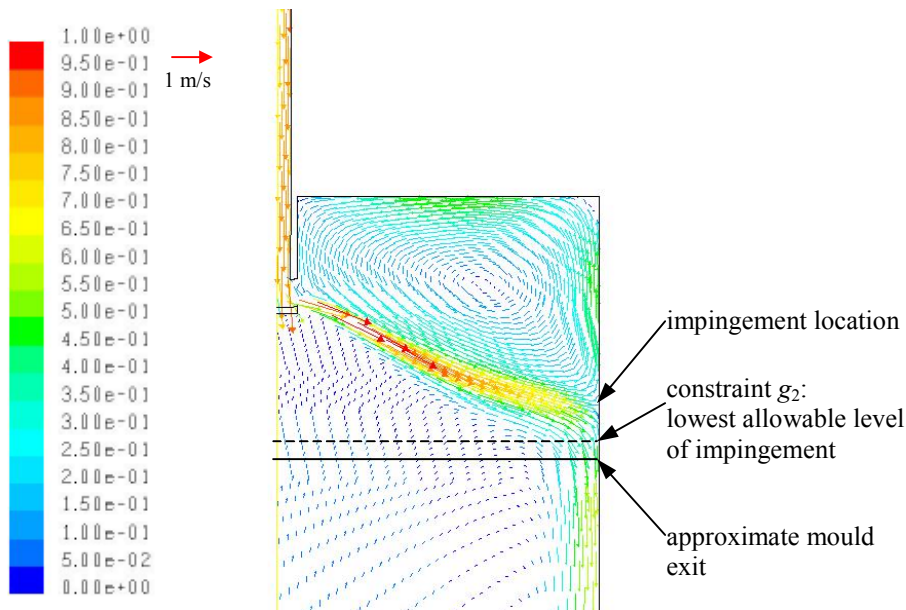


Figure 5.9: Flow pattern (velocity vectors) and point of impingement of initial design

5.5.6.2 Optimisation History

The optimisation results are shown in Figures 5.10 to 5.12. The optimisation history of the objective function (maximum TKE) is shown in Figure 5.10. The optimisation history of the maximum velocity on the meniscus is also shown in the same figure, showing the interdependence of the maximum TKE and velocity on the meniscus. The optimisation history of the constraint

functions g_1 and g_3 (in millimetres) is shown in Figure 5.11, while that of the design variables is shown in Figure 5.12.

The only active constraint function was g_4 , which monitored the minimum meniscus temperature. Although the constraint functions g_1 and g_3 in Figure 5.11 were never active at the design points (thus equal to or smaller than zero), it contains some telltale information regarding the optimisation process. After the first design iteration, the Optimiser enlarged the port height to its maximum bound, which is reflected in the fact that g_1 moves closer to zero as the design nears the manufacturing limit. However, throughout the optimisation process, g_1 never becomes active – all the designs are thus manufacturable. The constraint function g_3 follows the same trend as the port angle (in Figure 5.12), owing to the fact that they are linked algebraically: the lower the port angle, the likelihood that the jet will impinge directly into the meniscus, is reduced (and therefore the g_3 will be even more negative).

Interestingly, the optimisation process initially moved in the “wrong” direction, exploiting a design with an upward port angle design (iterations 1 to 3). From the fourth design iteration, a much smaller port angle was suggested by the Optimiser (Figure 5.12), with positive results: the maximum TKE on the meniscus was reduced significantly (Figure 5.10). As can be seen in Figures 5.10 to 5.12, further reductions of the port angle also resulted in the reduction of the maximum TKE.

The well depth was also enlarged only from the third design iteration, with success, as the maximum TKE was simultaneously reduced. This can be attributed to the fact that the well accelerates the dissipation of turbulent energy, resulting in a less concentrated jet.

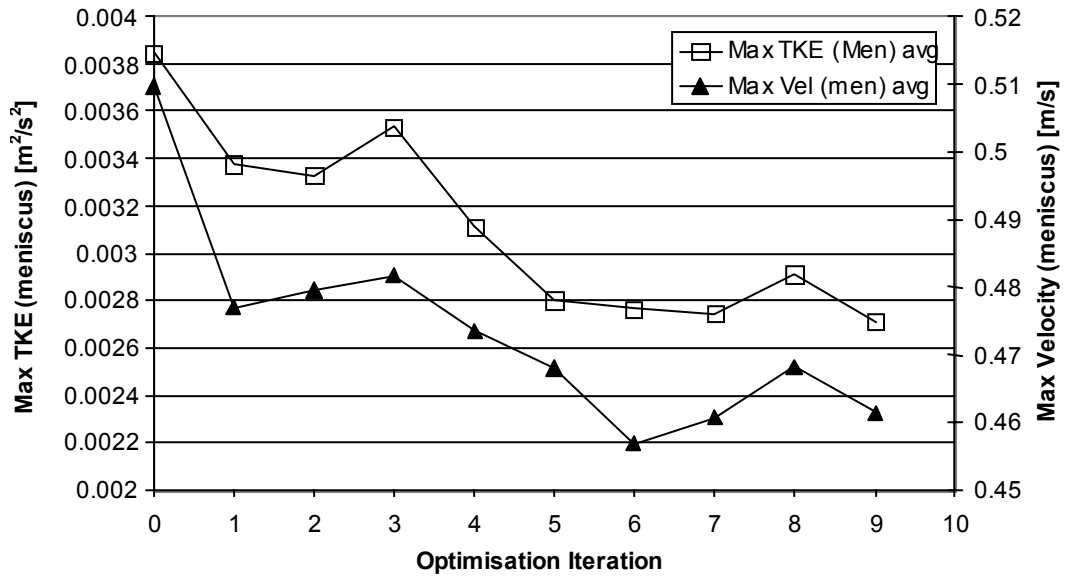


Figure 5.10: Optimisation history: Objective function (max TKE) and maximum velocity on meniscus

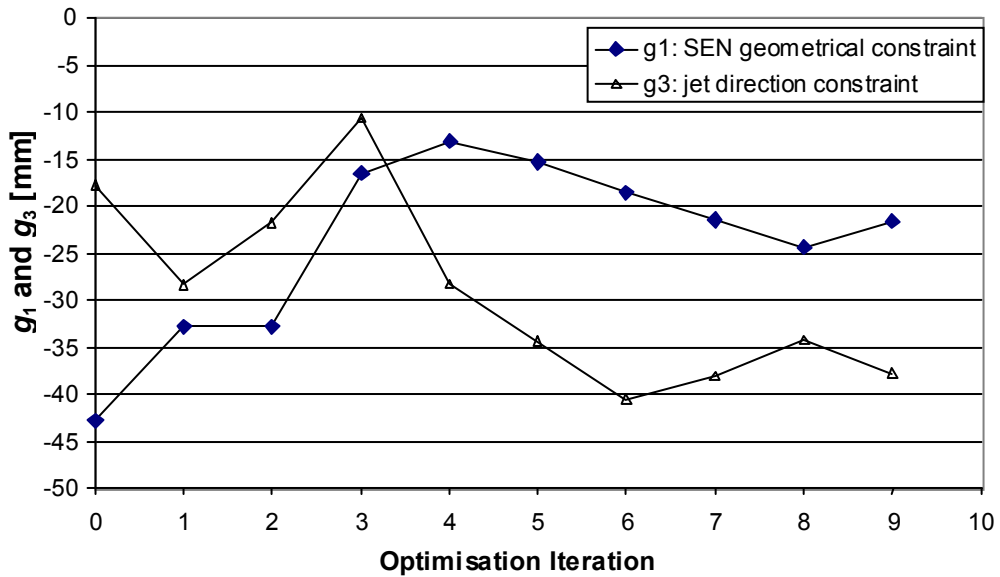


Figure 5.11: Optimisation history: Constraint functions g_1 (geometrical constraint) and g_3 (jet direction constraint)

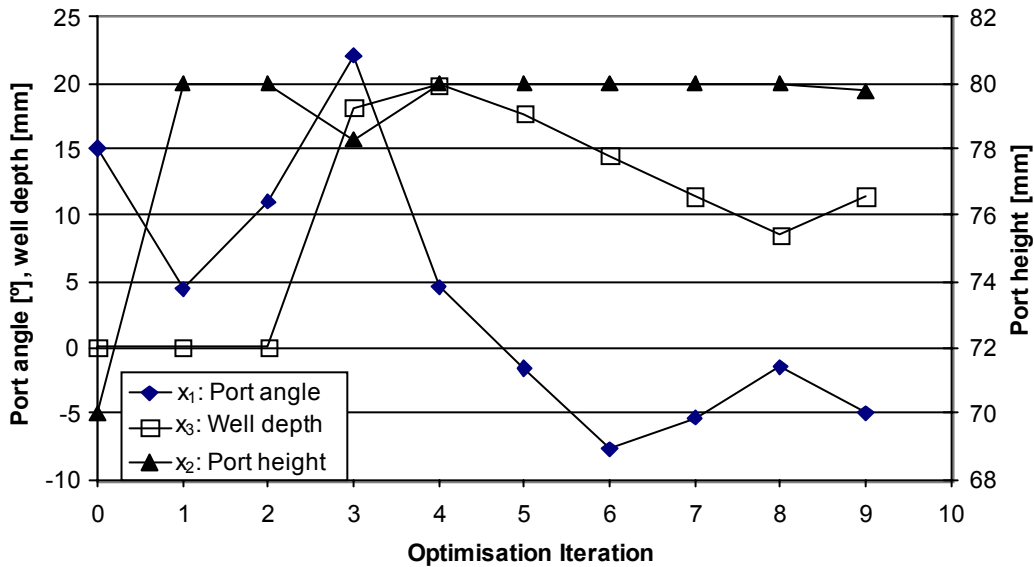


Figure 5.12: Optimisation history: Design variables

The Response Surface Method used by the Optimiser, generates 7 designs (x^1 to x^7) for 3 variables with each design iteration on the response domain [13], using the CFD solver to evaluate the objective function value for each design. A response surface (a linear surface for this study) is then fitted through these objective function values using the minimum error of the root mean squared – approach as explained in preceding sections. It is thus inevitable that extremely good or extremely bad designs (outliers) are discarded when using the Response Surface Method, especially when linear surfaces are used. However, these auxiliary designs are recorded and the best design (although not the optimum of the optimisation process) can surely be considered as an optimum design. In this optimisation exercise, however, the optimum design predicted by the optimiser was used.

5.5.7 Optimum design with design variables x^*

The optimum SEN design is considered to have been reached after 9 design iterations. The optimum design in terms of its design variables is displayed in Table 5.4, where a summary of the design optimisation results is shown. The

design variables of the optimum design in Table 5.4 have been rounded to the first decimal.

Table 5.4: Summary of design optimisation results

Case	x_1 : SEN port angle [°]	x_2 : SEN port height [mm]	x_3 : Well depth [mm]	Max. TKE on meniscus [m ² /s ²]	Impingement point below meniscus [mm]	Max. velocity on meniscus [m/s]
Initial	15	70	0.1	0.003847	521.99	0.5097
Optimum (x^*)	-5.0	79.8	11.5	0.002709	570.38	0.4614

The TKE on the meniscus surface of the initial design and the optimum design are plotted and compared in Figure 5.13. An improvement of 29.6% was achieved with the optimum design over the initial design, reducing the maximum TKE from 0.003847 m²/s² to 0.002709 m²/s². Note that the TKE on the meniscus is spread more evenly (although marginally) across the meniscus surface with the optimum design. This is thus a better design than the initial design according to Kubota *et al.* [56], who state that spreading the TKE over the meniscus surface while simultaneously reducing the maximum value, will reduce the chance of meniscus freezing in an inactive area and simultaneously reduce the likelihood of slag entrainment.

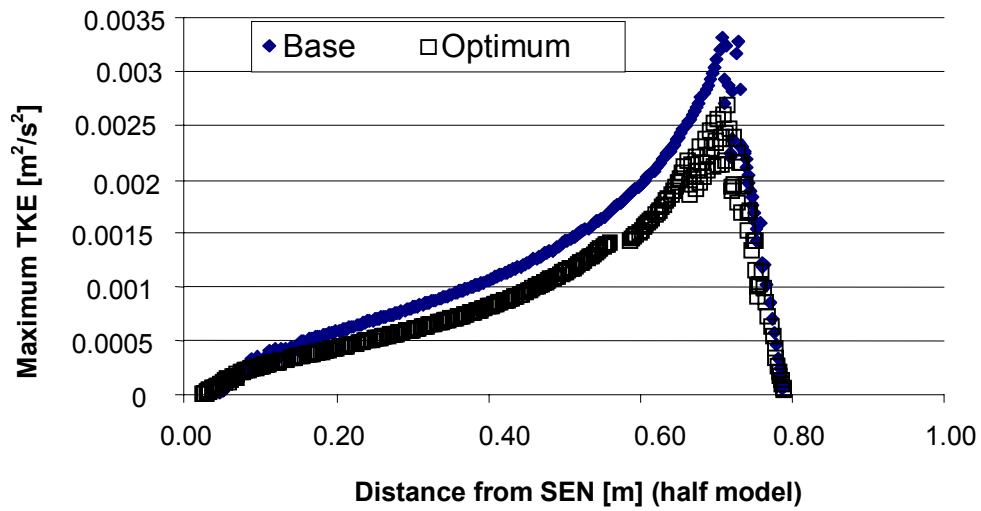


Figure 5.13: Comparison of turbulent kinetic energy on meniscus surface between initial design and optimum design (2D half model)

Figure 5.14 compares the flow pattern of the optimum design with that of the initial design. The colour scale in Figure 5.14 of the contours represents the TKE in the velocity flow field. The TKE content of the flow field is thus shown and the design improvement with respect to the objective function and impingement constraint are clearly visible at the meniscus surfaces (darker colours at or near the meniscus means less activity).

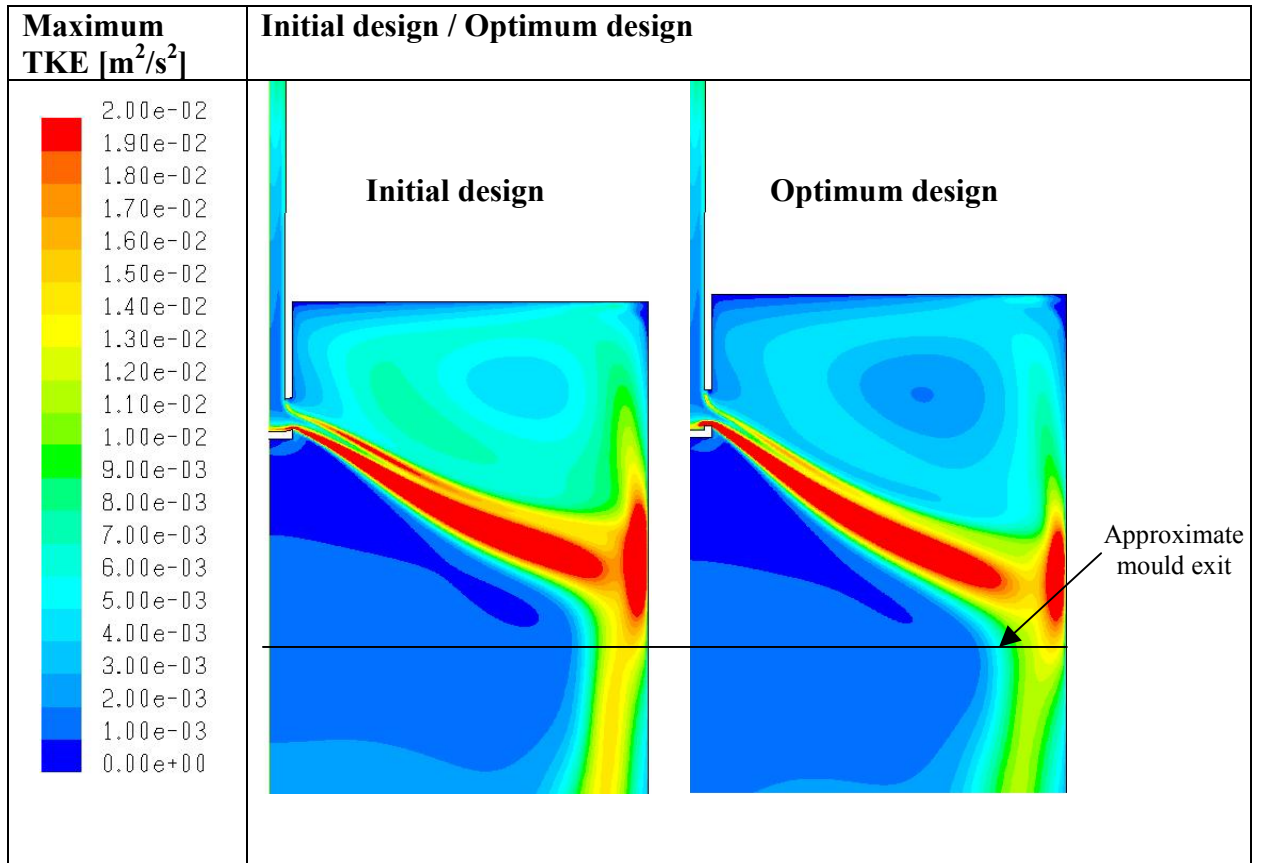


Figure 5.14: Turbulent kinetic energy [m^2/s^2] contours in flow field of optimum design compared with initial design

5.6 3D SEN optimisation: design space exploration

5.6.1 Computational expensive 3D modelling

Due to the computationally expensive 3D modelling, it is currently impossible to follow exactly the same procedure as in the previous 2D optimisation example (section 5.5).

Instead, a central-composite design method was followed to determine experimental points (similar to perturbations in normal LS-OPT optimisation

exercises). Using this method, an improved design can be estimated with much less CFD evaluations.

3D CFD simulations of the SEN and mould require considerably more computing power than 2D simulations, due to the following reasons:

More complex flow

The flow in 3D for a SEN and mould combination is much more complex than a 2D simulation, owing to the necessity of solving the Navier-Stokes equations in 3 dimensional space, as well as modelling turbulence in 3 dimensions. The isotropic turbulence assumption⁷ of the k- ϵ turbulence (Realisable) models [10], which has proven to be quite accurate for 2D simulations, no longer delivers accurate and repeatable 3D solutions. The only turbulence model that does not assume isotropic turbulence is the Reynolds Stress Model (RSM)⁸. However, this model requires a much finer mesh than the k- ϵ or k- ω models.

More cells (3D) essential

During initial investigation phases, the base case SEN design (as described in Chapter 4) with a submergence depth of 200mm, and a mould width of 1575mm, was modelled using the RSM turbulence model. The mesh consisted of approximately 3 million cells. In order to ensure convergence, the CFD model iterated for several months on a 3 GHz Intel Pentium 4, reaching approximately 44250 iterations. This proves that the RSM turbulence model is not suitable for general optimisation use.

Using the computationally less expensive k- ω turbulence model, a coarser mesh can be used. Subsequently, a meaningful optimisation study can be performed in a much more acceptable time frame.

⁷ Refer to Chapter 4 for discussion of different turbulence models, as well as the inter-relatedness of physically correct turbulence modelling and computational expensiveness.

⁸ The RSM model requires that 7 equations be solved during each iteration, as opposed to only 2 equations of the k- ϵ or k- ω models. Refer to Chapter 4 for more information. LES (Large Eddy Simulation) requires such an extremely fine mesh, that it is not even considered as an option due to limiting computing power.

Apart from the fact that more computing power is necessary, another problem surfaced concerning sequential 3D CFD simulations:

Wide mould: jet instability and convergence problems

The author noticed that (especially 3D) CFD solutions of any SEN and mould model proved to be much more stable (including repeatable convergence of solutions) in the event of a reduced mould width. Coincidentally, the main THRIP partner, Columbus Steel, Middelburg, required an optimum SEN design for their 1000mm to 1300mm slab widths (narrow to medium), as casting speed was increased by approximately 30% (from 1m/min to 1.3 m/min) for these widths. This 3D design space exploration study will thus focus on a narrower mould width of 1060mm and 1250mm (as opposed to the widest width of 1575mm of the 2D optimisation study). These two widths have been selected, as they are representative for the 1000mm – 1300mm range. Moreover, full-scale water model validations [32] are available for these widths.

5.6.2 Design space exploration

5.6.2.1 General and design variables

The experimental points or designs (using the central-composite design method) were chosen for the following three design variables:

- port angle
- port height
- well depth

Owing to the 3-dimensional nature of the SEN, a few parameters were assumed to be constant with respect to the automatic geometry generation:

- upper and lower ports have the same angle
- port width remains constant
- port curvature (top and bottom) remains constant
- well angle remains constant at 0 degrees (in other words, the bottom of the well is flat)

For this 3D optimisation study (or rather design space exploration), the three design variables will be optimised using the “worst case” submergence depth of 80mm. The latter submergence depth is the shallowest depth used by Columbus Stainless during normal casting operations. It is regarded as the worst case due to more meniscus activity (increased turbulent kinetic energy) resulting from the proximity of the exiting molten steel jets. The increased meniscus activity invariably causes slag entrainment, reducing the quality of the cast steel and resultant slab quality. Furthermore, the shallow jets can also prohibit a well-defined bottom barrel roll, further contributing to inferior quality steel due to the absence of a vehicle to remove impurities from the cast steel in the mould cavity.

All other constant operational parameters for this exploration study are indicated in Table 5.5.

Table 5.5: Constant parameters used in 3D design space exploration optimisation study: geometrical and steel properties

Description	Casting speed [mm/min]	Slab widths [mm]	Submergence depth [mm]	Steel dynamic viscosity [kg/(ms)]	Steel solidus temperature [K]/[°C]	Liquid steel density [kg/m ³]
Constant value	1300	1060 and 1250	80	0.0064	1725/1440	6975

The CFD model is assumed to be accurate for this design space exploration exercise, as the CFD model of the base case was validated using water model results in Chapter 4.

5.6.2.2 Formulation of multi-objective function

The basic objective function for this design space exploration is to minimise the meniscus turbulent kinetic energy as well as to limit excessive meniscus velocity, for both widths (1060 and 1250mm). The submergence depth will of course be kept constant at 80mm. All the different chosen SEN designs will be evaluated for both widths.

A combined objective function (multi-objective function) is defined as follows to achieve the basic objective of minimising meniscus turbulent kinetic energy:

$$\begin{aligned} \text{Multi-objective} = & (\text{Max_TKE_1060} + \text{Max_TKE_1250}) * 1000 \\ & + (\text{Max_maxVel_1060} + \text{Max_maxVel_1250}) * 10 \end{aligned}$$

where:

Max_TKE_width : average⁹ magnitudes of maximum turbulent kinetic energy on meniscus

Max_maxVel_width : average magnitudes of maximum meniscus velocity

Note that the maximum TKE values are multiplied by 1000, as opposed to only 10 for the velocity magnitudes, to ensure that the values are comparable (thus of the same order), preventing that only one factor dominates the multi-objective function.

5.6.2.3 Geometry and mesh (parameterisation of mesh)

The geometry was parameterised using the same principles as described in previous sections of this chapter. However, when parameterising 3D geometries, more complicated exceptions can occur during the generation of different geometries.

The author developed a 3D automatic geometry and mesh generator (consisting of a GAMBIT script file) based on the old Columbus SEN (without a well).

⁹ Instability of the CFD solutions causes the maximum TKE to vary from one CFD iteration to the next, despite the fact that the residuals have fallen sufficiently for general convergence. Consequently, the values of maximum TKE (as well as that of maximum velocity) are extracted from the last few thousand iterations and **averaged** for a more representative maximum TKE (or maximum velocity) value.

The approach employed by the script file was: generating a full 3D model using volumes as geometric building blocks, and dividing it in quarters afterwards to obtain the desired quarter model. Unfortunately, this method created 3D volumes in the SEN flow field that cannot be meshed using stable quadrilateral cells, and tetrahedral cells (tet-cells) had to be employed. The use of tetrahedral cells has a negative impact on especially complex jet flows, and must be avoided to obtain repeatable and believable solutions, as explained in Chapter 4. An example of the GAMBIT script file used to generate a SEN design (without the well) can be viewed in [Appendix M](#). This script file was never used for optimisation purposes, due to the unsuitability of the mesh.

However, as Columbus Stainless required a design suggestion using a wellled SEN, a new parameterisation method was required. A colleague at the University of Pretoria followed a different approach: the 3D quarter model was built up from scratch, starting with vertices or points in space, connecting the latter to form lines, forming surfaces with these lines, and ultimately linking the surfaces to create volumes. Using this (elaborate) method, more elemental volumes could be created, enabling hexahedral cells to be used throughout the SEN volume.

In order to parameterise the well depth, a minimum well depth of 1 mm had to be accepted as sufficient for a no-well condition, as the GAMBIT script file could not handle a 0mm well depth. The latter GAMBIT script file (also known as a journal file) was used to generate the geometry and mesh for the different SEN designs chosen in this design space exploration.

This journal file is approximately 2200 lines long: the excessive length of the file is due to all the exceptions that can occur in the geometry for the range of parameters chosen. The splitting of faces¹⁰ causes renaming by GAMBIT in a non-intuitive way, and the loops in the journal file in question test for these.

¹⁰ Splitting of faces: a necessary operation in GAMBIT during face and ultimately volume creation.

The file generates a mesh of about 500 000 cells depending on the geometry that is the starting mesh for the dynamic mesh adaption¹¹ used in FLUENT. This means that the mesh is refined and coarsened as the solution proceeds based on velocity gradients (in this case). This is an attempt to follow the formation of the SEN jet with grid clustering. A maximum cell count of about 850 000 is reached in this process depending on the complexity of the flow field in each case.

5.6.2.4 Boundary conditions and other settings

The boundary conditions are similar to that in the 2D optimisation exercise section 5.5. For the sake of completeness, the typical boundary conditions specified in FLUENT for this design space exploration, are shown in Figure 5.15.

Other settings are also similar to the 2D optimisation study, as well as the FLUENT script files used to follow a certain solution procedure to ensure convergence of critical residuals.

¹¹ Dynamic mesh adaption: refer to Chapter 4 for explanations and discussions.

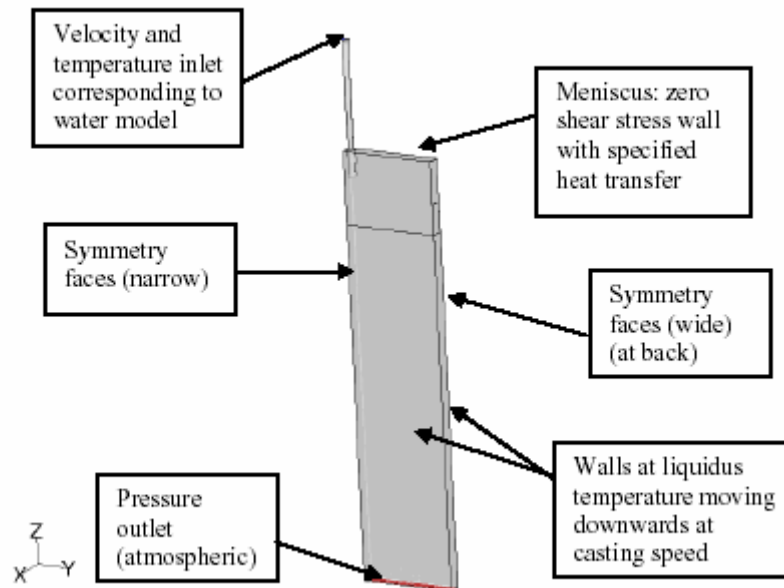


Figure 5.15: Typical boundary conditions for quarter model of 3D CFD SEN and mould model

5.6.2.5 Experimental design

A central-composite design was used in LS-OPT [30] for the three design variables considered, *i.e.*, port angle, port height and well depth. The old SEN design (base case design in Chapter 4) was added as experimental design point 1.0, or design $\mathbf{x}^{(1,0)}$ when using the same notation as in section 5.1.

All the experimental design points are listed in Table 5.6, including the base case (experimental design point 1.0) and the linear and quadratic optima fits as predicted by LS-OPT. Figure 5.16 illustrates the experimental design points listed in Table 5.6, simultaneously explaining the reason why this design is called central composite. The experimental points are chosen in the centre of the faces of the “design space” that was chosen by the user. The reason why “design space” is written in inverted commas is because the latter cannot be represented by a graph when there are more than 3 design variables. In this case it can be depicted diagrammatically as only 3 design variables are optimised.

Table 5.6: Experiments in central-composite design, including base case (experiment 1.0) and linear and quadratic optima fits by LS-OPT

Experimental design point	SEN port angle [°]	SEN port height [mm]	SEN well depth [mm]
1.0	15	70	1 \approx 0
1.1	0	55	20
1.2	7.9	69.9	32.1
1.3	-12.9	69.9	32.1
1.4	7.9	40.1	32.1
1.5	-12.9	40.1	32.1
1.6	7.9	69.9	8.9
1.7	-12.9	69.9	8.9
1.8	7.9	40.1	8.9
1.9	-12.9	40.1	8.9
1.10	-2.5	55	20.5
1.11	15	55	20.5
1.12	-2.5	80	20.5
1.13	-2.5	55	40
1.14	-20	55	20.5
1.15	-2.5	30	20.5
1.16	-2.5	55	1
2.0_linear	-20	80	1
2.0_quadratic	-20	55.56	40

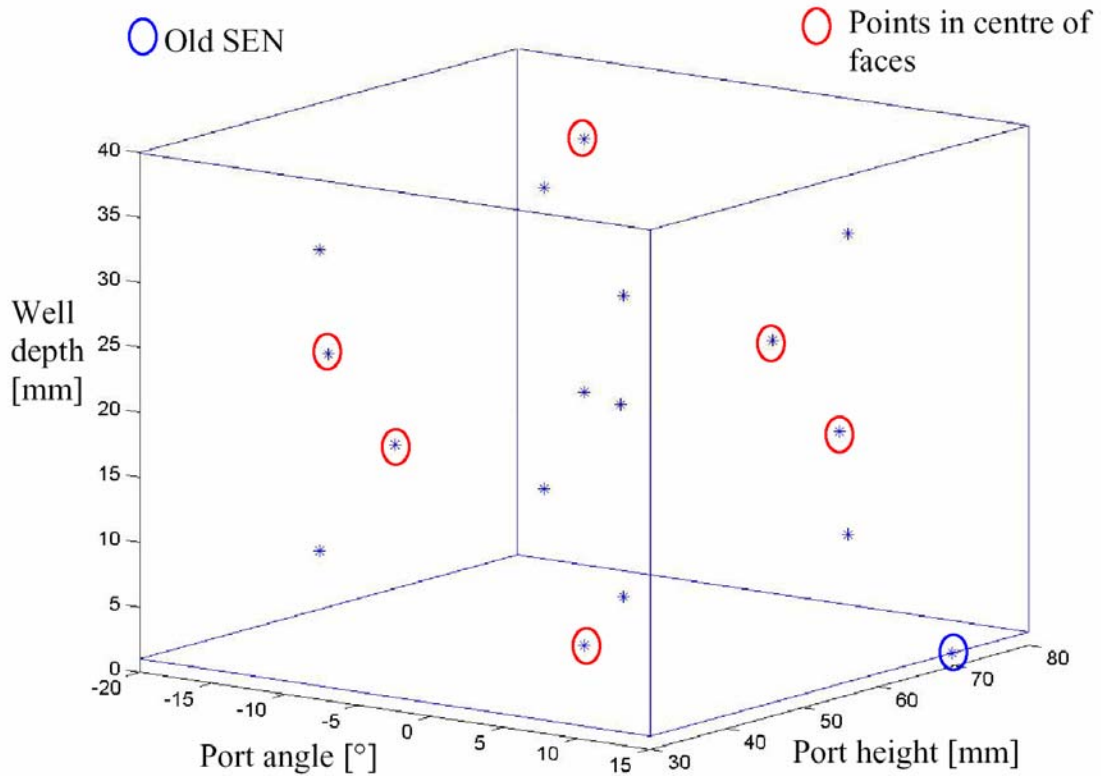


Figure 5.16: Central-composite design experimental points

5.6.3 Results: Design space exploration

Each experimental design point was evaluated using CFD techniques, as explained in Chapter 4.

All these CFD simulations (or evaluations) for all experimental design points as indicated in Table 5.6, were run for both slab widths (1060 and 1250mm), for a submergence depth of 80mm and a casting speed of 1.3m/min. Summary results¹² of all these cases can be viewed in [Appendix N](#).

The values of the multi-objective function of the 19 experiments (Table 5.6) are depicted graphically in Figure 5.17. Note that the basic objective of this exercise

¹² Summary results ([Appendix N](#)) include an executive summary of the maximum TKE as well as the maximum velocity on the meniscus for both widths. Furthermore, the contours of magnitude of velocity on the symmetry plane of each CFD simulation (converged) are also shown so that the reader can evaluate the physical flow.

is to find a SEN design with the lowest multi-objective value. Consequently, the four designs that performed well (indicated in Figure 5.16 with red circles) are: experimental designs 1.0, 1.7, 2.0_linear and 2.0_quadratic.

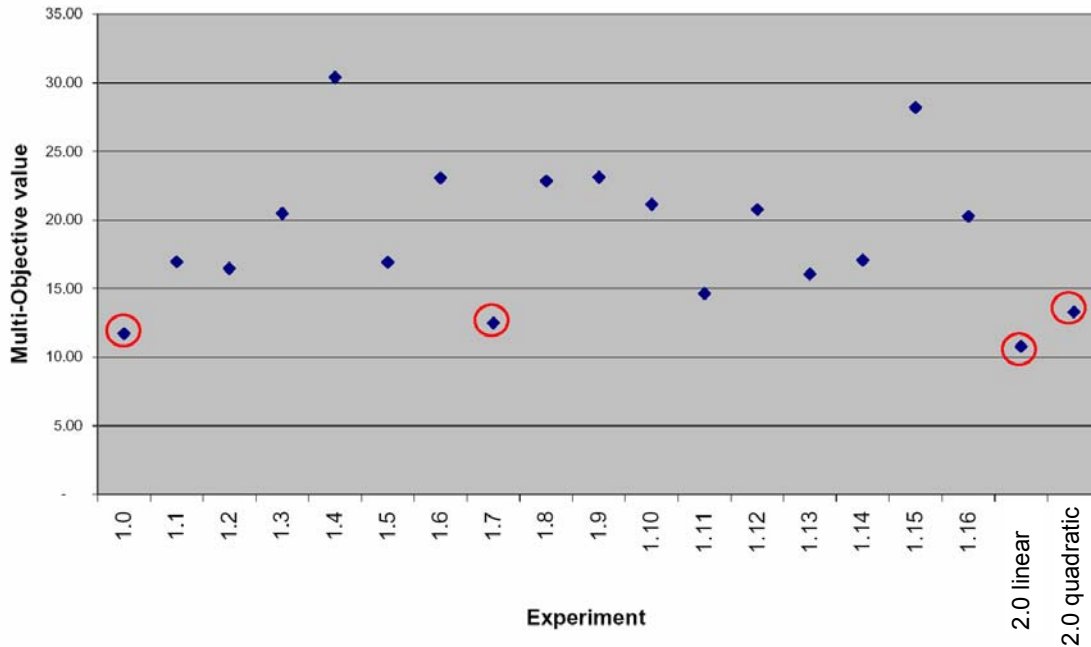


Figure 5.17: Multi-objective values of the experiments listed in Table 5.6

Considering the parameters of these designs, it can be seen that design 1.0 is the original Vesuvius SEN design (old SEN). Design 1.7 has a moderate well (9mm) and a downward angle of approximately 13° . Design 2.0_linear has a port height and downward angle as much as allowed with no well, while 2.0_quadratic has a moderate port height, with a maximum allowable downward angle and well depth.

The designs that performed the poorest (*i.e.*, 1.4 and 1.15) were those with small ports and medium to deep wells. From the data in [Appendix N](#), these designs have very shallow SEN jets, derogating the meniscus stability due to jet proximity. The instability of the CFD solution can also be observed by just viewing the quite unphysical velocity contours of these poor performers ([Appendix N](#)).

In order to select the best SEN design from the four best performers, more detail information and flow displays were extracted from the CFD solutions. In order to

evaluate the four best designs, the following contours of the CFD solution models were generated for each design (for both widths):

- contours of velocity on the symmetry plane
- contours of helicity¹³ on the symmetry plane
- contours of turbulent kinetic energy on symmetry plane
- contours of vorticity on the symmetry plane
- contours of shear stress on the wide mould walls
- contours of temperature on the symmetry plane
- path lines originating from the SEN inlet, coloured by vorticity magnitude

All these CFD results of the four best SEN designs are shown in [Appendix O](#).

Considering the results in [Appendix O](#), one often mistakes the flow as being similar to 2D flow, due to the customary display of the flow patterns on the symmetry plane of the 3D SEN and mould model. In order to demonstrate the 3-dimensional nature of the flow field, another display method is used: The jet is displayed in 3D by rendering iso-surfaces¹⁴ of velocity magnitude coloured by turbulent kinetic energy. Refer to [Appendix P](#) for these displays of the four best SEN designs.

Of course, it is important to verify the robustness of the chosen SEN design. Factors that may influence the performance of the new SEN design are:

- Initial tolerance differences due to manufacturing tolerances and errors
- Gradual internal geometry variances due to clogging and the presence of impurities
- Operational parameter variations due to control inadequacies of the casting speed, for example

¹³ Helicity was defined in Chapter 4, footnote 14 [10].

¹⁴ An iso-surface of velocity magnitude (for example) is when only the surface area, where a specified constant velocity magnitude is achieved in the entire flow field, is displayed. Of course, other properties may vary over this iso-surface, as turbulent kinetic energy for example.

Refer to Chapter 6 (Future Work and Conclusion) for remarks on this emerging topic, which is applicable to practically all CFD optimisation design exercises.

5.6.4 Design space exploration: Geometry of chosen design

The chosen design is the optimum predicted using the linear approximation of LS-OPT. The 2.0_linear design performed marginally better than the other four designs in the multi-objective function.

The 3D SEN design thus recommended for manufacture for a plant trial is depicted diagrammatically with a 3D solid surface rendering in Figure 5.18. This SEN design (Table 5.7) should perform satisfactorily for widths ranging from 1000 – 1300mm, at a casting speed of 1.3 m/min.

Table 5.7: Chosen design following 3D design space exploration

Experimental design point	SEN port angle [°]	SEN port height [mm]	SEN well depth [mm]
2.0_linear	-20	80	1 (no well recommended) ¹⁵

¹⁵ A 1mm well had to be simulated due to difficulties experienced in GAMBIT when a well of 0mm is endeavoured to be created using the GAMBIT script file.

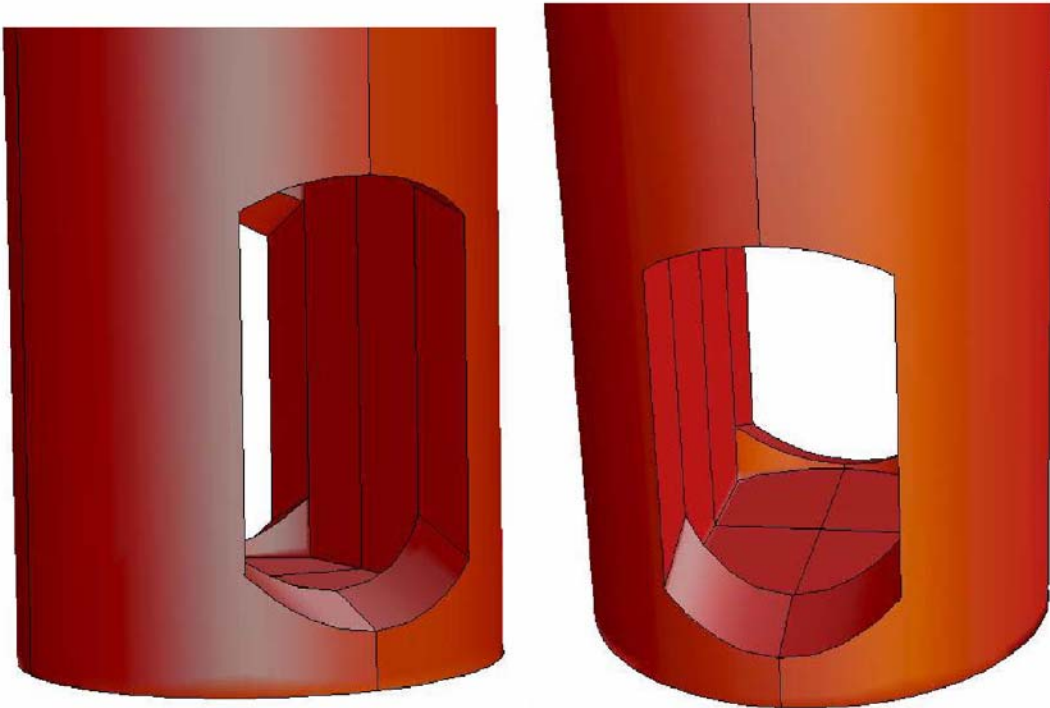


Figure 5.18: Geometry of chosen design (port angle = 20° downwards, port height = 80mm, no well)

5.6.5 Validation of chosen design with 40%-scaled water model

Using the modular SEN insert design, the 40%-scaled physical optimum Aluminium SEN design (port angle = 20° downwards, port height = 80mm (full-scale), no well) could easily be manufactured for water model testing.

If the CFD model compares favourably with the water model results of the optimum SEN, it will prove that the CFD model can be trusted for further optimisation work. This validation will simultaneously double as verification for the extension of the momentum-only CFD model to real plant circumstances, as well as proving that satisfying Fr-similarity is indeed sufficient for scaled water modelling testing.

The CFD results (depicted in Figures 5.19 – 5.20) reflect the plant circumstances (full scale), where liquid steel is used as the fluid.

The validation for the optimum SEN is performed at the wider width, 1250mm, as the wider CFD models tend to be less stable than the narrower models. The validation is also performed for three different submergence depths, namely 80mm, 150mm and 200mm. The CFD results for the 200mm submergence is shown below, and that of 80mm and 150mm are shown in [Appendix Q](#).

The CFD results of the optimum SEN (in Figures 5.19, 5.20 and [Appendix Q](#)) surprisingly correspond closely to the water model tests, which satisfy Fr-similarity.

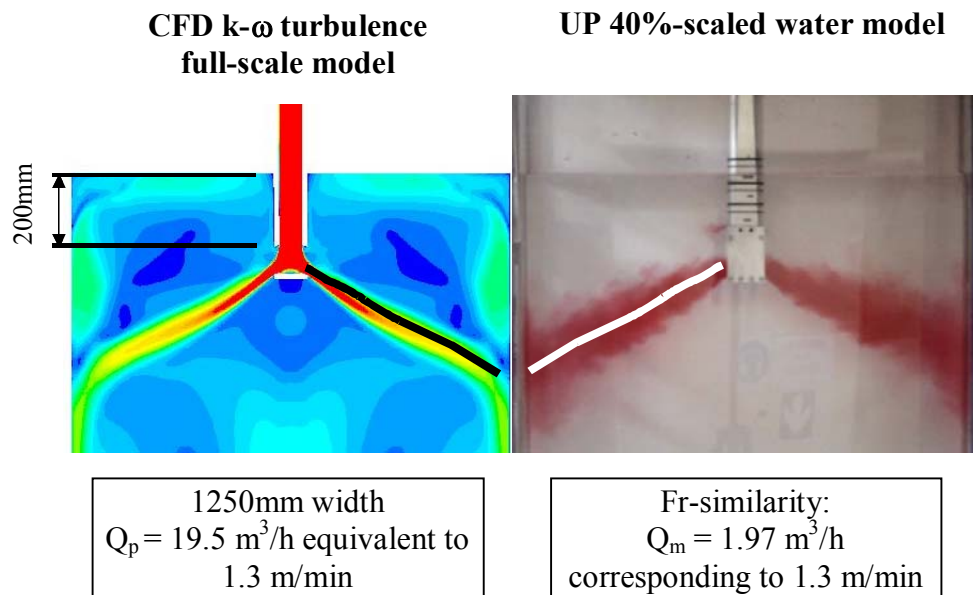


Figure 5.19: Validation of optimum SEN design at mould width 1250mm and 200mm submergence depth, using contours of velocity (scale 0 – 1 m/s)

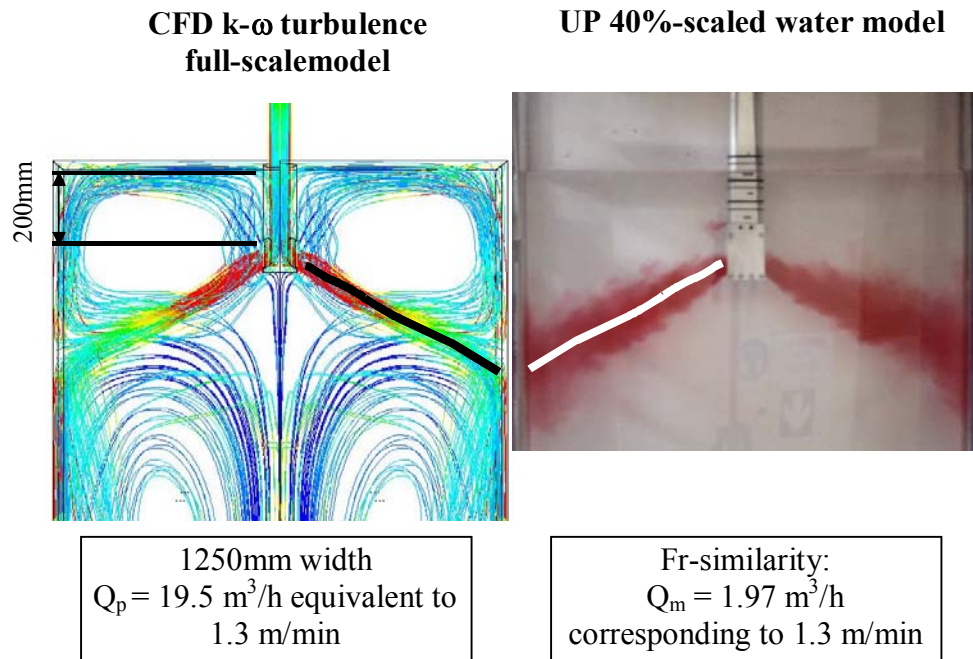


Figure 5.20: Validation of optimum SEN design at mould width 1250mm and 200mm submergence depth, using path lines coloured by velocity magnitude (scale 0 – 1 m/s)

The optimum design of the 3D design space exploration is thus validated and can confidently be recommended for manufacture for a first plant trial.

5.6.6 CFD comparison between chosen design and base case model

In order to show the potential of mathematical optimisation, the improved SEN design (from the 3D exploration study) is compared to the base case SEN design. Figure 5.21 compares the maximum TKE on the meniscus (top view) of the base case and that of the chosen design. Operational parameter values and design variable values are tabulated in Table 5.8.

Table 5.8: Values: comparison between base case and chosen design from 3D exploration study

Description	Base case SEN design	Improved / Chosen design from 3D exploration study
Experiment number	1.0	2.0 linear
SEN port angle (°)	15°	- 20°
SEN port height (mm)	70mm	80mm
SEN well depth	0mm (1mm)	0mm (1mm)
Submergence depth (mm)	200mm	200mm
Mould width (mm)	1060mm	1060mm
Mould thickness (mm)	200mm	200mm
Casting speed (m/min)	1.3 m/min	1.3 m/min

Using the same TKE range ($0 - 0.002 \text{ m}^2/\text{s}^2$) for both SEN designs, one can clearly graphically identify the best design when measured against the objective function (minimising the maximum TKE on the meniscus).

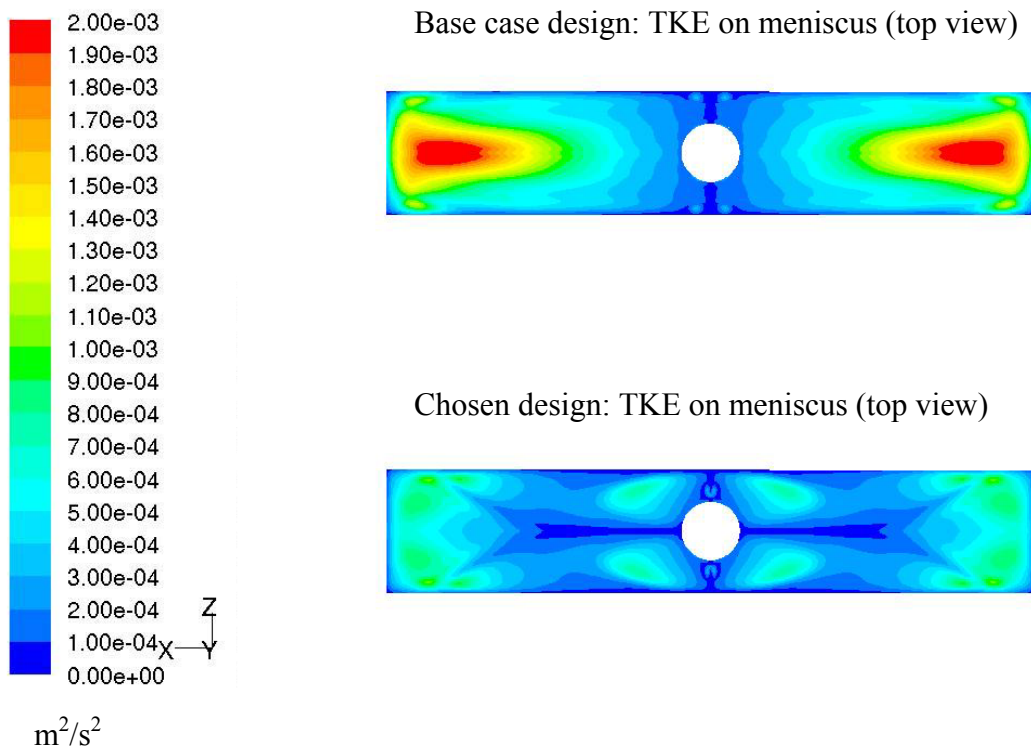


Figure 5.21: Comparison between TKE on the meniscus of the base case and chosen design from 3D exploration study for casting conditions indicated in Table 5.8

This comparison of the design space exploration optimum with the initial design (base case) concludes this chapter, which focused on mathematical optimisation of the continuous caster SEN using CFD simulations. Chapter 6 (Conclusion and Future Work) that follows, shall conclude the dissertation in its entirety.

CHAPTER 6: CONCLUSION AND FUTURE WORK

Briefly, this dissertation has highlighted the significant influence of the Submerged Entry Nozzle in the continuous casting process. Consequently, the potential of Mathematical Optimisation of the SEN design has been illustrated quite extensively. Of course, the verification of CFD models using water modelling is a necessity. Only if CFD models deliver reliable and repeatable solutions of different (arbitrary chosen) SEN designs, meaningful optimisation work can be performed based on these CFD results.

A main objective of this dissertation was verifying the CFD models of the SEN and mould with water modelling, using a specifically designed and built 40%-scaled water model. Initially, a purely theoretical optimisation study was expected, being a mere extension from the CFD tundish work (part of the THRIP project at the University of Pretoria), which preceded the SEN and mould work. The complexity and different behaviour of the turbulent jet flow into the mould cavity (as opposed to the mostly laminar and buoyancy-driven flow in tundishes) proved otherwise: extensive CFD model verification was necessary. Trial and error CFD modelling methods (with the aid of “correct” water model results) indicated crucial CFD assumptions, parameters, settings and procedures to ensure repeatable and believable CFD models (Chapter 4). The most critical CFD model parameters or settings were the choice of the correct turbulence model and the quality of the mesh (exclusive hexahedral cells a necessity to minimise CFD errors).

The correctness of the CFD models are measured against water model tests, as the CFD models are verified using water modelling. The reason why correct is written in inverted commas in the paragraph above, is because the water model tests are performed using a 40%-scale water model. Subsequently, experimental design is necessary: three dimensionless numbers have been identified that reflect the specific flow phenomena in the SEN and mould flow. The Fr-number was identified as more important than the Wb-number (which was discarded), second to the most important Re-number. However, an assumption that the flow is independent of Re-number

whilst satisfying Fr-similarity (during water model testing), was proven correct as the results closely corresponded to a full-scale water model in Chapter 3. (A full-scale model simultaneously satisfies Re-similarity and Fr-similarity.)

A further objective was illustrating the optimisation process, focusing on automation of optimisation. Automation in optimisation based on CFD evaluations, necessarily implies that parameterisation in the geometry and mesh is required. This was achieved using the scripting capabilities (ability to interpret text commands sequentially) of the pre-processor GAMBIT. Using the Optimiser (LS-OPT) as the coordinator of the optimisation process, the newly generated mesh geometries from GAMBIT are configured, initialised and solved (according to a predetermined solution procedure) in FLUENT. The optimisation process can be terminated as soon as the objective function (subjected to the constraint functions) has been improved sufficiently.

Lastly, owing to lack of computational power, a 3D design exploration was performed to also illustrate the approximation and global minimisation capabilities of the Optimiser.

However, during the execution of the work described in Chapters 1 to 5, a number of applicable study fields related to this topic, however beyond the scope of this dissertation, were noticed. These fields of study will be reported on in this final Chapter. Moreover, further avenues to explore as an extrapolation on ideas conceived in this work, as well as refinements to certain applications used, are also reported on.

6.1 3D Optimisation

6.1.1 CFD model: further refinements and comments

6.1.1.1 Symmetry assumption

The symmetry assumption used in both 2D (half models) and 3D (quarter models) CFD models proved to be not necessarily true when compared to water model tests. In fact, further work should be performed when one SEN port is clogged more than the other, to evaluate the effect on SEN design performance.

Moreover, the flow in the SEN shaft is not necessarily uniform as assumed, especially when a slide gate is used to control the flow rate through the SEN. This fact causes an asymmetrical flow inside the SEN shaft, which certainly has a significant influence on different jet angles and exit-velocities.

The CFD evaluation of full 3D models is also recommended to investigate the effect of asymmetry in typical plant circumstances, with regards to:

- Viewed from the top of the mould: positioning of SEN inside mould (not in centre of mould)
- Viewed from the side of the mould: angle of SEN with respect to meniscus (not necessarily exactly perpendicular to meniscus)

This topic is also closely related to Robustness studies on optimum designs as predicted by CFD techniques. Refer to section 6.2.

6.1.1.2 Steady / unsteady behaviour of SEN-mould solutions

Unsteady behaviour in some SEN and mould CFD models and water models was observed, especially the models with larger mould widths. Unsteady behaviour was also noticed on SEN designs with small ports and deep wells (refer to Chapter 5 for descriptions). It is believed that the apparent unsteady behaviour is caused by the fact that the flow becomes more complex,

especially in terms of shear flow spreading of the jet that becomes more erratic. Water model tests (refer to Chapter 3 and [Appendix F](#)) confirm that a SEN design of the well-type has a more erratic jet spread. CFD results (of the larger width models) also suggest a varying jet angle, oscillating about an apparent equilibrium jet angle.

Although a trial unsteady CFD model (RSM turbulence model) has been solved, using a steady converged solution as the initial solution, not much oscillation was noticed. However, some further work is required as the author suspects that unsteady behaviour takes place in some conspicuous SEN designs (deep well, small ports, large width mould, for example), which complicate the flow.

Furthermore, the choice of turbulence model certainly has a huge impact on the CFD results, as trial and error methods have proven to the author. The less complex the flow, the more capable an inexpensive turbulence model (as the $k-\epsilon$ for 2D flows, and the more advanced $k-\omega$ based on Wilcox for 3D flows) proves to be modelling SEN and mould flow situations. The assumption of these inexpensive turbulence models of isotropic turbulence seems to be quite fallacious as flow pattern complexity increases. These choices may have an influence on the steady (or unsteady) nature of a CFD solution.

Moreover, all CFD simulations were forced to yield a steady flow pattern, by assuming that $\frac{\partial}{\partial t} = 0$ and $\frac{d}{dt} = 0$ (refer to Chapter 2, Literature Survey, for application of these assumptions on the Navier-Stokes Equations). Erratic convergence or even the lack of complete physical convergence (*i.e.*, a physical parameter measured during the iteration or solution procedure that oscillates regardless of residual convergence) may be caused by flow fields that are indeed unsteady (besides the fact that steady behaviour is enforced by the solution algorithm).

6.1.1.3 More refined CFD models (especially on wide moulds)

A full Large Eddy Simulation (LES) model is recommended to be performed, especially for the wider mould widths (1575mm). Using LES modelling, the choice of a turbulence model is irrelevant, as the LES method requires such a fine mesh that a large-scale turbulence model is not necessary – the turbulence variations are computed directly, except for the subgrid scales. Obviously (and unfortunately), LES CFD models are extremely computational expensive. Furthermore, geometric complexity in the SEN design exponentially increases the need for extra-fine meshing.

Currently, however, the resources are lacking for conducting a full LES solution for the base case. However, it is recommended as invaluable future work as soon as an increase in computer power can justify such an exercise.

6.1.1.4 Temperature

The addition of the temperature equation in CFD modelling was required when the real plant circumstances (liquid steel) were modelled (as opposed to imitating the water model where temperature effects are neglected). This fact required additional boundary conditions to be specified on all boundary surfaces with regards to heat transfer. Examples of temperature related boundary conditions are: constant temperature, constant heat flux, varying heat flux, adiabatic, etc.

As specified in Chapter 4 (section 4.5), the constant temperature of the mould walls were specified at the liquidus temperature of liquid steel, as well as a heat flux was specified based on a 1-dimensional study. However, temperatures in the CFD models were not quite accurate – too low temperatures (below liquidus temperature) were obtained in most models.

Therefore, some trial and error work needs to be conducted to fine-tune the heat flux from the mould surfaces to ensure physically correct temperatures.

However, due to the simplifications and assumptions used in the CFD models in this dissertation, temperatures below liquidus temperature will always occur. Figure 6.1 shows the top view of the typical boundary conditions applied to a 3D CFD model. According to the model, the areas in the corners of the meniscus surface are subjected to 3 heat flux extractions, namely those at wide mould walls (\dot{Q}_1), narrow mould walls (\dot{Q}_2) and meniscus surface ($\dot{Q}_{meniscus}$). This fact causes temperatures below liquidus temperature in these affected areas in the mould corners, which necessarily suggests disastrous meniscus freezing (although plant experience of the base case proves the contrary). The true plant circumstances of course are much more complicated, preventing the unreasonably low temperatures in the corners:

- mould powder in the mould corners prevent excessive heat transfer
- mould oscillation prevents direct contact to walls, also significantly reducing the theoretical heat transfer
- mould powders melt (forming slag) and properties vary, increasing theoretical prediction errors

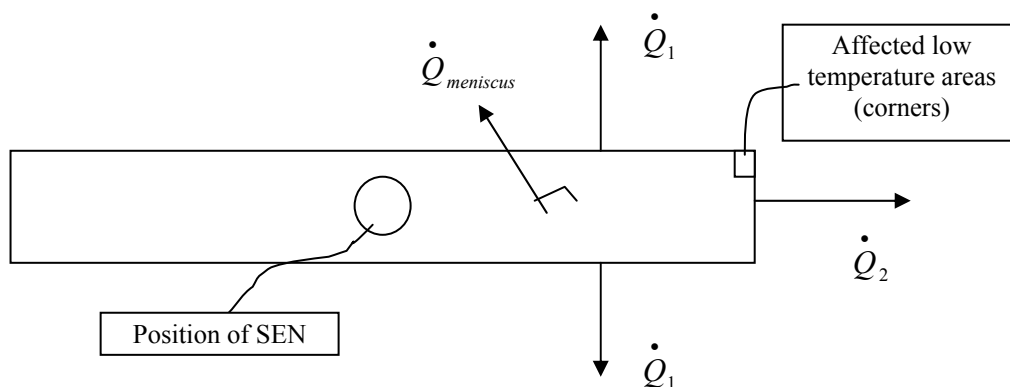


Figure 6.1: Top view of 3D model of SEN and mould, indicating heat flux boundary conditions causing areas of too low temperature

Future work would require extensive study of mould powder properties and behaviour, in an effort to include the (possibly varying) heat resistance of the mould powder (and slag) in the boundary condition of the mould walls and

meniscus surface. The addition of an oscillating mould area must also be considered, as heat flux may also be influenced significantly.

6.1.1.5 Complexity of flow: natural frequency in SEN design and mould widths

Future work is required to exactly ascertain the existence of natural frequencies¹ of a specific SEN design and its influence on flow patterns and meniscus behaviour. This is recommended after a significant increase in maximum turbulent kinetic energy (TKE) was observed when a SEN design was modelled in a wider mould during the 3D design exploration. The same casting speed, SEN design and boundary conditions were used.

The reason why natural frequency might be considered as the culprit for the increase in meniscus TKE for the one specific design, is because throughout the 3D design exploration, most SEN designs showed a decrease in meniscus TKE with an increase in mould width.

A full parametric study (in terms of width variance) should be conducted with a variety of representing SEN designs to evaluate the influence of natural frequency. Variables in this study are predicted to be connected to the specific steel grade (liquid steel density and other properties), mould width, and SEN design (SEN type (welled or not), port height, and port angle).

6.1.1.6 Volume of Fluid (VOF) method for meniscus modelling

Exact meniscus behaviour predictions will become increasingly important as the slag and mould powders need to be modelled for precise plant circumstances imitations. This will (for example) require a Volume of Fluid method of FLUENT to differentiate between three phases (liquid steel, solid

¹ The “natural frequency” of a SEN can be defined as certain operational parameters (cast speed, mould thickness, mould width, liquid steel properties, for example) where an unusual unsteady flow pattern occurs within the mould. It is therefore equivalent to the natural frequency of a rotating shaft, where the shaft experiences abnormal vibration and whip at its critical speed (corresponding to its natural frequency).

mould powders and air) over an interface surface. Other free surface methods are also available; refer to Reference [59].

As the exact meniscus behaviour was not important for the CFD simulations in this dissertation (slag entrainment was assumed to be a function of meniscus activity in terms of surface velocity and TKE), the meniscus was physically modelled as a zero shear stress wall. A comparison between a 2D model using an (unsteady) VOF method modelling the meniscus as a free surface, and a model using a slip wall, proved that the flow patterns inside the mould volume are remarkably similar. There had been decided to use the slip wall boundary condition for two reasons:

- a less expensive solution method (steady) can be used, and
- temperature boundary conditions, in particular a heat flux from the meniscus surface, can easily be added.

Currently, using the VOF-method, it will be extremely difficult to specify a heat flux over the free surface, as a heat flux can only be specified on top of the air layer (typically a slip wall), and more uncertainty will be built into this set-up: the heat transfer from the liquid phase to the air, and from the air to the wall, will be unknown. Only the heat extraction from the wall can be specified.

Other methods (than just VOF) must be considered to overcome the heat flux problem. A proposal to consider is to firstly compute the meniscus surface behaviour (wave formation etc.) using a momentum-only CFD model. Thereafter the exact meniscus behaviour (unsteady) must be applied on the meniscus surface, that is dynamically altered (the grid is altered to imitate the exact meniscus surface, yet a slip wall boundary condition is applied) as the unsteady energy activated solution proceeds. Of course, using this proposed method, it is assumed that the addition of heat does not significantly influence the meniscus shape. Some further investigation is thus necessary.

Perhaps other CFD packages with a similar VOF method, yet accommodating easier application of heat flux, can be evaluated and compared with similar FLUENT models (with slip wall boundary) and water model results.

6.1.2 Parameterisation: 3D full optimisation

Due to computational expense, a full 3D parameterisation optimisation study was not possible in this dissertation. The concept (full parameter optimisation) was however extensively illustrated using a 2D SEN optimisation design example.

As computational power increases², the possibility of conducting a full 3D optimisation study also increases. There is a need to explore the full implications of 3D geometry in the (arguably simple) SEN designs using parametric studies [25]. Unlike 2D SEN designs, there are a number of influential parameters that are yet to be analysed and screened using the full process described in Chapter 5, sections 5.1 to 5.5. These include the radii of the top ports and bottom ports (which need not be symmetrical), the curvature of the well inside the SEN, to name but a few.

A few design iterations will firstly indicate which parameters are significant (thus, significantly contribute to the improvement (or deterioration) of the objective function(s)). Thereafter, parametric studies and meaningful 3D optimisation can be conducted.

² Computational power is increasing faster than was anticipated. The average computer employed to perform initial CFD SEN and mould models in this dissertation was an Intel Pentium III 750MHz, 500MB memory. By the time of writing the report, the average system was (equivalent to) an Intel Pentium IV 3.0 to 3.2 GHz, 2GB memory.

6.2 Robustness studies on optimum designs

The robustness of optimum designs will need to be investigated using CFD in a sensitivity analysis. This sensitivity analysis is necessary to ascertain how the optimum design would compensate for manufacturing tolerances (effect on port angle, port height and well depth) as well as operating tolerances (effect on submergence depth and casting speed).

Typical sensitivity analyses require a sample quantity of at least a few thousand to be meaningful. Therefore, instead of performing thousands³ of CFD evaluations (of different designs imitating typical manufacturing tolerances and operational tolerances), curve fitting through a number of representing optimum design perturbations seems to be the logical approach.

The bounds of variables for the sensitivity analysis will be determined by the manufacturing tolerances. LTM Technologies specified the tolerance on all dimensions as $\pm 1\text{mm}$, and $\pm 1^\circ$ for the port angles. Of course operational parameter bounds should also be incorporated in the sensitivity analyses to determine the robustness (or lack of it) of the optimum design in question.

Typically, a sensitivity analysis would compare the objective function of the entire sample block, where each parameter is varied between its expected tolerance bounds. If the objective function value varies significantly for a small parameter deviation (within tolerance), the design will not be regarded as robust. On the other hand, a robust design will show negligible objection function value change for varying (most) parameters within their respective tolerance bounds.

The above explanations on robustness in CFD modelling are (very) brief remarks. Clearly, this subject involves much more detail and work, yet it is anticipated to have a significant impact on the ultimate choice of an “optimum” design. The robustness of

³ Performing thousands of 3D CFD model evaluations will literary take years, even taking into account that computing power will increase following the controversial Mohr’s law of computers, which states that average personal computer power will double every two years.

an initial optimum design following an optimisation exercise may be extremely poor; thus, the choice of a poorer (yet more robust) design may well be the better choice.

6.3 Other global approximation methods

6.3.1 Kriging and optimisation with CFD

Kriging can be summarised as a curve fitting method using an interpolation technique between a set of “points”. These points are typically similar to the design points explained in Chapter 5, where each point has a certain objective function value as a function of the variables of the design. Only in the case of a 2 variable optimisation exercise these design points can be represented by a 3D graph.

Using the 2 variable optimisation exercise case as an example, a curve can be fitted through a number of these points. Usually, a least squares regression type of fit is used (as used by LS-OPT), to fit a linear or quadratic curve through most of the points. Kriging fits a more accurate curve through these (arbitrary chosen) points, as it relies on a geostatistical approach to modelling. Instead of weighting nearby data points by some power of their inverted distance, Kriging relies on the spatial correlation structure of the data to determine the weighted values. This is a more rigorous approach to modelling, as correlation between data points determines the estimated value at an unsampled point. [Internet source: www.tiem.utk.edu/~sada/help]

Kriging is a powerful tool to be used for optimisation studies, as a more accurate curve will represent the entire design space. Other numerical global optimisation techniques can then be used to minimise the objective function in the domain. Although this method is not necessarily exclusively applicable to the CFD modelling and optimisation of the SEN and mould, it is especially appealing to

CFD optimisation in general, as less CFD model evaluations will be necessary to enable the Kriging surface to represent the entire domain of possible designs.

6.3.2 Neural network approximations

The topic of neural network approximations is well-known and needs no further discussion. These approximations can easily be applied to typical CFD design optimisation studies in an effort to reduce the number of CFD evaluations necessary to perform global optimisation.

6.4 Conclusion

These final remarks on possible future work (refinements to certain applications and further avenues to explore as an extrapolation on ideas conceived in this dissertation) concluded this dissertation.

REFERENCES

- [1] HARABUCHI T B and PEHLKE R D. 1988. *Continuous Casting. Volume Four. Design and Operations*. Publication of the Iron and Steel Society, Inc. ISBN 0-932897-29-0.
- [2] HUANG X, THOMAS B G, and NAJJAR F M. 1992. *Modeling Superheat Removal during Continuous Casting of Steel Slabs*. Metallurgical Transactions B. Volume 23B, p. 339.
- [3] THOMAS Brian G, O'MALLEY Ron, SHI Tiebiao, MENG Ya, CREECH David and STONE David. 2000. *Validation of Fluid Flow and Solidification Simulation of a Continuous Thin-Slab Caster*. Proceedings of Conference held August 2000, Aachen, Germany, pp. 769 – 776.
- [4] BAI Hua and THOMAS Brian G. 2001. *Turbulent Flow of Liquid Steel and Argon Bubbles in Slide-Gate Tundish Nozzles: Part I. Model Development and Validation*. Metallurgical and Materials Transactions B. Volume 32B, p. 253.
- [5] BAI Hua and THOMAS Brian G. 2001. *Turbulent Flow of Liquid Steel and Argon Bubbles in Slide-Gate Tundish Nozzles: Part II. Effect of Operation Conditions and Nozzle Design*. Metallurgical and Materials Transactions B. Volume 32B, p. 269.
- [6] IGUCHI Manabu and KASAI Norifumi. 2000. *Water Model Study of Horizontal Molten Steel - Ar Two-Phase Jet in a Continuous Casting Mold*. Metallurgical and Materials Transactions B. Volume 31B, p. 453.
- [7] THOMAS B G. 2001. *Continuous Casting: Modeling*. The Encyclopedia of Advanced Materials, (DANTZIG J, GREENWELL A, MICHALCZYK, eds.) Pergamon Elsevier Science Ltd., Oxford, UK. Volume 2, 8p.
- [8] IRVING W R. 1993. *Continuous Casting of Steel*. The Institute of Materials, 1 Carlton House Terrace, London.
- [9] WHITE Frank M. 1991. *Viscous Fluid Flow. Second Edition*. McGraw-Hill Inc., Singapore. Chapters 1,2 and 3.
- [10] FLUENT[®] Version 6.x.x. 2002 – 2004. Fluent Inc., Lebanon, NH, USA.
- [11] GAMBIT[®] Version 2.x.x. 2002 – 2004. Fluent Inc., Lebanon, NH, USA.

-
- [12] LS-OPT Version 2. 2002. Livermore Software Technology Corporation, Livermore, California.
- [13] STANDER N and CRAIG KJ. 2002. *On the Robustness of a Simple Domain Reduction Scheme for Simulated-based Optimization*. Engineering Computations, Vol. 19, No. 4.
- [14] SNYMAN J A. 2000. *The LFOPC leap-frog method for constrained optimization*. Computers Math. Applic., Vol. 40 (2000) pp. 1085-1096.
- [15] *Mold Powders for Continuous Casting and Bottom Pour Teaming*. 1987. Publication of the Iron and Steel Society, Inc., Warrendale, PA. ISBN 0-932897-18-5.
- [16] *The theory and practice of mold fluxes used in continuous casting*. 1979. A compilation of papers on continuous casting fluxes given at the 61st and 62nd National Open Hearth and Basic Oxygen Steel Conferences (Chicago and Detroit). A Publication of the Iron and Steel Society, Reference Text 101.
- [17] HEARD R A and MCLEAN A. 1988. *Continuous Casting. Volume Five. Horizontal Continuous Casting*. Publication of the Iron and Steel Society, Inc. ISBN 0-932897-32-0.
- [18] CRAIG Ken J, DE KOCK D J, MAKGATA K W and DE WET G J. 2001. *Design Optimization of a Single-strand Continuous Caster Tundish Using Residence Time Distribution Data*. ISIJ International. Volume 41, No. 10, pp. 1194 – 1200.
- [19] LÓPEZ-RAMIREZ S, DE J BARRETO J, PALAFAX-RAMOS J, MORALES R D and ZACHARIAS D. 2001. *Modeling Study of the Influence of Turbulence Inhibitors on the Molten Steel Flow, Tracer Dispersion, and Inclusion Trajectories in Tundishes*. Metallurgical and Materials Transactions B. Volume 32B, p. 615.
- [20] ZHANG Lifeng, TANIGUCHI Shoji and CAI Kaike. 2000. *Fluid Flow and Inclusion Removal in Continuous Casting Tundish*. Metallurgical and Materials Transactions B. Volume 31B, p. 253.
- [21] SINHA Asish Kumar and SAHAI Yogeshwar. 1993. *Mathematical Modeling of Inclusion Transport and Removal in Continuous Casting Tundishes*. ISIJ International. Volume 33, No. 5, pp. 556 – 566.
- [22] MIKI Yuji and THOMAS Brian G. 1999. *Modeling of Inclusion Removal in a Tundish*. Metallurgical and Materials Transactions B. Volume 30B, p. 639.
-

-
- [23] 4th International Conference Continuous Casting. Preprints 2. 1988. Proceedings of the 4th International Conference Continuous Casting, Brussels, May 17-19, 1988. Verlag Stahleisen mbH, Düsseldorf.
- [24] BAI Hua and THOMAS Brian G. 2001. *Effects of Clogging, Argon Injection, and Continuous Casting Conditions on Flow and Air Aspiration in Submerged Entry Nozzles*. Metallurgical and Materials Transactions B. Volume 32B, p. 707.
- [25] YUAN Q, SHI T, VANKA S P and THOMAS Brian G. 2001. *Simulation of Turbulent Flow and Particle Transport in the Continuous Casting of Steel*. Proceedings: Conference for Computational Modeling of Materials, Minerals and Metals Processing, Cross, Bailey, Evans, eds., Seattle, W A, February 2002. The Materials, Minerals, & Metals Society, Warrendale, PA, 2001, pp. 491 – 500.
- [26] 4th International Conference Continuous Casting. Preprints 1. 1988. Proceedings of the 4th International Conference Continuous Casting, Brussels, May 17-19, 1988. Verlag Stahleisen mbH, Düsseldorf.
- [27] BUSH Alan W., LEWIS Barry A. and WARREN Michael D., 1989. *Flow Modelling in Industrial Processes*. Ellis Horwood Limited, Market Cross House, Cooper Street, Chichester, West Sussex, PO19 1EB, England.
- [28] LOMAX Harvard, PULLIAN H. Thomas and Zingg David W. 1999. *Fundamentals of Computational Fluid Dynamics*. Electronic version.
- [29] PATANKAR S V. 1980. *Numerical heat transfer and fluid flow*. Hemisphere Publishing Corporation. ISBN 0-89116-522-3.
- [30] LEUTLOFF D, SRIVASTAVA R C et al. 1995. *Computational Fluid Dynamics*, Springer. Pp 13-25.
- [31] *Application of Mathematical and Physical Models in the Iron and Steel Industry*. 1982. Proceedings of the 3rd Process Technology Conference, Pittsburgh, Pennsylvania, March 1982. Publication of the Iron and Steel Society of AIME.
- [32] ADVENT. 1999. Full scale water model test performed on Columbus old design SEN, Canada.
- [33] WHITE Frank M. 1999. *Fluid Mechanics. Fourth Edition*. McGraw-Hill Book Co – Singapore. ISBN 0-07-116848-6.
-

-
- [34] LEE Joonho and MORITA Kazuki. 2002. *Evaluation of Surface Tension and Adsorption for Liquid Fe-S Alloys*. ISIJ International, Vol 42 (2002).
- [35] CCC '96 7th International Continuous Casting Conference, *The Window to VAIdeas in Continuous Casting*. 1996. Proceedings of the 7th International Continuous Casting Conference, May 20-22, 1996, Brucknerhaus / Linz, Austria. Paper 16, p. 5.
- [36] THOMAS Brian G and BAI Hua. 2001. *Tundish Nozzle Clogging – Application of Computational Models*. 2001 Steelmaking Conference Proceedings. p. 895.
- [37] THOMAS Brian G and VANKA S P. 2002. *Flow Dynamics and Inclusion Transport in Continuous Casting of Steel*. NSF Design, Service, Manufacturing and Industrial Innovation Research Conference Proceedings.
- [38] YUAN Quan, VANKA S P and THOMAS Brian G. 2001. *Large Eddy Simulations of Turbulent Flow and Inclusion Transport in Continuous Casting of Steel*. Proceedings of Conference Turbulence and Shearflow Phenomena, Stockholm, June 2001. TSFP-2, Edition LINDBORG E et al.
- [39] YUAN Q, SHI T, VANKA S P and THOMAS B G. 2000. *Simulation of turbulent flow and particle transport in the continuous casting of steel*. Report. The Continuous Casting Consortium at the University of Illinois at Urbana-Champaign (UIUC).
- [40] ZHANG Lifeng and THOMAS Brian G. 2002. *Alumina Inclusion Behaviour During Steel Deoxidation*. 7th European Electric Steelmaking Conference, Venice, Italy, Associazione Italiana di Metallurgia, Milano, Italy, May 2002.
- [41] ZHANG Lifeng, PLUSCHKELL Wolfgang and THOMAS Brian G. 2002. *Nucleation and Growth of Alumina Inclusions During Steel Deoxidation*. 85th Steelmaking Conference, (March 2002, Nashville, TN). Proceedings Volume 85, ISS, Warrendale, PA, 2002, pp. 463 – 476.
- [42] THOMAS B G, YUAN Quan, SIVARAMAKRISHNAN S and VANKA S P. 2002. *Transient Fluid Flow in a Continuous Steel-Slab Casting Mold*. JOM-e (Journal of Metals - electronic edition), www.tms.org/jom.html.
- [43] THOMAS B G, YUAN Quan, SIVARAMAKRISHNAN S, SHI T, VANKA S P and ASSAR M B. 2001. *Comparison of Four Methods to Evaluate Fluid Velocities in a Continuous Slab Casting Mould*. ISIJ International, 41(10) (2001), p. 1262.
-

-
- [44] THOMAS B G and ZHANG L. 2001. *Mathematical Modeling of Fluid Flow in Continuous Casting*. ISIJ International, 41(10) (2001), p. 1181.
- [45] YOKOYA S, TAKAGI S, TADA K, IGUCHI M, MARUKAWA K and HARA S. 2001. *Swirling Flow Effect in Bottomless Immersion Nozzle on Bulk Flow in High Throughput Slab Continuous Casting Mold. Part I*. ISIJ International, 41(10) (2001), p. 1201.
- [46] YOKOYA S, TAKAGI S, TADA K, IGUCHI M, MARUKAWA K and HARA S. 2001. *Swirling Flow Effect in Bottomless Immersion Nozzle on Bulk Flow in High Throughput Slab Continuous Casting Mold. Part II*. ISIJ International, 41(10) (2001), p. 1208.
- [47] KUBO N, KUBOTA J and ISHII T. 2001. *Simulation of Sliding Nozzle Gate Movements for Steel Continuous Casting*. ISIJ International, 41(10) (2001), p. 1221.
- [48] HARADA H, TOH T, ISHII T, KANEKO K and TAKEUCHI E. 2001. *Effect of Magnetic Field Conditions on the Electromagnetic Braking Efficiency*. ISIJ International, 41(10) (2001), p. 1236.
- [49] TAKATANI K, TANIZAWA Y, MIZUKAMI H and NISHIMURA K. 2001. *Mathematical Model for Transient Fluid Flow in a Continuous Casting Mold*. ISIJ International, 41(10) (2001), p. 1252.
- [50] WILCOX D C. 1998. *Turbulence for CFD modelling*. DCW Industries, Inc., La Canada, California.
- [51] MENTER F R. 1994. *2-Equation Eddy-viscosity Turbulence Models for Engineering Application*. AIAA Journal. Vol. 32, No. 8, p. 1598 – 1605.
- [52] MENG Ya and THOMAS Brian G. 2003. *Heat transfer and solidification model of continuous slab casting: CONID*. Metallurgical and Materials Transactions B: Process Metallurgy and Materials Processing Science, Vol. 34, No. 5, October, 2003, p 685-705.
- [53] CHAKRABORTI N and MUKHERJEE A. 2000. *Optimization of continuous casting mould parameters using genetic algorithms and other techniques*. Ironmaking and Steelmaking. Volume 27, No. 3, p. 243.
- [54] LI Baokuan, OKANE Toshimitsu and UMEDA Takateru. 2000. *Modeling of Molten Metal Flow in a Continuous Casting Process Considering the Effects of Argon Gas Injection and Static Magnetic-Field Application*. Metallurgical and Materials Transactions B. Volume 31B, p. 1491.
-

-
- [55] KUBOTA J, OKIMOTO K, SHIRAYAMA A and MURAKAMI H. 1991. *74th Steelmaking Conference Proceedings*. ISS-AIME, Warrendale, PA. pp. 233 – 238.
- [56] *Continuous Casting of Steel*. 1977. Proceedings of an International conference organized by The Metals Society, London, and L’Institut de Recherches de la Sidérurgie Francaise (IRSID), held in Biarritz, France, May – June 1976. pp. ix – xi.
- [57] STANDER Nielen. 2002. *LS-OPT Design Optimisation for Engineering Analysis: Theory; Command Language*. Presentations during March 2002 on behalf of Livermore Software Technology Corporation at Solihull, UK.
- [58] CRAIG K J, STANDER N, DOOGE D A and VARADAPPA S. 2005. Automotive crash worthiness design using response surface-based variable screening and optimisation. *Engineering Computations*. Vol. 22, No. 1, p. 38 – 61.
- [59] THOMAS Brian G, YUAN Quan, SIVARAMAKRISHNAN Sivaraj, SHI Tiebiao, VANKA S P and ASSAR Mohammad B. 2001. *Comparison of Four Methods to Evaluate Fluid Velocities in a Continuous Slab Casting Mold*. ISIJ International. Vol. 41, No. 10, pp. 1262 – 1271.
- [60] *Solid Edge Version 14 (Academic version)*. 2004. Electronic Data Systems Corporation. Legacy Drive, Plano, Texas, USA.
- [61] NAJJAR Fady M, THOMAS Brian G and HERSHEY Donald E. 1995. *Numerical Study of Steady Turbulent Flow through Bifurcated Nozzles in Continuous Casting*. Metallurgical and Materials Transactions B. Volume 26B, August, p. 749.
- [62] THOMAS Brian G. 2003. *Fluid flow in the Mold*, Chapter 14 in *Making, Shaping and Treating of Steel, 11th Edition*. Vol 5, Casting Volume, A Cramb, Editor, AISE Steel Foundation, Pittsburgh, PA, pp. 14.1 – 14.41.

APPENDIX A

A. Related literature on continuous casting

As explained in the text, these references are shown only for the sake of completeness, as this dissertation is part of an ongoing continuous casting CFD modelling exercise at the University of Pretoria in collaboration with THRIP partners¹ from the industry.

Firstly, the Tundish references diagram is shown to show the resemblances to the classification of typical literature.

A.1 Tundish diagram

¹ THRIP: Technology and Human Resources for Industry Programme of South Africa; a partnership programme funded by the Department of Trade and Industry (DTI) and managed by the National Research Foundation (NRF)

Industry THRIP partners to University of Pretoria, Department Mechanical and Aeronautical Engineering, cfd-labs : Columbus Stainless (main partner), LTM technologies and Foseco

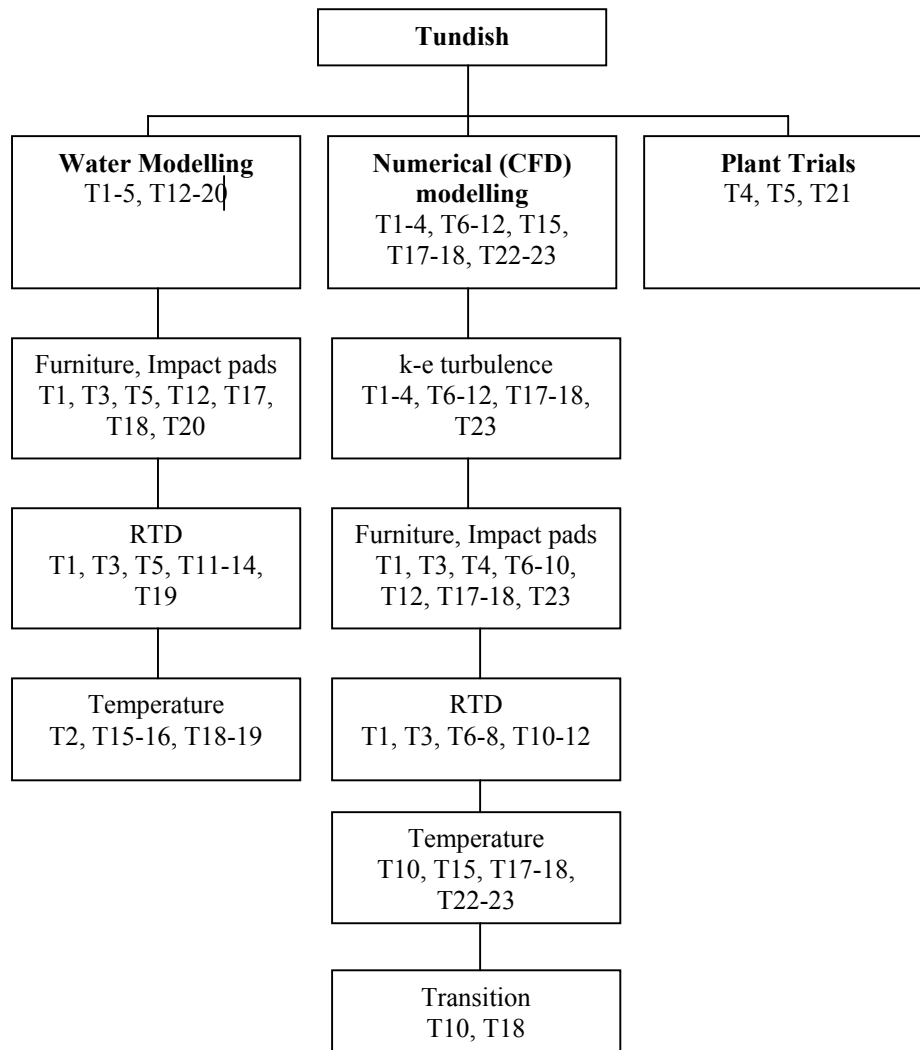


Diagram A.1: Tundish classification of literature

A.2 Tundish (T), Inclusions (I) and Ladle (L) references

T: Tundish

- 1) R. D. Morales, J. deJ Barreto, S. Lopez-Ramirez and J. Palafox-Ramos, Melt Flow Control in a multistrand tundish using a turbulence inhibitor, *Metall. Trans. B.*, 31B (2000), 1505.
- 2) D. Y. Sheng and L. Jonsson, Two-Fluid Simulation on the Mixed Convection Flow Pattern in a Nonisothermal Water Model of Continuous Casting Tundish, *Metall. Trans. B.*, 31B (2000), 867.
- 3) S. Lopez-Ramirez, J. deJ Barreto, J. Palafox-Ramos, R. D. Morales and D. Zacharias, Modeling Study of the Influence of Turbulence Inhibitors on the

- Molten Steel Flow, Tracer Dispersion, and Inclusion Trajectories in Tundishes, *Metall. Trans. B.*, 32B (2001), 615.
- 4) L. Zhang, S. Taniguchi and K. Cai, Fluid Flow and Inclusion Removal in Continuous Casting Tundish, *Metall. Trans. B.*, 31B (2000), 253.
 - 5) M.A. Schueren, J. Schade and R. J. Komanecky, Quality and Productivity Improvements with a Revised Tundish Flow System at AK Steel's Middletown Works, unknown. 2001 and 2002 ISS award winner.
 - 6) Craig, K.J., de Kock, D.J., Makgata, K.W. & de Wet, G.J. Design Optimization of a Single-Strand Continuous Caster Tundish Using RTD Data, *ISIJ International*, Vol.41, No.10, pp.1194-1200, 2001.
 - 7) De Kock, D.J., Craig, K.J. & Pretorius, C.A., Mathematical Maximisation of the Minimum Residence Time for a Two-Strand Continuous Caster, accepted, *Ironmaking and Steelmaking*, Dec. 2002.
 - 8) De Kock, D.J., Craig, K.J. & Pretorius, C.A., Mathematical Maximisation of the Minimum Residence Time for a Two-Strand Continuous Caster, 4th European Continuous Casting Conference, 14-16 October 2002, Birmingham, UK.
 - 9) S. Joo, J.W. Han and R.I.L. Guthrie, Inclusion Behavior and Heat transfer Phenomena in Steelmaking Tundish Operations: Part III. Applications – Computational Approach to Tundish Design, *Metall. Trans. B.*, 24B (1993), 779.
 - 10) C. Damle and Y. Sahai, Modeling of Grade Change Operations During Continuous Casting of Steel – Mixing in the Tundish, Transactions of the ISS, June 1995, 49.
 - 11) P.K. Jha and S.K. Dash, Effect of Outlet Positions and Various Turbulence Models on Mixing in a Single and Multi Strand Tundish, *International Journal of Numerical Methods for Heat and Fluid Flow*, 12(5) (2002), 560.
 - 12) S. Joo and R.I.L. Guthrie, Inclusion Behavior and Heat transfer Phenomena in Steelmaking Tundish Operations: Part I. Aqueous Modelling, *Metall. Trans. B.*, 24B (1993), 755.
 - 13) Y. Sahai and T. Emi, Melt Flow Characterization in Continuous Casting Tundishes, *ISIJ International*, 36(6) (1996), 667.
 - 14) Y. Sahai and R.Ahuja, Fluid Flow and Mixing of Melt in Steelmaking Tundishes, *Ironmaking and Steelmaking*, 13(5) (1986), 241.
 - 15) D.Y. Sheng, C.S. Kim, J.K. Yoon and T.C. Hsiao, Water Model Study on Convection Pattern of Molten Steel Flow in Continuous Casting Tundish, *ISIJ International*, 38(8) (1998), 843.
 - 16) A.K. Sinha and A. Vassilicos, Physical Modelling of Thermal Effects on Steel Flow and Mixing in Tundish, *Ironmaking and Steelmaking*, 25(5) (1998), 387.
 - 17) R. D. Morales, S Lopez-Ramirez, J. Palafox-Ramos and D. Zacharias, Numerical and Modeling Analysis of Fluid Flow and Heat Transfer of Liquid Steel in a Tundish with Different Flow Control Devices, *ISIJ International*, 39(5) (1999), 455.
 - 18) D. Y. Sheng and L. Jonsson, Investigation of Transient Fluid Flow and Heat Transfer in a Continuous Casting Tundish by Numerical Analysis Verified with Nonisothermal Water Model Experiments, *Metall. Trans. B.*, 30B (1999), 979.
 - 19) M.L. Lowry and Y. Sahai, Thermal Effects on the Flow of Liquid Steel in Continuous Casting Tundishes, Transactions of the ISS, March 1992, 81.
 - 20) R.W. Crowley, G.D. Lawson and B.R. Jardine, Cleanliness Improvements Using a Turbulence-Suppressing Tundish Impact Pad, 1995 Steelmaking Conference Proceedings, 629.

- 21) H. Tanaka, R. Nishihara, I. Kitagawa and R. Tsujina, Quantitative Analysis of Contamination of Molten Steel in Tundish, *ISIJ International*, 33(12) (1993), 1238.
 - 22) S. Joo, J.W. Han and R.I.L. Guthrie, Inclusion Behavior and Heat transfer Phenomena in Steelmaking Tundish Operations: Part II. Mathematical Model for Liquid Steel in Tundishes, *Metall. Trans. B.*, 24B (1993), 767.
 - 23) Y. Miki and B.G. Thomas. Modeling of Inclusion Removal in a Tundish, *Metall. Trans. B.*, 30B (1999), 639.
-

I: Inclusions and Steel Cleanliness

- 1) L. Shang and B.G. Thomas, Alumina Inclusion Behavior during Steel Deoxidation, *7th European Electric Steelmaking Conference*, Venice, Italy, May 26-29, 2002.
 - 2) L. Zhang and B.G. Thomas, State of the Art in Evaluation and Control of Steel Cleanliness, *ISIJ International*, 43(3) (2003), 271.
 - 3) L. Zhang, W. Pluschkell, B.G. Thomas, Nucleation and Growth of Alumina Inclusions during Steel Deoxidation, *85th Steelmaking Conference*, (Mar. 10-13, 2002, Nashville, TN), Vol.85, ISS, Warrendale, PA, 2002, 463.
-

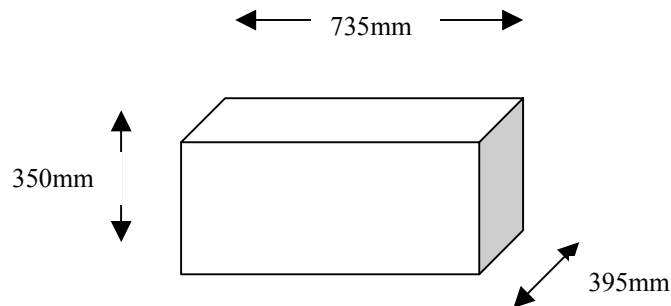
L: Ladle

- 1) L. Zhang, Mathematical Simulation of Fluid Flow in Gas-Stirred Liquid Systems, *Modelling Simul. Mater. Sci. Eng.*, 8 (2000), 463.
- 2) B. Barber, G. Watson and L. Bowden, Optimum Ladle Design for Heat Retention during Continuous Casting, *Ironmaking and Steelmaking*, 21(2) (1994), 150.

APPENDIX B

B. Detail drawings of bottom tank (2.5mm sheets)

The basic dimensions of the rectangular bottom tank are:



The bottom tank is designed from 2.5mm stainless steel, and consists of 7 pieces of sheet metal welded together using a TIG welding process.

7 pieces of sheet metal:

- belly or base
- top with holes
- side (left)
- side (right – with exit hole)
- support and baffle (right)
- support and baffle (identical for middle and left)

The detail drawings (extracted from Solid Edge [60]) are shown in Figures B.1 to B.6. It is interesting to note that the tank sheets are drawn in the folded position using Solid Edge, but can be automatically unfolded using Solid Edge to generate drawings of the flat sheets. The folded open sections are preferred by the laser cutting industry for obvious reasons.

Additional stainless steel sections needed to be welded onto the top section after the tank has been welded together. The function of these protruding sections is to facilitate sealing of the wide and narrow mould walls during operation of the water model.

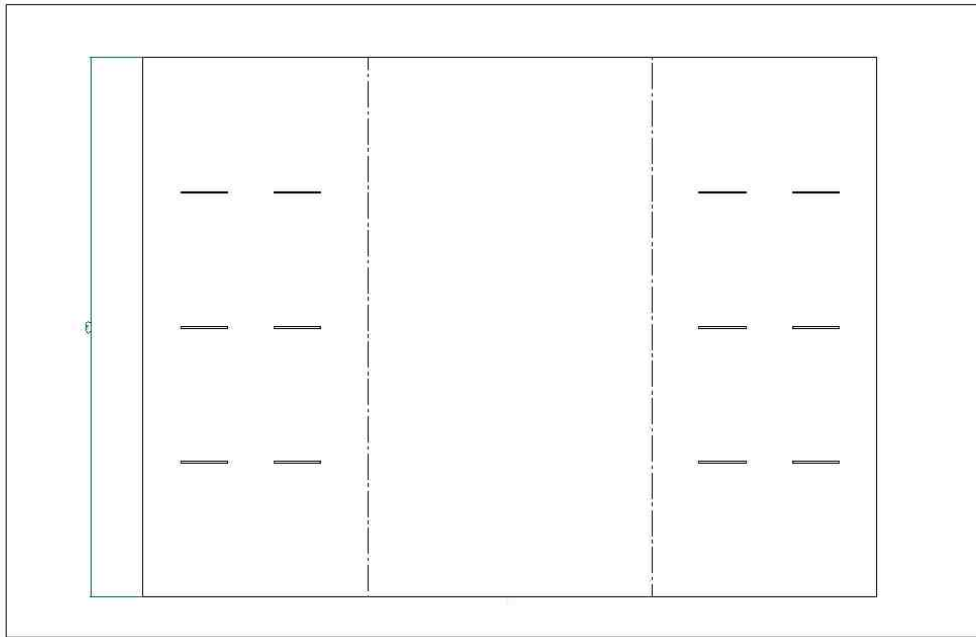


Figure B.1: Detail folded open drawing extracted from Solid Edge: Belly or base

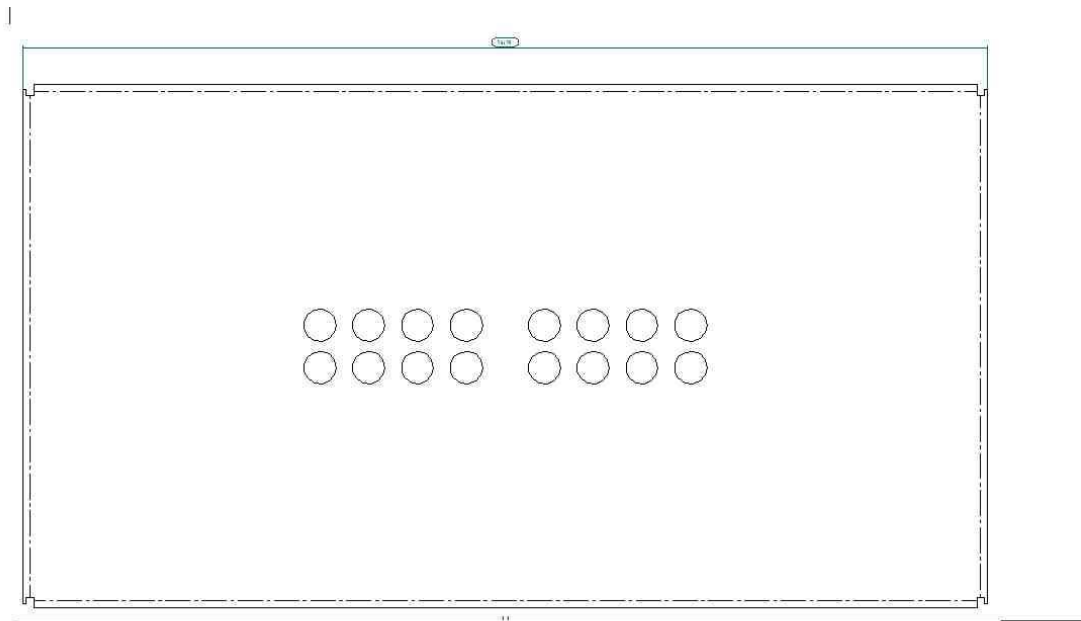


Figure B.2: Detail folded open drawing extracted from Solid Edge: Top

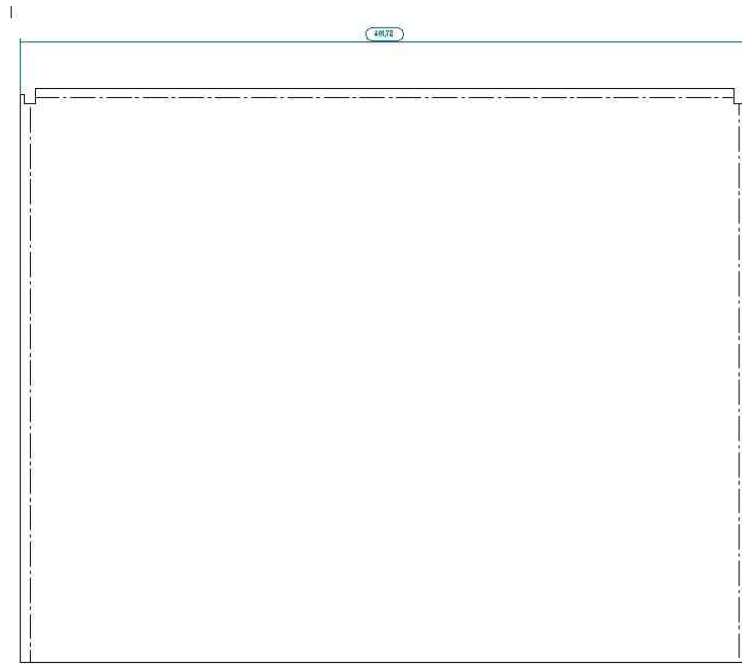


Figure B.3: Detail folded open drawing extracted from Solid Edge: Side, left

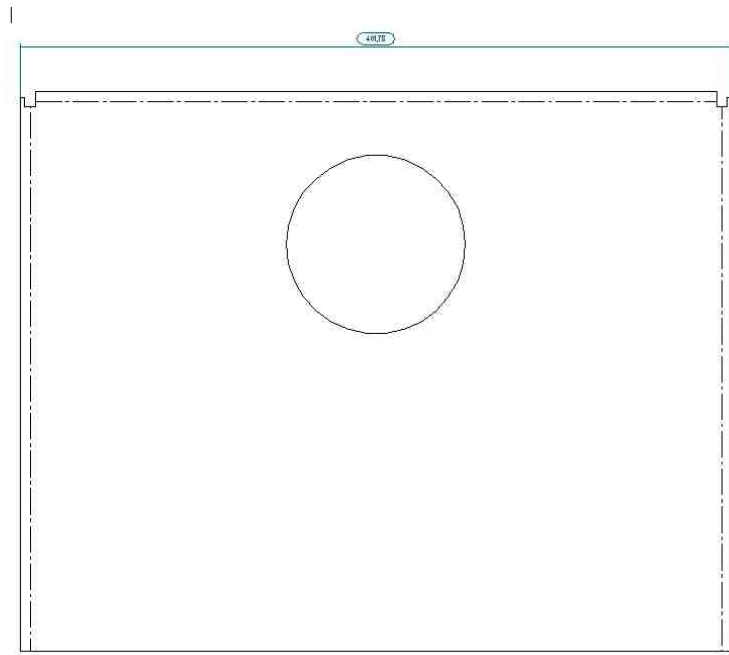


Figure B.4: Detail folded open drawing extracted from Solid Edge: Side, right

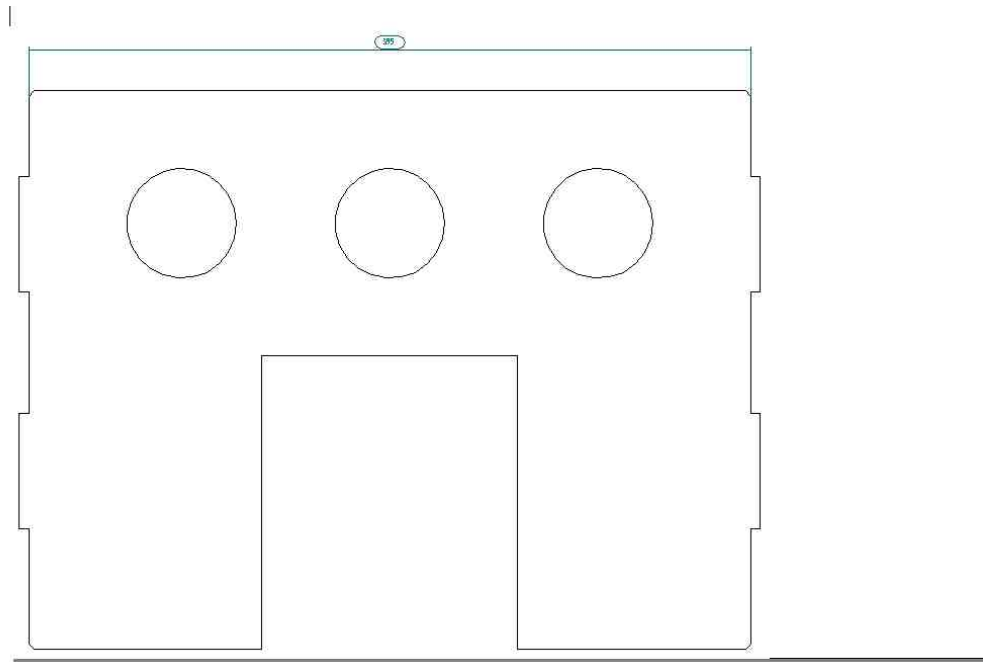


Figure B.5: Detail folded open drawing extracted from Solid Edge: Support and baffle, right

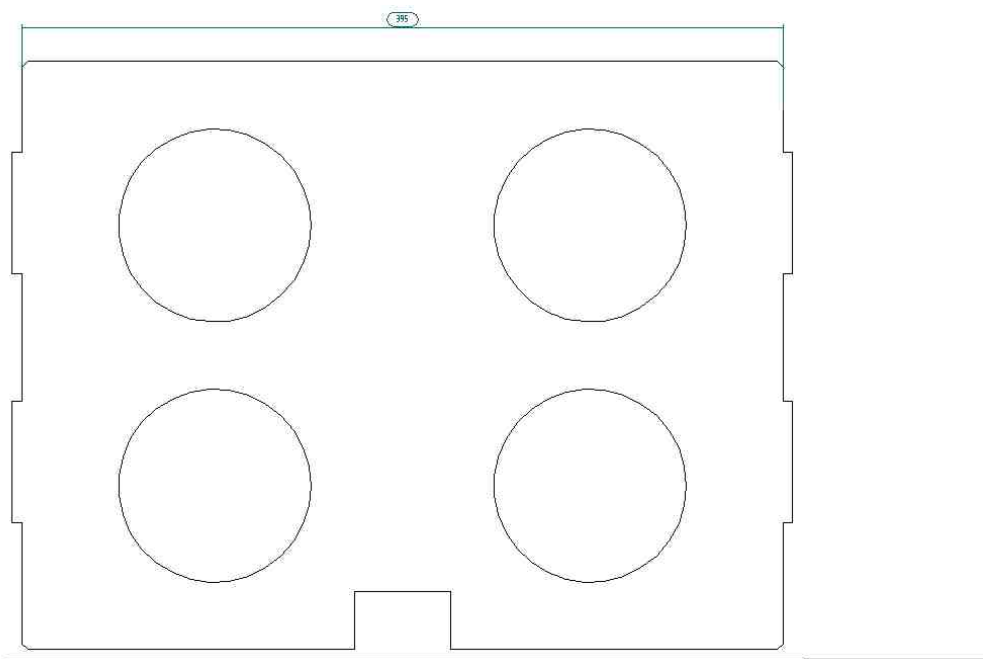


Figure B.6: Detail folded open drawing extracted from Solid Edge: Support and baffle, middle and left

APPENDIX C

C. Chosen steel sections for frame / structure and accompanying drawings

C.1 Chosen steel sections for frame/structure

The frame was designed to accommodate the following loads:

- mass of the water inside the perspex mould
- mass of the (full with water) top cylindrical tank
- forces due to the water pressure ($\approx \rho gh$) inside the perspex mould

Table C.1: Steel sections for water model frame

Member description	Subjected to:	Steel section
Legs (x4)	Axial load (as a column member), as well as bending from the opposing bolt forces)	Angle section, 50 x 50 (cross sectional) x 6 mm (thickness)
Feet (x2)	Bending at bolted sections	Angle section, 50 x 50 x 6 mm
Separator (horizontal) sections (x4)	Bending due to opposing bolt forces and possible frame movement	Square tubing section, 75 x 75 x 3 mm
Hanging members (x4)	Bending due to opposing bolt forces.	Square tubing, 75 x 75 x 3 mm
Perspex supporting beams (x4 for both sides)	Bending due to hydrostatic pressure	Angle section, 30 x 30 x 3 mm
Supporting beams for torsional stability (x8)	Axial and compressive loads	Angle section, 30 x 30 x 3 mm
Support for bottom tank (x2)	Bending due to weight of filled perspex mould and filled bottom tank	Angle section, 50 x 50 x 6 mm
Support for top tank (x2)	Bending due to weight of top tank and mass of supply pipe	Angle section, 50 x 50 x 6 mm
Diagonal struts for stiffness	Axial and compressive loads	Angle section, 50 x 50 x 6 mm

All the sections were chosen to exhibit a Safety Factor of at least 2 during the maximum loaded cases.

C.2 Detail hand drawings of frame

Figures C.1 to C.3 depict the front, side and top view of the assembled frame respectively.

Figure C.4 shows more detail of the four (identical) hanging sections.

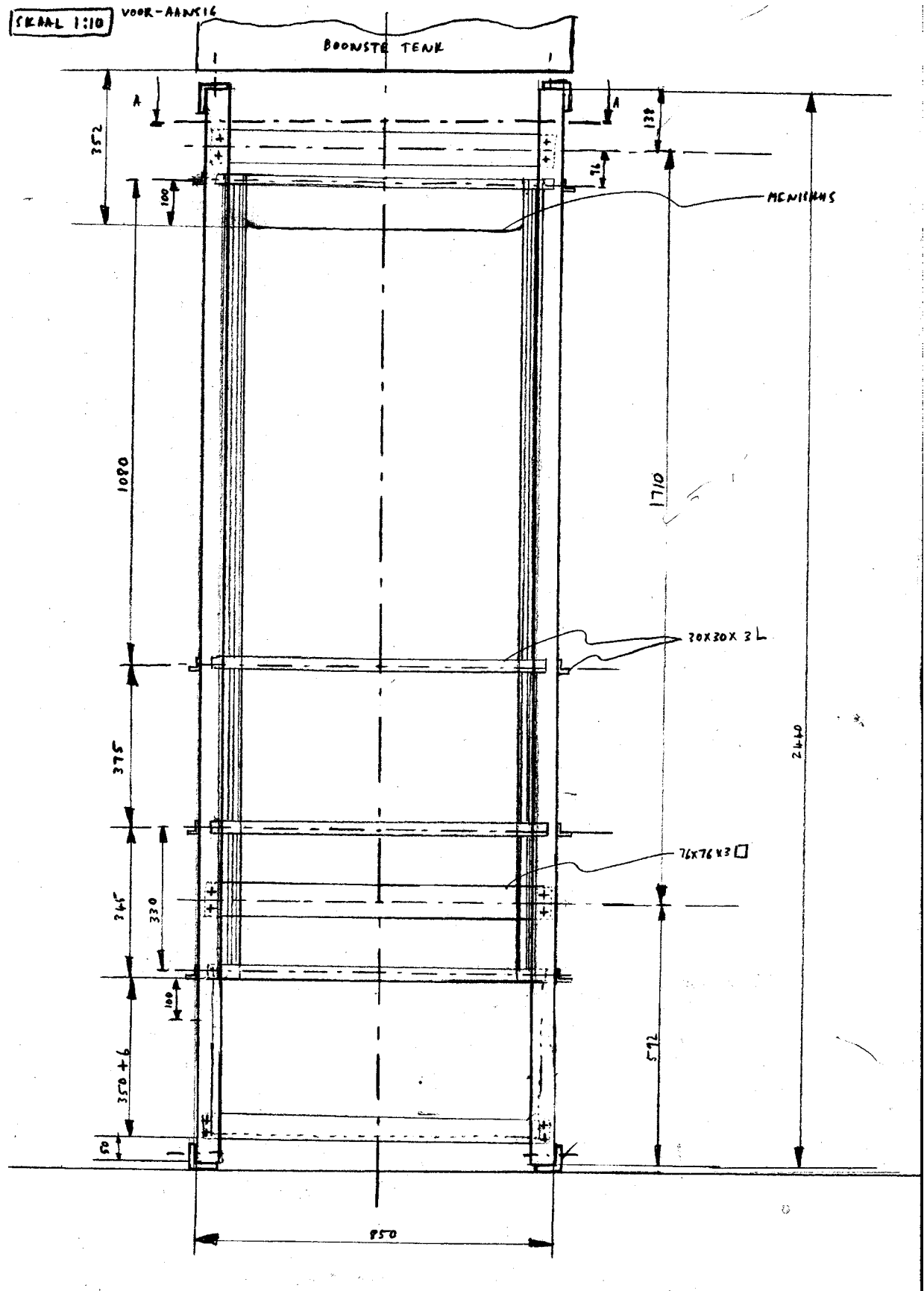


Figure C.1: Water model frame, front view: Detail hand drawing

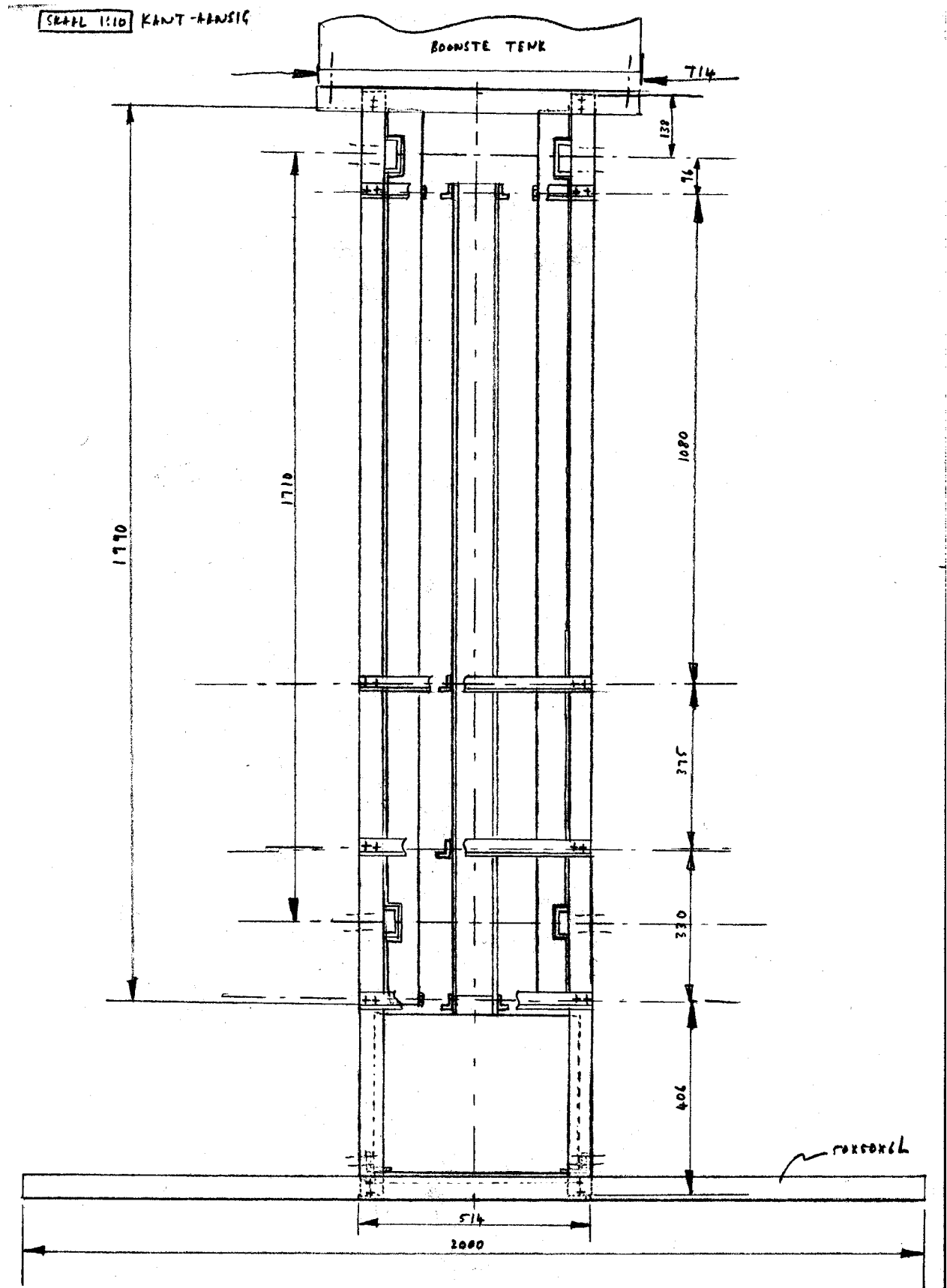


Figure C.2: Water model frame, side view: Detail hand drawing

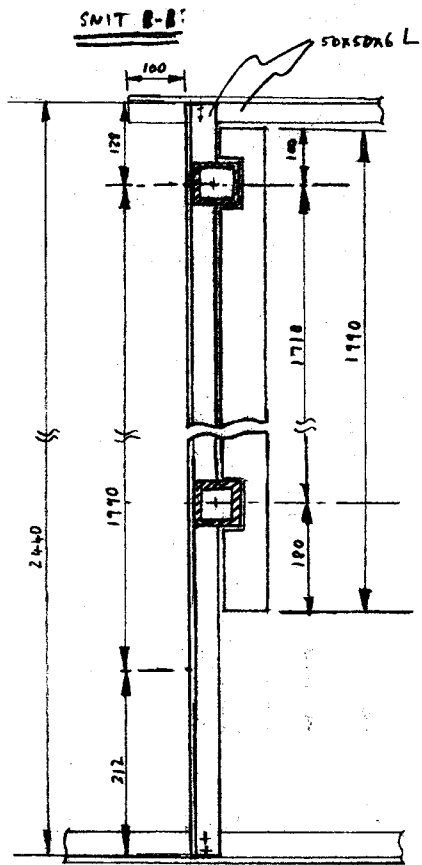
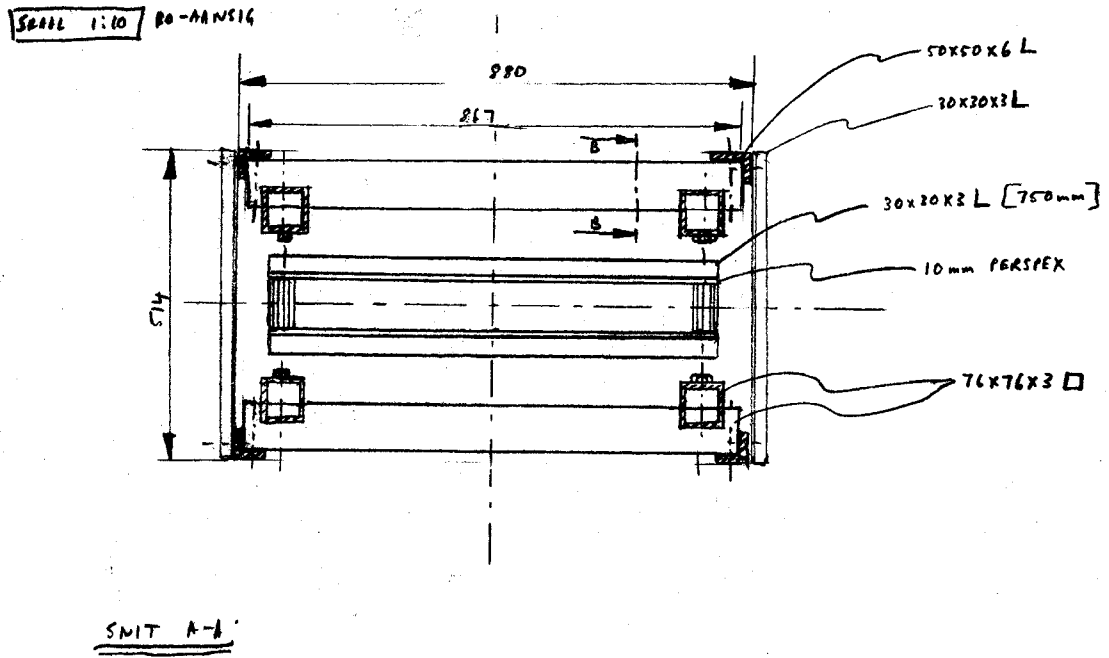


Figure C.3: Water model frame, top view and detail: Detail hand drawing

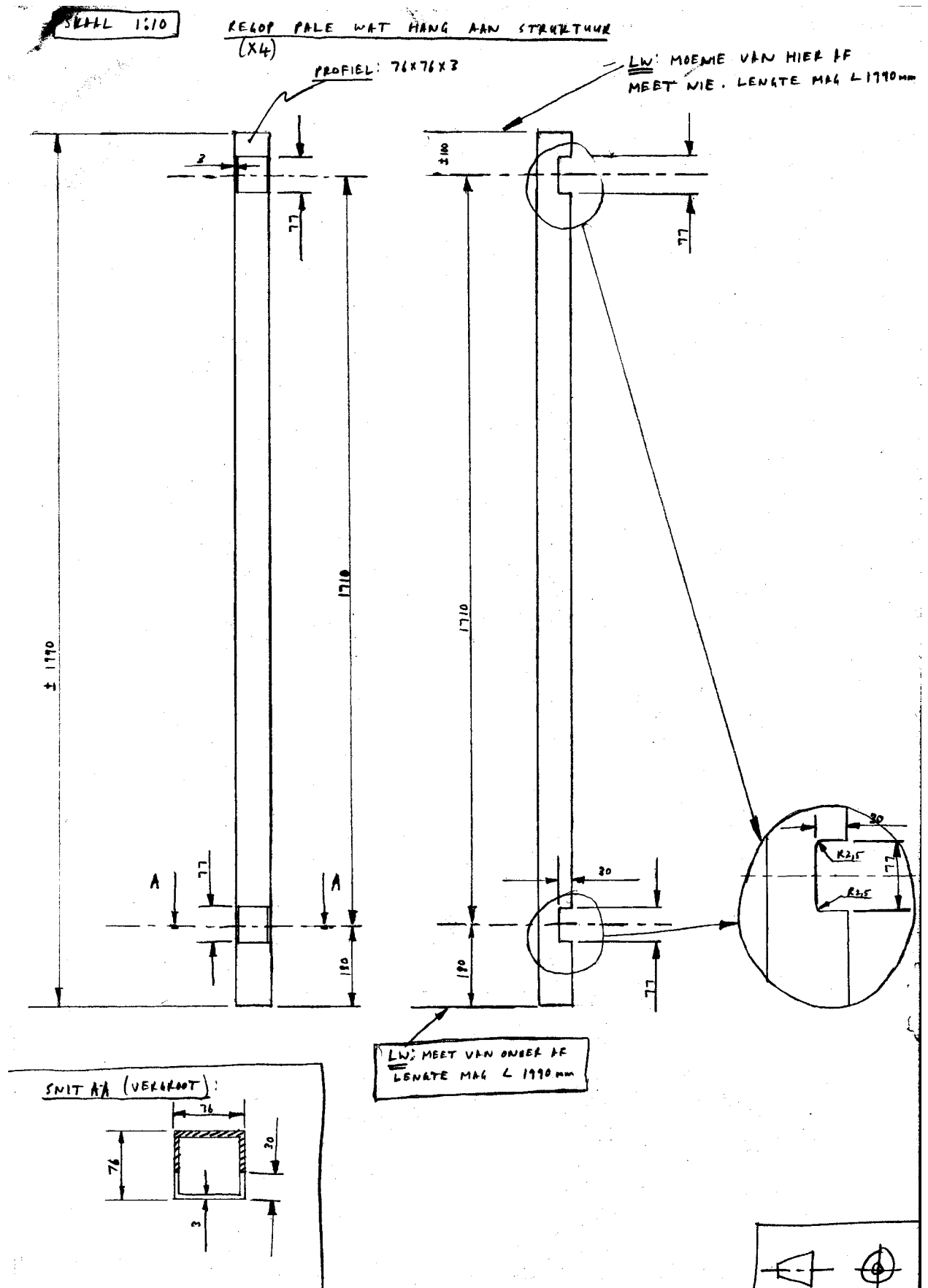


Figure C.4: Water model frame: detail of hanging sections: Detail hand drawing

APPENDIX D

D. Aluminium 40% scaled SEN: hand drawings for manufacture

Some detail drawings for the Aluminium SEN are presented in Figures D.1 to D.3 below, and the following information will be presented:

- Assembly drawing: full section
- Assembly drawing: side view
- Auxiliary sections and views

Figure D.4 is the detail drawing of the mandrel required to manufacture all three parts of the SEN. The mandrel is the positive geometry of the inside of the SEN, and will be manufactured from copper to be used during the spark erosion technique.

Figure D.5 is a dimensional assembly drawing of the 40% scaled stopper and SEN upper part.

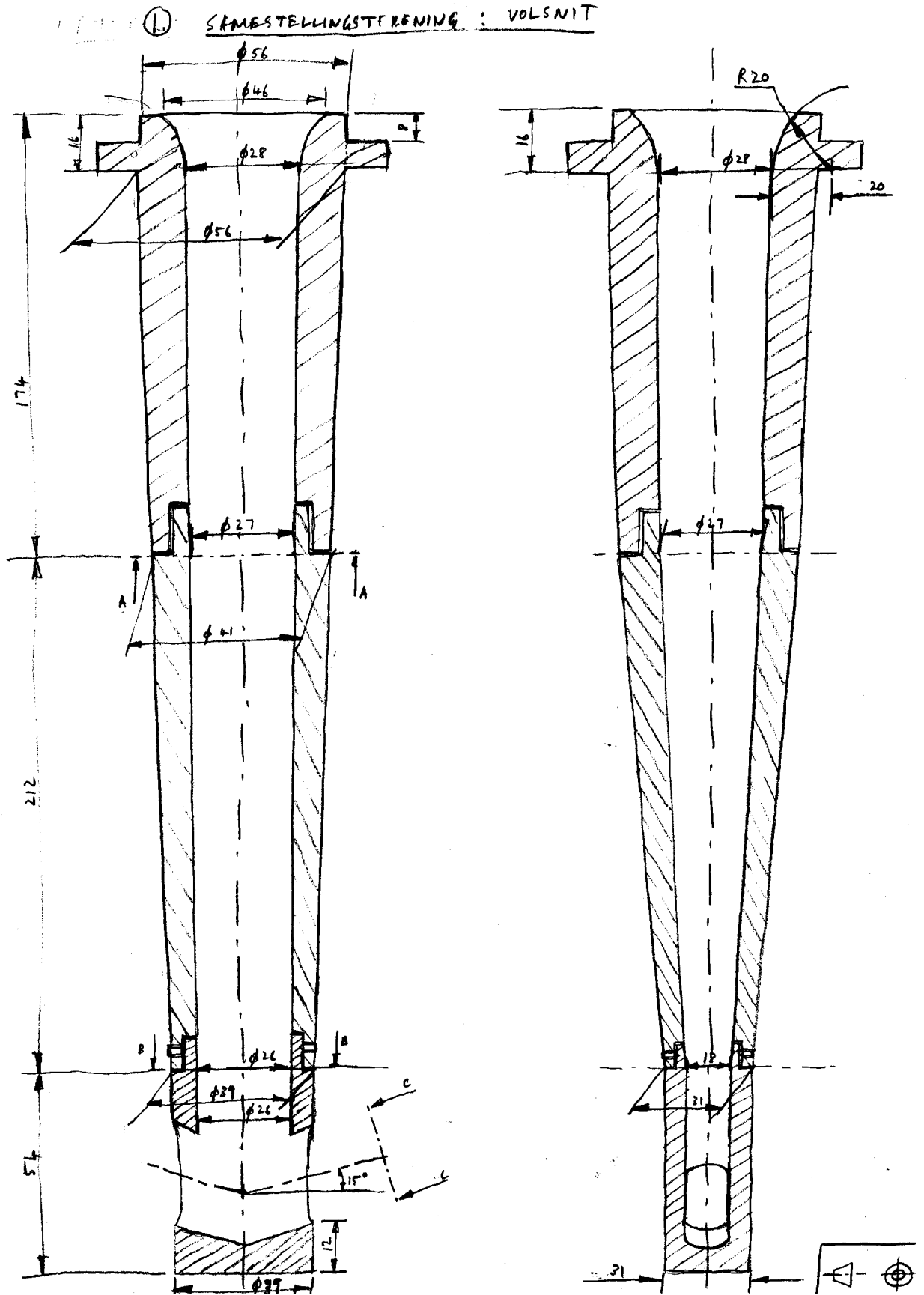


Figure D.1: Aluminium SEN: Assembly drawing: full section

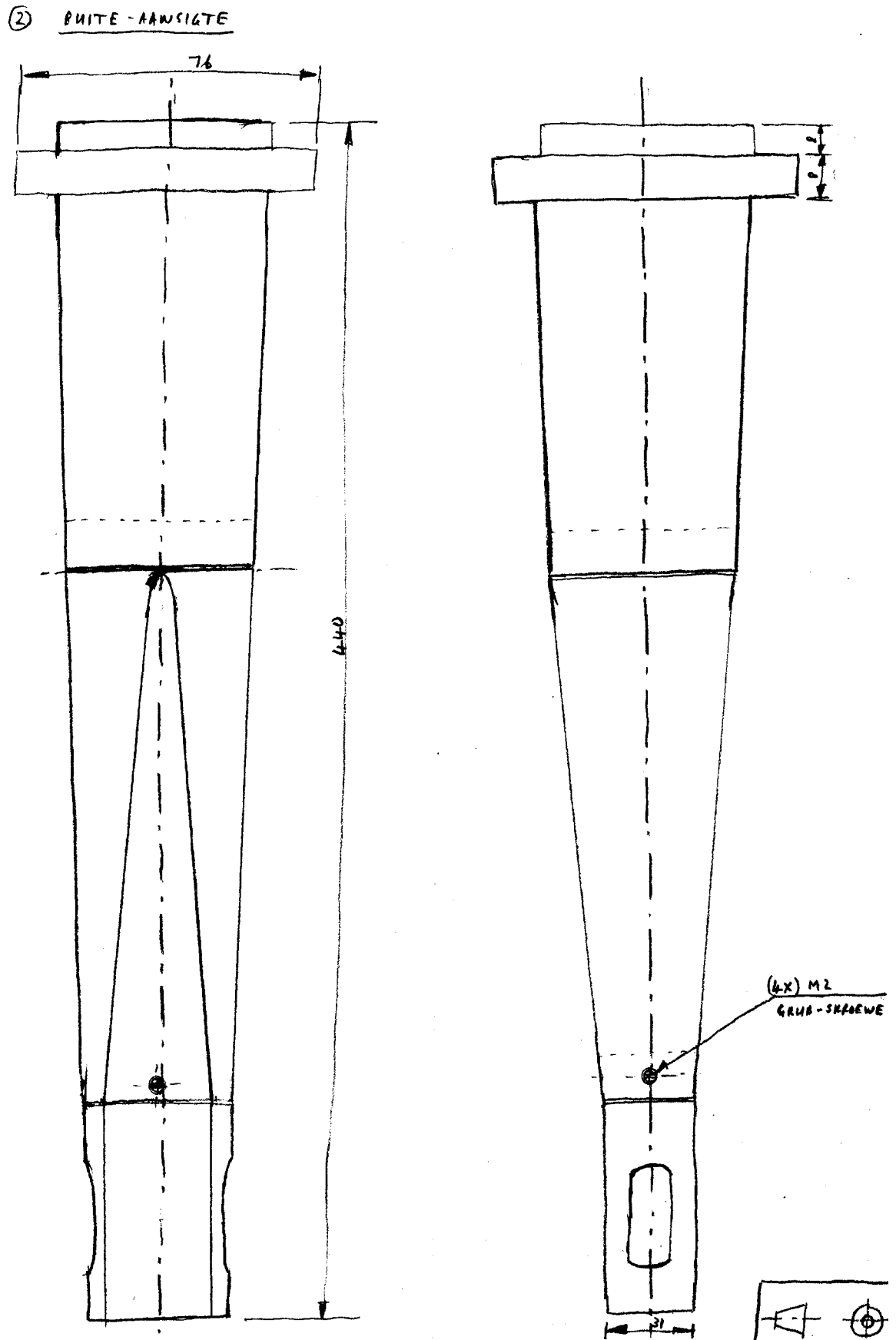
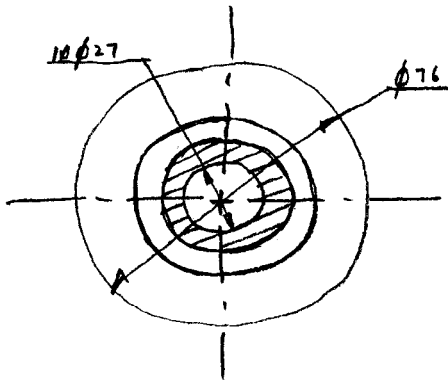


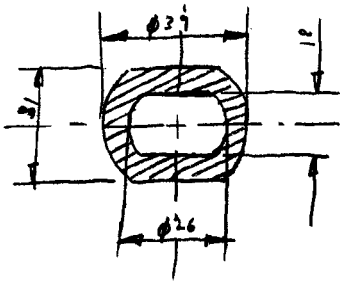
Figure D.2: Aluminium SEN: Assembly drawing: side view

③ HULPSNITTE EN -ANSIGTE

SNIT A-A:



SNIT A-B:



ANSIG C-C:

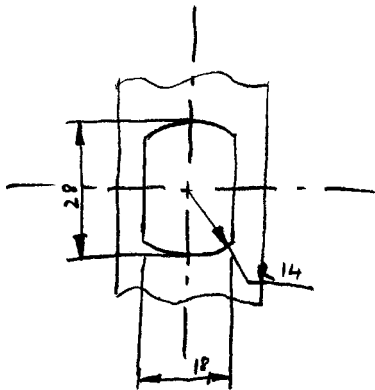


Figure D.3: Aluminium SEN: Auxiliary sections and views

⑤ DREWEL TEKENINGE

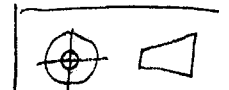
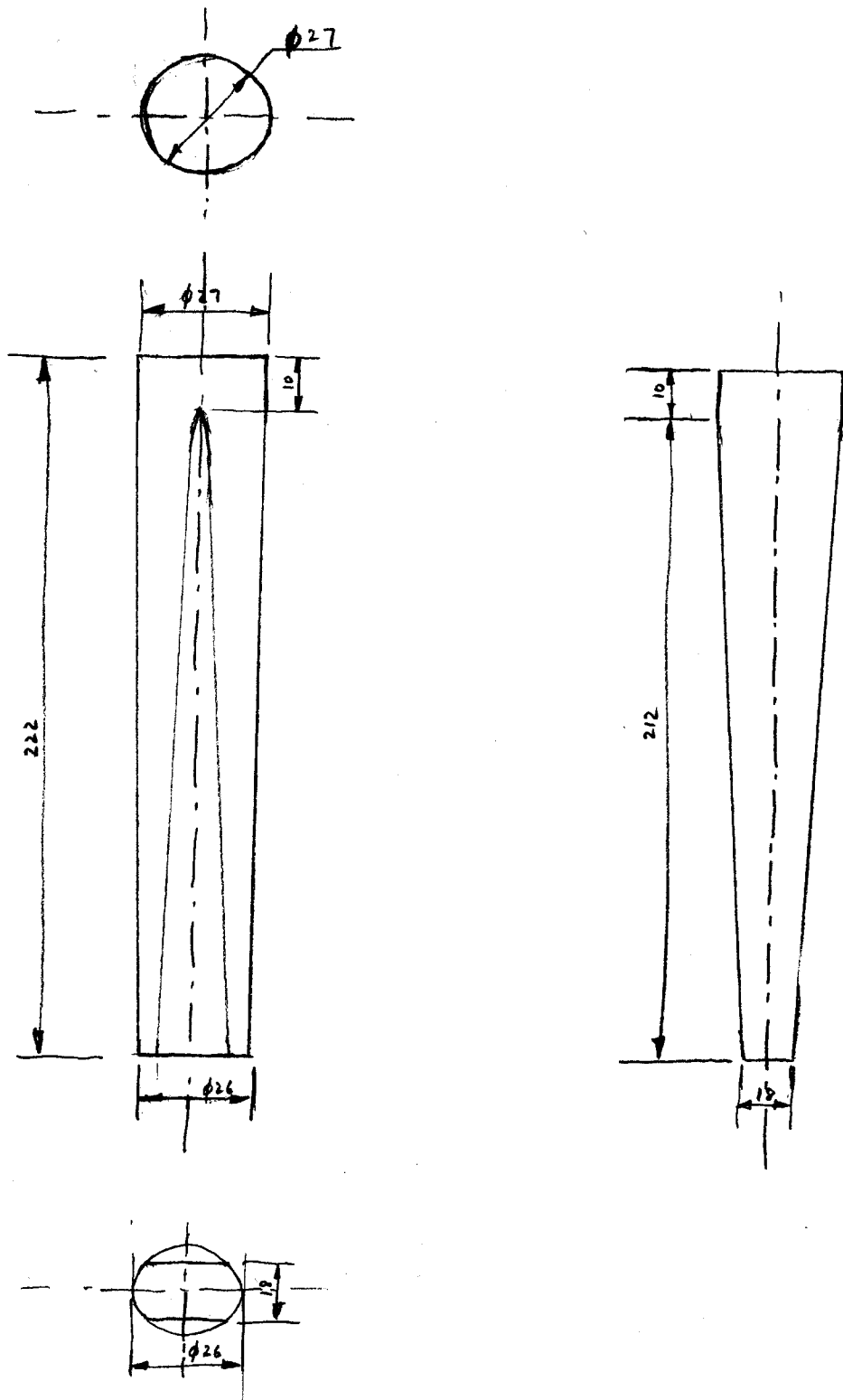


Figure D.4: Mandrel for manufacture of Aluminium SEN inside

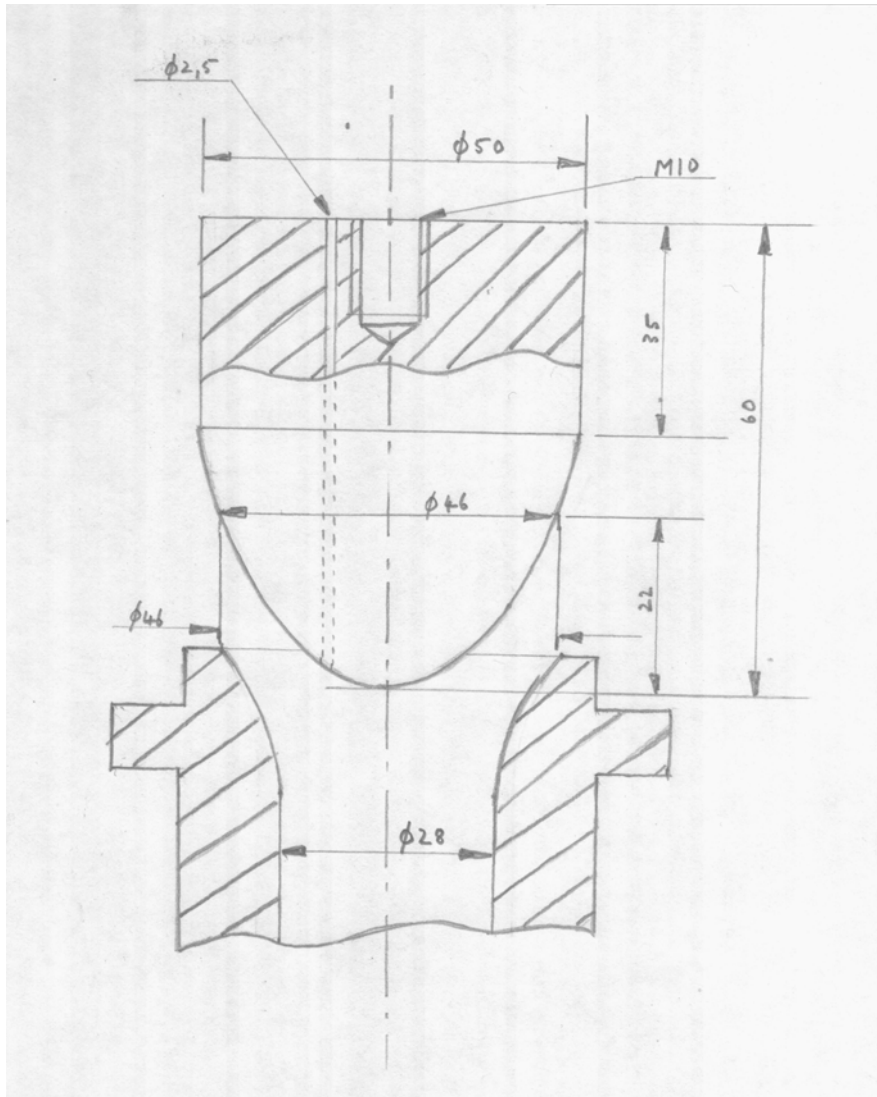


Figure D.5: Assembly drawing of 40%-scaled stopper and SEN upper part

APPENDIX E

E. Water model construction

E.1 Construction process

The construction of the water model comprised of the following processes (in that particular order):

- Identify and order all loose parts and material
 - Steel for the frame
 - Bolts and nuts
 - Perspex
 - Pipes, elbows, T-sections, gate valves, reducers, pipe clips, plumber's tape, nipples (male to male BSP pipe sections), and all other small items to insignificant to mention
- Outsource of top tank, bottom tank and Aluminium SEN manufacturing
 - Prepare design drawings for manufacturing of top tank, bottom tank and SEN
 - Requesting quotations, placing the orders and co-ordinating payment of companies
 - Establish completion dates
 - Ensure that outsourced manufacturing quality is sufficient and ensure integration of outsourced components into final water model product
- Frame construction
 - Mark-off using specially designed die for accurate, repeatable marking on angled sections for holes
 - Drill of holes
 - Construction of frame
 - Preliminary fitment of perspex mould to establish position of holes in the hanging beams
 - Manufacturing of extra long bolts, using threaded rods and nuts
 - Paint for aesthetic purposes and to prevent rust

- Perspex mould construction
 - Prepare drawings for perspex sheet sizes and information for narrow wall cuts
 - Establish a seal mechanism between the narrow walls and wide walls, as well as between the perspex mould and the bottom tank
 - Manufacture narrow walls by bonding 3 perspex sheets (cut to size) together
- Pipes, T-pieces, valves, etc.
 - Take into account all distances of pipes and T-pieces to ensure location of water model remains in the desired position
 - Ensure all connections are leak-free
- Pump installation
 - The installation of the pump was postponed until high speed tests are desired

E.2 Construction Gantt-chart

Refer to the following page(s) for the Gantt-chart of the construction process of the water model.

ID	Task Name	Duration	f 1	2002, Half 2			2003, Half 1		2003, Half 2		2004, Half 1		2004, Half 2		2005, Ha
			Qtr 2	Qtr 3	Qtr 4	Qtr 1	Qtr 2	Qtr 3	Qtr 4	Qtr 1	Qtr 2	Qtr 3	Qtr 4	Qtr 1	
1	Concept design	2 wks													
2	Detail design	4 wks													
3	Construction	302 days?													
4	Identify all material and loose parts	20 days													
5	Steel for frame	1 wk													
6	Bolts and nuts	2 days													
7	Perspex	3 days													
8	Pipes, elbows, T-sections, gate valves, reducers, pipe clips, plumber's tape, nipples (male to male BSP pipe sections), and all other small items to insignificant to mention	2 wks													
9	Outsourcing of top tank, bottom tank and Aluminium SEN	156 days													
10	Prepare design drawings for manufacturing of top tank, bottom tank and SEN [Sept-Oct]	4 wks													
11	Request quotations	1 wk													
12	Place orders	1 wk													
13	Coordinating payments	4 wks													
14	Ensure quality of outsourced components	1 wk													
15	Receive Aluminium SEN	1 day													
16	Receive top and bottom tank	1 day													
17	Frame design and construction	253 days													
18	Design and manufacture special mark-off die	2 wks													
19	Mark-off	1 wk													
20	Cut correct lengths and drill holes	2 wks													
21	Construction of frame	2 days													
22	Preliminary fitment of perspex sheets	2 days													
23	Paint for esthetic purposes and to prevent rust	4 days													
24	Perspex mould construction	5 days?													
25	Prepare drawings for perspex sheet sizes and mould walls	2 days													
26	Fit bottom, top tanks	1 day?													
27	Establish seal mechanism	1 day													

Project: Watermodel_Gantt Date: 2004/12/07	Task		Milestone		External Tasks	
	Split		Summary		External Milestone	
	Progress		Project Summary		Deadline	

ID	Task Name	Duration	f 1	2002, Half 2			2003, Half 1		2003, Half 2		2004, Half 1		2004, Half 2		2005, Ha
			Qtr 2	Qtr 3	Qtr 4	Qtr 1	Qtr 2	Qtr 3	Qtr 4	Qtr 1	Qtr 2	Qtr 3	Qtr 4	Qtr 1	
28	Manufacture narrow walls: glue	1 day													
29	Pipes, T-pieces, valves etc.	5 days													
30	Measure pipe lengths and valve lengths: location of water model 12 September ope dag...	3 days													
31	Ensure connections are leak-free	2 days													
32	Pump installation	0 days													
33	Cancelled	0 days													
34	Commissioning 24 Sept	6 days													
35	Leak-test	1 day													
36	Preliminary water model test	1 day													
37	Water model tests: 2003 (10 - 14 Nov)	5 days													
38	Water model test: 1575mm (full-scale); Old SEN	2.5 days													
39	Water model test: 1575mm (full-scale); New SEN	2.5 days													
40	Water model upgrade (Marius Botha)	120 days													
41	New carbon perspex sheet	120 days													
42	Install flow meter	120 days													
43	Strengthen critical columns	120 days													
44	Aluminium SEN insert: new design	120 days													
45	Water model tests: 2004	10 days													
46	Water model test: 1060mm (full-scale); Old/New	5 days													
47	Water model test: 1250mm (full-scale); Old/New	5 days													



Project: Watermodel_Gantt
Date: 2004/12/07

Task		Milestone		External Tasks	
Split		Summary		External Milestone	
Progress		Project Summary		Deadline	

APPENDIX F

F. Water model Results

F.1 General

Two widths will be tested for both SEN designs, each at two different flow speeds (equivalent to casting speeds) and two different submergence depths:

- Widths: 1060mm and 1250mm
- Submergence depths: 80mm and 150mm
- Water model flow rates satisfying Fr-similarity for a casting speed of 1.0 m/min
 - 1060mm width: 1.28 m³/h
 - 1250mm width: 1.52 m³/h

F.2 Visualisation methods

Although the flow field is assumed to be steady (does not change with passing time), a dye injected into the top of the SEN will highlight the steady flow patterns. However, as the jet mixes with the water in the mould cavity, the jet becomes less visible until the entire mould cavity is the same colour. The double barrel and upward swirling of the jets can also be visualised.

In order to illustrate the three-dimensional flow field, the results will be shown as a series of 4 “snapshots”, exactly as the water model test would unfold before an observer.

F.3 Results

The water model results of the experiments (listed in Table F.1) will be presented in Figures F.1 to F.15. All tests were performed for casting speeds of 1.0m/min and 1.1 m/min (satisfying Fr-similarity). However, the results for the two different flow rates were almost identical (as shown in Figures F.1 and F.2). Consequently, only the results of the 1.0 m/min casting speed tests are displayed in this Appendix.

Table F.1: List of water model experiments and reference Figure number

Figure F.	SEN design	Mould Width (full-scale) [mm]	Submergence depth (full-scale) [mm]	Q_{model}^1 (Fr-similarity) [m³/h]	v_{cast} (full-scale) [m/min]
1	Old	1060	150	1.42	1.1
2	Old	1060	150	1.28	1.0
3	New	1060	150	1.28	1.0
4	Old	1060	80	1.28	1.0
5	New	1060	80	1.28	1.0
6	Old	1250	150	1.52	1.0
7	New	1250	150	1.52	1.0
8	Old	1250	80	1.52	1.0
9	New	1250	80	1.52	1.0

¹ Refer to Chapter 3 for derivation of eq 3-7 used to calculate the flow rate of the model, satisfying Fr-similarity.

Old SEN, 1060 mm width, 150mm submergence depth, 1.1 m/min full-scale cast speed



Figure F.1: Old SEN (1060mm width, 150mm submergence depth, 1.1 m/min full-scale cast speed) snapshots

Old SEN, 1060 mm width, 150mm submergence depth, 1.0 m/min full-scale cast speed

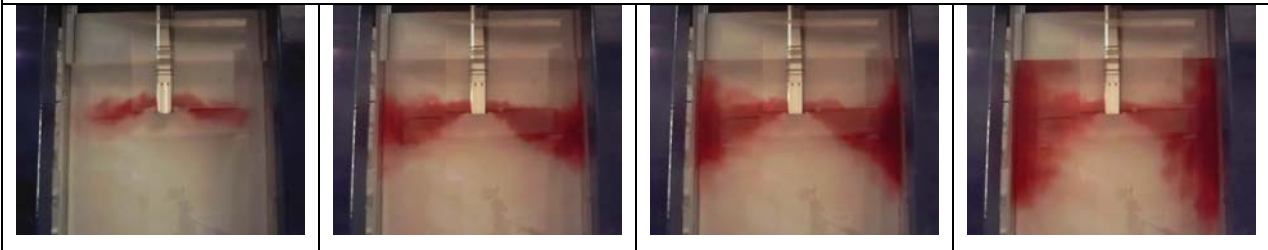


Figure F.2: Old SEN (1060mm width, 150mm submergence depth, 1.0 m/min full-scale cast speed) snapshots

New SEN, 1060 mm width, 150mm submergence depth, 1.0 m/min full-scale cast speed

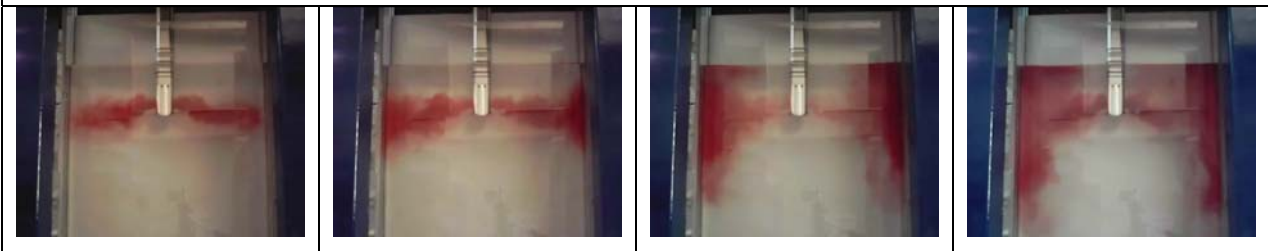


Figure F.3: New SEN (1060mm width, 150mm submergence depth, 1.0 m/min full-scale cast speed) snapshots

Old SEN, 1060 mm width, 80mm submergence depth, 1.0 m/min full-scale cast speed

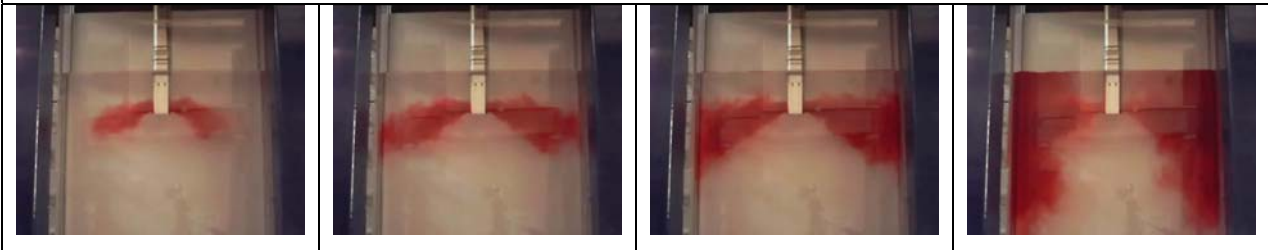


Figure F.4: Old SEN (1060mm width, 80mm submergence depth, 1.0 m/min full-scale cast speed) snapshots

New SEN, 1060 mm width, 80mm submergence depth, 1.0 m/min full-scale cast speed

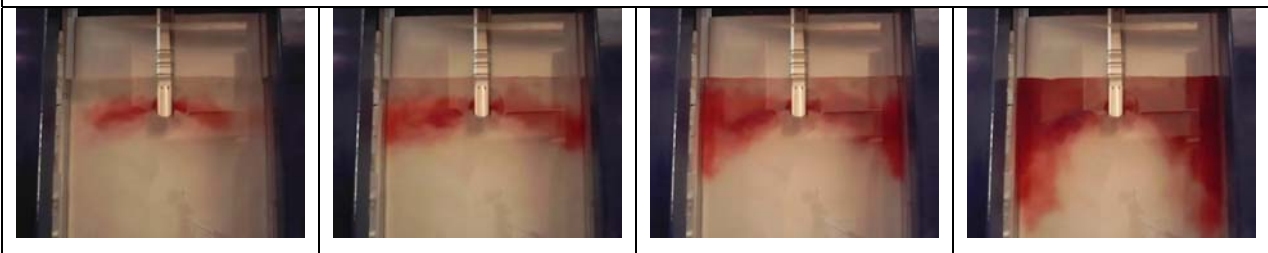


Figure F.5: New SEN (1060mm width, 80mm submergence depth, 1.0 m/min full-scale cast speed) snapshots

Old SEN, 1250 mm width, 150mm submergence depth, 1.0 m/min full-scale cast speed

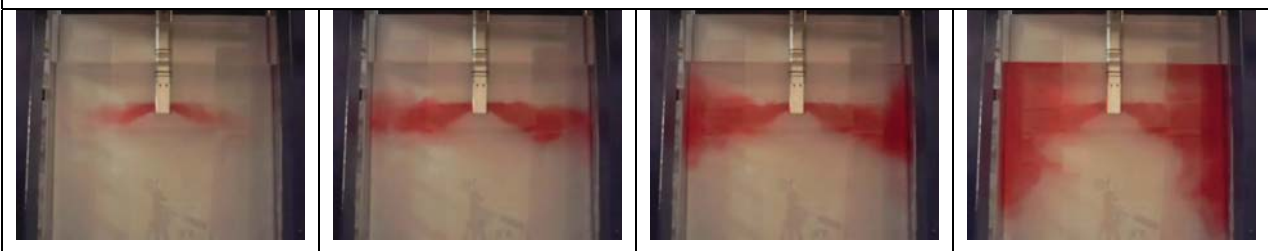


Figure F.6: Old SEN (1250mm width, 150mm submergence depth, 1.0 m/min full-scale cast speed) snapshots

New SEN, 1250 mm width, 150mm submergence depth, 1.0 m/min full-scale cast speed

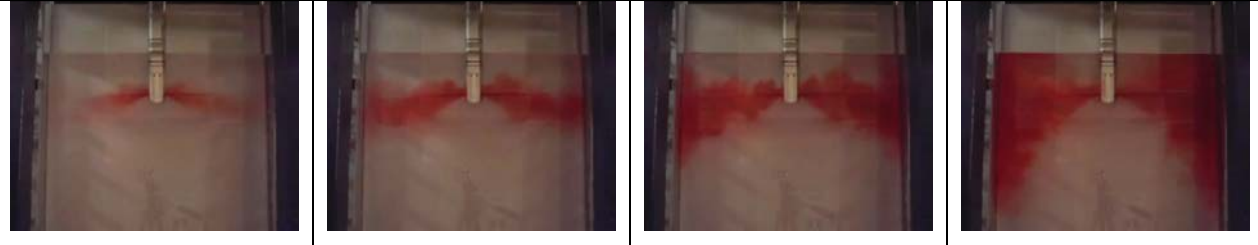


Figure F.7: New SEN (1250mm width, 150mm submergence depth, 1.0 m/min full-scale cast speed) snapshots

Old SEN, 1250 mm width, 80mm submergence depth, 1.0 m/min full-scale cast speed

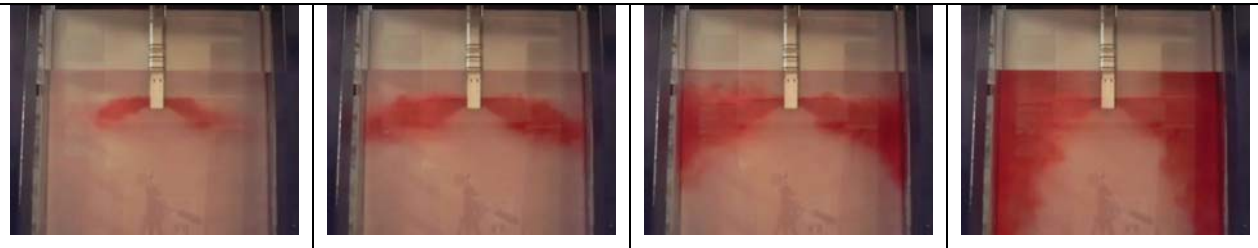


Figure F.8: Old SEN (1250mm width, 80mm submergence depth, 1.0 m/min full-scale cast speed) snapshots

New SEN, 1250 mm width, 80mm submergence depth, 1.0 m/min full-scale cast speed

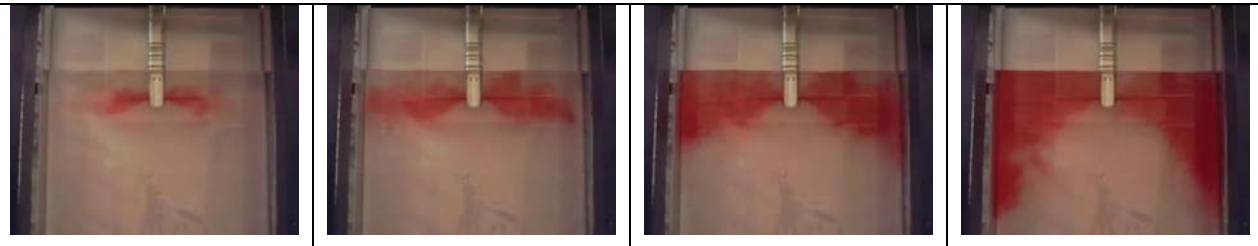


Figure F.9: New SEN (1250mm width, 80mm submergence depth, 1.0 m/min full-scale cast speed) snapshots

APPENDIX G

G. Columbus Stainless base case SEN design: drawings

G.1 Base case SEN design: general

Although the base case SEN design (also referred to as the Old SEN) is described in the main text, the basic parameters and description will be repeated for the sake of completeness.

Typical old SEN parameters:

- SEN total length: 1100 mm
- Shape: morphs from circular cross section (top) to a rectangular cross section (bottom)
- Design type: Bifurcated ports without a well
- Port height: 70 mm
- Port width: 45 mm
- Port radii: 35mm (all radii on ports)
- Port angle: 15 ° upwards
- Typical submergence depths: 80 mm – 200mm (defined from the top of the port to the meniscus surface)

G.2 Base case SEN: drawings (copyright)

Refer to Figure G.1 below for the drawings of the old SEN of Columbus Stainless, Middelburg, South Africa.

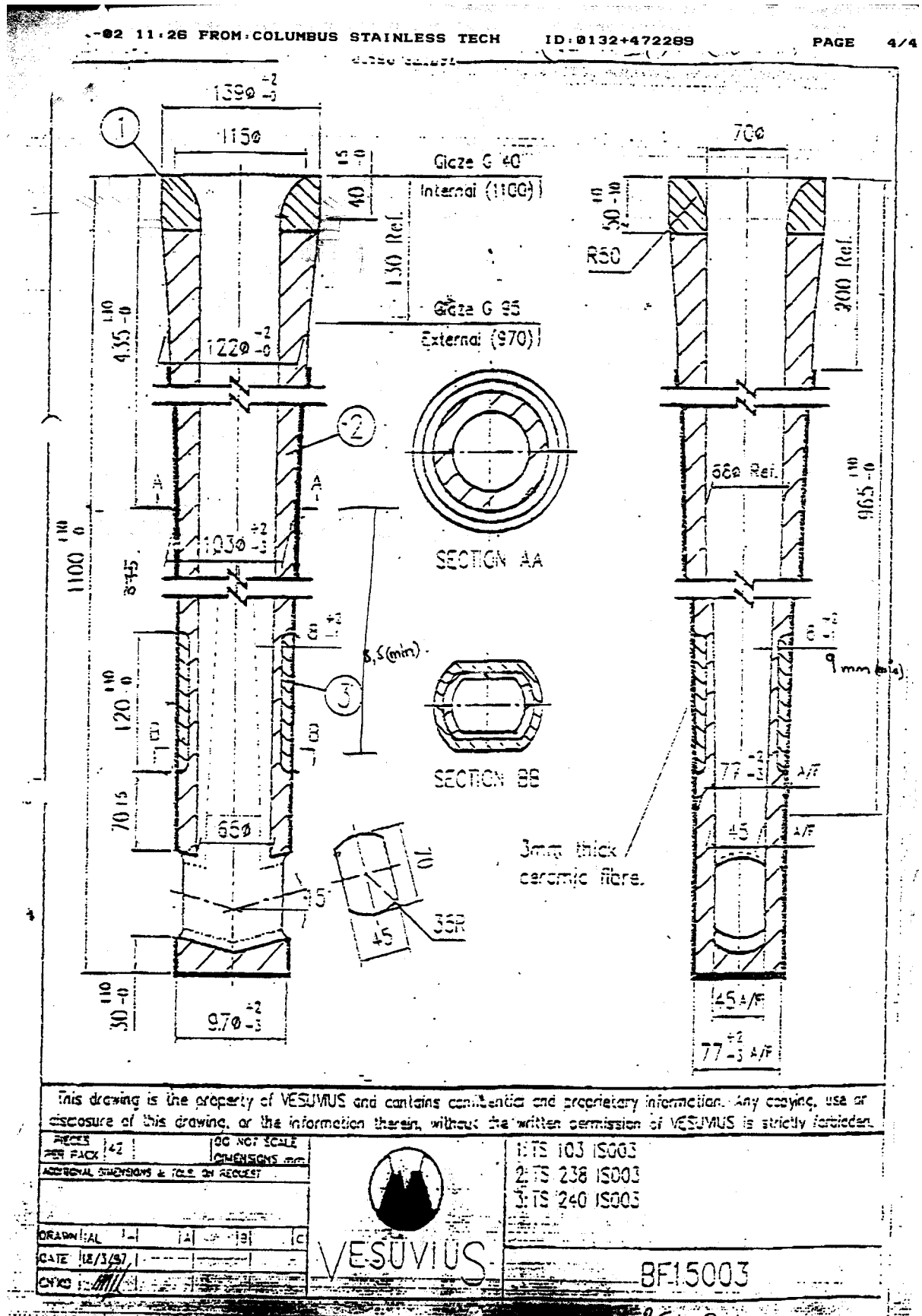


Figure G.1: Old SEN Columbus Stainless: Official Drawings (copyright Vesuvius)

APPENDIX H

H. Columbus Stainless new SEN design: drawings

H.1 New SEN design: general

As the new SEN design is mostly used for comparisons in an effort to optimise the CFD model for later optimisation, the details of this design will only be presented in this Appendix.

Columbus Stainless made use on this design type a few months after this study commenced with their old SEN design as the original base case. The main difference between the new SEN and the previous SEN (base case for Chapter 4) is that a well (40mm depth) is made provision for, at the cost of smaller port heights (only 60mm instead of 70mm). The angle of both bifurcated nozzle ports remain at an angle of 15° upwards.

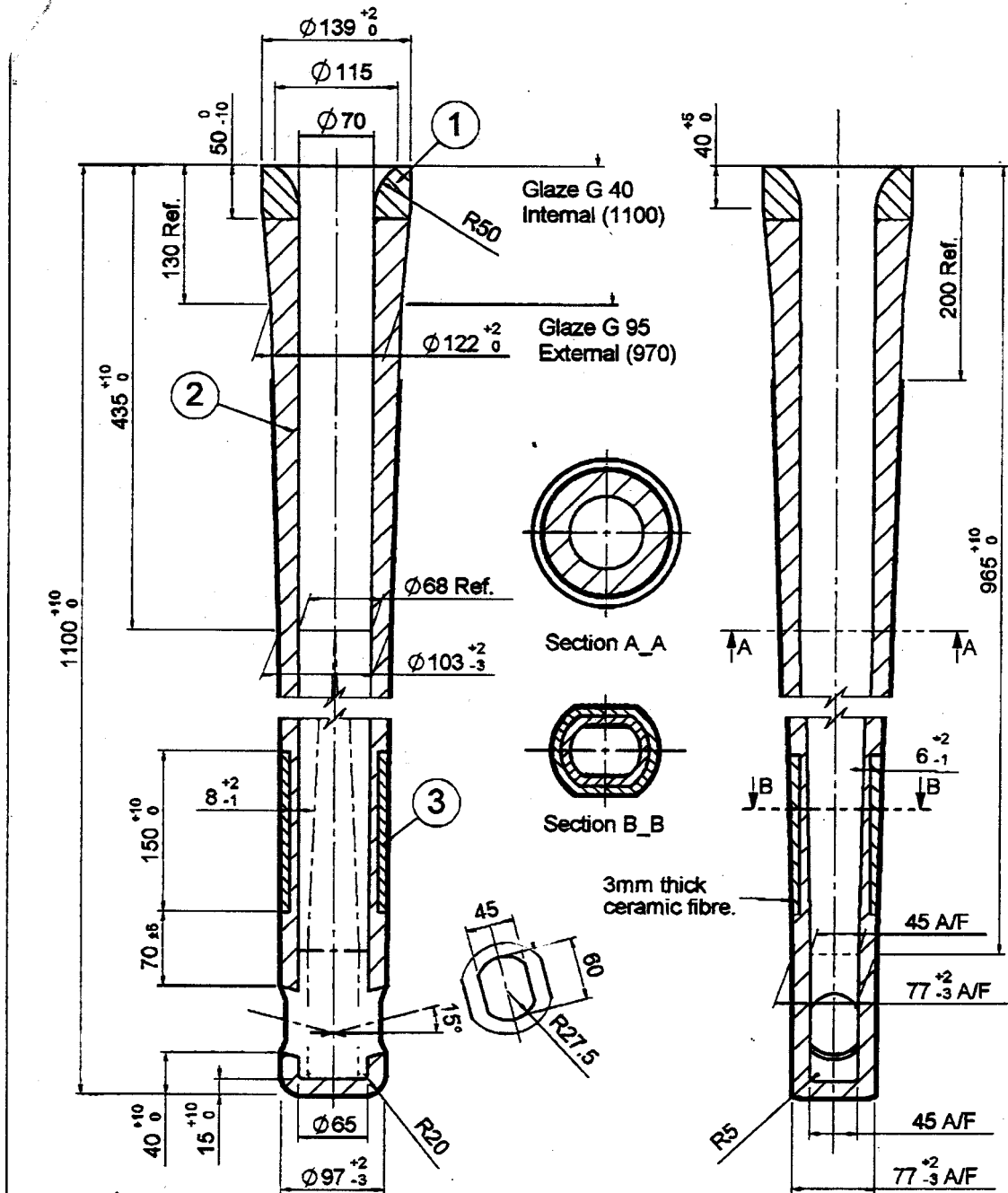
The rest of the SEN design is identical to the old SEN, as can be verified by comparing the drawings of the new design (Figure H.1 below) with that of the old base case SEN (Figure G.1 in [Appendix G](#)).

The effect of the perceived small changes (well added and port height reduced) made to the old SEN is quite extensive, as pointed out in the main text and as depicted in [Appendix F](#) (water model experiments). This fact collaborates with a main assumption that justifies this study: small, inexpensive changes on the SEN can influence the flow pattern in the mould and resultant desired steel quality. The challenge is to quantify these changes (to design variables) in an effort to find an optimum (or optima) design(s).

H.2 **Base case SEN: drawings (copyright)**

Refer to Figure H.1 below for the drawings of the new¹ SEN of Columbus Stainless, Middelburg, South Africa.

¹ This is the SEN currently (2003) in use at Columbus Stainless, Middelburg, South Africa.



This drawing is the property of VESUVIUS and contains confidential and proprietary information. Any copying, use or disclosure of this drawing, or the information therein, without permission of VESUVIUS is strictly forbidden.

Pieces per Pack	42	Do not scale	
DIMENSIONS mm			
Additional Dimensions and tolerances on request			
D/mm	IAL	-	A
Date	07/05/02		



VESUVIUS

- 1: TS 00103 IS003
- 2: TS 00238 IS003
- 3: TS 00371 IS003

BF26489

Figure H.1: New SEN Columbus Stainless: Official Drawings (copyright Vesuvius)

APPENDIX I

I. Comparison: meniscus boundary condition: Free surface vs. slip wall (zero-shear stress wall)

The comparison between the slip wall and free surface were conducted to ensure that the flow (of the steel or water) inside the mould is similar, irrespective of the type of boundary condition selected. The comparison in this Appendix is based on the base case (old SEN) and the new SEN.

The Volume of Fluid (VOF) method in FLUENT is used to evaluate a typical two-phase flow. The physical volume above the meniscus (or the free surface between the two phases) must be sufficiently large to ensure that a free atmosphere is simulated (refer to Figures I.1 and I.2)

The details of the comparisons are presented in Table I.1.

Table I.1: Details of comparison between the two boundary condition options (slip wall vs. free surface)

Figure I.	SEN design	Mould Width [mm]	Submergence depth (full-scale) [mm]	Q_{model}^1 (Fr-similarity) [m ³ /h]	V_{cast} (full-scale) [m/min]
1	Old	1575	200	1.72	1.0
2	New	1575	200	1.72	1.0

¹ Refer to Chapter 3 for derivation of [eq 3-7] used to calculate the flow rate of the model, satisfying Fr-similarity.

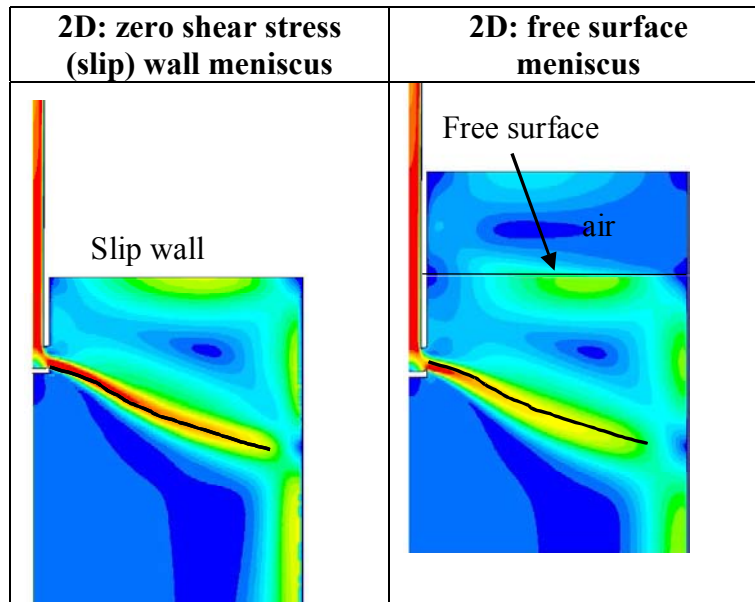


Figure I.1: 2D CFD-model meniscus boundary condition comparison: base case (**Old SEN**) (comparing velocity contours of magnitude)

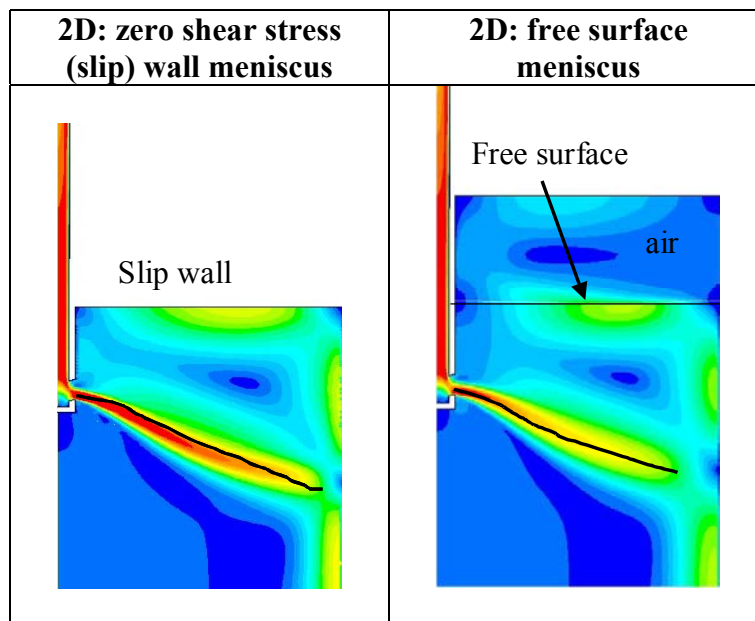


Figure I.2: CFD-model (2D) meniscus boundary condition comparison: base case (**New SEN**) (comparing velocity contours of magnitude)

Discussion:

As can be observed in the figures above, the difference between the flow patterns in the 2D CFD models using the different boundary conditions for the meniscus is remarkably negligible. The choice between a slip wall and free surface boundary condition is also assumed to have negligible influence on 3D CFD modelling.

The CFD models in both Figures I.1 and I.2 above are momentum-only models, and subsequently imitate the physical water model experiments (water as fluid, no temperature effects). When temperature effects have to be included in the CFD models (as have been later in Chapter 4 and throughout Chapter 5), a heat extraction flux has to be included in the boundary condition of the meniscus surface. Using a slip (or rather zero-shear stress) wall, a heat extraction heat flux can easily be added to this wall as a boundary condition. Currently, using the VOF-method, it is very difficult to obtain the same result, as a heat flux need to be specified on top of the air layer (refer to Figures I.1 and I.2). Subsequently, the exact heat flux over the free surface (interface between phase 1 and phase 2) cannot be determined exactly.

However, as mentioned in the main text, when meniscus behaviour becomes important for exact meniscus layer simulation, the free surface VOF-method necessarily needs to be employed.

Nevertheless, for the purposes of this study (including optimisation in Chapter 5), the meniscus boundary condition will be a zero-shear stress wall. The heat flux through the meniscus slip wall will be added when necessary (when plant conditions and circumstances are modelled using the energy equation in FLUENT).

APPENDIX J

J. GAMBIT script file (for automatic geometry and mesh rendering)

J.1 General

In order for one to later edit the GAMBIT script file, it is customary to make notes in the script file, which must obviously be ignored by the GAMBIT interpreter. Thus, all text in a line following a forward slash or “/”, are notes and will be ignored.

Exceptions and parameterisation:

The script file (below in section J.2) may seem excessively long for creating a mere 2D geometry and mesh.

The reason for this is that certain exceptions may occur whenever the port angle varies from positive to negative (for example):

- different equations might be necessary
- different reference points or vertices are necessary to compute next vertex positions

Categories in typical GAMBIT script file

The typical GAMBIT script file usually contains the following tasks in this specific order (exactly the same order in which a “manual” geometry and mesh would have been generated using GAMBIT’s GUI):

1. List all parameters (and dependent¹ variables)
2. Build model
 - 2.1 Create outline of geometry based on given parameters

¹ Dependent variables are variables that need to be defined as their values are determined by the chosen parameters or design variables.

- 2.2 Divide geometry into mesh-able areas and name areas (or volumes with a 3D model)
3. Mesh the geometry
4. Define and name all boundary surfaces

Refer to section J.2 on the following page for the GAMBIT script file used to generate 2D SEN and mould models (half models due to symmetry assumption).

J.2 GAMBIT script file

The script file was used to create the geometry and mesh for 2D half models, similar to Figure 5.1 (Chapter 5).

```

/ Journal File for GAMBIT 2.0.4 :paramsen2d2.jou - vanaf paramsen2d1.jou

/ Nuwe leer vir 2d parametrisering

/1 Spesifisering en Beskrywing van veranderlikes

/ 11 Parameters (wat verander kan word)

/ $x1 = hoek van SENpoort met horisontaal in grade
/ $x3 = wydte van gietstuk in mm
/ $x4 = hoogte van poort in die middelsnit van poort (LW vir eers reeds h2d) (loodreg
op poort)
/ $x6 = lengte van gietstuk in mm
/ $x7 = meniskusposisie tov bo-punt van die poort (dus ondergedompelde diepte) in mm
/ [$x7 = 120 mm vir base case]
/ $x8 = diepte van versinking (LW: indien x8 = 0, dan verskil program later...)
/ $x9 = radius van poort - LW word eers later in aanmerking geneem
/ $x20 = h3d (loodreg) in mm ($x4 of h2d word later... dan hiervanaf bereken)
/ $x21 = wydte van poort in mm ($x4 of h2d word later... dan hiervanaf bereken)

$x1 = 15
$x3 = 1575
/ $x4
$x6 = 3000
$x7 = 120
$x8 = 0

$x9 = 35
$x20 = 70
$x21 = 45

/ 12 Berekening van h2d of $x4
/ Laat $x40 die area wees onder sirel vanaf 0 tot halfwydte van die poort
/ $x41 = halfwydte
/ Laat $x42 die gem_hoogte wees
/ dan is hlaer = radius - hgem
/ en dus h2d = h3d - 2*hlaer
/ inisialiseer eers
$x40 = 0
$x41 = 0
$x42 = 0

$x41 = $x21/2
$x40 = (($x9*$x9)/2)*((DEG2RAD*(asin($x41/$x9))+($x41/($x9*$x9))*sqrt(($x9*$x9)-
($x41*$x41)))) - 0)
$x42 = $x40/($x41-0)
$x4 = $x20 - 2*($x9 - $x42)

/ 13 Veranderlikes om bewerkings te verrig (word in GAMBIT bereken)

/ $x2 = meniskusafstand (y) vanaf globale oorsprong (funksie van x1 en x4 en x8) -
word self bereken
/ $x5 = poortas afstand van onderkant van SEN af in mm (funksie van x1, x4 en x8) -
word self bereken
/ LW: indien $x8>0, is die poortas nie meer relevant nie: bereken direk dy(A1-A2) =
x5
/ $x10 = veranderlike gebruik om pt A1 te skep
/ $x11 = veranderlike gebruik om pt A2 te skep
/ $x12 = veranderlike gebruik om pt A3 te skep

```

```

/ $x13 = veranderlike gebruik om pt A4 te skep
/ $x14 = veranderlike gebruik om pt A5 te skep (as x8 > 0 )
/ $x15, 16 = veranderlike gebruik om E1 en E2 te bereken
/ $x30 = veranderlike gebruik om koördinate aan te dui en klein berekeninkies te
voltooi
/ $x50, 51, 52 = veranderlikes gebruik om F1, F3 en F4 te bereken

/ 13 Inisialiseer alle berekeningsveranderlikes [is dit nodig?]
$x10 = 0
$x11 = 0
$x12 = 0
$x13 = 0
$x14 = 0
$x15 = 0
$x16 = 0
$x30 = 0

/2 Begin van modelbou

/ 21 Vaste punte (irrelevant van veranderlikes)
vertex create "C1" coordinates 0 0 0
vertex create "C2" coordinates 0 395 0
vertex create "C3" coordinates 0 435 0
vertex create "C4" coordinates 55 435 0
vertex create "C5" coordinates 35 395 0
vertex create "C6" coordinates 34 0 0
vertex create "C7" coordinates 0 -530 0
vertex create "C8" coordinates 32.5 -530 0
vertex cmove "C5" multiple 1 offset 50 0 0
vertex modify "vertex.9" label "T1"
edge create "C45" center2points "T1" "C5" "C4" minarc arc
vertex delete "T1"
vertex create "C9" coordinates 0 -665 0
vertex create "C10" coordinates 48.5 -665 0
edge create "C34" straight "C3" "C4"
edge create "C23" straight "C3" "C2"
edge create "C12" straight "C1" "C2"
edge create "C56" straight "C5" "C6"
edge create "C68" straight "C6" "C8"
edge create "C78" straight "C8" "C7"
edge create "C17" straight "C1" "C7"
edge create "C16" straight "C1" "C6"
edge create "C25" straight "C2" "C5"

/ Van hier af sal die joernaalleer verskil
////////////////////////////////////
/ AFDELING 1
/ Geen insinking: dus $x8 = 0 - onthou else aan die einde en endif aan heel einde
IF COND ($x8 .EQ. 0)

/ 22 Skep van poortpunte A1 tot A4 en verbinding van pte

/ $x5 = poortas van onder af in mm - word vervolgens bereken
/ As hoek 0 is, maak effense positiewe hoek anders faal jou-leer
IF COND ($x1 .EQ. 0)
$x1 = 0.1
ENDIF

/ As hoek positief is,
IF COND ($x1 .GT. 0)
$x5 = 17.00446417 + (0.5*$x4)/(cos($x1))

/ As hoek negatief is
ELSE
$x5 = 17.00446417 + (0.5*$x4)/(cos($x1)) + 48.5*tan(-$x1)
ENDIF

$x10 = $x5 - (0.5*$x4)/(cos($x1))
vertex cmove "C9" multiple 1 offset 0 $x10 0

```

```

vertex modify "vertex.11" label "A1"
$x11 = 48.5*tan($x1)
vertex cmove "A1" multiple 1 offset 48.5 $x11 0
vertex modify "vertex.12" label "A2"

$x12 = $x4/(cos($x1))
vertex cmove "A2" multiple 1 offset 0 $x12 0
vertex modify "vertex.13" label "A3"

$x13 = 16*tan($x1)
vertex cmove "A3" multiple 1 offset -16 -$x13 0
vertex modify "vertex.14" label "A4"
/ LW: as x1 positief is, sal x13 positief wees: moet dus afgetrek word en vice versa

/verbind nou die punte
edge create "A1C7" straight "A1" "C7"
edge create "C8A4" straight "C8" "A4"
edge create "A4A3" straight "A4" "A3"
edge create "A3A2" straight "A3" "A2"
/ edge create "A2A1" straight "A2" "A1"
edge create "A2C10" straight "A2" "C10"
edge create "C10A9" straight "C10" "C9"

/ 23 Skep van punte B1 tot B4

/ Berekening van meniskushoogte tov oorsprong afhangend of die hoek x1 positief of
negatief is
IF COND ($x1 .GT. 0)
$x2 = 17.00446417 + $x4/cos($x1) + 48.5*tan($x1) + $x7 -665
ELSE
$x2 = 17.00446417 + $x4/cos($x1) + $x7 -665
ENDIF

vertex create "B1" coordinates 48.745265 $x2 0
$x30 = 0.5*$x3
vertex create "B2" coordinates $x30 $x2 0
vertex create "B3" coordinates $x30 -900 0
vertex create "B4" coordinates 0 -900 0

/ 24 Skep van punt D3
vertex create "D3" coordinates 0 -765 0

/ 25 Skep van punte E1 tot E4
/$x15 is die globale y-waarde van pt E1
$x15 = $x2 - 700
vertex create "E1" coordinates 0 $x15 0
vertex create "E2" coordinates $x30 $x15 0
$x16 = $x15 - ($x6 - 700)
vertex create "E3" coordinates $x30 $x16 0
vertex create "E4" coordinates 0 $x16 0

/ 26 Skep van punte F1 tot F4

vertex create "F1" coordinates $x30 -765 0
vertex create "F2" coordinates $x30 -665 0
/$x50 is x-afstand van pt A2,A3 na pt F3,F4
$x50 = $x30 - 48.5
vertex cmove "A2" multiple 1 offset $x50 0 0
vertex modify "vertex.28" label "F3"
vertex cmove "A3" multiple 1 offset $x50 0 0
vertex modify "vertex.29" label "F4"

/ 27 Skep pt G1 vir ekstra blok in SENpoortvlak
$x13 = 16*tan($x1)
vertex cmove "A2" multiple 1 offset -16 -$x13 0
vertex modify "vertex.30" label "G1"

/ 27 Verbind pte A, B D en E
edge create "A3B1" straight "A3" "B1"
edge create "B1B2" straight "B1" "B2"
edge create "B2F4" straight "B2" "F4"
edge create "A3F4" straight "A3" "F4"

```

```

edge create "F43" straight "F4" "F3"
edge create "A2F3" straight "A2" "F3"

edge create "F32" straight "F3" "F2"
edge create "C10F2" straight "C10" "F2"
edge create "F21" straight "F2" "F1"
edge create "D3F1" straight "D3" "F1"
edge create "F1B3" straight "F1" "B3"

edge create "B34" straight "B3" "B4"
edge create "B4D3" straight "B4" "D3"
edge create "D3C9" straight "D3" "C9"

edge create "B3E2" straight "B3" "E2"
edge create "B4E1" straight "B4" "E1"
edge create "E12" straight "E1" "E2"
edge create "E23" straight "E2" "E3"
edge create "E34" straight "E3" "E4"
edge create "E14" straight "E1" "E4"

edge create "A4G1" straight "A4" "G1"
edge create "A1G1" straight "A1" "G1"
edge create "G1A2" straight "G1" "A2"

/3 Skep van vlakke
face create "tuit" wireframe "C34" "C45" "C25" "C23"
face create "rgtskag" wireframe "C25" "C56" "C16" "C12"
face create "morfdeel" wireframe "C16" "C68" "C78" "C17"
face create "SENpoortLK" wireframe "C78" "C8A4" "A4G1" "A1G1" "A1C7"
face create "SENpoortRK" wireframe "A43" "A32" "G1A2" "A4G1"
face create "jetvoll1" wireframe "A3B1" "B12" "B2F4" "A3F4"
face create "jetvol2" wireframe "A3F4" "F43" "A2F3" "A32"
face create "jetvol3" wireframe "F32" "C10F2" "A2C10" "A2F3"
face create "gietstuk1" wireframe "C10F2" "F21" "D3F1" "D3C9" "C109"
face create "gietstuk2" wireframe "D3F1" "F1B3" "B34" "B4D3"
face create "gietstuk3" wireframe "B34" "B3E2" "E12" "B4E1"
face create "ondergietstuk" wireframe "E12" "E23" "E34" "E14"

/4 Meshing
solver select "FLUENT 5/6"

/ 41 Pas vorm-funksie toe op meshvol
sfunction create sourceedges "A32" startsize 4 growthrate 1.1 distance 150 \
  sizelimit 10 attachfaces "meshvol" fixed

/ 42 Mesh alles behalwe ondergietstuk in onderstaande spesifieke volgorde

face mesh "SENpoortRK" map size 5
/maak "A3F4" in size 15 inkremente
/maak "A3B1" "C10A2" en "D3C9" in size 5 inkremente
face mesh "jetvolume2" submap size 15
face mesh "jetvolume1" submap size 15
face mesh "jetvolume3" submap size 15
/maak "D3F1" in size 15 inkremente
face mesh "gietstuk2" submap size 15
face mesh "gietstuk1" submap size 15
face mesh "gietstuk3" submap size 15

face mesh "rgtskag" map size 5
face mesh "morfdeel" map size 5
face mesh "tuit" map size 5
face mesh "SENpoortLK" map size 5

/ 43 Mesh nou ondergietstuk met uitrekfunksie
edge picklink "E23"
edge mesh "E23" firstlength ratio1 15 size 25
edge picklink "E14"
edge mesh "E14" firstlength ratio1 15 size 25
face mesh "ondergietstuk" map size 15

```

```

/5 RVW vir FLUENT

physics create "SENinlaat" btype "VELOCITY_INLET" edge "C34"
physics create "gietstuk uitlaat" btype "PRESSURE_OUTLET" edge "E34"
physics create "SENmuur_buite" btype "WALL" edge "C45" "C56" "C68"
physics create "SENmuur_binne" btype "WALL" edge "A3B1" "A2C10" "C109"
physics create "SENpoortmuur_binne" btype "WALL" edge "C8A4" "A43" "G1A2" "A1G1"
physics create "gietstukmuur_nou" btype "WALL" edge "B2F4" "F43" "F32" "F21" "F1B3"
"B3E2"
physics create "ondermould_nou" btype "WALL" edge "E23"
physics create "simmetrie_nou" btype "SYMMETRY" edge "C23" "C12" \
"C17" "A1C7" "D3C9" "B4D3" "B4E1" "E14"
physics create "meniskusvlak" btype "WALL" edge "B12"
physics create "meshvolvlak1" btype "INTERIOR" edge "A3F4"
physics create "meshvolvlak2" btype "INTERIOR" edge "A2F3"
physics create "binnemould_vlak" btype "INTERIOR" edge "B34"
physics create "ondermould_vlak" btype "INTERIOR" edge "E12"
physics create "SENpoortuitlaat" btype "INTERIOR" edge "A32"
physics create "ondertuit_vlak" btype "INTERIOR" edge "C25"
physics create "onderrgtstkag_vlak" btype "INTERIOR" edge "C16"
physics create "ondermorfdeel_vlak" btype "INTERIOR" edge "C78"

////////////////////////////////////
////
/AFDELING 2
/ Insinking vind wel plaas: Dus $x8 > 0

/ Optimering randvoorwaardes
/ LW: As x1 > 0 deg; moet x8 > 32.5*tan(x1)
/     As x1 < 0 deg; moet x8 > 16*tan(-x1)

ELSE

/ 22 Skep van poortpunte A1 tot A6 en verbinding van pte

/ $x5 = dy van A1 na A2 in mm - word vervolgens bereken
/ As hoek 0 is, maak effense positiewe hoek anders faal jou-leer
IF COND ($x1 .EQ. 0)
$x1 = 0.1
ENDIF

$x5 = 15 + $x8 + 16*tan($x1)
vertex cmove "C9" multiple 1 offset 0 15 0
vertex modify "vertex.11" label "A1"
vertex cmove "C10" multiple 1 offset 0 $x5 0
vertex modify "vertex.12" label "A2"

$x12 = $x4/(cos($x1))
vertex cmove "A2" multiple 1 offset 0 $x12 0
vertex modify "vertex.13" label "A3"

$x13 = 16*tan($x1)
vertex cmove "A3" multiple 1 offset -16 -$x13 0
vertex modify "vertex.14" label "A4"
/ LW: as x1 positief is, sal x13 positief wees: moet dus afgetrek word en vice versa

vertex cmove "A1" multiple 1 offset 32.5 0 0
vertex modify "vertex.15" label "A5"
vertex cmove "A5" multiple 1 offset 0 $x8 0
vertex modify "vertex.16" label "A6"

/verbind nou die punte
edge create "A1C7" straight "A1" "C7"
edge create "C8A4" straight "C8" "A4"
edge create "A43" straight "A4" "A3"
edge create "A32" straight "A3" "A2"
edge create "A26" straight "A2" "A6"
edge create "A65" straight "A6" "A5"
edge create "A51" straight "A5" "A1"
edge create "A46" straight "A4" "A6"

edge create "A2C10" straight "A2" "C10"
edge create "C109" straight "C10" "C9"

```



```

/ 23 Skep van punte B1 tot B4

/ Berekening van meniskushoogte tov oorsprong ongeag of die hoek x1 positief of
negatief is
 $\$x2 = 15 + \$x8 + 16 * \tan(\$x1) + \$x4 / \cos(\$x1) + \$x7 - 665$ 

vertex create "B1" coordinates 48.745265  $\$x2$  0
 $\$x30 = 0.5 * \$x3$ 
vertex create "B2" coordinates  $\$x30$   $\$x2$  0
vertex create "B3" coordinates  $\$x30$  -900 0
vertex create "B4" coordinates 0 -900 0

/ 24 Skep van punte D3
vertex create "D3" coordinates 0 -765 0

/ 25 Skep van punte E1 tot E4
/  $\$x15$  is die globale y-waarde van pt E1
 $\$x15 = \$x2 - 700$ 
vertex create "E1" coordinates 0  $\$x15$  0
vertex create "E2" coordinates  $\$x30$   $\$x15$  0
 $\$x16 = \$x15 - (\$x6 - 700)$ 
vertex create "E3" coordinates  $\$x30$   $\$x16$  0
vertex create "E4" coordinates 0  $\$x16$  0

/ 26 Skep van punte F1 tot F4

vertex create "F1" coordinates  $\$x30$  -765 0
vertex create "F2" coordinates  $\$x30$  -665 0
/  $\$x50$  is x-afstand van pt A2,A3 na pt F3,F4
 $\$x50 = \$x30 - 48.5$ 
vertex cmove "A2" multiple 1 offset  $\$x50$  0 0
vertex modify "vertex.30" label "F3"
vertex cmove "A3" multiple 1 offset  $\$x50$  0 0
vertex modify "vertex.31" label "F4"

/ 27 Verbind pte A, B D en E

edge create "A3B1" straight "A3" "B1"
edge create "B12" straight "B1" "B2"
edge create "B2F4" straight "B2" "F4"
edge create "A3F4" straight "A3" "F4"
edge create "F43" straight "F4" "F3"
edge create "A2F3" straight "A2" "F3"

edge create "F32" straight "F3" "F2"
edge create "C10F2" straight "C10" "F2"
edge create "F21" straight "F2" "F1"
edge create "D3F1" straight "D3" "F1"
edge create "F1B3" straight "F1" "B3"

edge create "B34" straight "B3" "B4"
edge create "B4D3" straight "B4" "D3"
edge create "D3C9" straight "D3" "C9"

edge create "B3E2" straight "B3" "E2"
edge create "B4E1" straight "B4" "E1"
edge create "E12" straight "E1" "E2"
edge create "E23" straight "E2" "E3"
edge create "E34" straight "E3" "E4"
edge create "E14" straight "E1" "E4"

/3 Skep van vlakke

face create "tuit" wireframe "C34" "C45" "C25" "C23"
face create "rgtskag" wireframe "C25" "C56" "C16" "C12"
face create "morfdeel" wireframe "C16" "C68" "C78" "C17"
face create "SENpoortLK" wireframe "C78" "C8A4" "A46" "A65" "A51" "A1C7"
face create "SENpoortRK" wireframe "A43" "A32" "A26" "A46"
face create "jetvoll" wireframe "A3B1" "B12" "B2F4" "A3F4"

```

```

face create "jetvol2" wireframe "A3F4" "F43" "A2F3" "A32"
face create "jetvol3" wireframe "F32" "C10F2" "A2C10" "A2F3"
face create "gietstuk1" wireframe "C10F2" "F21" "D3F1" "D3C9" "C109"
face create "gietstuk2" wireframe "D3F1" "F1B3" "B34" "B4D3"
face create "gietstuk3" wireframe "B34" "B3E2" "E12" "B4E1"
face create "ondergietstuk" wireframe "E12" "E23" "E34" "E14"

/4 Meshing
solver select "FLUENT 5/6"

face mesh "SENpoortRK" map size 5
/maak "A3F4" in size 15 inkremente
/maak "A3B1" "C10A2" en "D3C9" in size 5 inkremente
face mesh "jetvolume2" submap size 15
face mesh "jetvolume1" submap size 15
face mesh "jetvolume3" submap size 15
/maak "D3F1" in size 15 inkremente
face mesh "gietstuk2" submap size 15
face mesh "gietstuk1" submap size 15
face mesh "gietstuk3" submap size 15

face mesh "rgtskag" map size 5
face mesh "morfdeel" map size 5
face mesh "tuit" map size 5
face mesh "SENpoortLK" map size 5

/ 43 Mesh nou ondergietstuk met uitrekfunksie
edge picklink "E23"
edge mesh "E23" firstlength ratio1 15 size 25
edge modify "E41" backward
edge picklink "E41"
edge mesh "E41" firstlength ratio1 15 size 25
face mesh "ondergietstuk" map size 15

/5 RVW vir FLUENT
physics create "SENinlaat" btype "VELOCITY_INLET" edge "C34"
physics create "gietstuk_uitlaat" btype "PRESSURE_OUTLET" edge "E34"
physics create "SENmuur_buite" btype "WALL" edge "C45" "C56" "C68"
physics create "SENmuur_binne" btype "WALL" edge "A3B1" "A2C10" "C109"
physics create "SENpoortmuur_binne" btype "WALL" edge "C8A4" "A43" "A26" "A65" "A51"
physics create "gietstukmuur_nou" btype "WALL" edge "B23" "B3E2"
physics create "ondermould_nou" btype "WALL" edge "E23"
physics create "simmetrie_nou" btype "SYMMETRY" edge "C23" "C12" \
"C17" "A1C7" "D3C9" "B4D3" "B4E1" "E41"
physics create "meniskusvlak" btype "WALL" edge "B1D1" "D1B2"
physics create "meshvolvlak1" btype "INTERIOR" edge "D12"
physics create "meshvolvlak2" btype "INTERIOR" edge "D23"
physics create "binnemould_vlak" btype "INTERIOR" edge "B34"
physics create "ondermould_vlak" btype "INTERIOR" edge "E12"
physics create "SENpoortuitlaat" btype "INTERIOR" edge "A32"
physics create "ondertuit_vlak" btype "INTERIOR" edge "C25"
physics create "onderrgtskag_vlak" btype "INTERIOR" edge "C16"
physics create "ondermorfdeel_vlak" btype "INTERIOR" edge "C78"

ENDIF
/ einde van groot IF-stelling, nl die x8 > 0 of x8 = 0

```

APPENDIX K

K. FLUENT script file (for set-up and run)

K.1 General

Unlike the GAMBIT script files, the FLUENT commands are more explanatory; consequently less notes need to be made by the user. However, notes can be made by inserting an exclamation mark or “!” in the beginning of the line – the line will be ignored.

As explained in Chapter 5, the Optimiser (LS-OPT) acts as coordinator for the optimisation process. Consequently, all values indicated between double greater than – smaller than signs (“<<value>>”) are controlled by LS-OPT. The first example in the FLUENT script file in section K.2, is <<inlaatsnelheid>>, which is the inlet velocity specified by LS-OPT, as the inlet velocity is computed from the cast speed in the LS-OPT com-file (refer to [Appendix L](#)).

Tasks to be performed by typical FLUENT script file:

The FLUENT script file is used to perform the following tasks (in that specific order):

1. Set-up

- Import mesh file from GAMBIT
- Test mesh file for integrity
- Define models
 - energy model on/off
 - turbulence model and accompanying settings
- Define materials and material properties
- Define operating conditions
- Define all boundary conditions (and insert values)
 - Inlet: velocity inlet

- Meniscus: zero shear stress wall
 - Outlet: pressure outlet
 - Mould walls
 - Symmetry faces
 - Define and set-up monitors
 - E.g.: Maximum velocity magnitude on meniscus: record for each iteration. Specify files to write measurements to, etc.
 - Initialise solution
 - Ensure correct discretisation settings for momentum, pressure and energy
2. Run (solution procedure)
- Set residual monitors and convergence criteria
 - Ensure discretisation schemes for pressure, momentum and turbulence model (k and ε in this case) is correct
 - Run procedure:
 - Set number of iterations
 - After each set of iterations, apply grid adaption to eradicate mass imbalances and ensure correct y^+ settings (refer to Chapter 4, section 4.4.3, for details)
 - Switch from first order discretisation to second order when sufficient initial convergence has been achieved
 - Adjust under- and over-relaxation factors according to predetermined solution procedure

Refer to section K.2 on the following page for the FLUENT script file, which performs the functions described above.

K.2 FLUENT script file

```

!echo Gestadigde toestand: Opstelling - slegs momentum met moving walls: weergawe
2002-12-05
!echo LW Wees in regte directory: LW: vir pressure outlet, nie outflow:
!echo LW vir LSOPT met impakpt-grens asook turb_meniskus uitvoer en k_e_meniskus
uitvoer vir check
!echo Modifikasies Ken Craig
!echo Sit energievergelyking by met temperatuurrandwaardes en meniskus temp en
snelheid monitor
!echo Verhoog iterasies vir konvergensie van maks TKE
!echo Skryf meniskus temperatuur uit vir onttrekking van minimum waarde deur cat
!echo Skryf meniskus snelheid uit vir onttrekking van maksimum, negatief, waarde deur
cat
file/read-case
2dsen_mesh.msh
!echo 1 Grid
grid/check
grid/scale 0.001 0.001
define/models/energy yes no no no yes
define/units temperature c
!echo 2 Definieer modelle
define/models/viscous/ke-realizable yes
!echo 3 Definieer materiaal
define/materials/copy/fluid water-liquid
define/materials/change-create water-liquid steel yes constant 6975 yes constant 817.3
yes constant 30 yes constant 0.0064 yes 55.8 no no no yes
define/boundary-conditions/fluid fluid yes steel no no yes 0 0 no no no
!echo 4 Definieer bedryfstoestande
define/operating-conditions/gravity yes 0 -9.81
!echo 5 Definieer RVW - onthou simmetrie bly dieselfde
!echo Fluent version 6.1 needs backflow direction specification method
define/boundary-conditions/velocity-inlet seninlaat no no yes yes no
<<inlaatsnelheid>> no <<inlaattertemperatuur>> no no no yes 10 0.115
define/boundary-conditions/pressure-outlet gietstuk_uitlaat no 0 no
<<uitlaattertemperatuur>> no yes no no no yes 10 <<Dhidroulies>>
define/boundary-conditions/wall meniskusvlak 0 no 0 no yes heat-flux no
<<hittevloedopmeniskus>> no yes shear-bc-spec-shear 0 0.5 no 0 no 0
define/boundary-conditions/wall ondermould_nou 0 no 0 no yes temperature no
<<wandtemperatuur>> yes motion-bc-moving no no <<SIGietspoed>> 0 -1 no 0 0.5
define/boundary-conditions/wall gietstukmuur_nou 0 no 0 no yes temperature no
<<wandtemperatuur>> yes motion-bc-moving no no <<SIGietspoed>> 0 -1 no 0 0.5
define/boundary-conditions/wall senpoortmuur_binne 0 no 0 no no no 0 no 0 0.5
define/boundary-conditions/wall senmuur_buite 0 no 0 no no no 0 no 0 0.5
define/boundary-conditions/wall senmuur_binne 0 no 0 no no no 0 no 0 0.5
!echo 5b Verander temperatuur eenhede terug na K sodat temp monitor werk
define/units temperature k
!echo 6 Monitering
solve/monitors/residual plot yes print yes check-convergence yes yes yes yes yes q
q q
solve/monitors/surface/set-monitor ypluskant y-plus gietstukmuur_nou yes 1 yes yes
ypluskant.out "Vertex Average"
solve/monitors/surface/set-monitor max_ke_men turb-kinetic-energy meniskusvlak yes 2
yes yes turb_ke_men.out "Facet Maximum"
!echo 6a Sit minimum temperatuur monitor in
solve/monitors/surface/set-monitor min_temp_men temperature meniskusvlak yes 3 yes yes
tempmin_men.out "Facet Minimum"
!echo 6b Sit maksimum snelheids monitor in
solve/monitors/surface/set-monitor max_vel_men velocity-magnitude meniskusvlak

yes 4 yes yes velmax_men.out "Facet Maximum"
!echo 7 Inisialiseer
solve/initialize/compute-defaults/all-zones
solve/initialize/initialize-flow
!echo 8 Leer-hantering
file/auto-save/case-frequency 2000
file/auto-save/data-frequency 2000
file/auto-save/root-name 2dsentoets.gz
!echo 9 Kry druk d-s reg, nl PRESTO!
solve/set/ds/p 14
!echo 10 Konvergensie metode volg nou

!echo Gestadigde toestand: Slegs momentum - Konvergensiemetodiek: weergawe 2002-10-26
!echo 2D -geval

```

```

!echo 1st Order: LW: Probeer eers 1ste orde konvergeer
!echo 3 Stel kgensie kontinuïteit vir 5ordes 0.00001
solve/monitors/residual/convergence-crit 0.00001 0.001 0.001 0.000001 0.001 0.001
!echo 1 Itereer
solve/iter 500
!echo 5 2de Orde en p=PRESTO!
solve/set/ds/p 14
solve/set/ds/mom 1
solve/set/ds/k 1
solve/set/ds/e 1
solve/set/ds/temperature 1
!echo 6 Itereer
solve/iter 1500
!echo 7 Aanpas y+ en mi
adapt/aty+ 50 200 0 0 yes
adapt/miir no mass-imbalance -0.00001 0.00001
!echo adapt only in jet region y=-1m
adapt/mark-inout-rectangle yes no -100 100 -1 100
adapt/change-register

adapt/combine-register 0 1
adapt/atr

0 0 yes
!echo 8 Itereer
solve/iter 1000
!echo 9 Relax mom=0.4, k,e=0.7
solve/set/ur/mom 0.4
solve/set/ur/k 0.7
solve/set/ur/e 0.7
!echo 10 Itereer
solve/iter 2000
!echo 13 Save einde
file/write-c-d einde_run_2dsen_temp.gz
!echo 14 Skryf uit fluent_export_men_TKE.txt
file/export/ascii fluent_export_men_TKE.txt meniskusvlak

no yes turb-kinetic-energy q no

q
!echo 14a Skryf uit fluent_export_men_temp.txt
file/export/ascii fluent_export_men_temp.txt meniskusvlak

no yes temperature q yes

q
!echo 14b Skryf ui fluent_export_men_velmag.txt
file/export/ascii fluent_export_men_velmag.txt meniskusvlak

no yes velocity-magnitude q no q q
!echo 14c Skryf uit impakpt.txt
file/export/ascii impakpt.txt gietstukmuur_nou

no yes y-coordinate wall-shear q yes

q exit yes

```

APPENDIX L

L. LS-OPT com-file (for coordinating design optimisation process)

L.1 General

The function of the LS-OPT com-file is explained in detail in Chapter 5, section 5.1.

Briefly, the com-file contains all information necessary for the entire optimisation process, including design variables, dependent variables, objective and constraint functions, as well as information to edit the GAMBIT and FLUENT script files (examples of these in [Appendices J](#) and [K](#) respectively) for automated optimisation.

Tasks of the LS-OPT script file:

The LS-OPT script file coordinates the optimisation process, and this function is best described using a diagram. The diagram from Chapter 5 section 5.1 is repeated here for the sake of completeness:

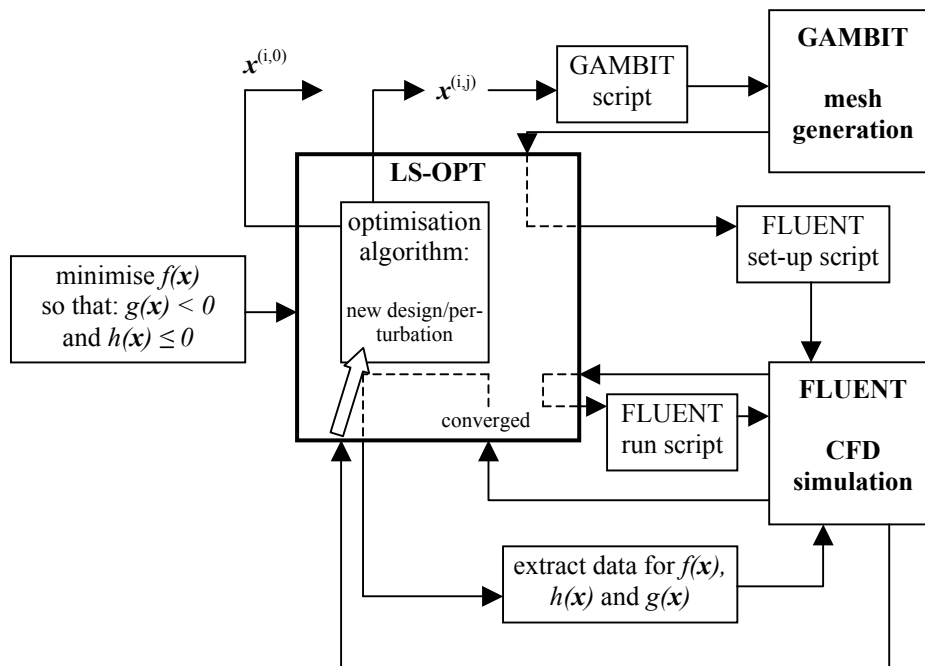


Figure L.1: Diagram depicting the tasks (including coordinating tasks) performed by LS-OPT during the design optimisation process

Refer to section L.2 for the LS-OPT com-file, which was used in the 2D design optimisation exercise presented in Chapter 5, section 5.5.

L.2 LS-OPT com-file

```
"2D SEN optimering"
Author "Gideon Jacobus de Wet"
$ Created on Mon Nov 11 12:36:43 2002
solvers 1
responses 2
$
$ NO HISTORIES ARE DEFINED
$
$
$ DESIGN VARIABLES
$
variables 4
Variable 'hoek' 15
  Lower bound variable 'hoek' -25
  Upper bound variable 'hoek' 25
Variable 'onderdompeling' 120
  Lower bound variable 'onderdompeling' 50
  Upper bound variable 'onderdompeling' 250
Variable 'versinkingsdiepte' 0.1
  Lower bound variable 'versinkingsdiepte' 0.1
  Upper bound variable 'versinkingsdiepte' 50
Variable 'poorthoogte3D' 70
  Lower bound variable 'poorthoogte3D' 30
  Upper bound variable 'poorthoogte3D' 80
$
$ CONSTANTS
$
```


APPENDIX M

M. GAMBIT script file for 3D Old SEN design (for automatic geometry and mesh rendering)

M.1 General

In order for one to later edit the GAMBIT script file, it is customary to make notes in the script file, which must obviously be ignored by the GAMBIT interpreter. Thus, all text in a line following a forward slash or “/”, are notes and will be ignored.

Exceptions and parameterisation:

The script file (below in section M.2) may seem excessively long for creating a 3D geometry and mesh of a SEN and mould.

The reason for this is that certain exceptions may occur whenever the port angle vary from positive to negative (for example):

- different equations might be necessary
- different reference points are necessary to compute next positions

Categories in typical GAMBIT script file

The typical GAMBIT script file usually contains the following tasks in this specific order (exactly the same order in which a “manual” geometry and mesh would have been performed using GAMBIT’s GUI):

1. List all parameters (and dependent¹ variables)
2. Build model
 - 2.1 Create outline of geometry based on given parameters
 - 2.2 Divide geometry into mesh-able areas and name areas (or volumes with a 3D model)

¹ Dependent variables are variables that need to be defined as their values are determined by the chosen parameters or design variables.

3. Mesh the geometry
4. Define and name all boundary surfaces

Refer to section M.2 on the following page for the GAMBIT script file used to generate 3D SEN (of the old type without a well) and mould models (quarter model due to assumption of symmetry). As mentioned in the main text, this GAMBIT script file (also known as a journal file) firstly creates a full model using elementary volumes, after which it is divided into quarters. Only the one quarter is kept to be exported as the mesh file for FLUENT.

M.2 GAMBIT journal file for 3D SEN and mould (Old SEN design)

```

/ Journal File for GAMBIT 2.0.4 :meiparamsen3.jou
/ Weergawe 2002-05-09, 21:30

/ Verbetering op vorige teks-leer, nl aprilparamsen2.jou , en ...
/ Journal File for GAMBIT 1.3.2: senkwartjetvolvfyfyn.jou

/ Hierdie jou-leer maak ekstra volume om gietstuk-RVW in ag te kan neem

/ 1 Spesifisering van veranderlikes
/ $x1 = hoek van SENpoort met horisontaal in grade
/ $x2 = meniskusafstand vanaf onderpunt van SEN (funksie van x1 en x4) - word self
bereken
/ $x3 = wydte van gietstuk in mm
/ $x4 = afstand waarmee poort vergroot word in mm
/ $x5 = poortas afstand van onderkant van SEN af in mm (funksie van x1) - word self
bereken
/ $x6 = lengte van gietstuk in mm
/ $x7 = afwyking van die normale meniskusposisie (dus ondergedompelde diepte) in mm
/      [$x7 > 0 : dieper; daarteenoor as $x7 < 0 : vlakker]
$x1 = 15
$x3 = 1575
$x4 = 0
$x6 = 3000
$x7 = 0

/ 2 Begin van modelbou
volume create height 395 radius1 34 radius3 35 offset 0 0 197.5 zaxis frustum
vertex create coordinates 0 0 305
coordinate create cartesian oldsystem "c_sys.1" offset 0 0 305 axis1 "x" \
  angle1 0 axis2 "y" angle2 0 axis3 "z" angle3 0 rotation
coordinate activate "c_sys.1"
volume create height 305 radius1 51.5 radius3 61 offset 0 0 152.5 zaxis frustum
coordinate activate "c_sys.2"
volume create height 90 radius1 61 radius3 69.5 offset 0 0 45 zaxis frustum
coordinate create cartesian oldsystem "c_sys.2" offset 0 0 90 axis1 "x" \
  angle1 0 axis2 "y" angle2 0 axis3 "z" angle3 0 rotation
vertex create coordinates 85 0 0
vertex create coordinates 69.5 0 40
vertex create coordinates 0 0 40
edge create radius 50 startangle -90 endangle 0 center "vertex.8" zxplane arc
edge create straight "vertex.10" "vertex.9"
edge split "edge.7" parameter 0.590333 connected
edge delete "edge.9" "edge.8" lowertopology
vertex create coordinates 69.5 0 40
edge create straight "vertex.14" "vertex.13"
edge create straight "vertex.14" "vertex.6"
edge create straight "vertex.6" "vertex.1"
face create wireframe "edge.7" "edge.8" "edge.9" "edge.10" real
vertex delete "vertex.8"
volume create revolve "face.10" dangle 360 vector 0 0 1 origin 0 0 0 draft 0 \
  extended
coordinate activate "c_sys.1"
volume create height 530 radius1 32.5 radius3 34 offset 0 0 -265 zaxis frustum
volume create height 530 radius1 48.2 radius3 51.5 offset 0 0 -265 zaxis frustum
volume create height 530 sides 4 radius1 31.81980515 radius2 70 radius3 \
  48.08326112 offset 0 0 -265 zaxis pyramid
volume intersect volumes "volume.7" "volume.5"
volume create height 530 sides 4 radius1 54.44722215 radius2 85 radius3 \
  72.83199846 offset 0 0 -265 zaxis pyramid
volume intersect volumes "volume.8" "volume.6"
/ File closed at Mon Nov 12 11:48:36 2001, 9.47 cpu second(s), 3141768 maximum memory.
coordinate delete "c_sys.3" "c_sys.2"
vertex delete "vertex.3"
volume create translate "face.39" vector 0 0 -135
volume create translate "face.29" vector 0 0 -70
coordinate create cartesian oldsystem "c_sys.1" offset 0 0 -665 axis1 "x" \
  angle1 0 axis2 "y" angle2 0 axis3 "z" angle3 0 rotation

////////////////////////////////////
/ Hoek word hier verander
/ $x5 = poortas (voor verlenging) van onder af in mm - word vervolgens bereken

```

```

/ As hoek 0 is, maak effense positiewe hoek anders faal jou-leer
IF COND ($x1 .EQ. 0)
$x1 = 0.1
ENDIF

/ As hoek positief is, gebruik eerste vergelyking; andersins tweede een
IF COND ($x1 .GT. 0)
$x5 = 17.00446417 + 35/(cos($x1))
/ As hoek negatief is
ELSE
$x5 = 17.00446417 + 35/(cos($x1)) + 48.5*tan(-$x1)
ENDIF

coordinate create cartesian oldsystem "c_sys.2" offset 0 0 $x5 \
  axis1 "x" angle1 $x1 axis2 "y" angle2 0 axis3 "z" angle3 0 rotation
////////////////////////////////////

volume create height 100 radius1 35 radius3 35 offset 0 50 0 yaxis frustum
volume create height 100 sides 4 radius1 70 radius2 31.81980515 radius3 70 \
  offset 0 50 0 yaxis pyramid
volume intersect volumes "volume.12" "volume.11"
volume create translate "face.62" vector 0 -30 -4.82965e-11
volume unite volumes "volume.12" "volume.13"
coordinate create cartesian oldsystem "c_sys.3" offset 0 -40 0 axis1 "x" \
  angle1 0 axis2 "y" angle2 0 axis3 "z" angle3 0 rotation
volume create width 100 depth 150 height 100 offset 50 75 -50 brick
volume create width 100 depth 150 height 100 offset -50 75 -50 brick
volume unite volumes "volume.14" "volume.13"
volume intersect volumes "volume.14" "volume.12" keeporiginals
volume delete "volume.14" lowertopology
volume subtract "volume.12" volumes "volume.15" keeptool

////////////////////////////////////
/ Poort word hier vergroot

/ As poort met 0 vergroot word, maak dit 0.1 anders faal jou-leer
IF COND ($x4 .EQ. 0)
$x4 = 0.1
ENDIF

volume move "volume.12" offset 0 0 $x4
volume create translate "face.92" vector 0 7.451e-12 $x4
////////////////////////////////////

volume unite volumes "volume.12" "volume.16" "volume.15"
coordinate activate "c_sys.2"
volume create width 100 depth 100 height 200 offset -50 -50 100 brick
volume create width 100 depth 100 height 200 offset 50 -50 100 brick
volume unite volumes "volume.13" "volume.14"
volume subtract "volume.12" volumes "volume.13"
volume copy "volume.12" to "volume.13"
volume reflect "volume.13" vector 0 1 0 origin 0 0 0
volume unite volumes "volume.12" "volume.13"
volume intersect volumes "volume.12" "volume.9" keeporiginals
volume unite volumes "volume.13" "volume.10"
volume delete "volume.12" lowertopology
volume subtract "volume.9" volumes "volume.13" keeptool
coordinate delete "c_sys.3" "c_sys.4"
face create wireframe "edge.12" real
volume create stitch "face.148" "face.11" "face.1" real
volume create stitch "face.1" "face.3" "face.2" real

////////////////////////////////////
/ $x2 = meniskus z-posisie t.o.v. onderkant van SEN in mm
/ $x3 = wydte van gietstuk
/ Berekening van meniskushoogte verskil afhangend of die hoek x1 positief of negatief
is

IF COND ($x1 .GT. 0)
$x2 = 17.00446417 + 70/cos($x1) + $x4/cos($x1) + 48.5*tan($x1) + 120 + $x7
ELSE
$x2 = 17.00446417 + 70/cos($x1) + $x4/cos($x1) + 120 +$x7
ENDIF

coordinate create "meniskusas" cartesian oldsystem "c_sys.2" offset 0 0 \
  $x2 axis1 "x" angle1 0 axis2 "y" angle2 0 axis3 "z" angle3 0 rotation

```

```

face create "meniskus" width 200 height $x3 xyplane rectangle
////////////////////////////////////

/ lengte van gietstuk hier
volume create "gietstuk" translate "meniskus" vector 0 0 -$x6
////////////////////////////////////

volume subtract "volume.3" volumes "volume.1" keeptool
volume subtract "volume.2" volumes "volume.21" keeptool
volume intersect volumes "gietstuk" "volume.15" keeporiginals
volume subtract "volume.22" volumes "volume.14" keeptool
volume delete "volume.19" "volume.3" "volume.2" "volume.15" lowertopology

/ maak nou 'n kwartmodel
volume create "bo" width 110 depth 800 height 1110 offset 55 400 555 brick
volume create "onder" width 110 depth 800 height 4500 offset 55 400 -2250 brick
volume unite volumes "onder" "bo"

volume intersect volumes "onder" "volume.20" keeporiginals
volume intersect volumes "onder" "volume.21" keeporiginals
volume intersect volumes "onder" "volume.14" keeporiginals
volume intersect volumes "onder" "volume.22" keeporiginals
volume intersect volumes "onder" "volume.9" keeporiginals
volume intersect volumes "onder" "volume.13" keeporiginals
volume intersect volumes "onder" "gietstuk" keeporiginals
volume delete "onder" "volume.20" "volume.21" "volume.14" "volume.22" \
"volume.9" "volume.13" lowertopology
volume delete "gietstuk" lowertopology
volume subtract "volume.31" volumes "volume.28" "volume.27" "volume.29" \
"volume.30" keeptool
volume delete "volume.31"
face subtract "face.335" faces "face.296" keeptool
volume create stitch "face.305" "face.316" "face.351" "face.352" "face.310" \
"face.315" "face.246" "face.245" "face.338" "face.335" "face.296" \
"face.275" real
volume modify "volume.25" label "tuit"
volume modify "volume.26" label "rgtskag"
volume modify "volume.27" label "morfdeel"
volume modify "volume.30" label "SENpoort"
volume modify "volume.31" label "gietstuk"
volume delete "volume.28" "volume.29" lowertopology

/ heg los vlakke aan mekaar
face connect "face.201" "face.215" real
face connect "face.232" "face.218" real
face connect "face.230" "face.299" real
/ einde van model

/3 Aanpassings vir jetvolume voor meshing begin
coordinate create "jetvolas" cartesian oldsystem "meniskus" offset 0 0 -450 \
axis1 "x" angle1 0 axis2 "y" angle2 0 axis3 "z" angle3 0 rotation
volume create "tydelikonder" width 250 depth 1000 height 4000 offset 125 500 \
-2000 brick
volume intersect volumes "gietstuk" "tydelikonder" keeporiginals
volume subtract "gietstuk" volumes "volume.33" keeptool
volume delete "tydelikonder" lowertopology
volume modify "volume.33" label "gietstukonder"
volume modify "gietstuk" label "jetvolume"
face connect "face.380" "face.377" real

/32 Addisionele aanpassings vir ekstra volume vir maasvereenvoudiging
coordinate activate "c_sys.2"
coordinate create "meshvolas" cartesian oldsystem "c_sys.2" offset 0 0 -100 \
axis1 "x" angle1 0 axis2 "y" angle2 0 axis3 "z" angle3 0 rotation
volume create "meshvol" width 110 depth 180 height 450 offset 55 90 225 brick
volume intersect volumes "jetvolume" "meshvol" keeporiginals
volume delete "meshvol" lowertopology
volume subtract "jetvolume" volumes "volume.35" keeptool
volume modify "volume.35" label "meshvol"
face delete "face.321" "face.322" "face.339"
face connect "face.410" "face.416" real
face connect "face.412" "face.415" real
face connect "face.399" "face.296" real

/33 Addisionele aanpassings vir ekstra volume vir gietstuk-RVW

```

```

volume create "gietstukvol" translate "face.380" vector 0 0 -250
volume subtract "gietstukonder" volumes "gietstukvol" keeptool
volume modify "volume.37" label "gietstukvol"
volume modify "volume.38" label "jetvolume"

/4 Begin met Meshing
solver select "FLUENT 5/6"

/ 41 Mesh gietstuk
/voorbereiding en mesh vir jetvolume, gietstukvol se mesh
edge picklink "edge.847" "edge.850" "edge.907" "edge.902" "edge.911" \
  "edge.666"
edge mesh "edge.666" "edge.911" "edge.902" "edge.907" "edge.850" "edge.847" \
  successive ratio1 1 size 5
edge picklink "edge.977" "edge.975"
edge mesh "edge.975" "edge.977" successive ratio1 1 size 5
volume mesh "jetvolume" submap size 15
volume mesh "gietstukvol" map size 15

/ 42 Mesh meshvol
sfunction create "SENpoortbron" sourcefaces "face.399" startsize 4 growthrate 1.1 \
  distance 50 sizelimit 10 attachvolumes "meshvol" fixed
volume mesh "meshvol" tetrahedral size 10

/ 43 Mesh SENpoort, tuit, rgtskag en morfdeel
volume modify "volume.36" label "SENpoort"
volume mesh "SENpoort" tetrahedral size 4
volume mesh "tuit" cooper source "face.204" "face.201" size 5
volume mesh "rgtskag" cooper source "face.232" "face.201" size 5
volume mesh "morfdeel" tetrahedral size 4

/44 Mesh onder gietstuk
edge modify "edge.785" backward
edge picklink "edge.785"
edge modify "edge.785" successive ratio1 1 size 1
edge mesh "edge.978" "edge.785" "edge.980" "edge.979" firstlength ratio1 15 \
  size 25.5
volume mesh "gietstukonder" map size 15

/45 Vee uit ekstra edges
edge delete "edge.509" "edge.511" "edge.513" "edge.522" "edge.527" "edge.591" \
"edge.694" "edge.726" "edge.733" "edge.756" "edge.761"

/5 Vir Fluent: Randvoorwaardes (definiëring van vlakke)
physics create "SENinlaat" btype "VELOCITY_INLET" face "face.204"
physics create "gietstuk uitlaat" btype "PRESSURE_OUTLET" face "face.367"
physics create "SENmuur_buite" btype "WALL" face "face.217" "face.216" "face.202" \
  "face.229" "face.233"
physics create "SENmuur_binne" btype "WALL" face "face.402" "face.398" "face.401" \
  "face.400" "face.405"
physics create "SENpoortmuur_binne" btype "WALL" face "face.290" "face.300" \
  "face.295" "face.301"
physics create "gietstukmuur_nou" btype "WALL" face "face.310" "face.433"
physics create "gietstukmuur_wyd" btype "WALL" face "face.386" "face.396" \
  "face.430"
physics create "ondermould_wyd" btype "WALL" face "face.366"
physics create "ondermould_nou" btype "WALL" face "face.378"
physics create "simmetrie_nou" btype "SYMMETRY" face "face.197" "face.208" \
  "face.234" "face.302" "face.395" "face.427" "face.431" "face.441"
physics create "simmetrie_wyd" btype "SYMMETRY" face "face.205" "face.219" \
  "face.223" "face.413" "face.285" "face.352" "face.432" "face.440"
physics create "meniskusvlak" btype "WALL" face "face.428" "face.414"
physics create "meshvolvlak1" btype "INTERIOR" face "face.410"
physics create "meshvolvlak2" btype "INTERIOR" face "face.412"
physics create "binnemould_vlak" btype "INTERIOR" face "face.380"
physics create "ondermould_vlak" btype "INTERIOR" face "face.438"
physics create "SENpoortuitlaat" btype "INTERIOR" face "face.399"

/ File closed at Tue Apr 16 17:12:45 2002, 13215.00 cpu second(s), 79360040 maximum
memory.

```

APPENDIX N

N. Summary: CFD results of 3D design exploration

N.1 CFD set-up data

The CFD set-up data is repeated here very briefly for the sake of completeness:

- Liquid steel properties used for temperature on settings
- Turbulence model: k- ω standard
- Dynamic grid adaption employed: based on velocity gradients as adaption criterion
- Initial grid size: 500 000 cells; Final grid size: approximately 800 000 cells
- First-order discretisation schemes followed by second-order discretisation

N.2 Experimental designs

The experiments used for the 3D exploration study are presented in Table N.1 below. The relevant Figure numbers are also shown in Table N.1.

Firstly, the constant operational parameters (constant for all results in this Appendix) will be listed below:

- Submergence depth: 80mm (regarded as a worst case)
- Casting speed (directly proportional to flow rate through CFD models): 1.3 m/min
- Mould width: 1060mm and 1250mm for each SEN design type

Table N.1: Experiments in central-composite design, including base case (experiment 1.0) and linear and quadratic optima fits by LS-OPT

Figure N._	Experiment designation	SEN port angle [°]	SEN port height [mm]	SEN well depth [mm]
2	1.0	15	70	1 ≈ 0
3	1.1	0	55	20
4	1.2	7.9	69.9	32.1
5	1.3	-12.9	69.9	32.1
6	1.4	7.9	40.1	32.1
7	1.5	-12.9	40.1	32.1
8	1.6	7.9	69.9	8.9
9	1.7	-12.9	69.9	8.9
10	1.8	7.9	40.1	8.9
11	1.9	-12.9	40.1	8.9
12	1.10	-2.5	55	20.5
13	1.11	15	55	20.5
14	1.12	-2.5	80	20.5
15	1.13	-2.5	55	40
16	1.14	-20	55	20.5
17	1.15	-2.5	30	20.5
18	1.16	-2.5	55	1
19	2.0_linear	-20	80	1
20	2.0_quadratic	-20	55.56	40

N.3 Summary results data

After each CFD model evaluation, the maximum TKE and the maximum velocity on the meniscus surface (averaged over the last 5000 iterations), are calculated using the post-processing capabilities of FLUENT. These values are listed in Table N.2 below, and will be used to determine the multi-objective values for each experimental design (and optima predicted by LS-OPT).

Table N.2: Summary Results data: maximum TKE and maximum velocity on meniscus of each SEN design for both widths (1060 and 1250mm)

Experiment designation	1060 mm width		1250 mm width	
	Maximum velocity [m/s]	Maximum TKE [m ² /s ²]	Maximum velocity [m/s]	Maximum TKE [m ² /s ²]
1.0	3.87E-01	2.55E-03	3.98E-01	1.33E-03
1.1	4.63E-01	2.61E-03	5.34E-01	4.37E-03
1.2	4.68E-01	2.09E-03	5.88E-01	3.84E-03
1.3	5.23E-01	4.14E-03	5.16E-01	5.95E-03
1.4	5.54E-01	9.98E-03	5.44E-01	9.43E-03
1.5	4.36E-01	2.42E-03	5.88E-01	4.25E-03
1.6	5.49E-01	5.58E-03	5.90E-01	6.10E-03
1.7	3.39E-01	2.35E-03	4.84E-01	1.90E-03
1.8	3.13E-01	5.34E-03	4.84E-01	9.53E-03
1.9	4.06E-01	2.22E-03	6.95E-01	9.88E-03
1.10	4.92E-01	3.16E-03	6.86E-01	6.20E-03
1.11	4.49E-01	2.75E-03	4.97E-01	2.43E-03
1.12	4.82E-01	3.24E-03	5.80E-01	6.90E-03
1.13	4.71E-01	2.86E-03	5.44E-01	3.05E-03
1.14	3.83E-01	3.10E-03	5.46E-01	4.69E-03
1.15	5.72E-01	6.77E-03	6.00E-01	9.72E-03
1.16	5.55E-01	4.11E-03	6.07E-01	4.53E-03
2.0_linear	2.63E-01	1.47E-03	4.45E-01	2.24E-03
2.0_quadratic	3.70E-01	3.21E-03	4.21E-01	2.17E-03

The values tabulated in Table N.2 are depicted graphically in Figure N.1 below:

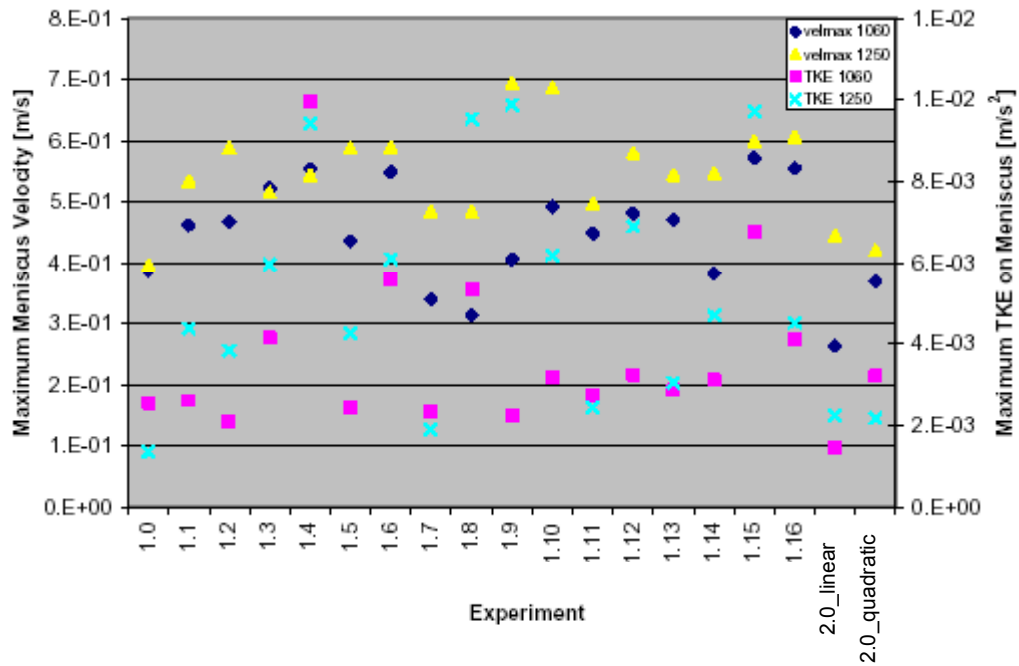


Figure N.1: Graphical display of data in Table N.2

The multi-objective values that are calculated from the data in Table N.2 and Figure N.1 above are displayed in the main text (Chapter 5) in Figure 5.17.

The velocity contours on the centre plane of each design follows in section N.4.

N.4 CFD Results: velocity contours of magnitude on centre plane (last iterations)

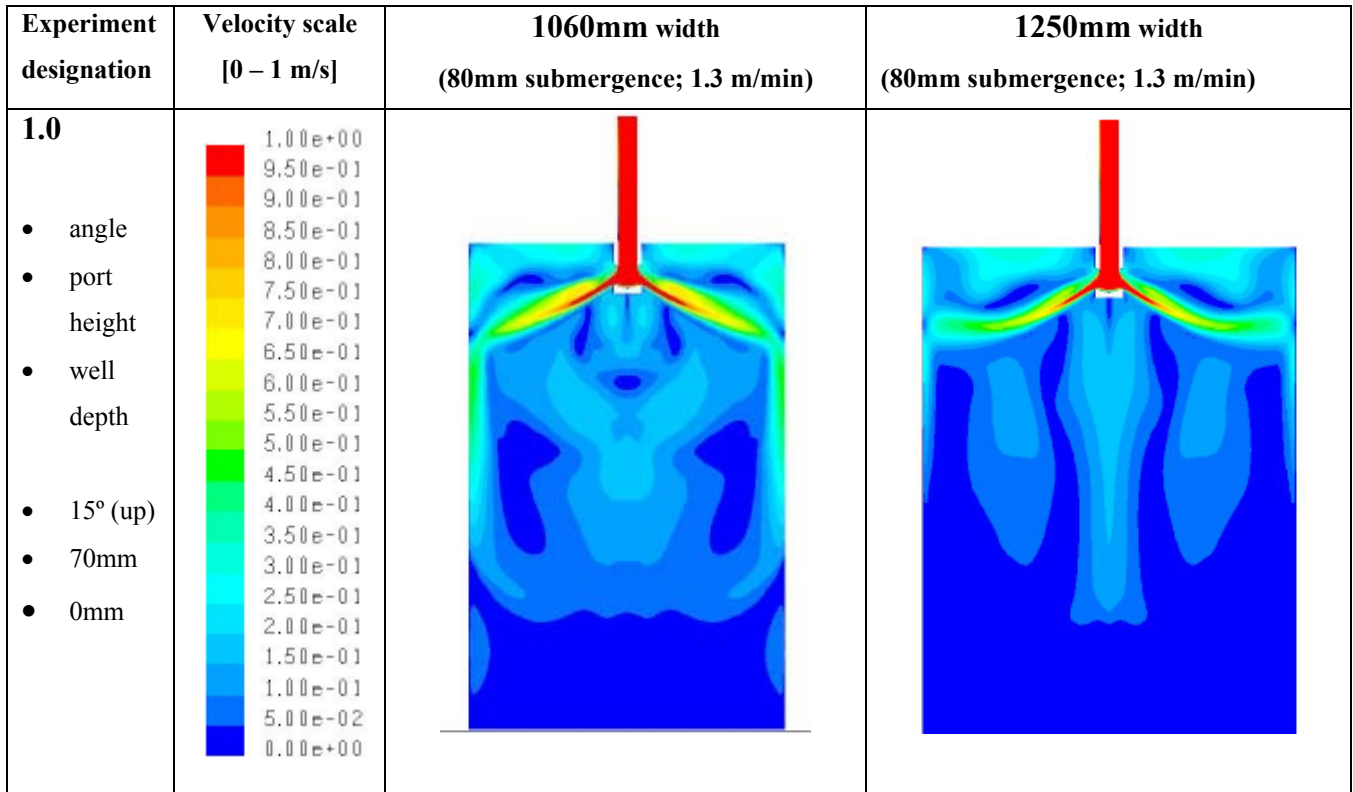


Figure N.2: Experiment 1.0 contours of velocity magnitude on centre plane (range 0 – 1 m/s)

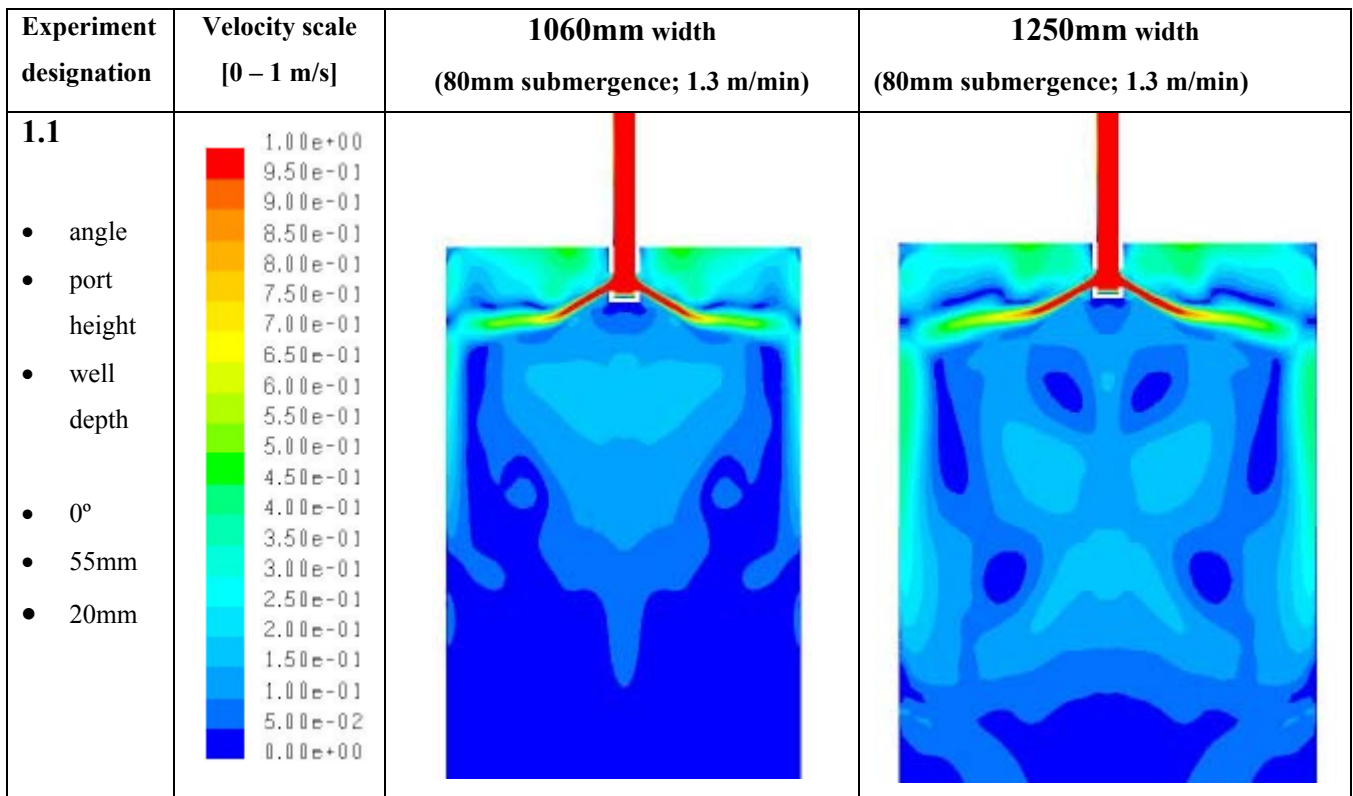


Figure N.3: Experiment 1.1 contours of velocity magnitude on centre plane (range 0 – 1 m/s)

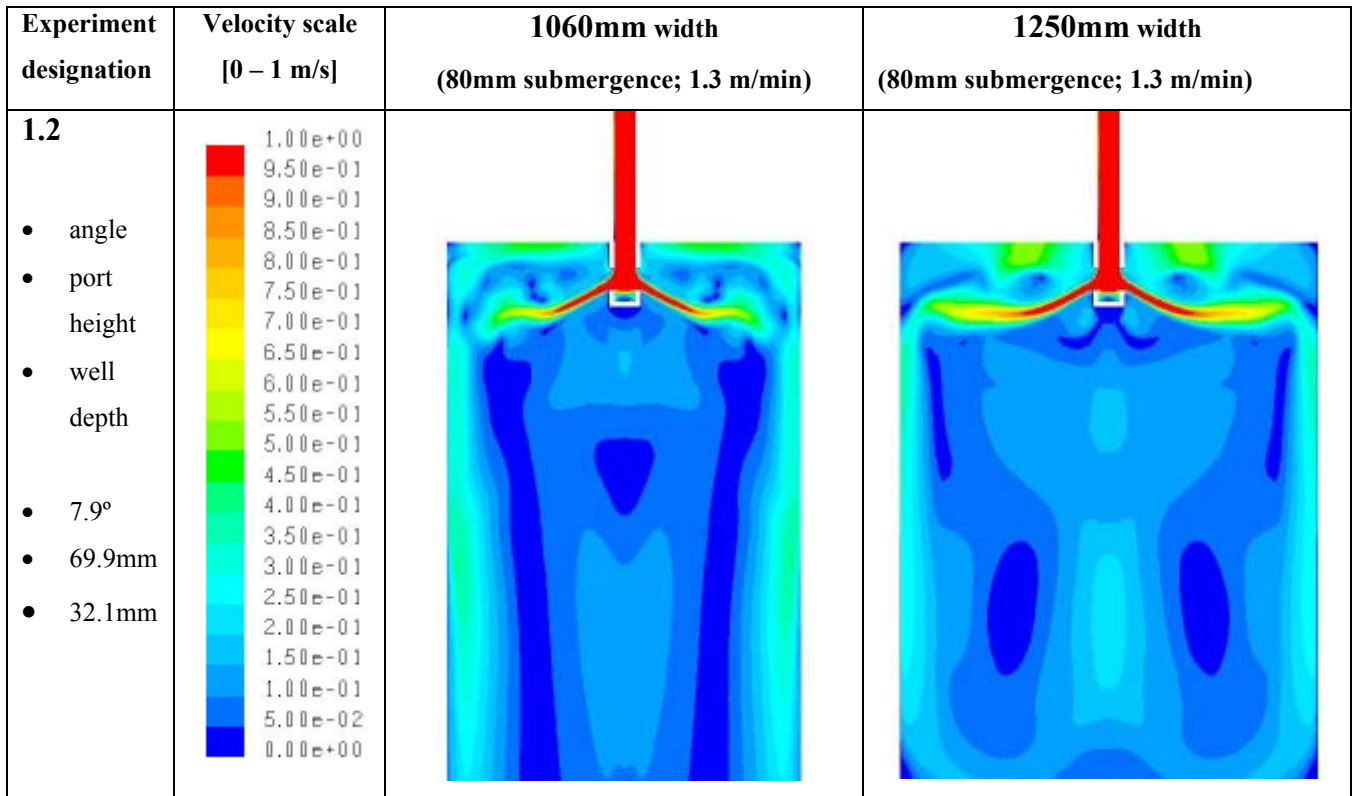


Figure N.4: Experiment 1.2 contours of velocity magnitude on centre plane (range 0 – 1 m/s)

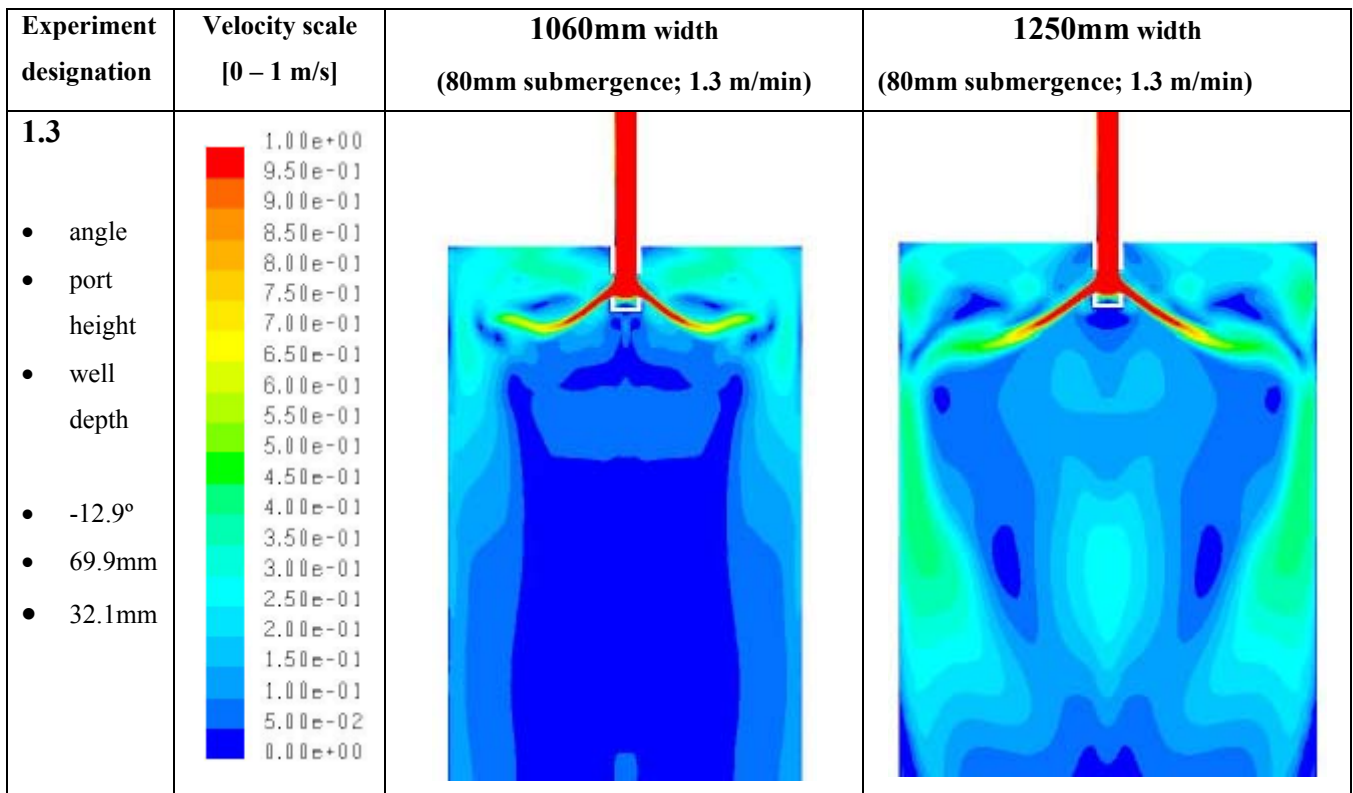


Figure N.5: Experiment 1.3 contours of velocity magnitude on centre plane (range 0 – 1 m/s)

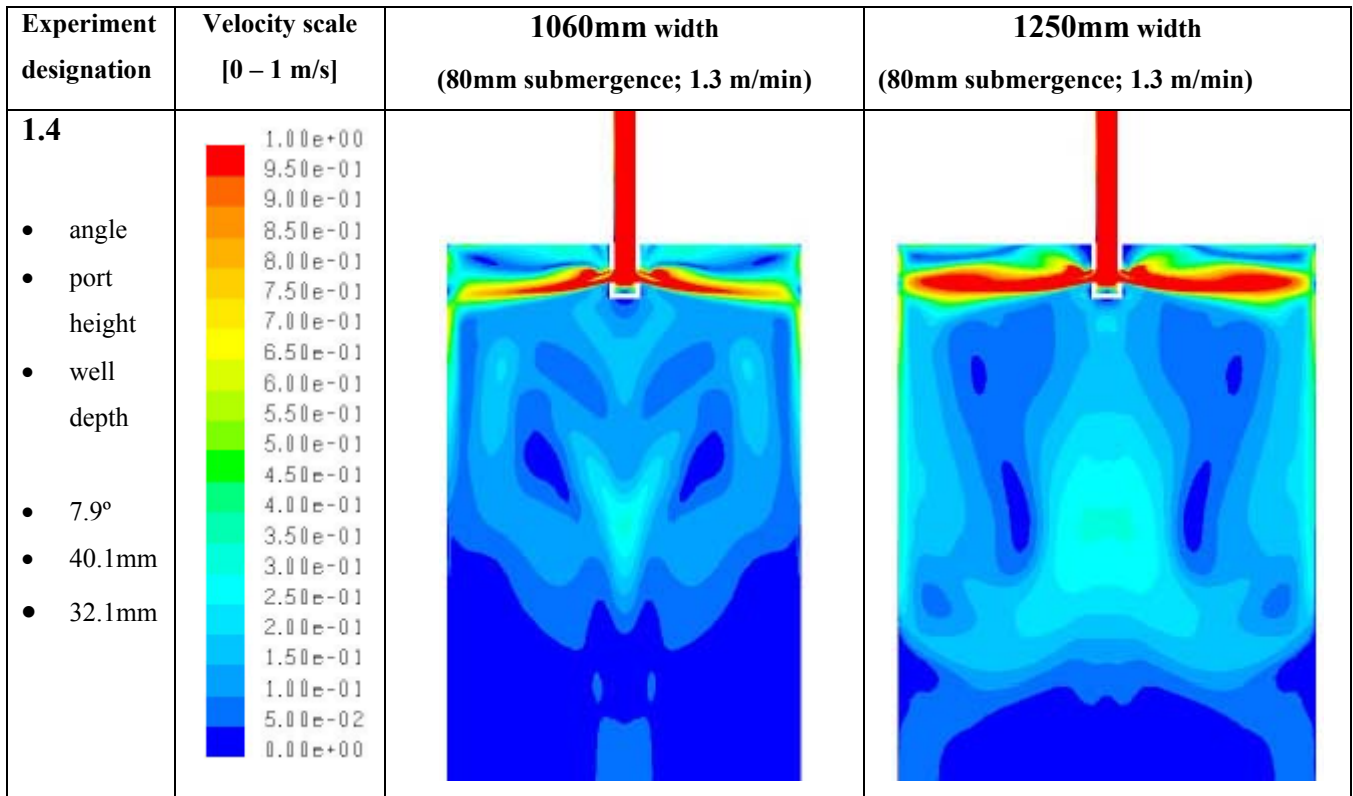


Figure N.6: Experiment 1.4 contours of velocity magnitude on centre plane (range 0 – 1 m/s)

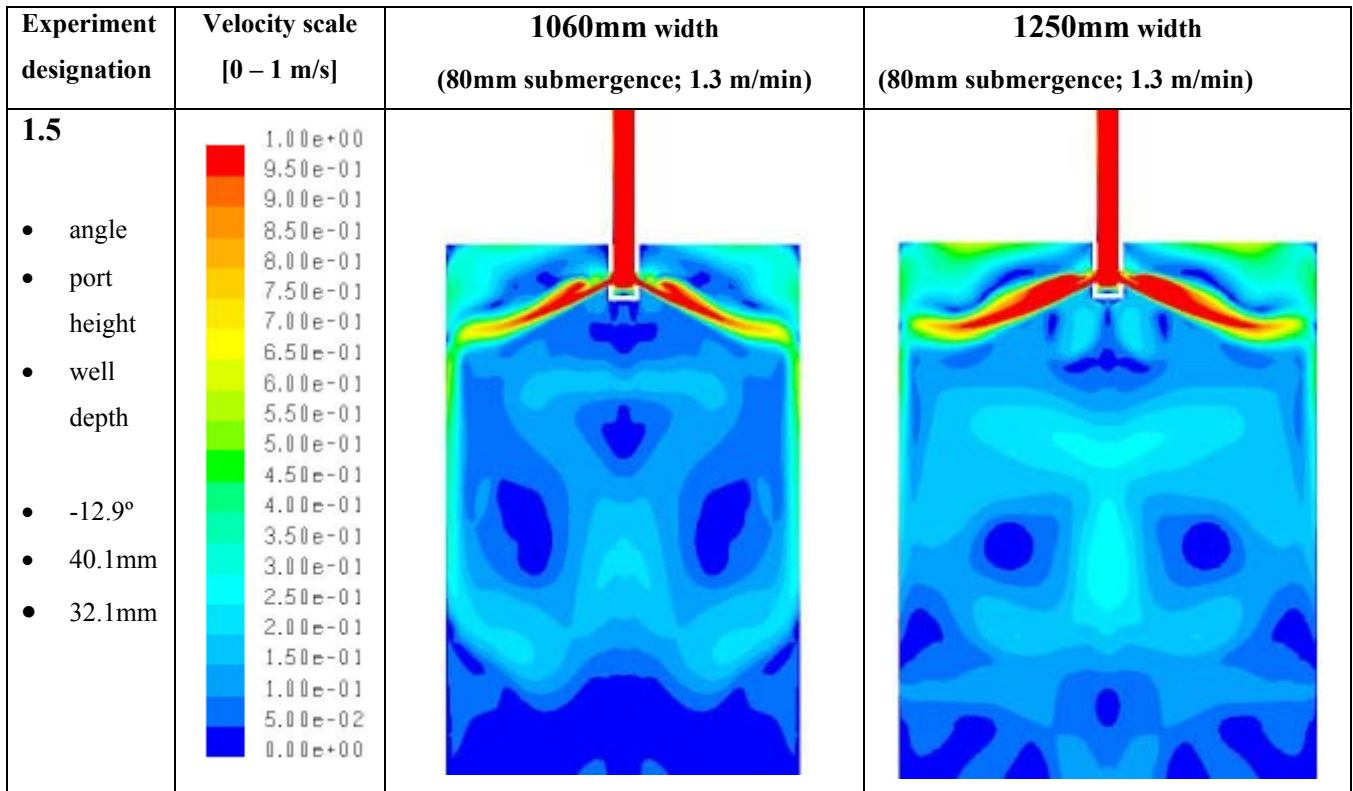


Figure N.7: Experiment 1.5 contours of velocity magnitude on centre plane (range 0 – 1 m/s)

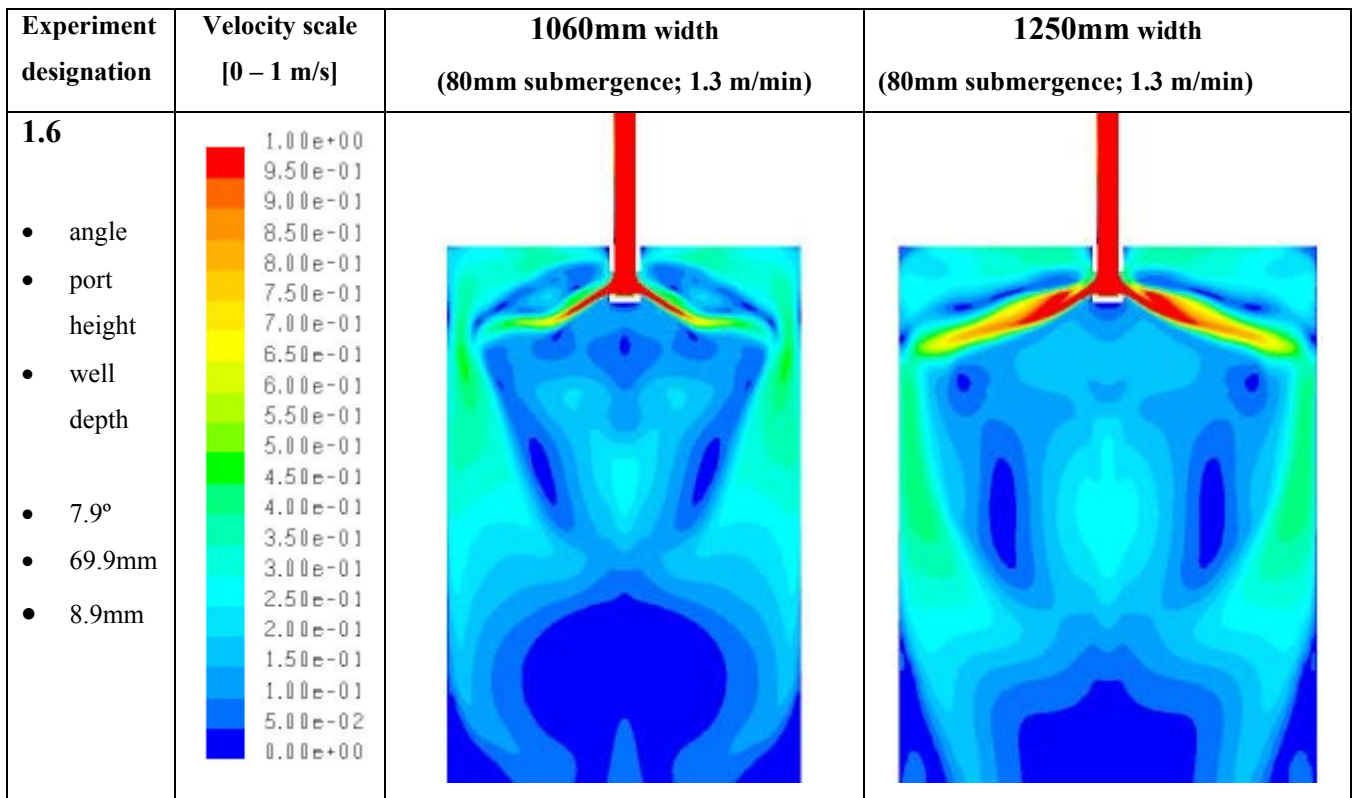


Figure N.8: Experiment 1.6 contours of velocity magnitude on centre plane (range 0 – 1 m/s)

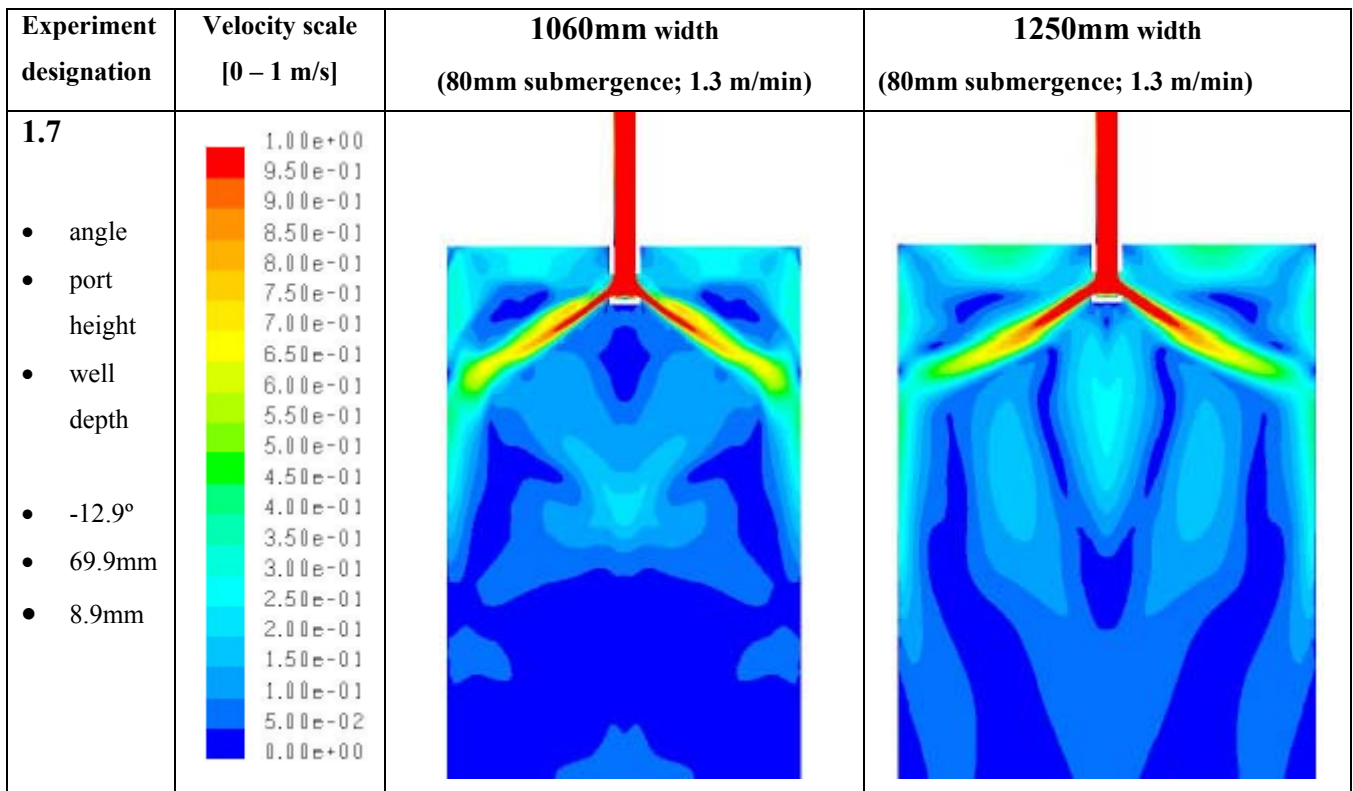


Figure N.9: Experiment 1.7 contours of velocity magnitude on centre plane (range 0 – 1 m/s)

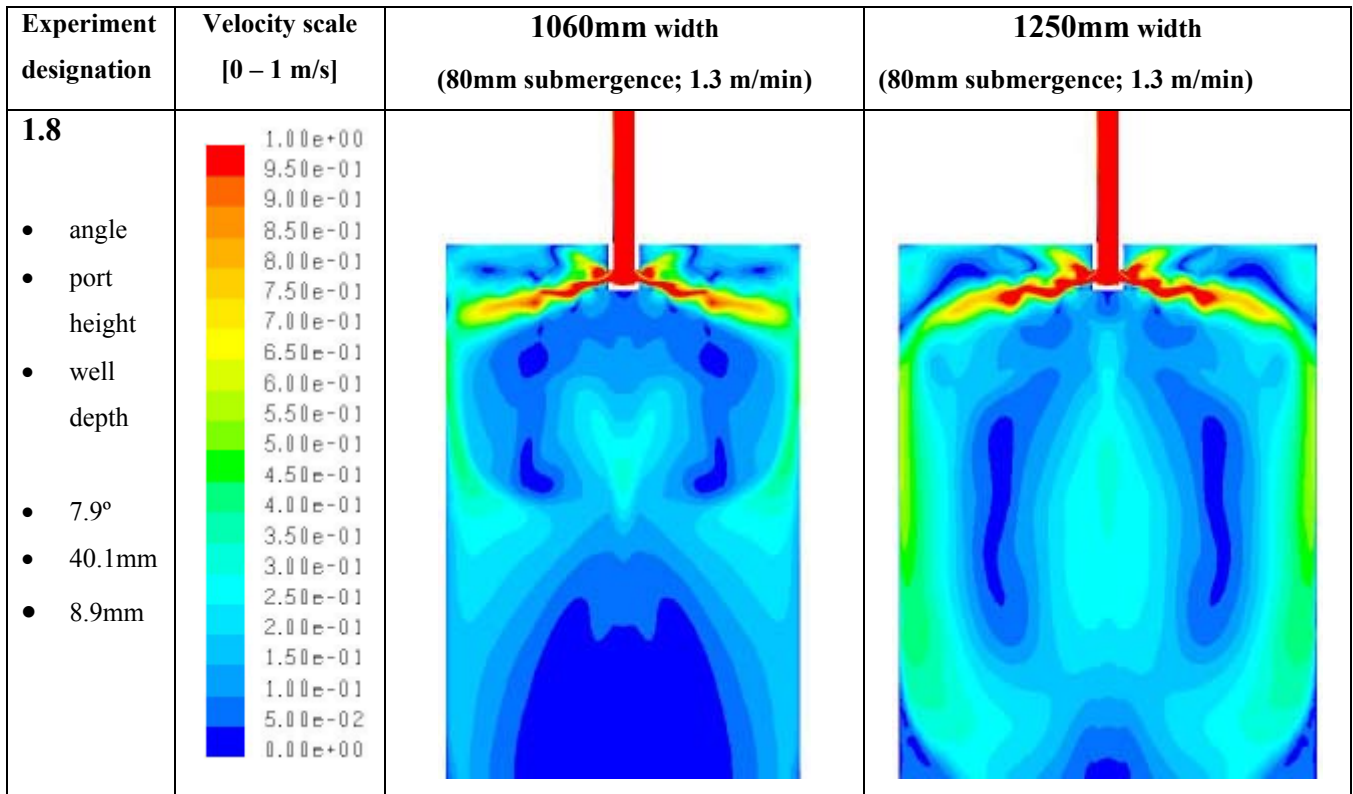


Figure N.10: Experiment 1.8 contours of velocity magnitude on centre plane (range 0 – 1 m/s)

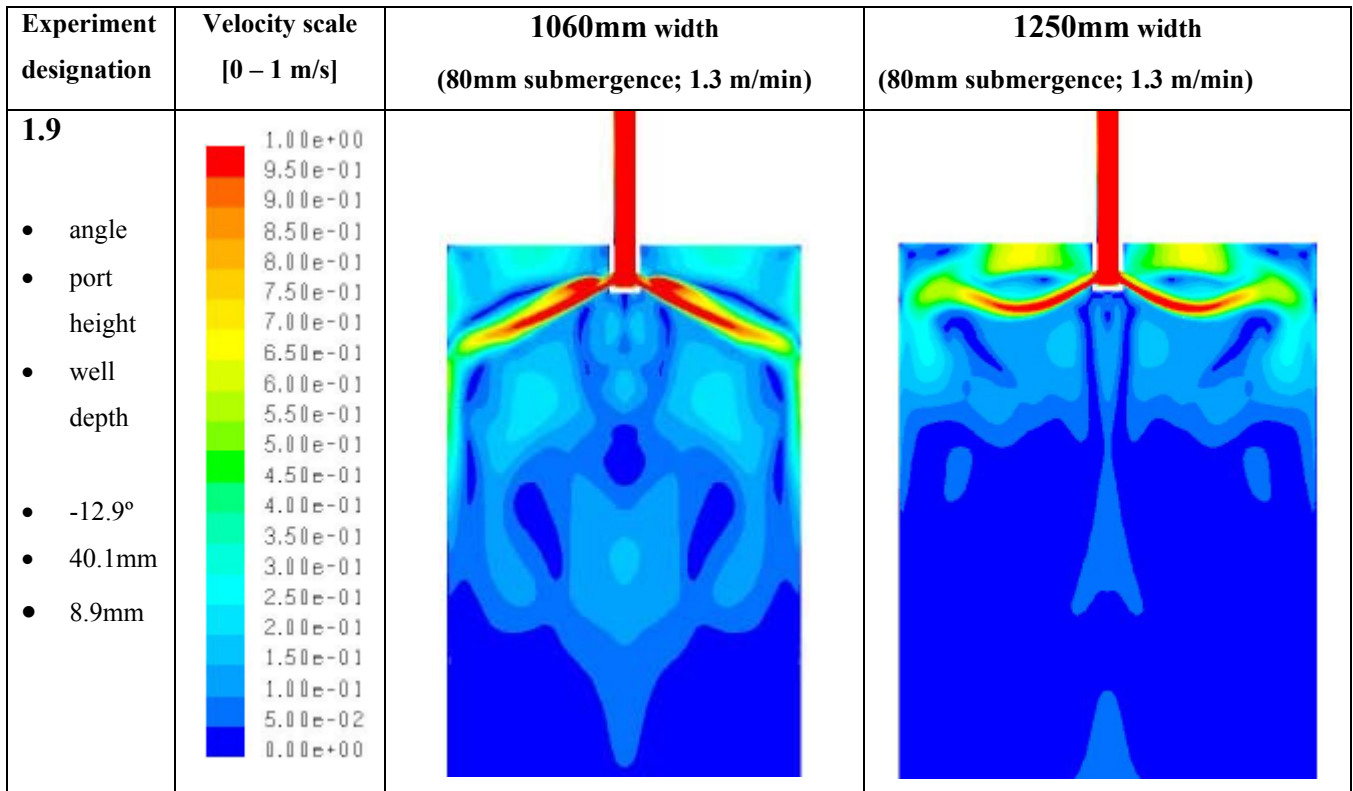


Figure N.11: Experiment 1.9 contours of velocity magnitude on centre plane (range 0 – 1 m/s)

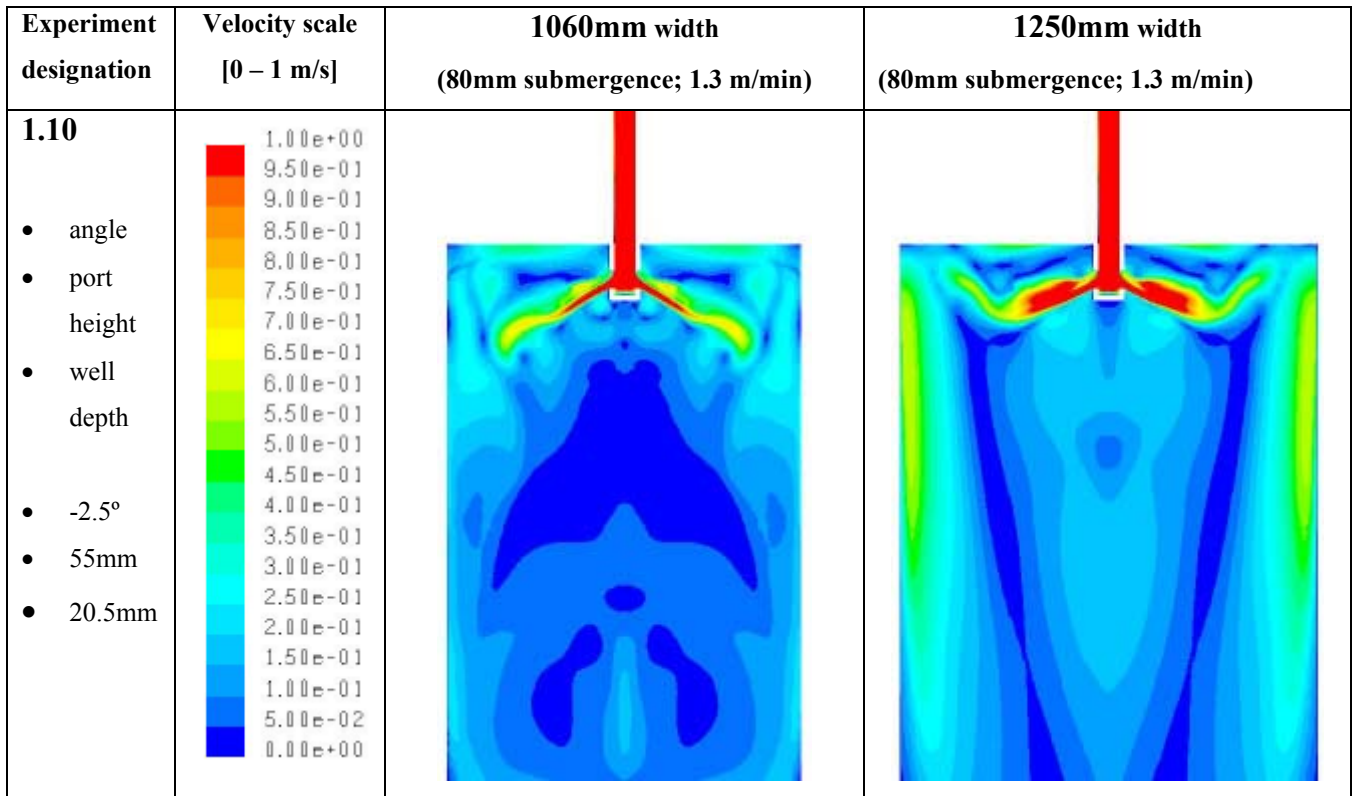


Figure N.12: Experiment 1.10 contours of velocity magnitude on centre plane (range 0 – 1 m/s)

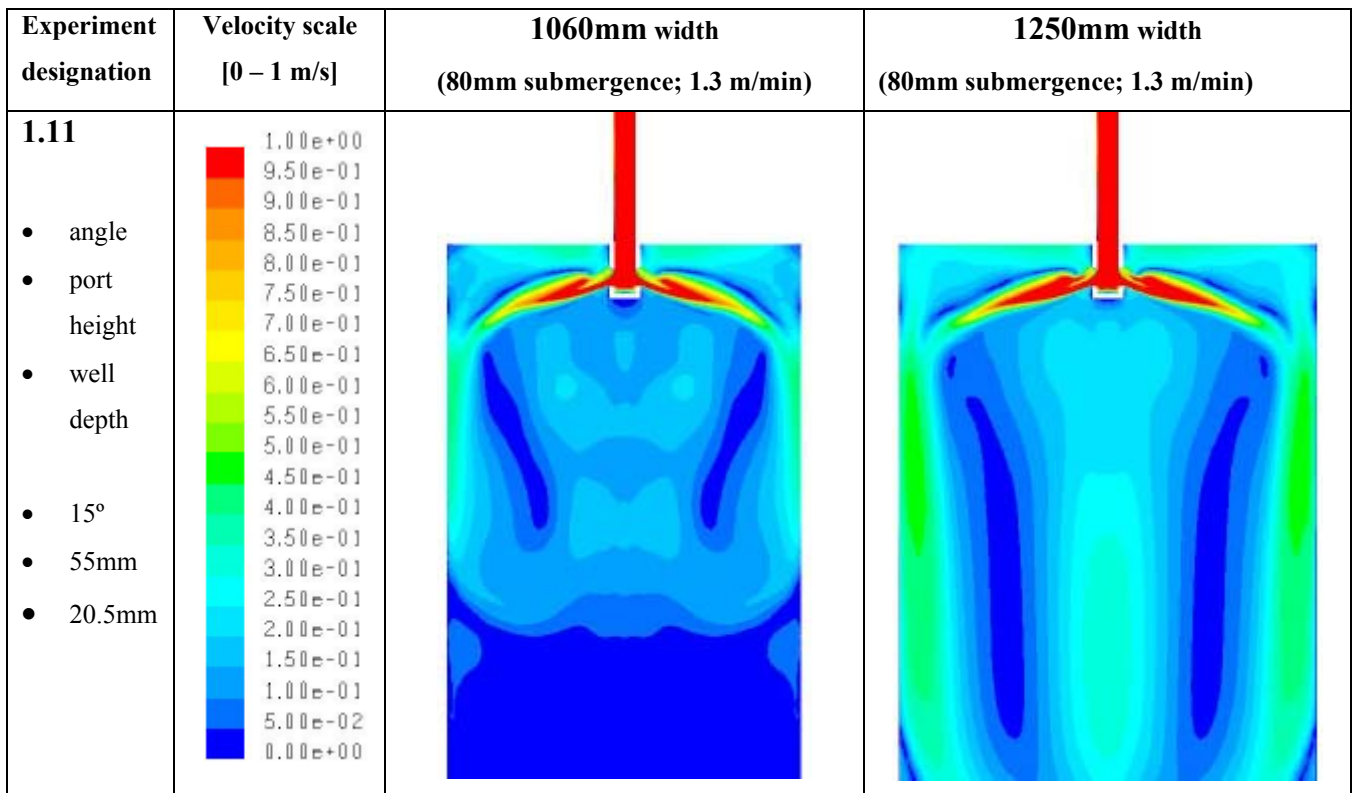


Figure N.13: Experiment 1.11 contours of velocity magnitude on centre plane (range 0 – 1 m/s)

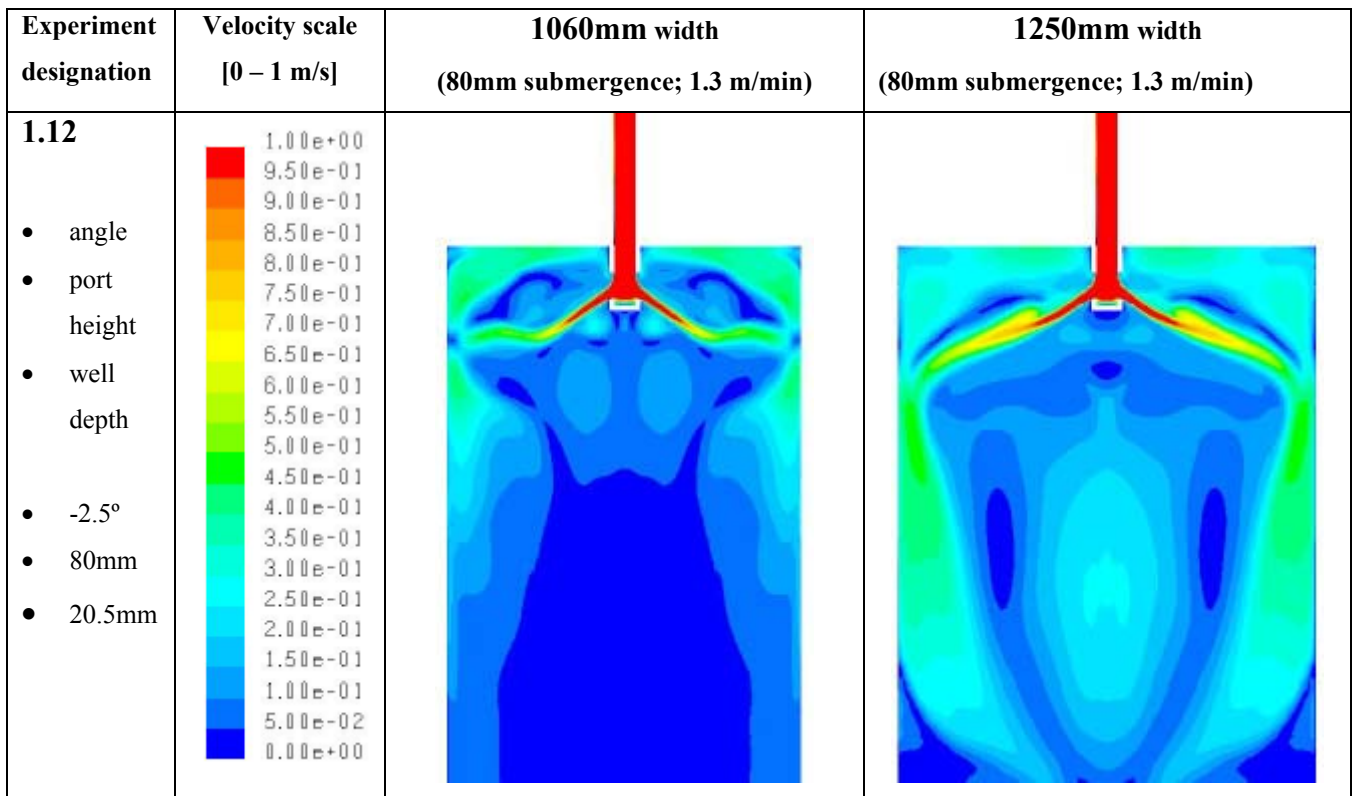


Figure N.14: Experiment 1.12 contours of velocity magnitude on centre plane (range 0 – 1 m/s)

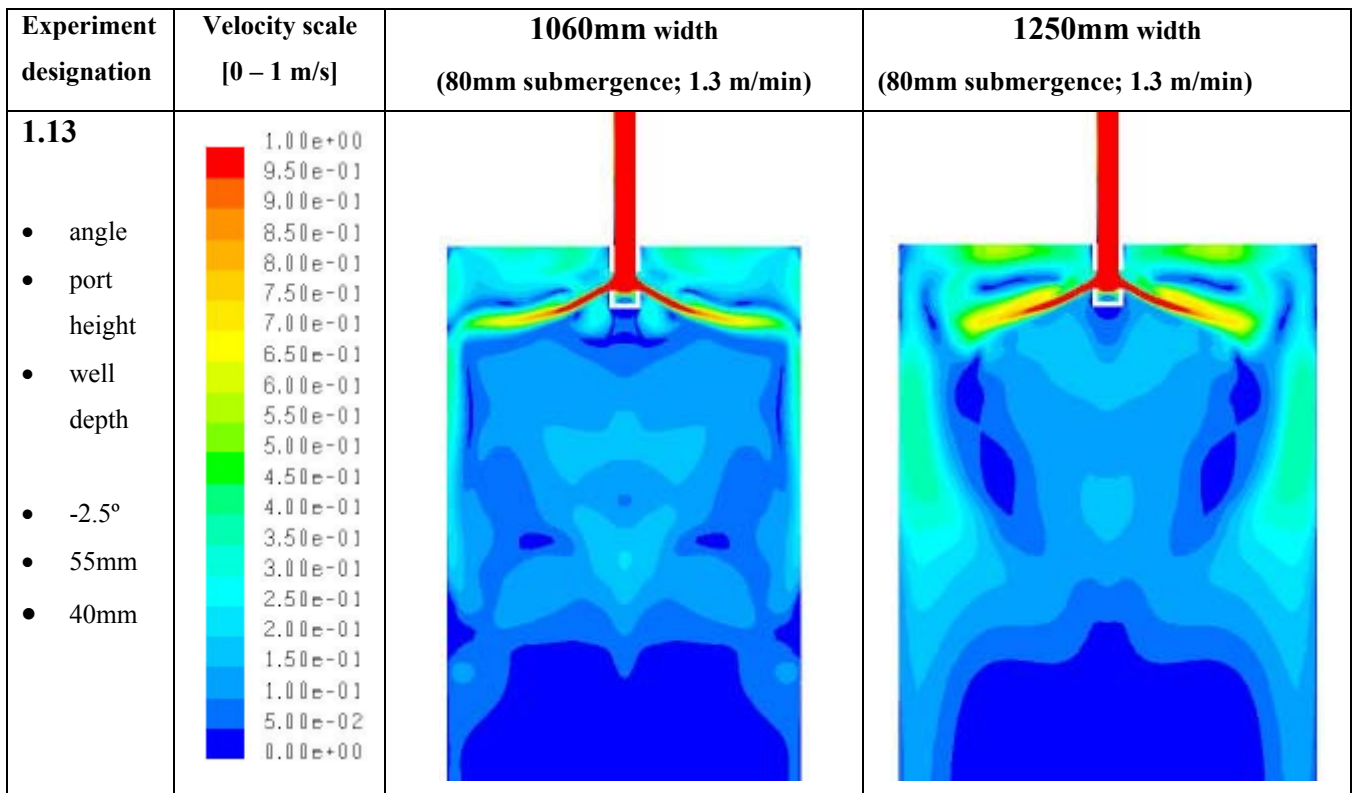


Figure N.15: Experiment 1.13 contours of velocity magnitude on centre plane (range 0 – 1 m/s)

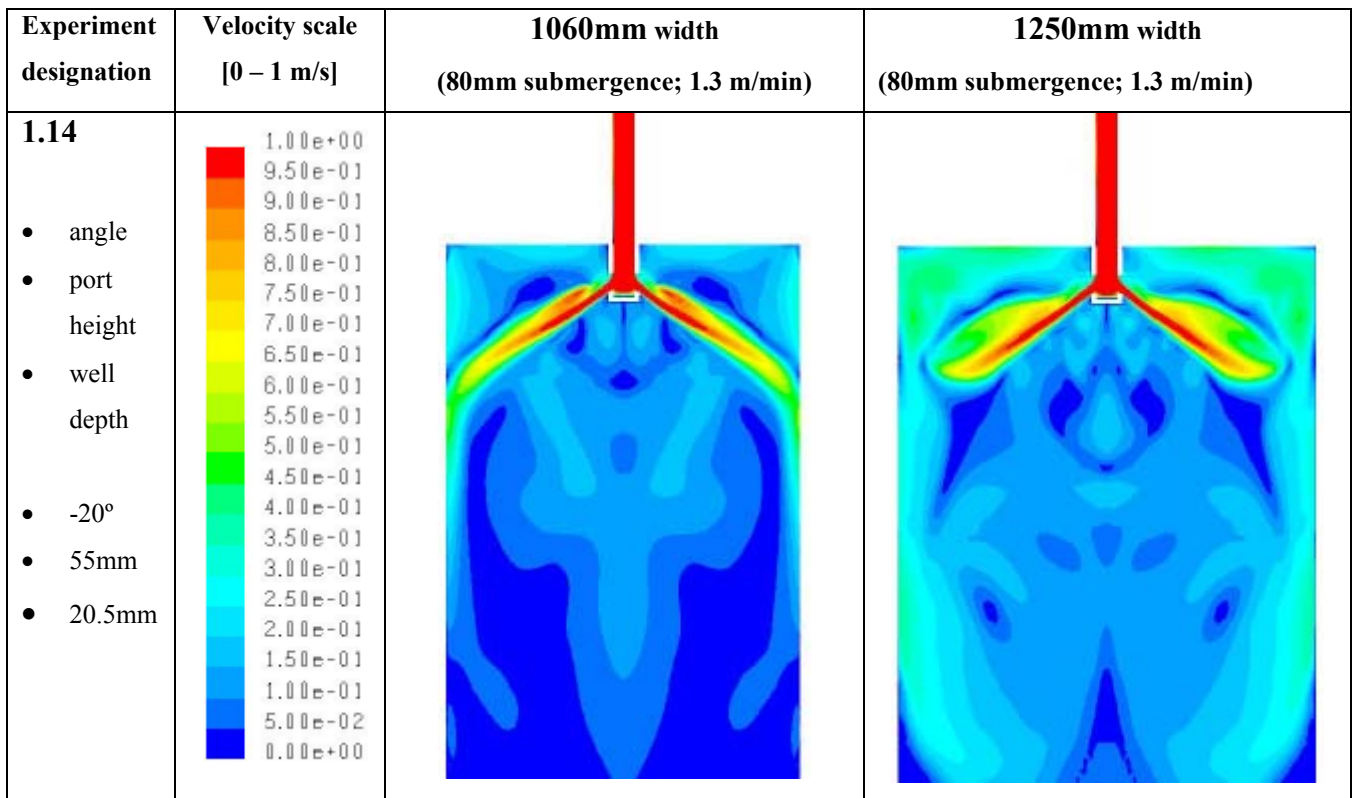


Figure N.16: Experiment 1.14 contours of velocity magnitude on centre plane (range 0 – 1 m/s)

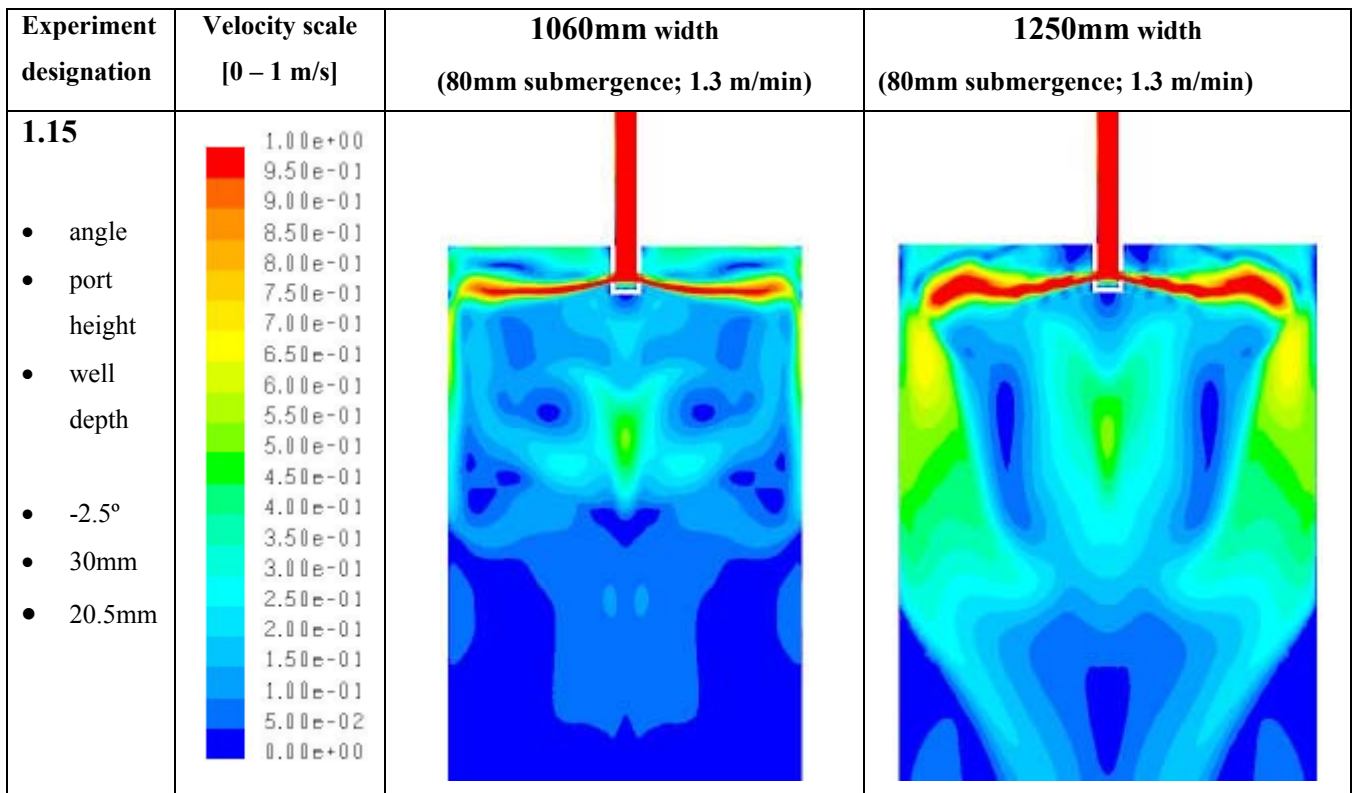


Figure N.17: Experiment 1.15 contours of velocity magnitude on centre plane (range 0 – 1 m/s)

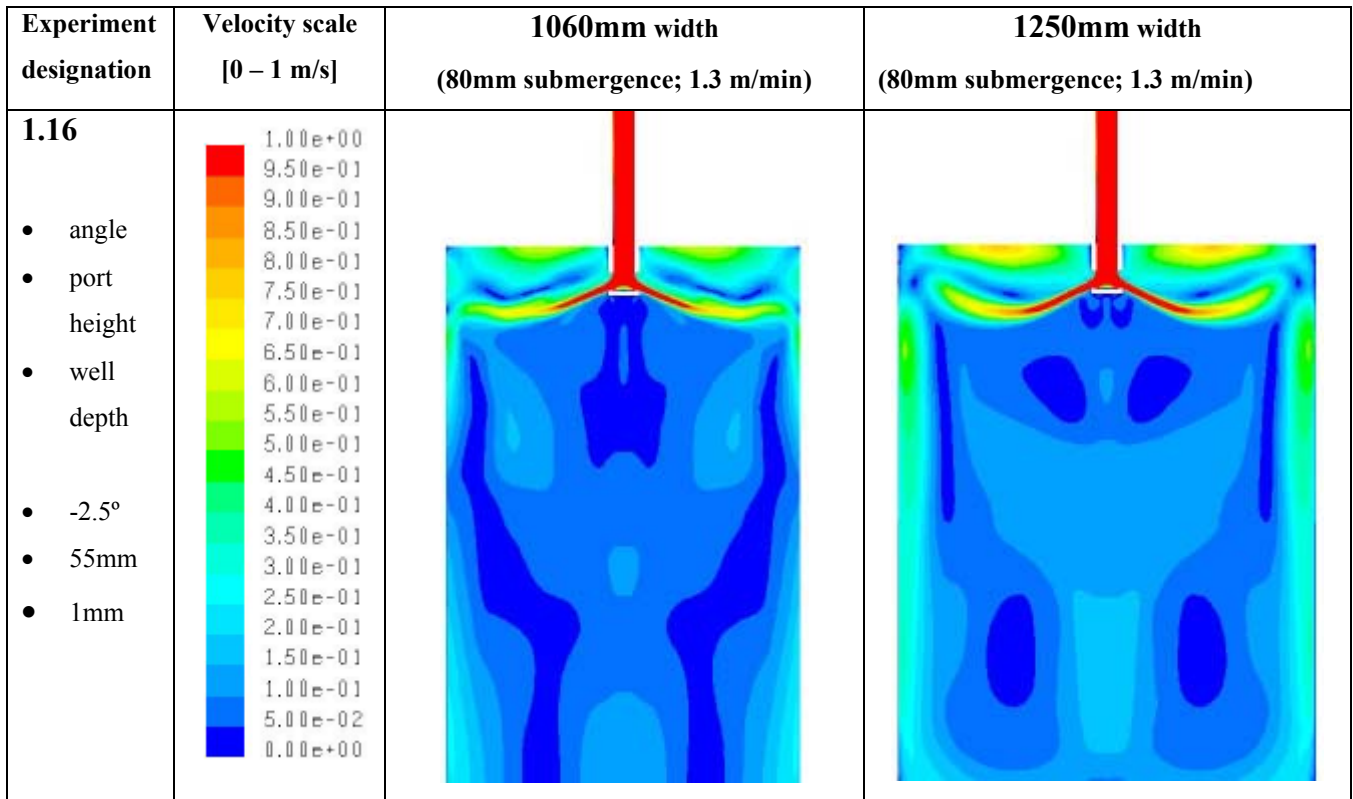


Figure N.18: Experiment 1.16 contours of velocity magnitude on centre plane (range 0 – 1 m/s)

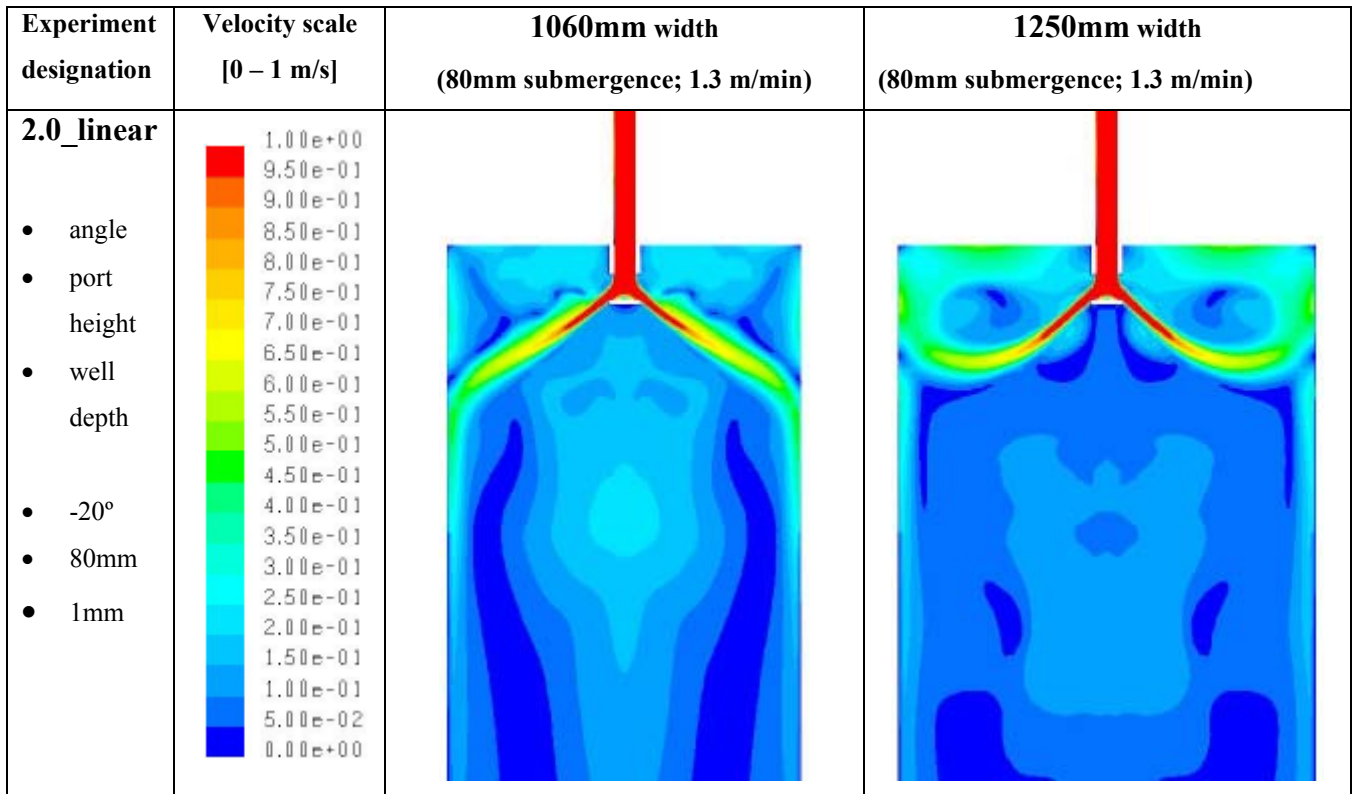


Figure N.19: Experiment 2.0_linear contours of velocity magnitude on centre plane (range 0 – 1 m/s)

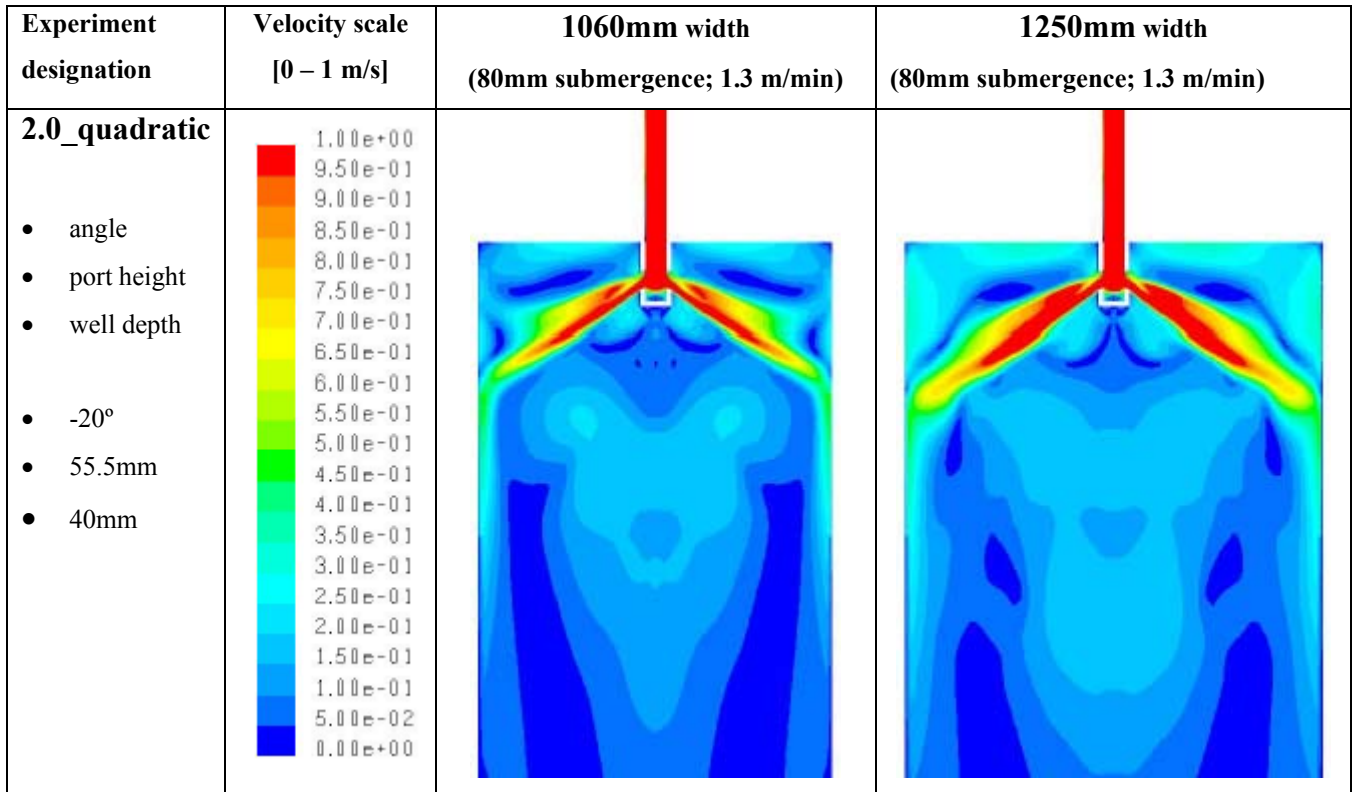


Figure N.20: Experiment 2.0_quadratic contours of velocity magnitude on centre plane (range 0 – 1 m/s)

APPENDIX O

O. Summary: CFD results of best 4 SEN designs of 3D design exploration

O.1 Summary of Results

The four best designs (lowest multi-objective values) to further explore are:

- 1.0
- 1.7
- 2.0_linear
- 2.0_quadratic

The flow fields in each of these cases (for both widths of 1060 and 1250mm) are shown in section O.2, using the following contours of magnitude, as well as 3D path lines:

- contours of velocity on the symmetry plane
- contours of helicity¹ on the symmetry plane
- contours of turbulent kinetic energy on symmetry plane
- contours of vorticity on the symmetry plane
- contours of shear stress on the wide mould walls
- contours of temperature on the symmetry plane
- path lines originating from the SEN inlet, coloured by vorticity magnitude

These views were generated using FLUENT's post-processing capabilities.

¹ Helicity was defined in Chapter 4, footnote 14 [10].

O.2 CFD Results: contours of magnitude on symmetry plane (last iterations) and path lines

O.2.1 Experiment 1.0

Figures O.1 – O.7

O.2.2 Experiment 1.7

Figures O.8 – O.14

O.2.3 Experiment 2.0 linear

Figures O.15 – O.21

O.2.4 Experiment 2.0 quadratic

Figures O.22 – O.28

O.2.1 Experiment: 1.0

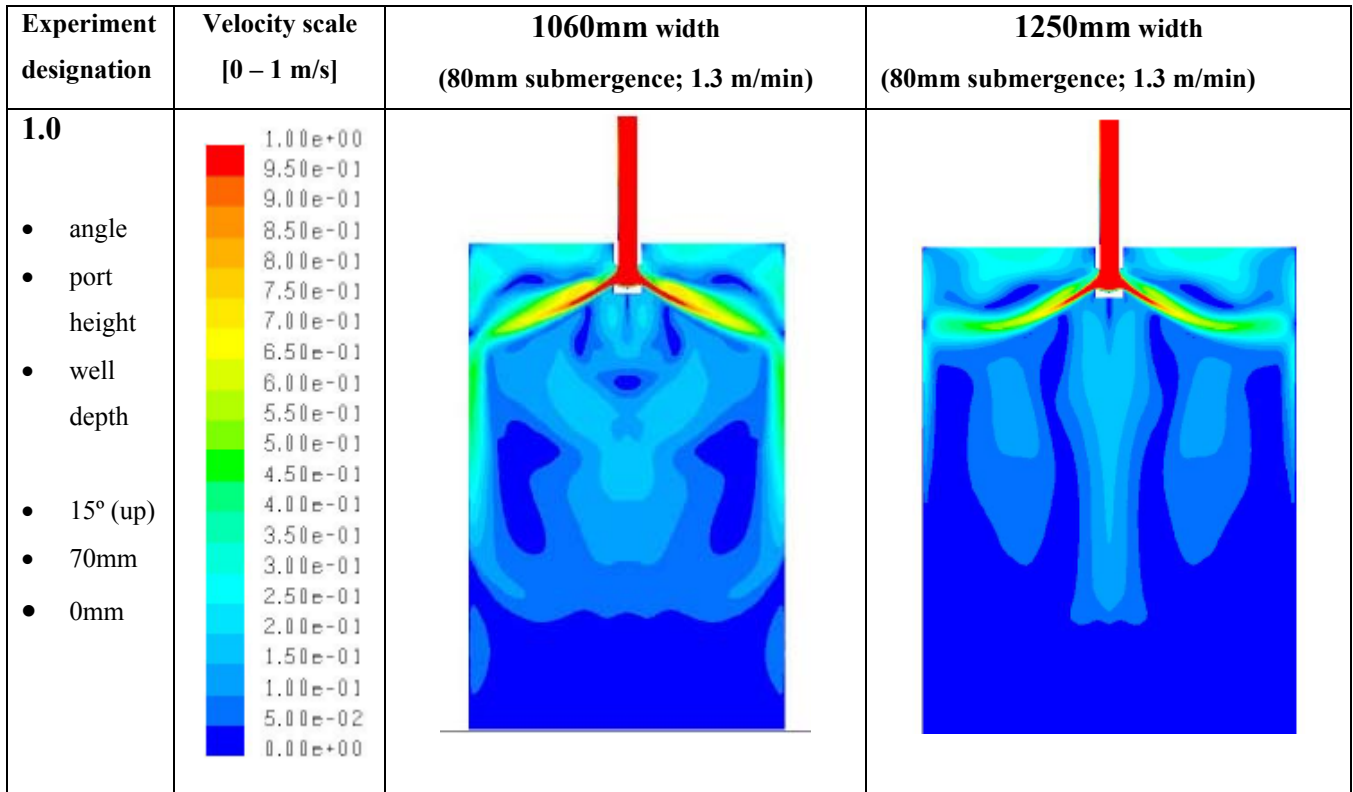


Figure O.1: Contours of velocity magnitude on the symmetry plane (range 0 – 1 m/s)

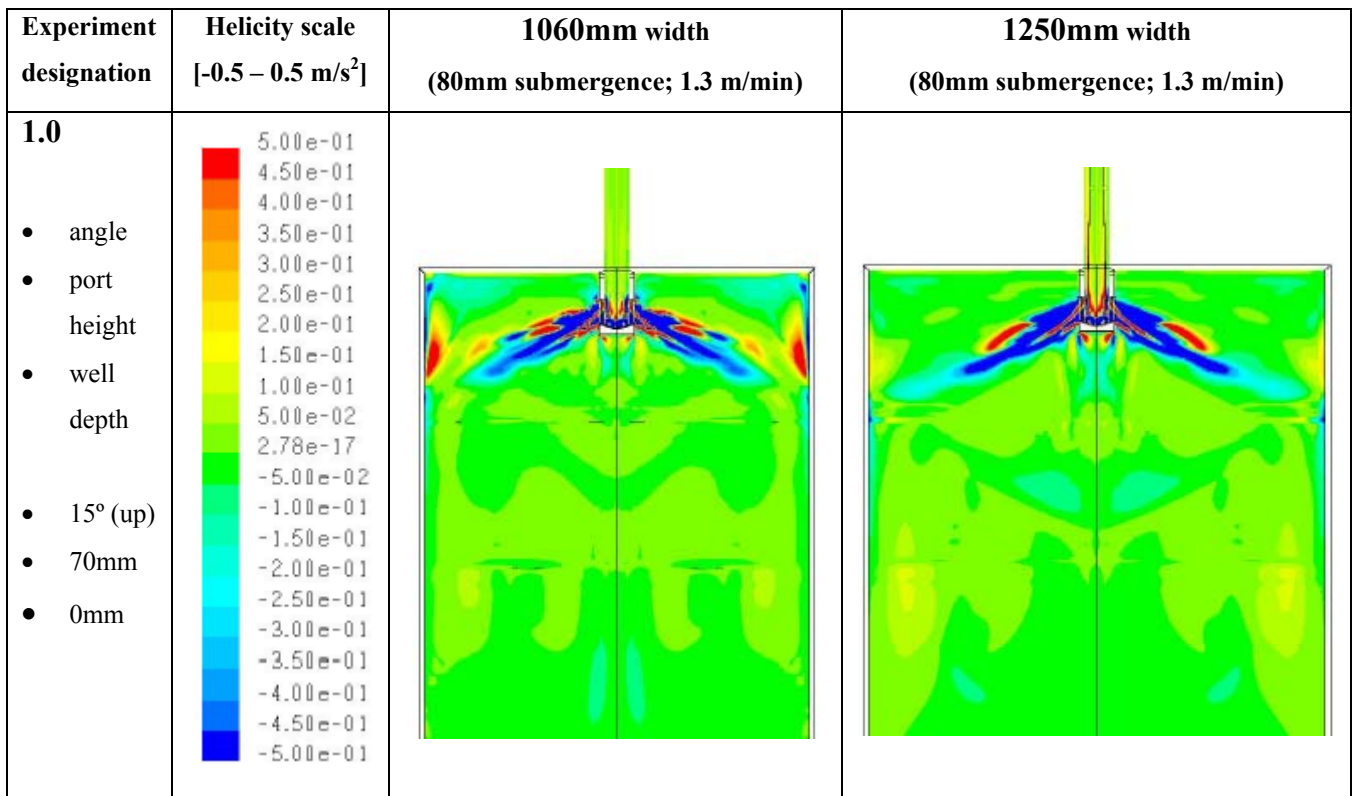


Figure O.2: Contours of helicity on the symmetry plane (range -0.5 – 0.5 m/s²)

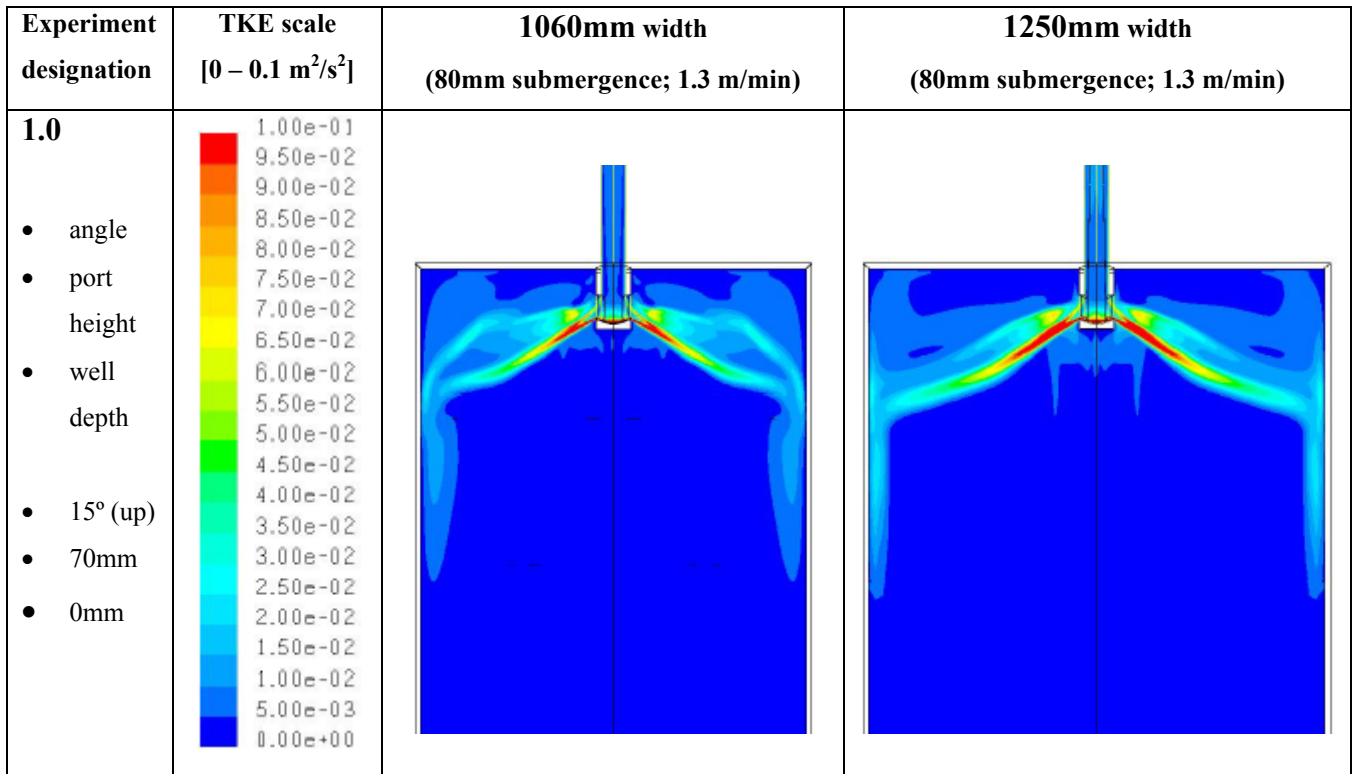


Figure O.3: Contours of turbulent kinetic energy on symmetry plane (range 0 – 0.1 m²/s²)

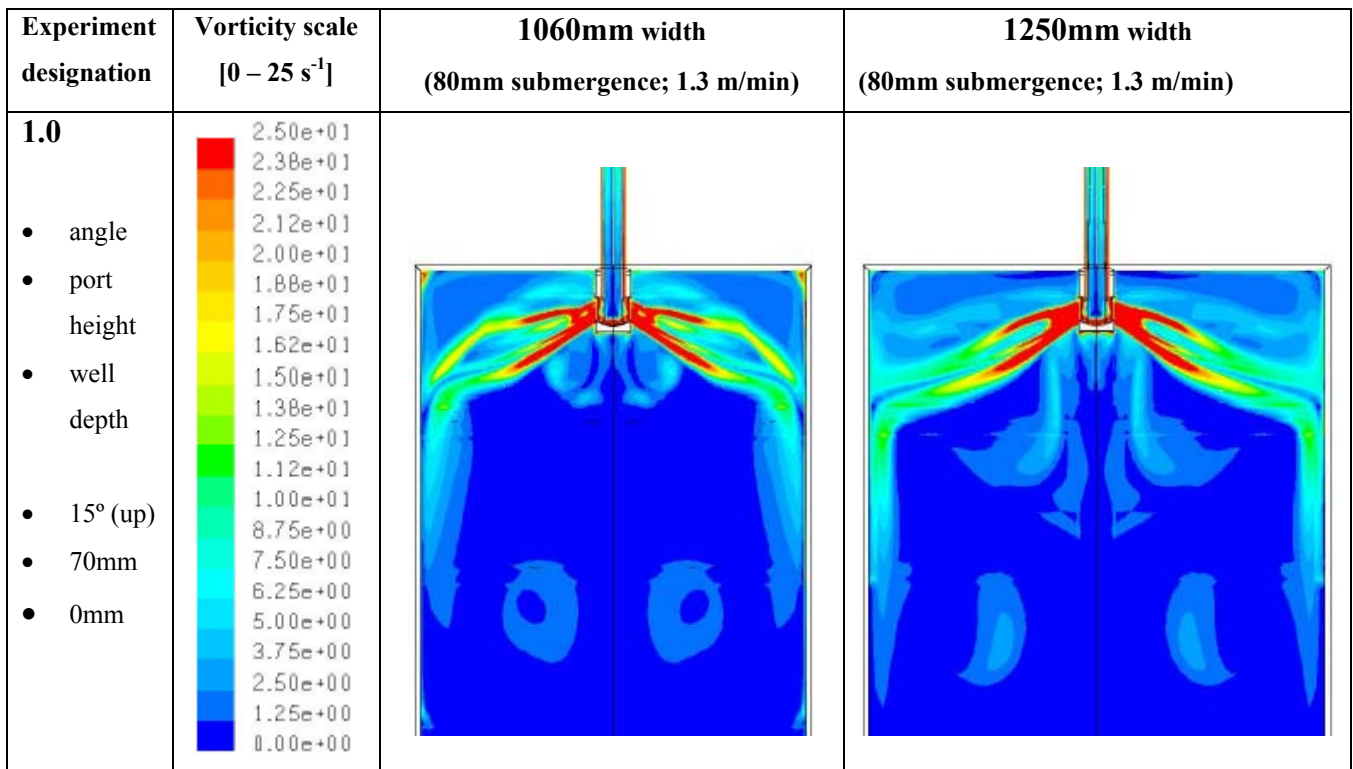


Figure O.4: Contours of vorticity on the symmetry plane (range 0 – 25 s⁻¹)

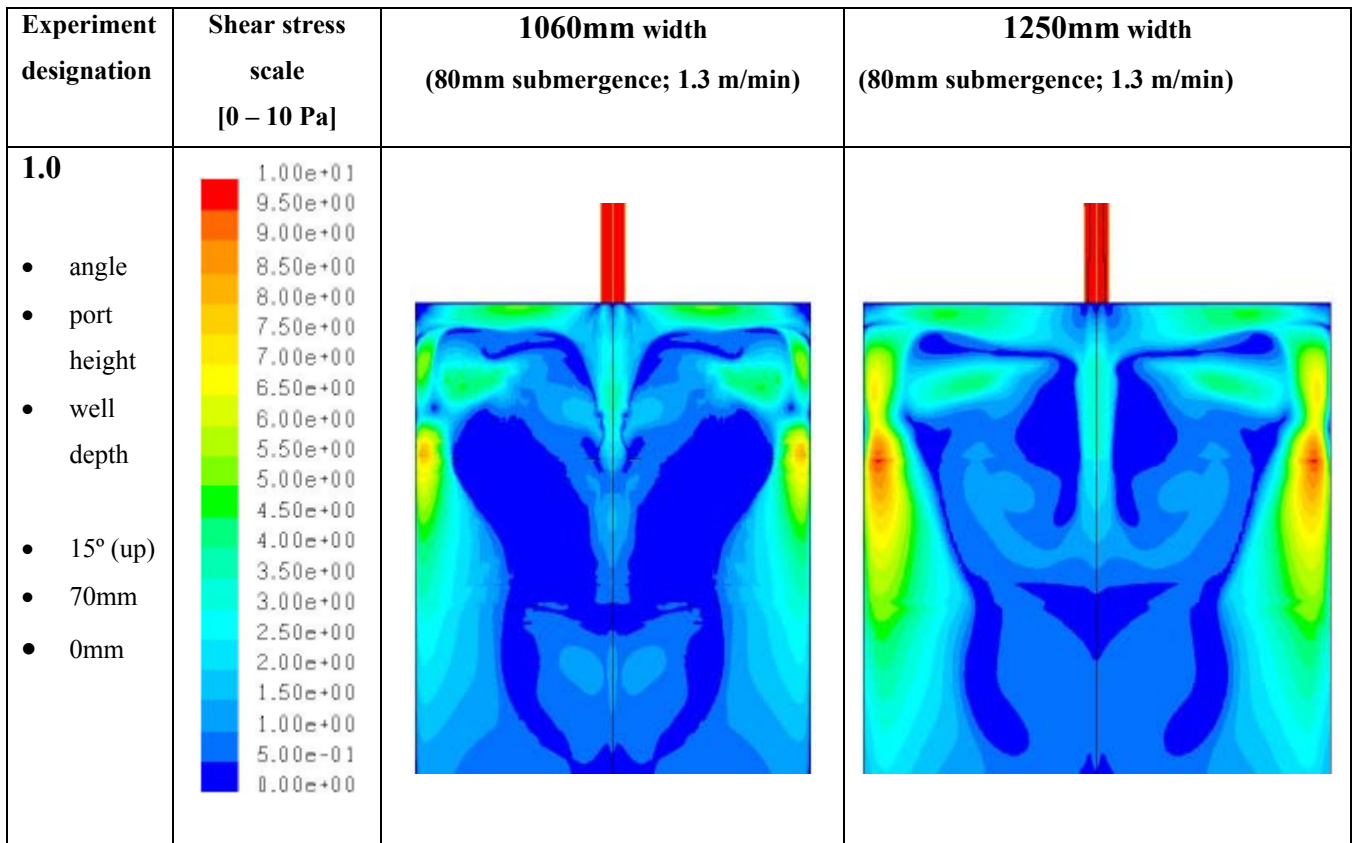


Figure O.5: Contours of shear stress on the wide mould walls (range 0 – 10 Pa)

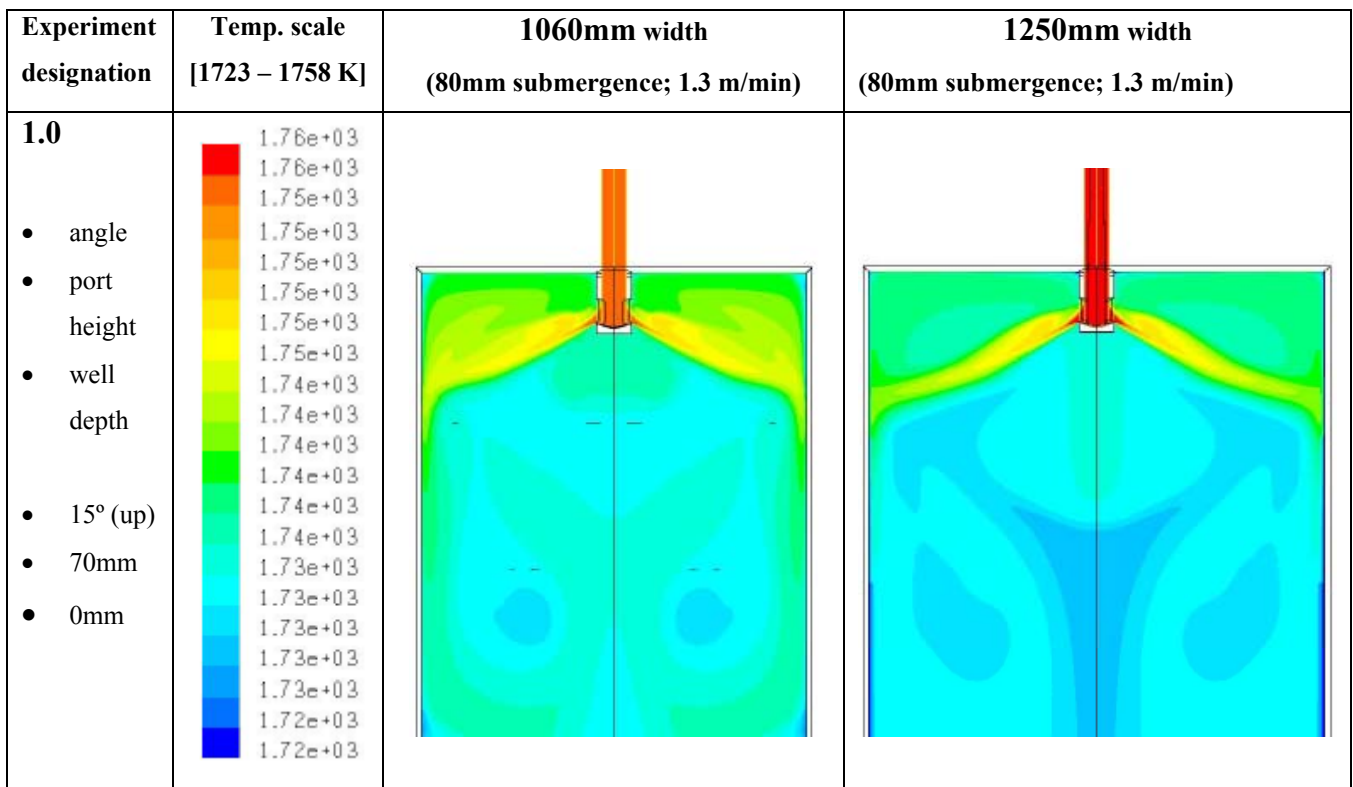


Figure O.6: Contours of temperature on the symmetry plane (range 1723 – 1758 K)

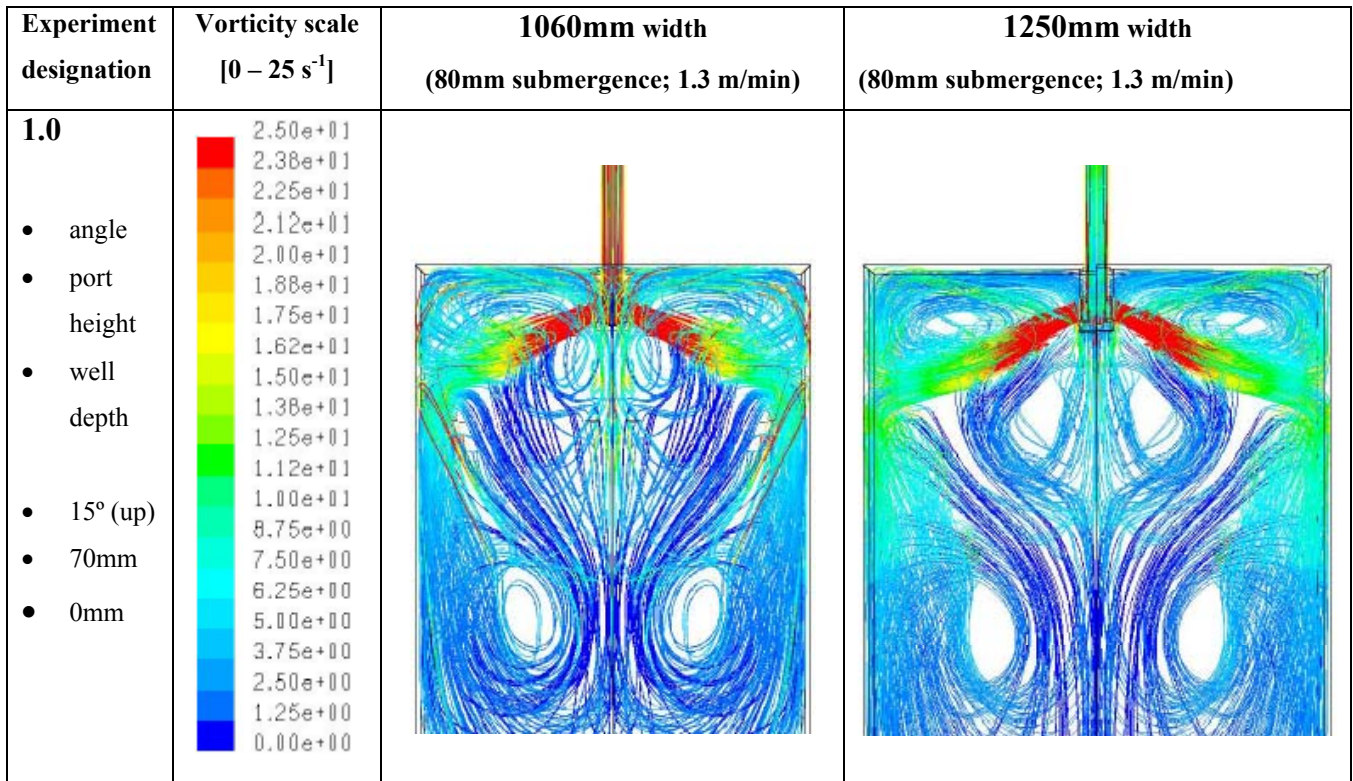


Figure O.7: Path lines originating from the SEN inlet, coloured by vorticity magnitude (range of vorticity 0 – 25 s⁻¹)

O.2.2 Experiment: 1.7

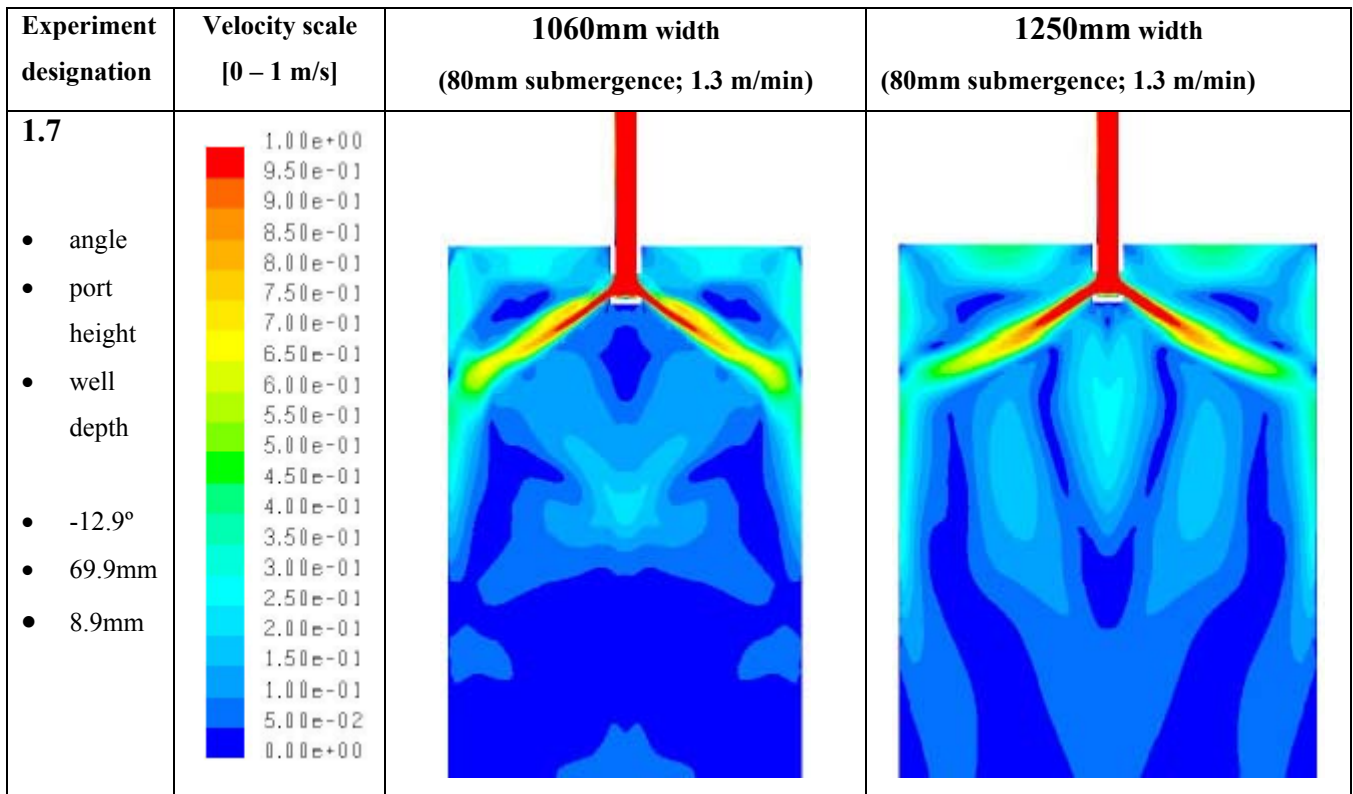


Figure O.8: Contours of velocity magnitude on the symmetry plane (range 0 – 1 m/s)

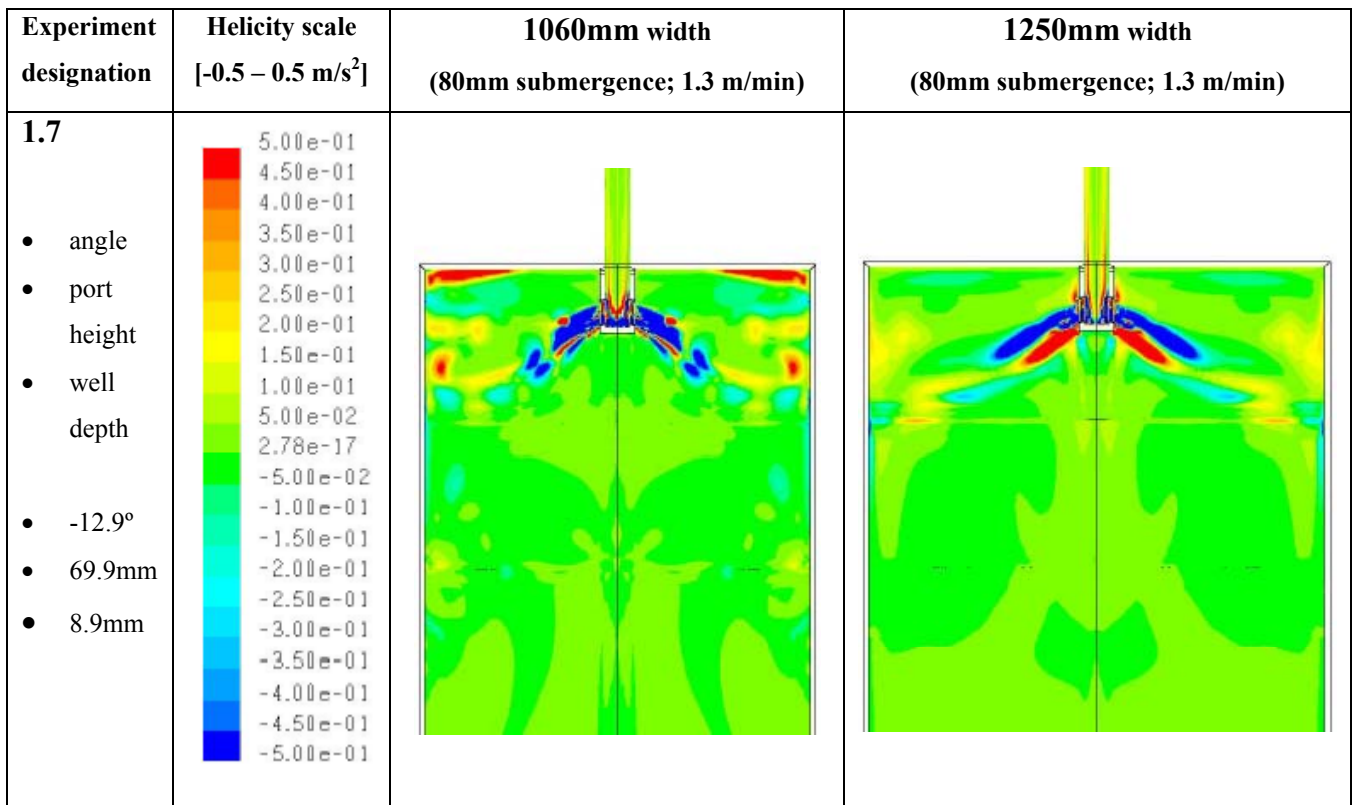


Figure O.9: Contours of helicity on the symmetry plane (range -0.5 – 0.5 m/s²)

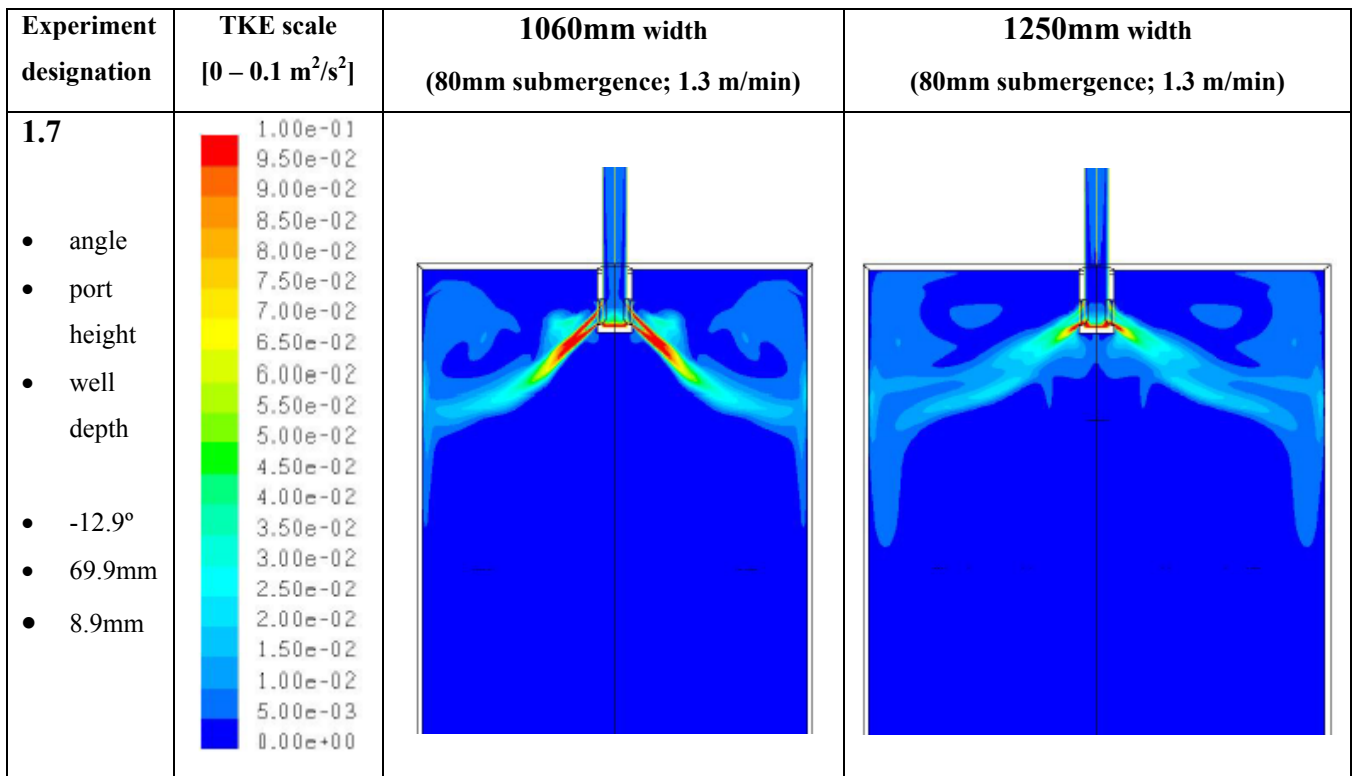


Figure O.10: Contours of turbulent kinetic energy on symmetry plane (range 0 – 0.1 m²/s²)

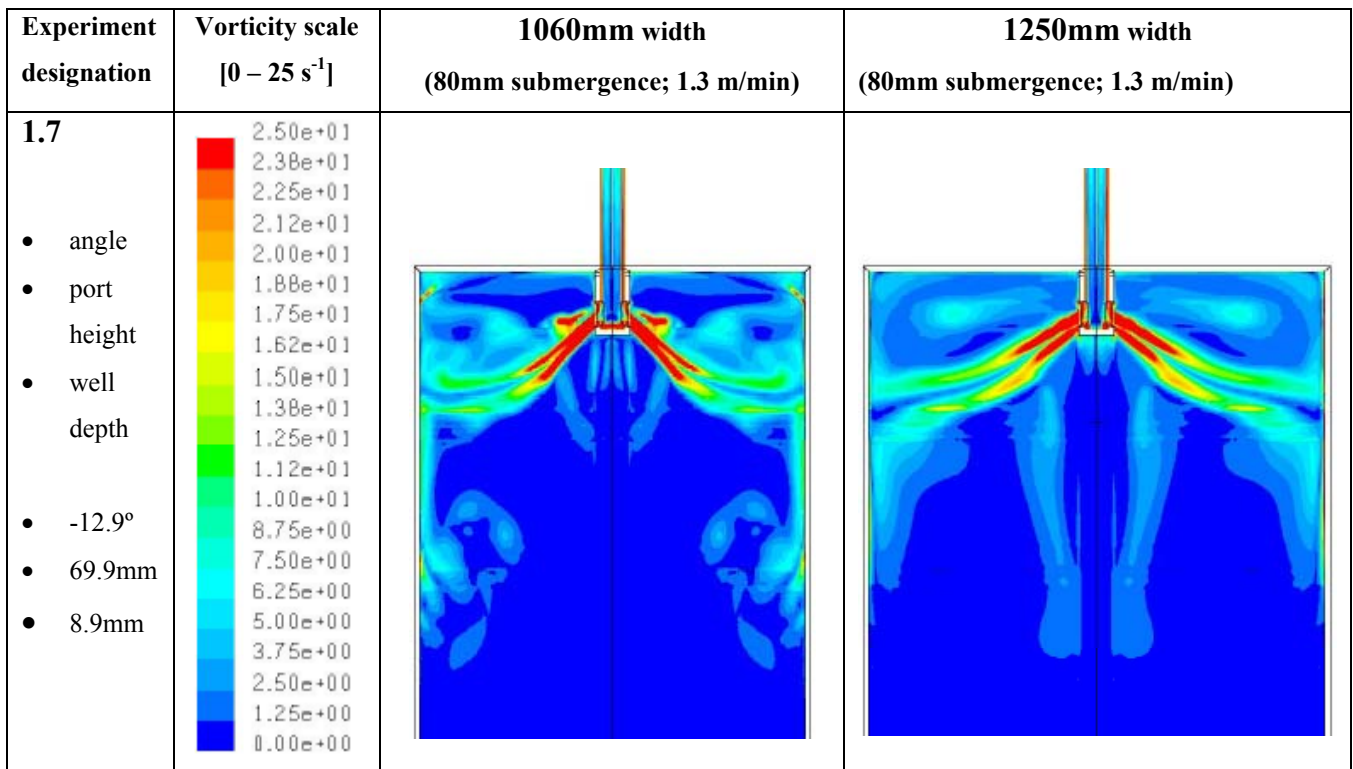


Figure O.11: Contours of vorticity on the symmetry plane (range 0 – 25 s⁻¹)

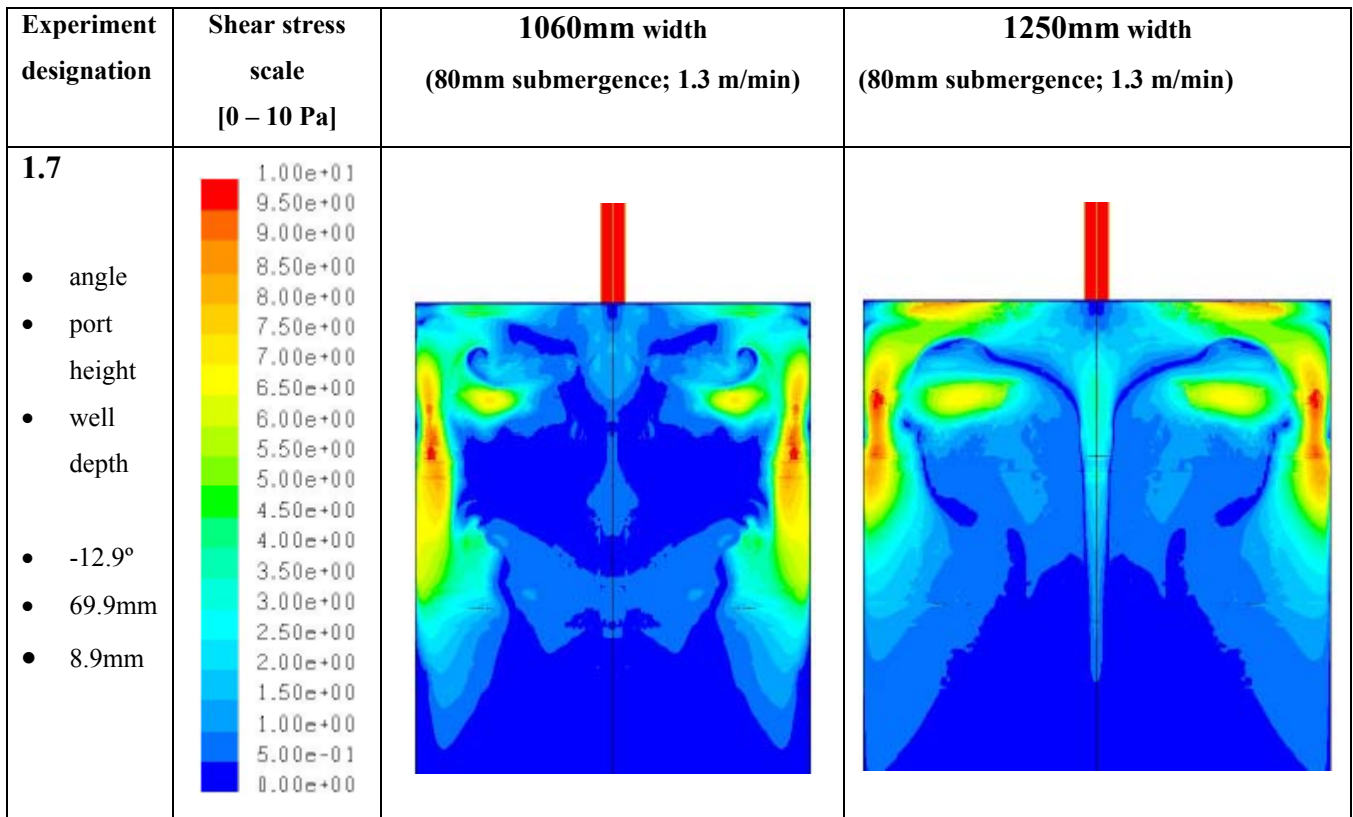


Figure O.12: Contours of shear stress on the wide mould walls (range 0 – 10 Pa)

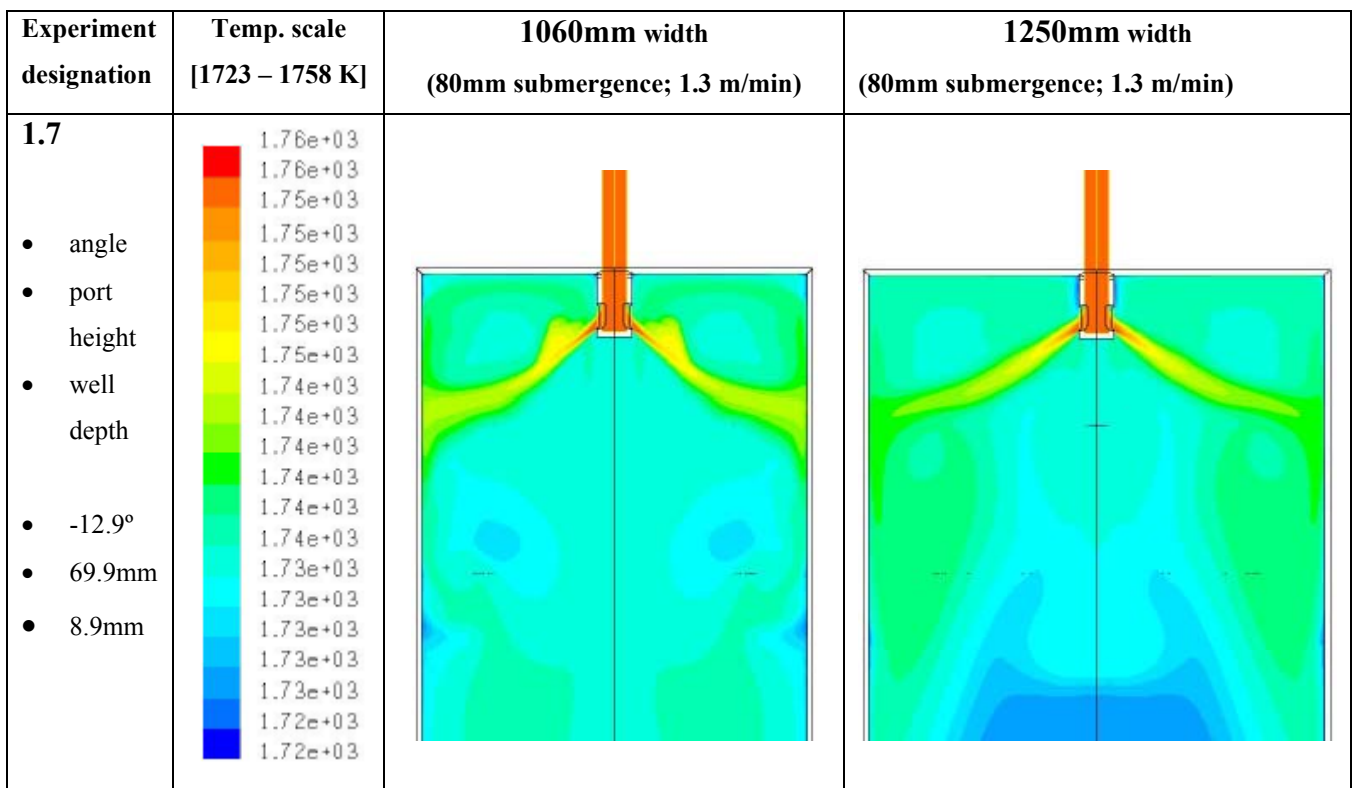


Figure O.13: Contours of temperature on the symmetry plane (range 1723 – 1758 K)

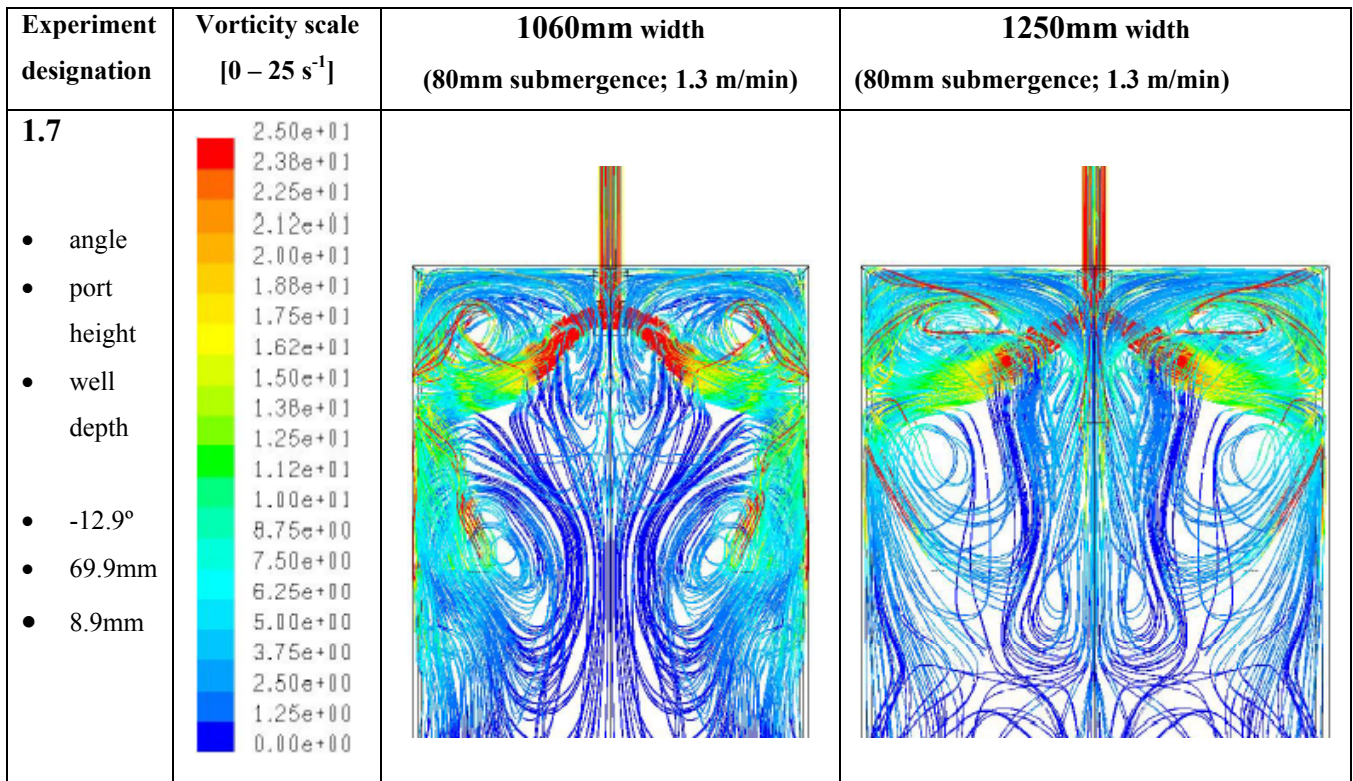


Figure O.14: Path lines originating from the SEN inlet, coloured by vorticity magnitude (range of vorticity 0 – 25 s⁻¹)

O.2.3 Experiment: 2.0 linear

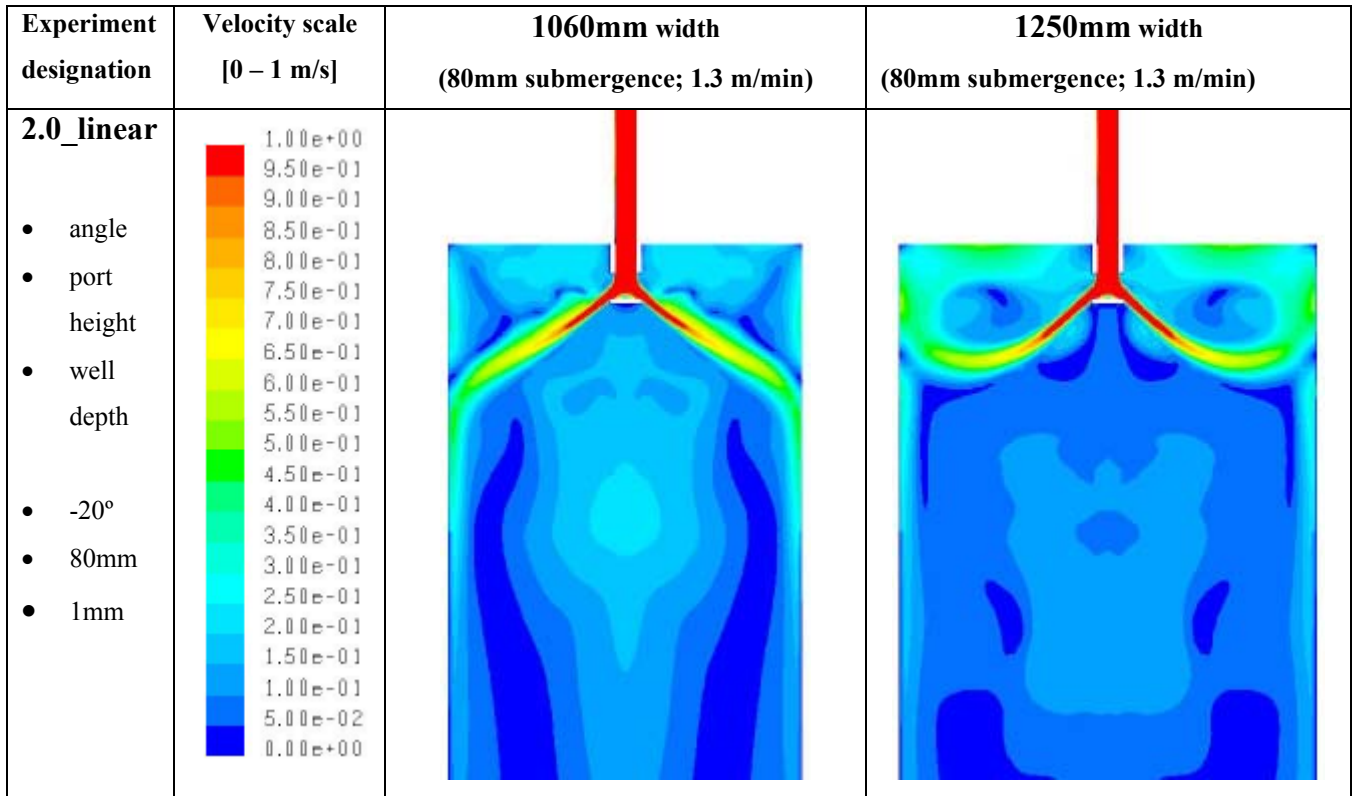


Figure O.15: Contours of velocity magnitude on the symmetry plane (range 0 – 1 m/s)

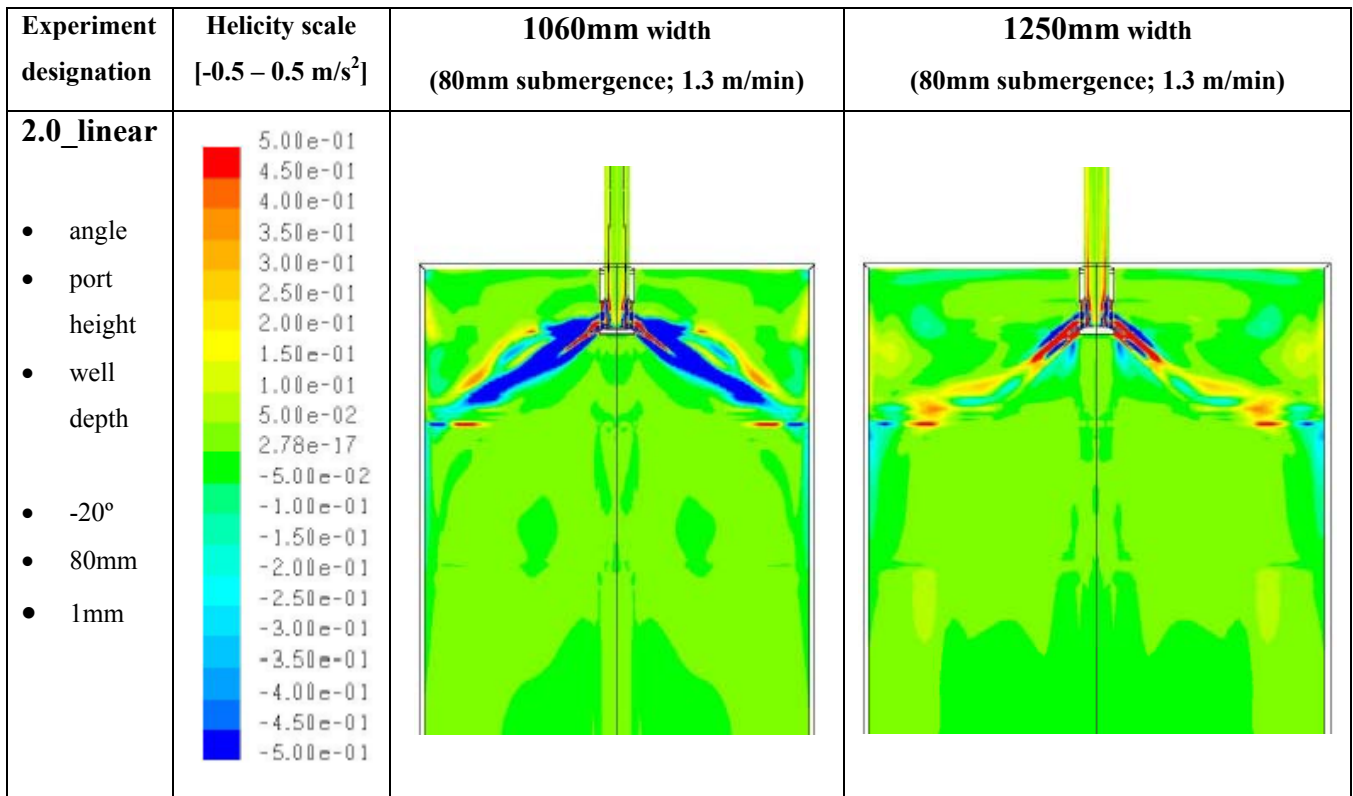


Figure O.16: Contours of helicity on the symmetry plane (range -0.5 – 0.5 m/s²)

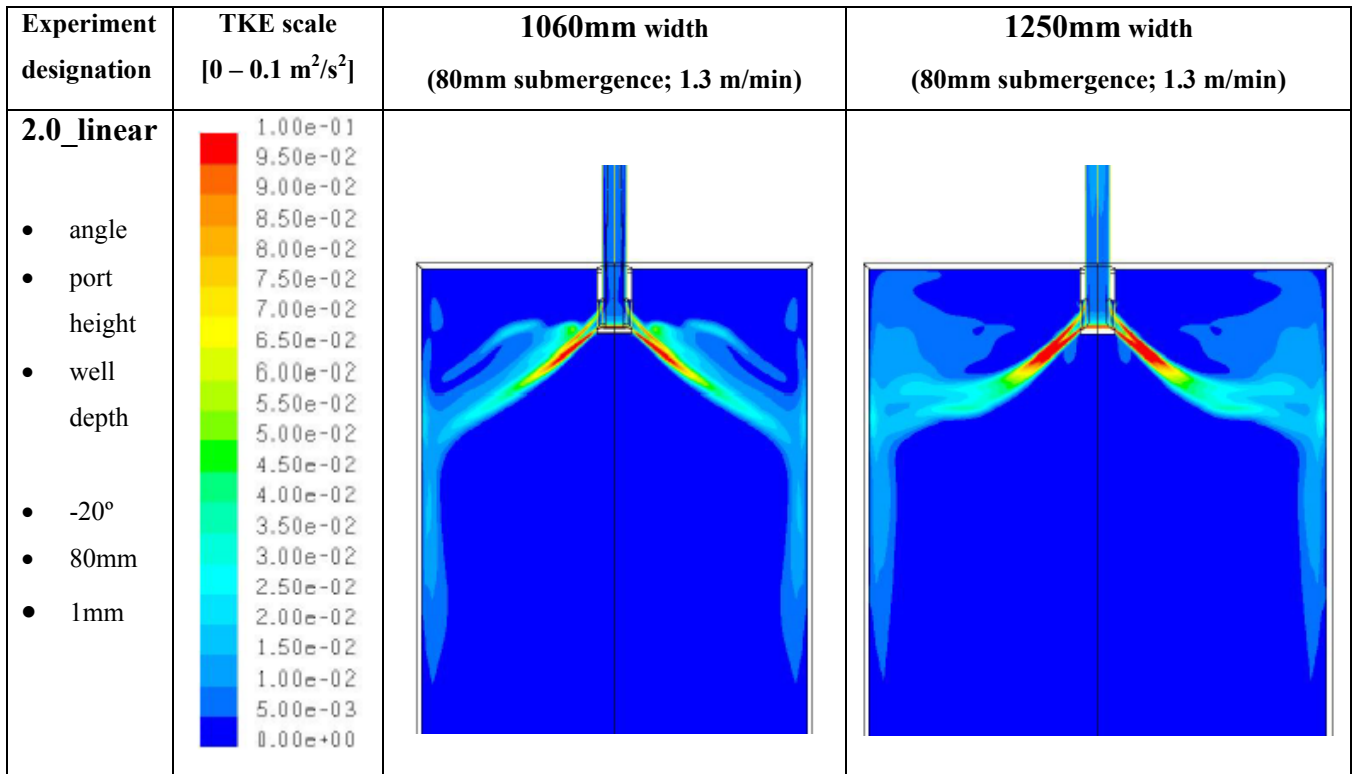


Figure O.17: Contours of turbulent kinetic energy on symmetry plane (range 0 – 0.1 m²/s²)

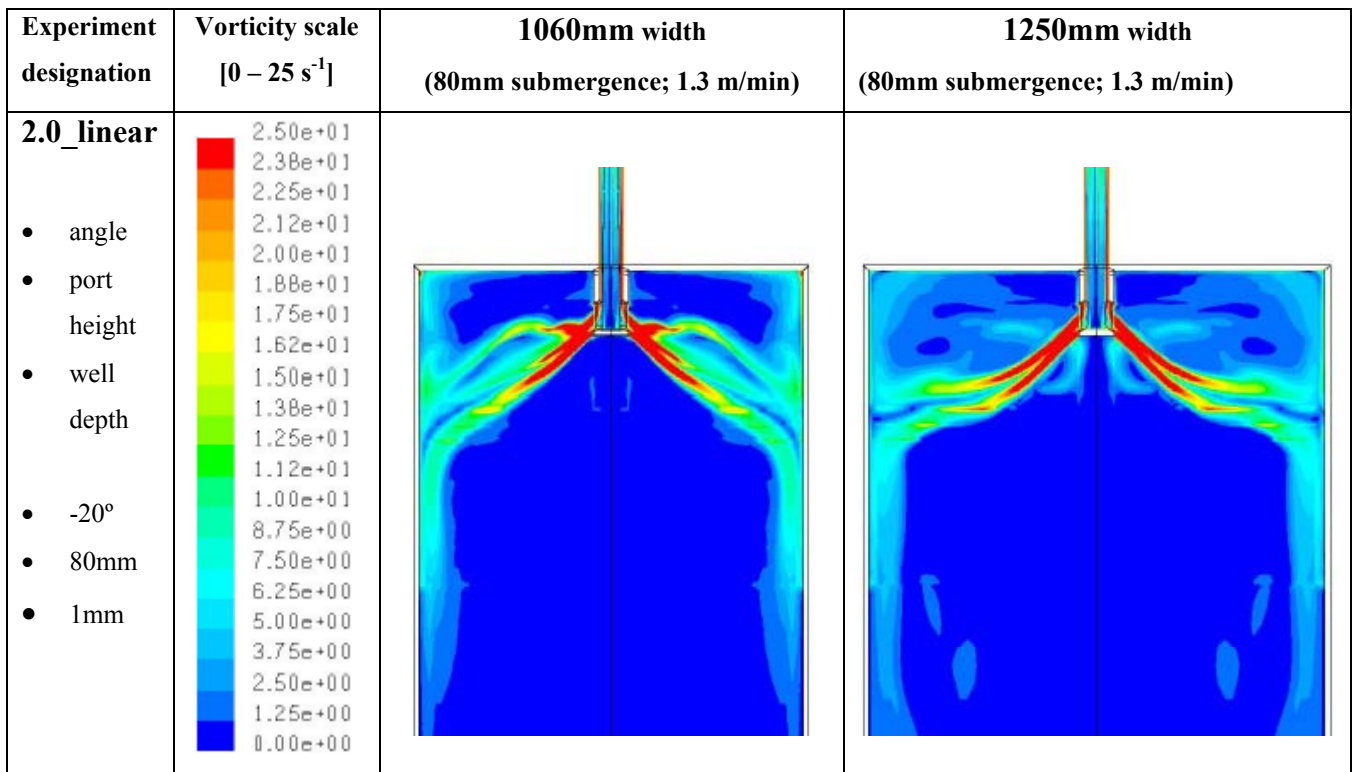


Figure O.18: Contours of vorticity on the symmetry plane (range 0 – 25 s⁻¹)

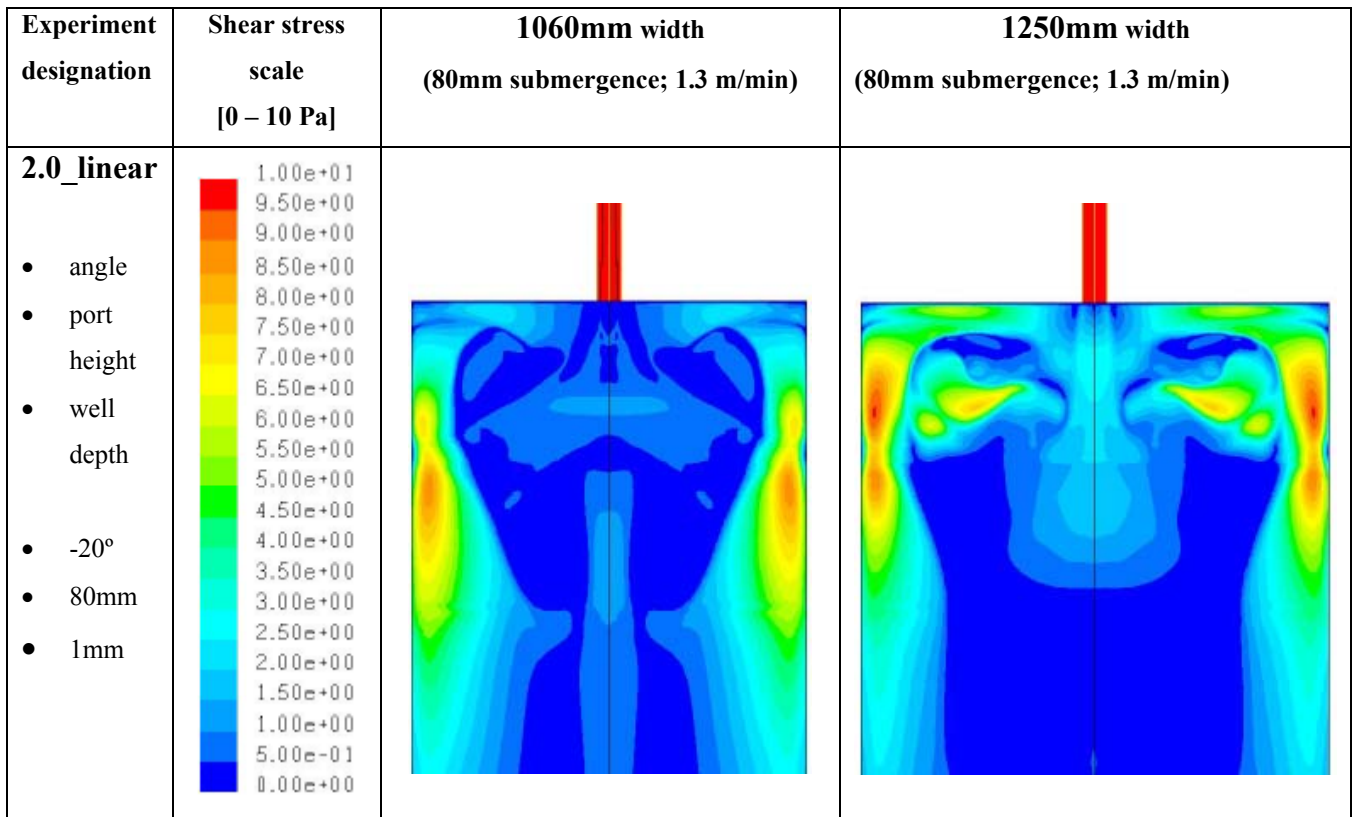


Figure O.19: Contours of shear stress on the wide mould walls (range 0 – 10 Pa)

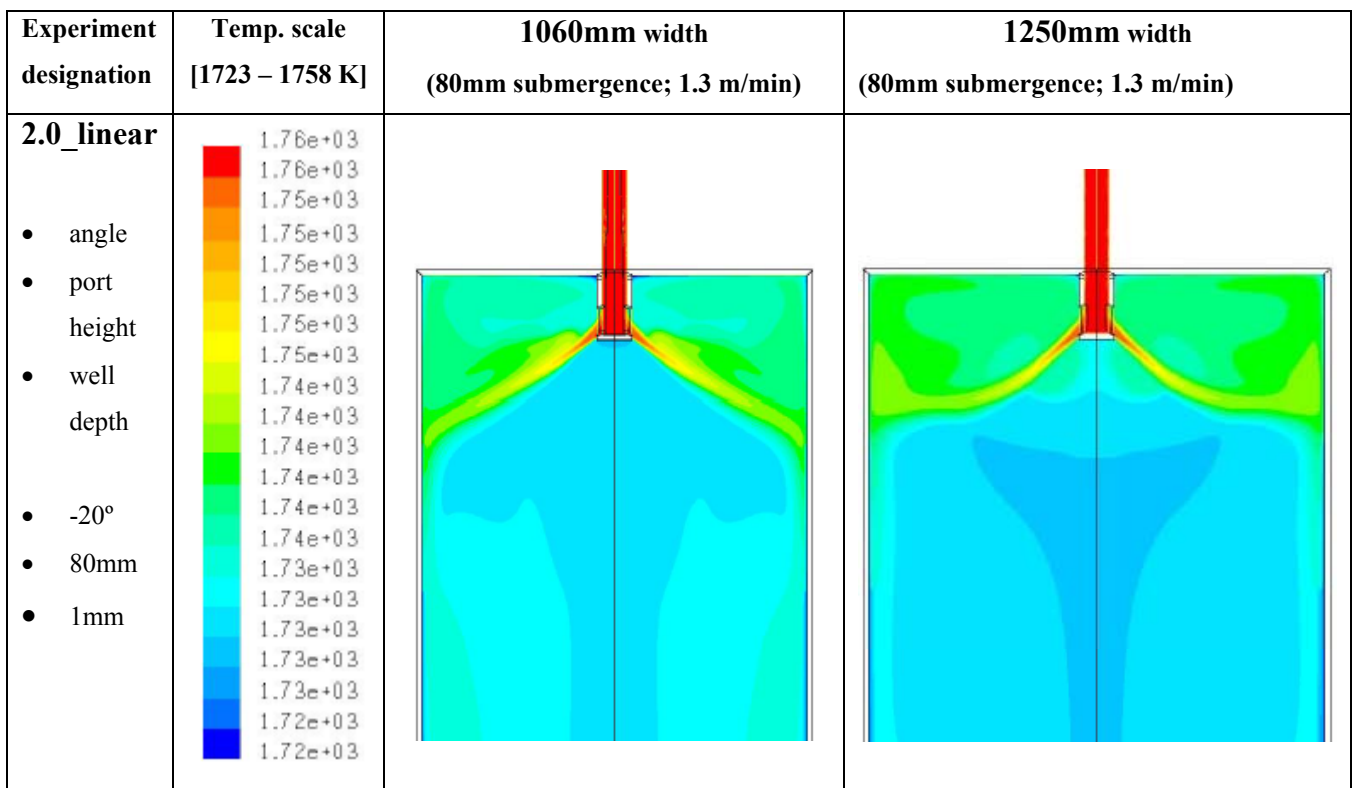


Figure O.20: Contours of temperature on the symmetry plane (range 1723 – 1758 K)

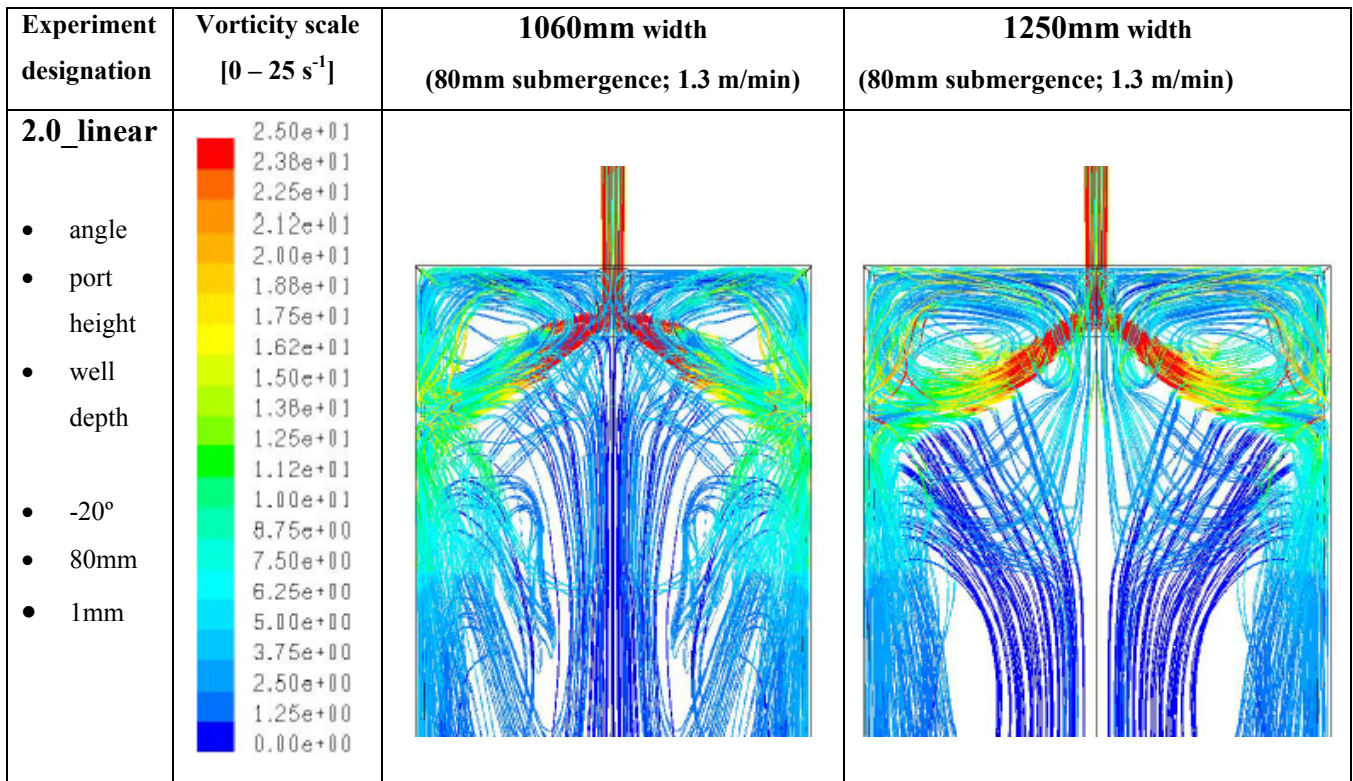


Figure O.21: Path lines originating from the SEN inlet, coloured by vorticity magnitude (range of vorticity 0 – 25 s⁻¹)

O.2.4 Experiment: 2.0 quadratic

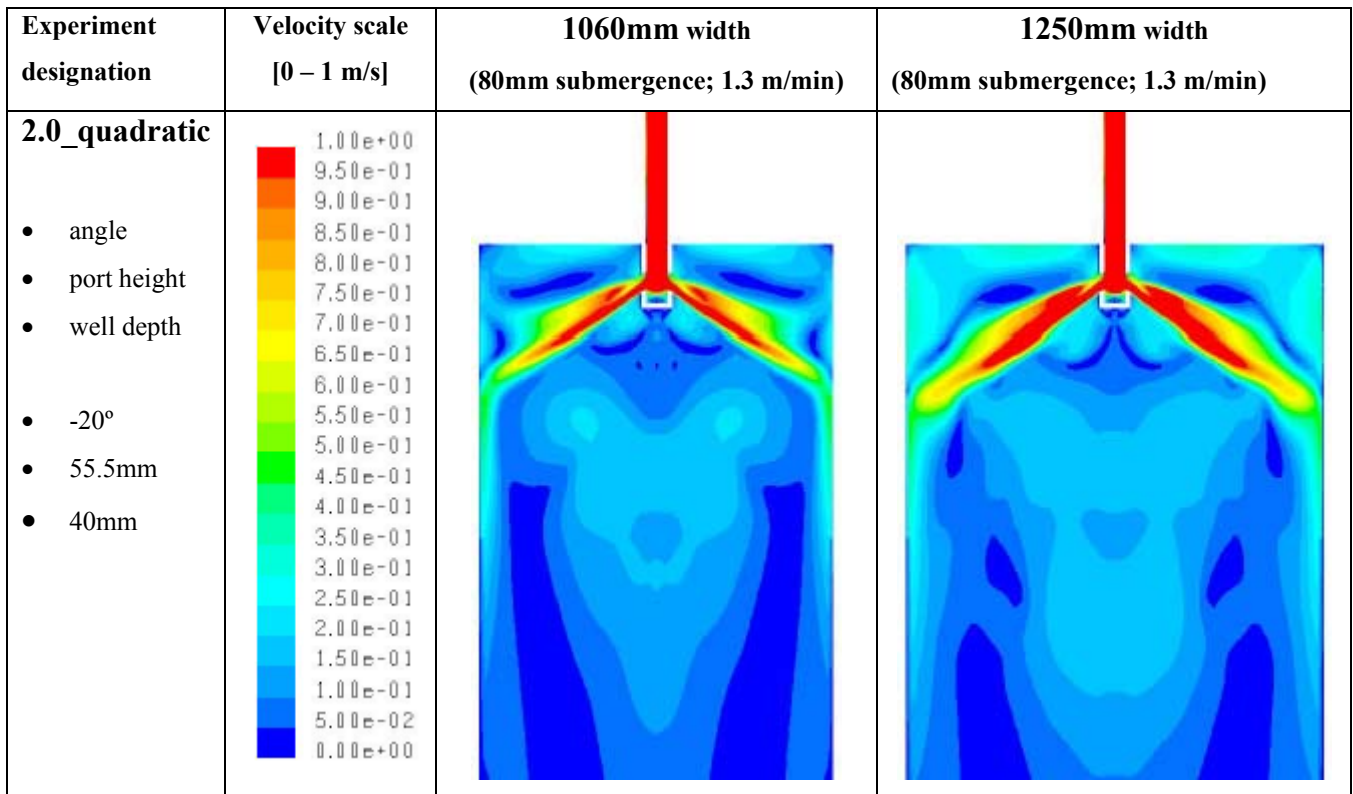


Figure O.22: Contours of velocity magnitude on the symmetry plane (range 0 – 1 m/s)

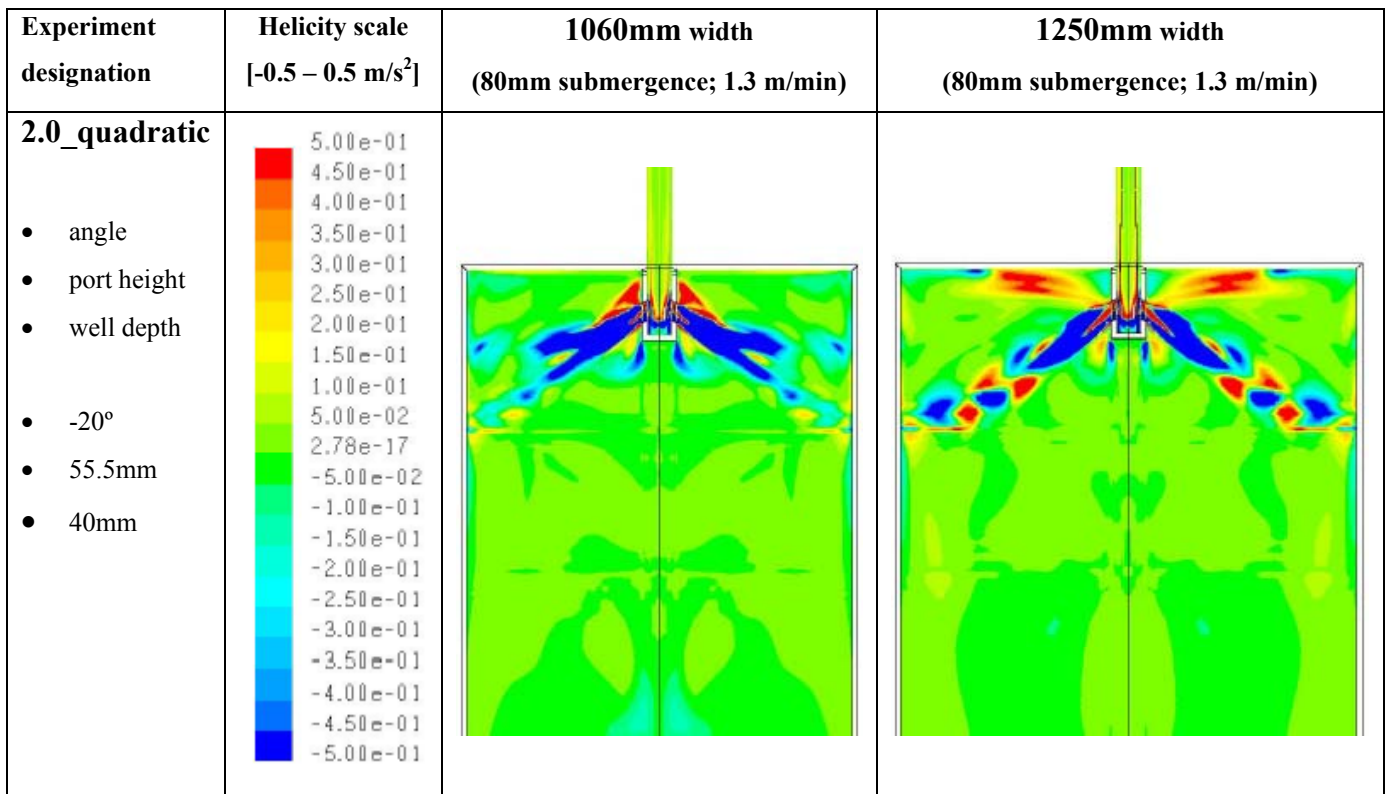


Figure O.23: Contours of helicity on the symmetry plane (range -0.5 – 0.5 m/s²)

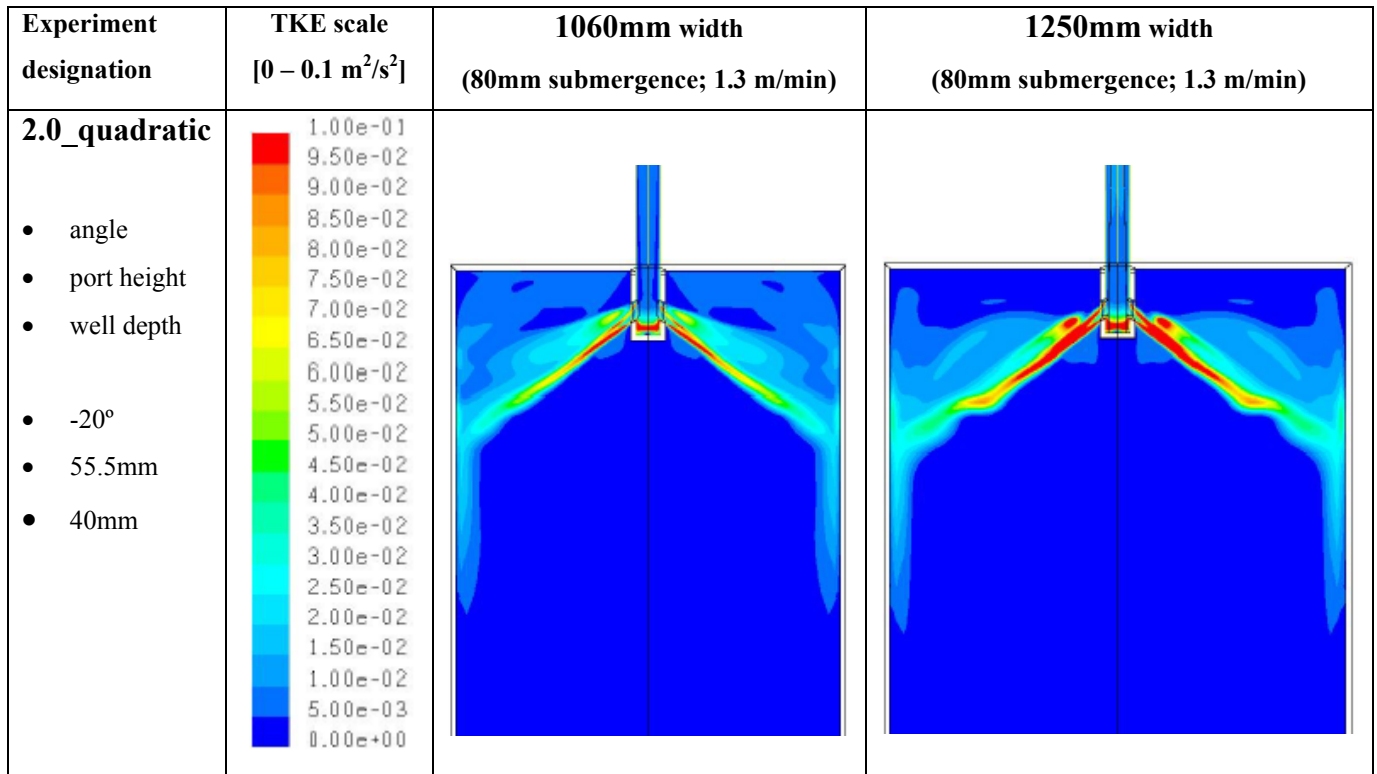


Figure O.24: Contours of turbulent kinetic energy on symmetry plane (range 0 – 0.1 m²/s²)

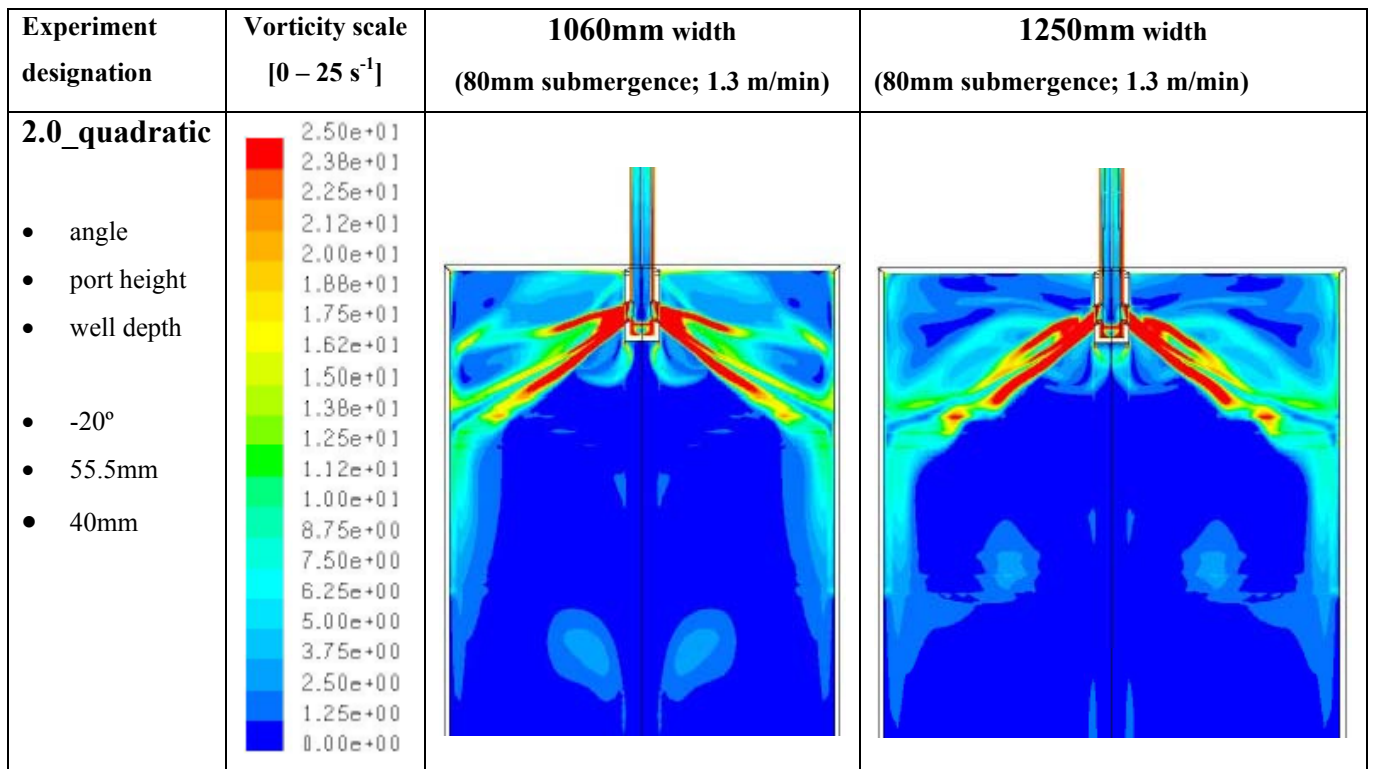


Figure O.25: Contours of vorticity on the symmetry plane (range 0 – 25 s⁻¹)

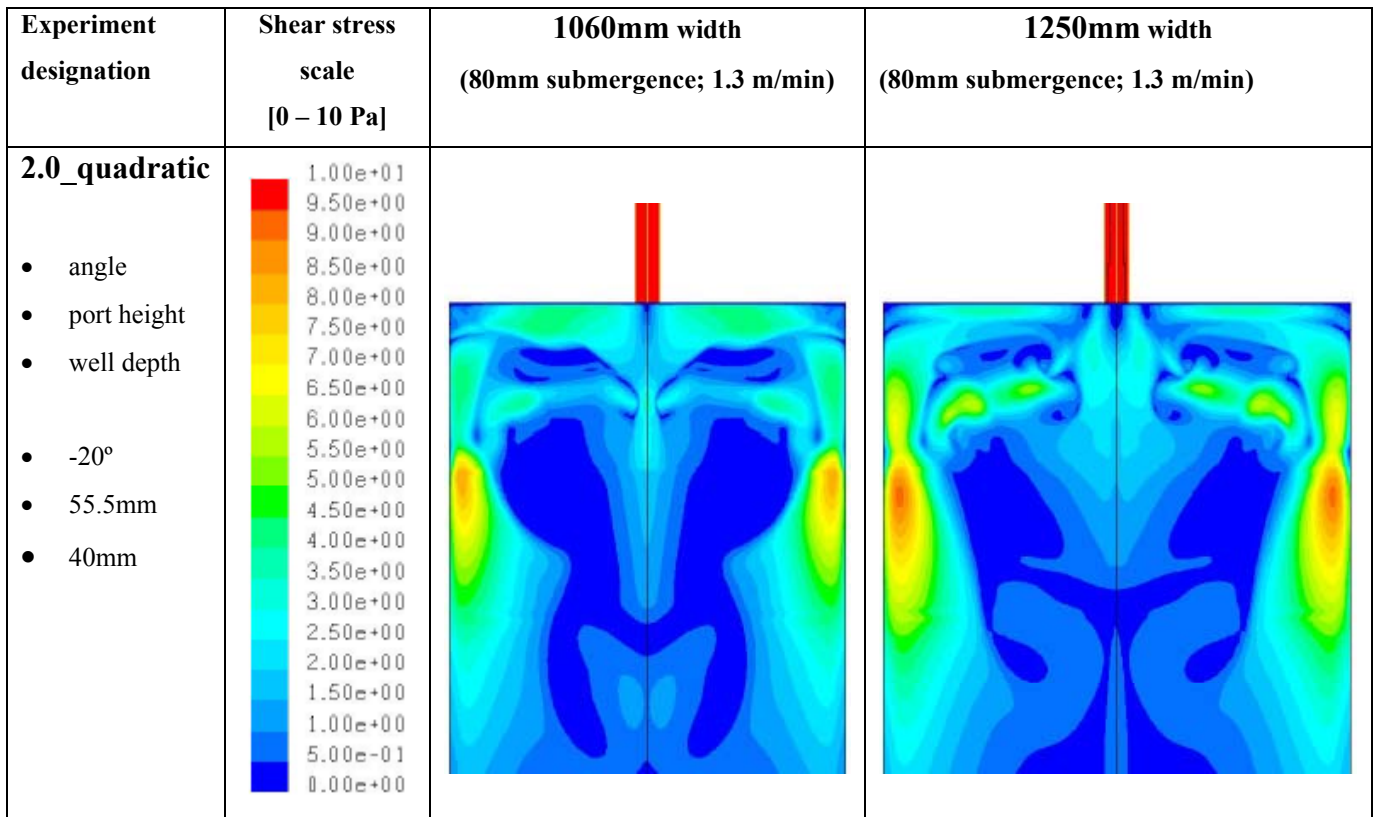


Figure O.26: Contours of shear stress on the wide mould walls (range 0 – 10 Pa)

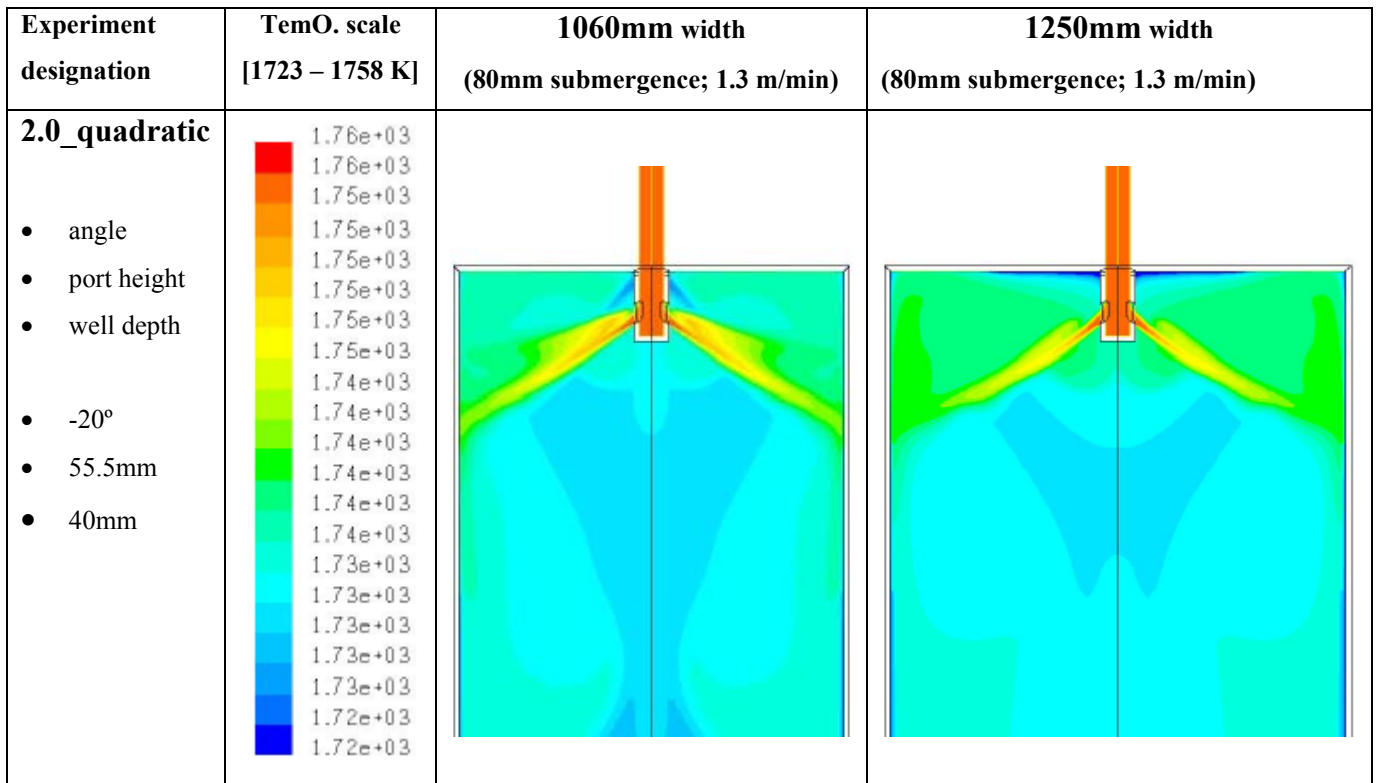


Figure O.27: Contours of temperature on the symmetry plane (range 1723 – 1758 K)

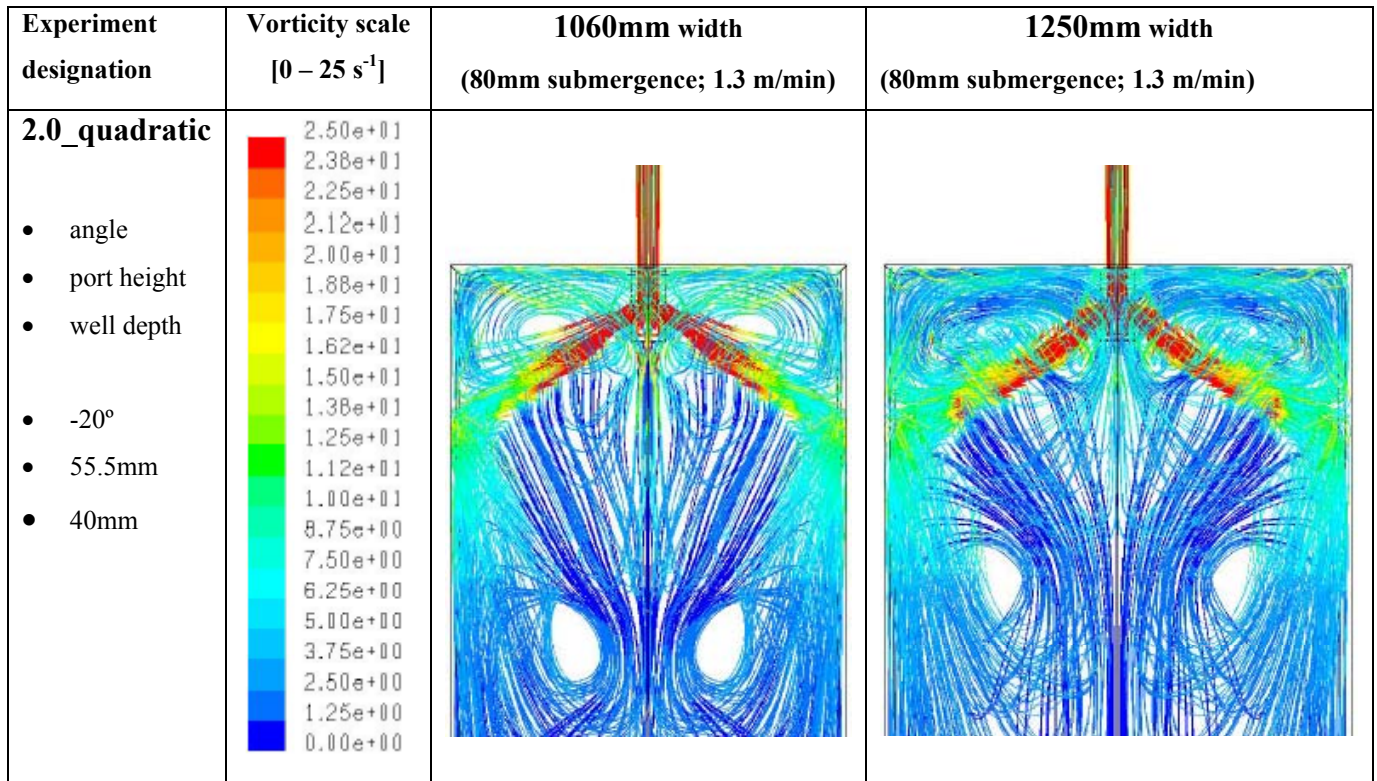


Figure O.28: Path lines originating from the SEN inlet, coloured by vorticity magnitude (range of vorticity 0 – 25 s⁻¹)

APPENDIX P

P. CFD results of best 4 SEN designs: iso-surfaces to indicate 3D nature of flow

P.1 General

In order to demonstrate the 3 dimensional nature of the flow field, another display method is used: The jet is displayed in 3D by rendering iso-surfaces¹ of velocity magnitude coloured by turbulent kinetic energy.

The four best designs (lowest multi-objective values) that will be displayed are:

- 1.0
- 1.7
- 2.0_linear
- 2.0_quadratic

The iso-surface of velocity magnitude was in each case chosen to indicate the jet as it emerges from the SEN ports. In Figures P.1 to P.4, one can clearly observe that the jet path varies as the jet moves closer to the wide walls of the mould. Therefore, much of the flow follows an entire different path from the centre plane; consequently, the effect of the walls is quite significant. Thus; meaningful optimisation studies certainly need to take into account the full 3 dimensional flow in typical SEN and mould CFD models.

Refer to section P.2 for the visual depiction of the 3D nature of flow inside the mould cavity.

¹ An iso-surface of velocity magnitude (for example) is when only the surface area where a specified constant velocity magnitude is achieved in the entire flow field is displayed. Of course, other properties may vary over this iso-surface, as turbulent kinetic energy for example.

P.2 CFD Results: Iso-surfaces of velocity magnitude coloured by vorticity
(last iterations)

P.2.1 Experiment 1.0

Figure P.1

P.2.2 Experiment 1.7

Figure P.2

P.2.3 Experiment 2.0 linear

Figure P.3

P.2.4 Experiment 2.0 quadratic

Figure P.4

P.2.1 Experiment: 1.0

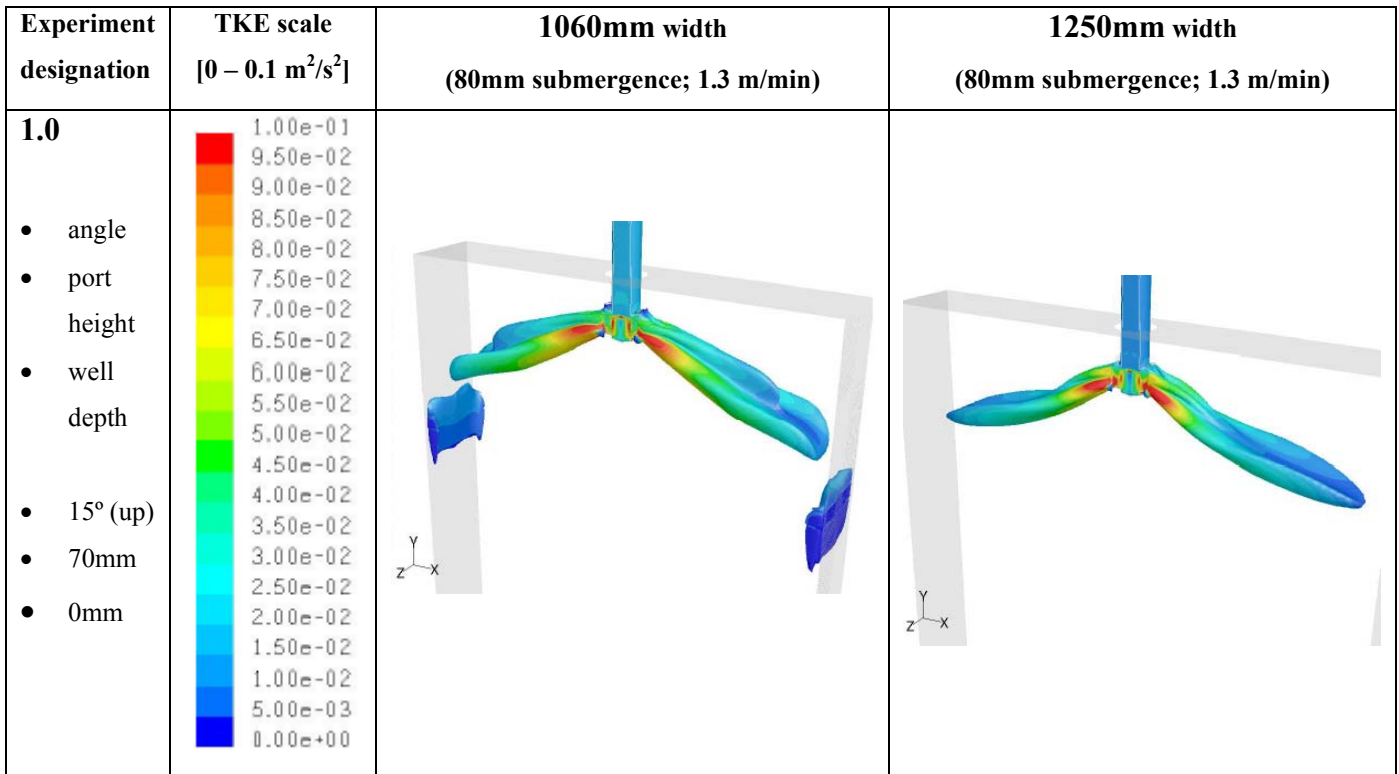


Figure P.1: Iso-surface of velocity coloured by turbulent kinetic energy (range 0 – 0.1 m²/s²)

P.2.2 Experiment: 1.7

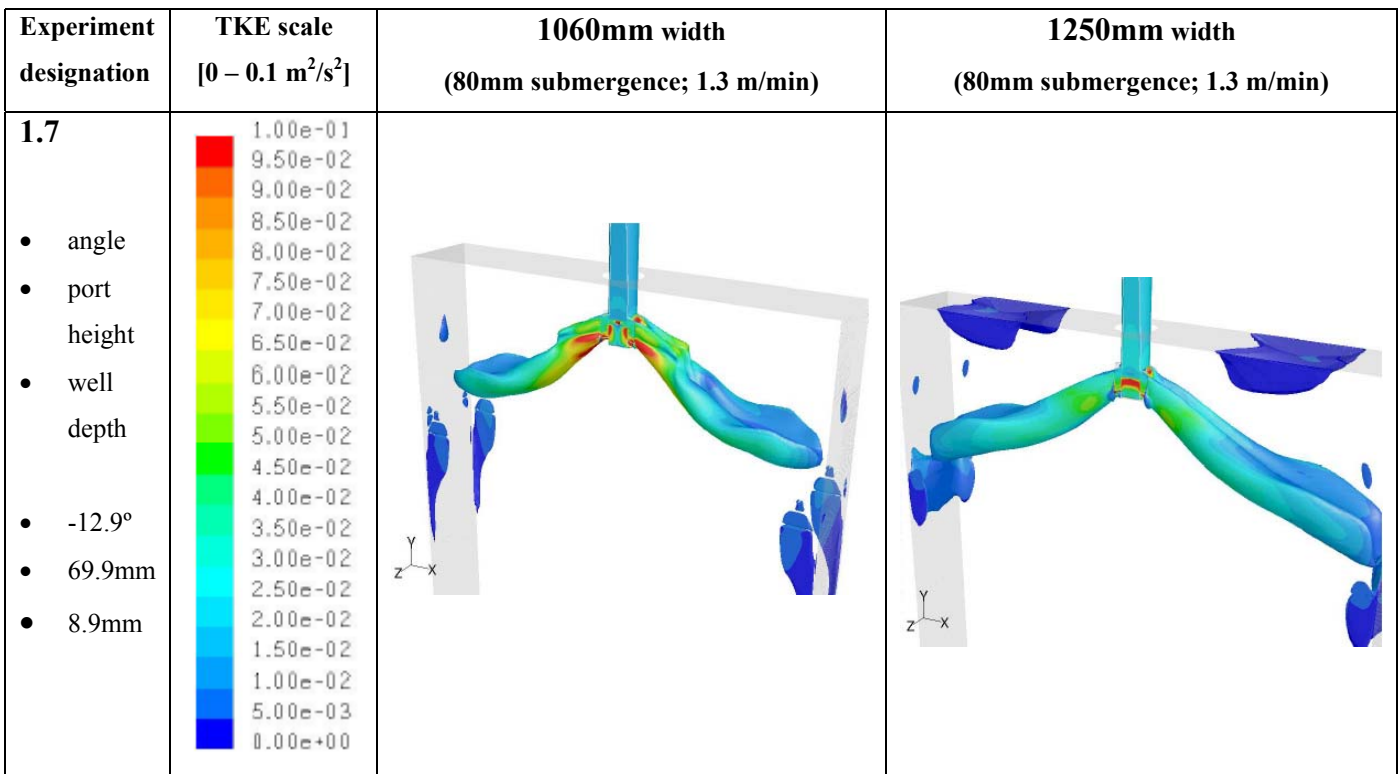


Figure P.2: Iso-surface of velocity coloured by turbulent kinetic energy (range 0 – 0.1 m²/s²)

P.2.3 Experiment: 2.0 linear

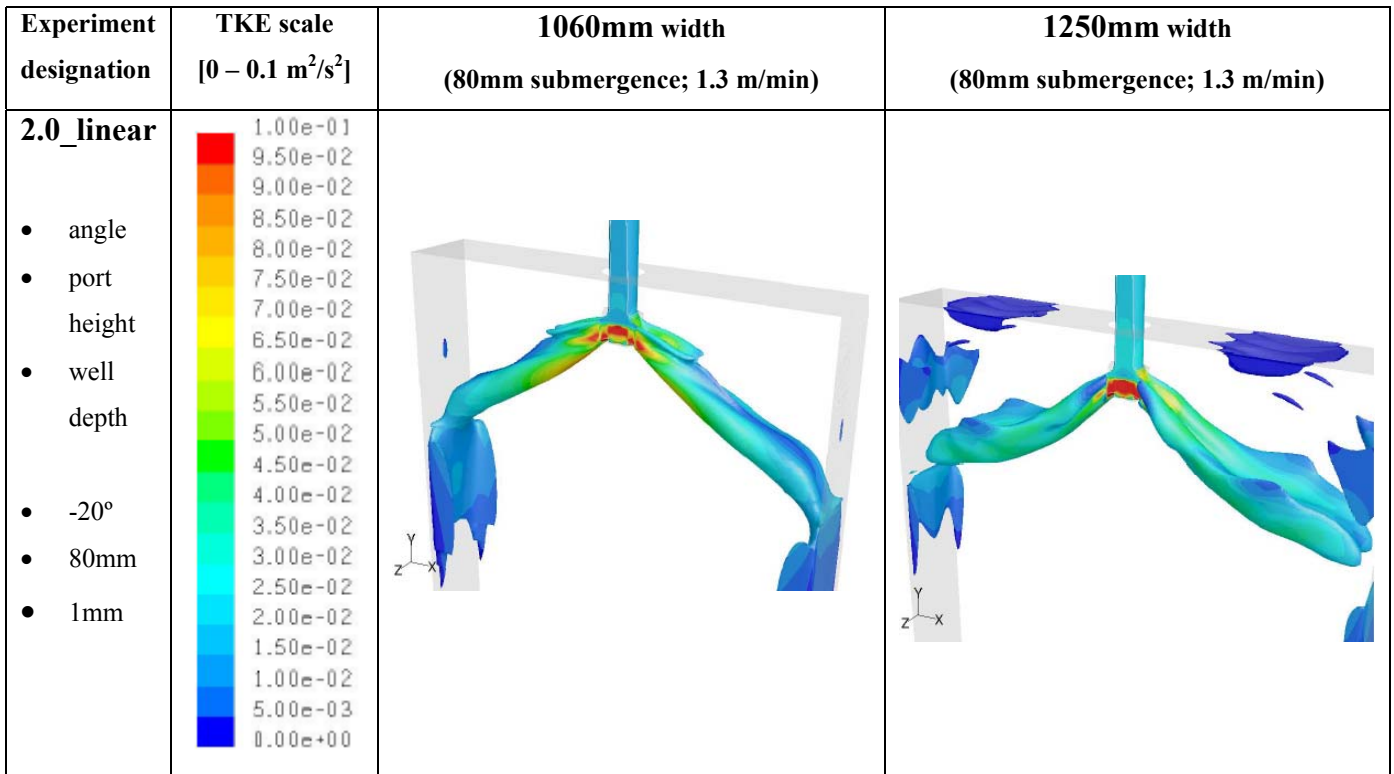


Figure P.3: Iso-surface of velocity coloured by turbulent kinetic energy (range 0 – 0.1 m²/s²)

P.2.4 Experiment: 2.0 quadratic

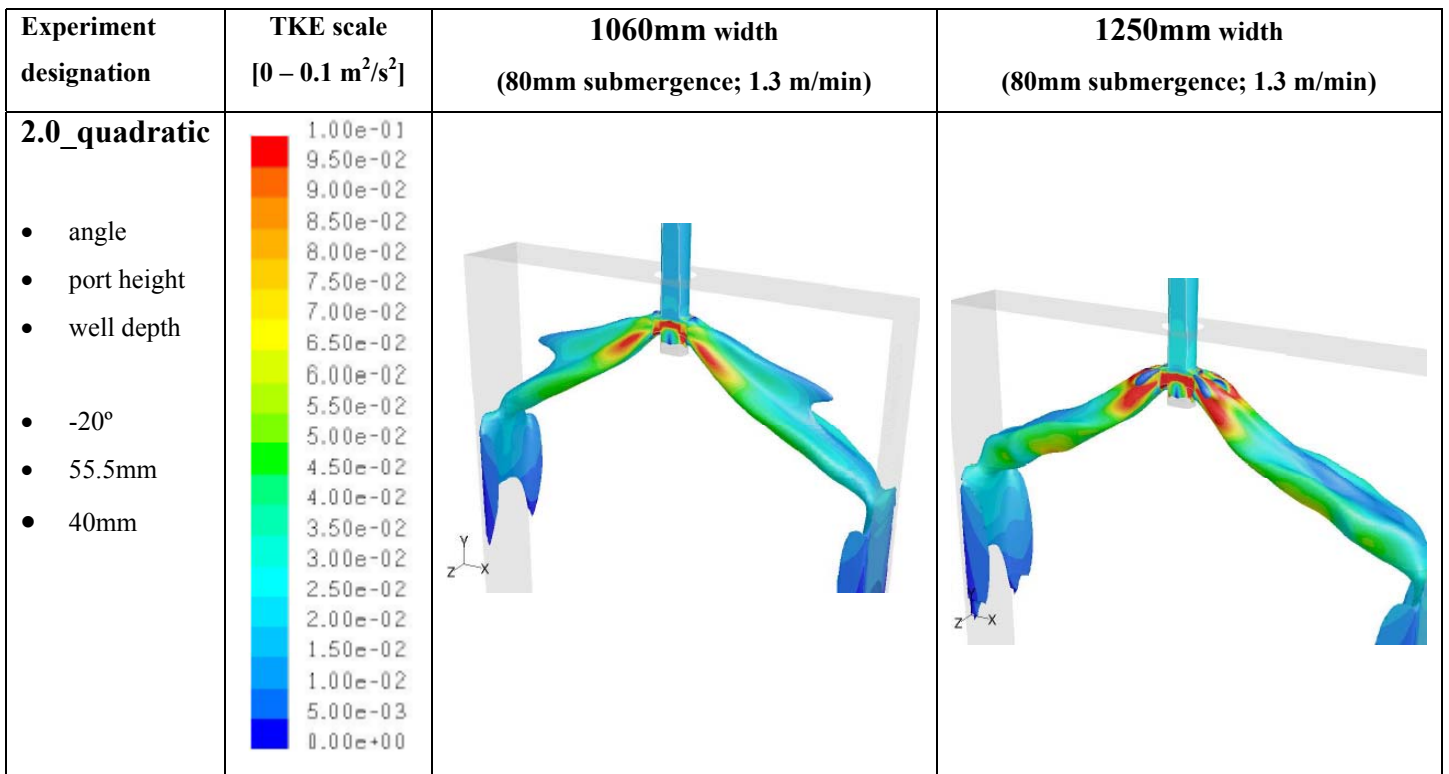


Figure P.4: Contours of turbulent kinetic energy on symmetry plane (range 0 – 0.1 m²/s²)

APPENDIX Q

Q. Validation of optimum SEN design: CFD results compared with water model tests at 80mm and 150mm submergence depth

Q.1 General

The optimum design chosen from the 3D design exploration is the 2.0_linear experiment.

This optimum design is validated at the widest width, namely 1250mm, as the CFD solutions tend to be problematic with increasing width.

The optimum CFD models (full-scale) reflect the real plant circumstances, as liquid steel is used as the fluid. In section Q.2, the 40%-scaled water model results for submergence depths of 80mm and 150mm are compared with the corresponding full-scale CFD models (using contours of velocity and path lines).

The excellent correspondence between the 40%-scaled water model and CFD results (Figures Q.1 to Q.4) simultaneously verifies the assumption that only satisfying Fr-similarity is adequate for typical flow verification.

Q.2 Optimum SEN CFD results validation: 80mm and 150mm submergence

Q.2.1 Submergence depth: 80mm

Figures Q.1 and Q.2

Q.2.2 Submergence depth: 150mm

Figures Q.3 and Q.4

Q.2.1 Submergence depth: 80mm

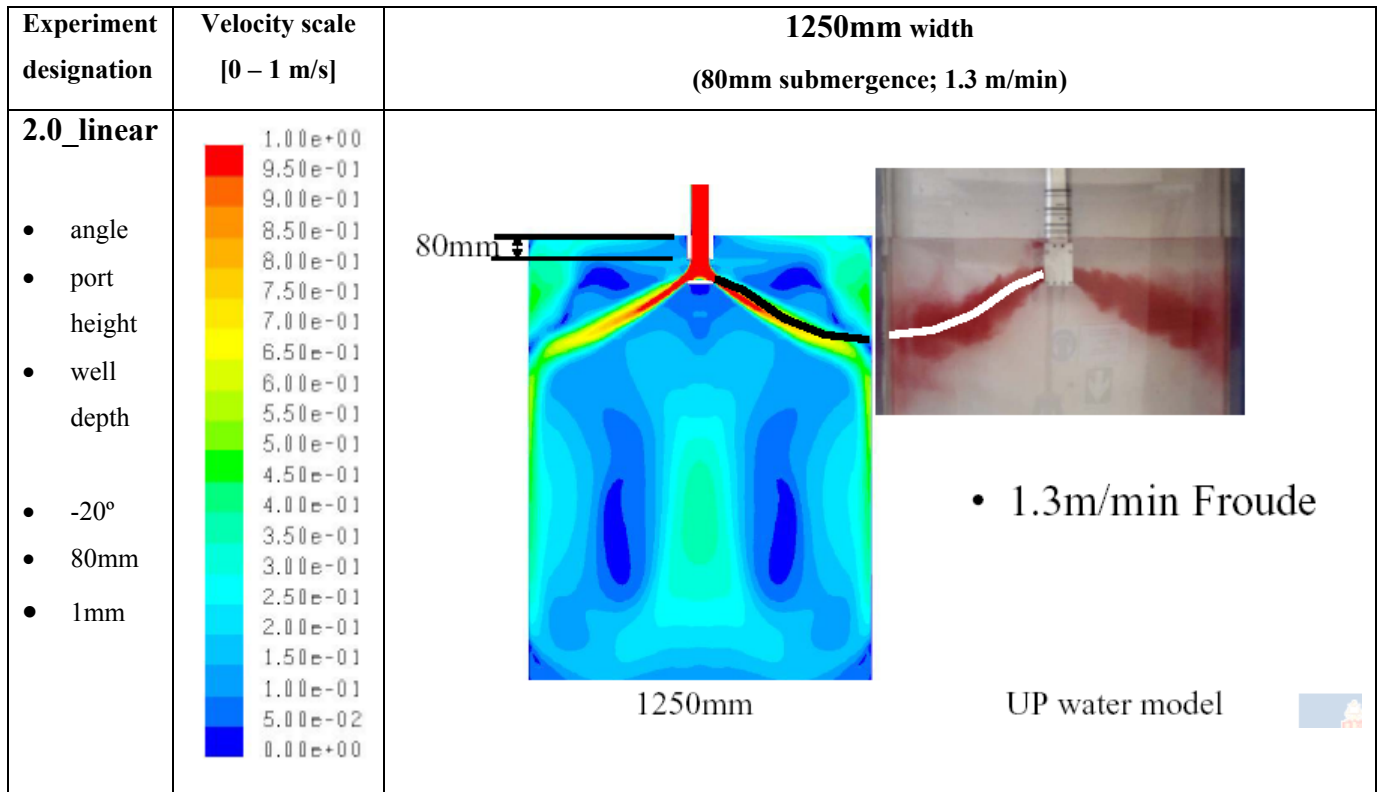


Figure Q.1: Validation of optimum SEN design at 80mm submergence depth, using contours of velocity (scale 0 – 1 m/s)

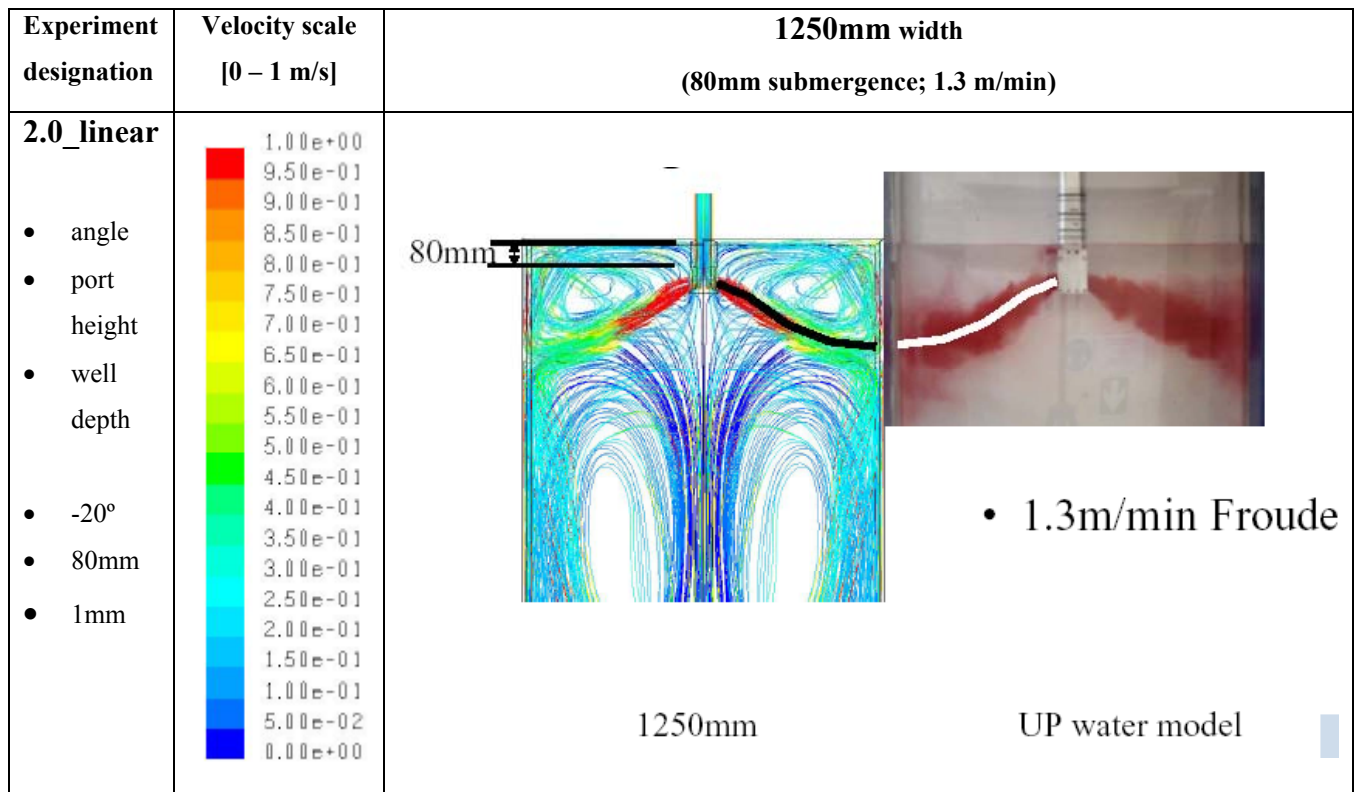


Figure Q.2: Validation of optimum SEN design at 80mm submergence depth, using path lines coloured by velocity magnitude (scale 0 – 1 m/s)

Q.2.2 Submergence depth: 150mm

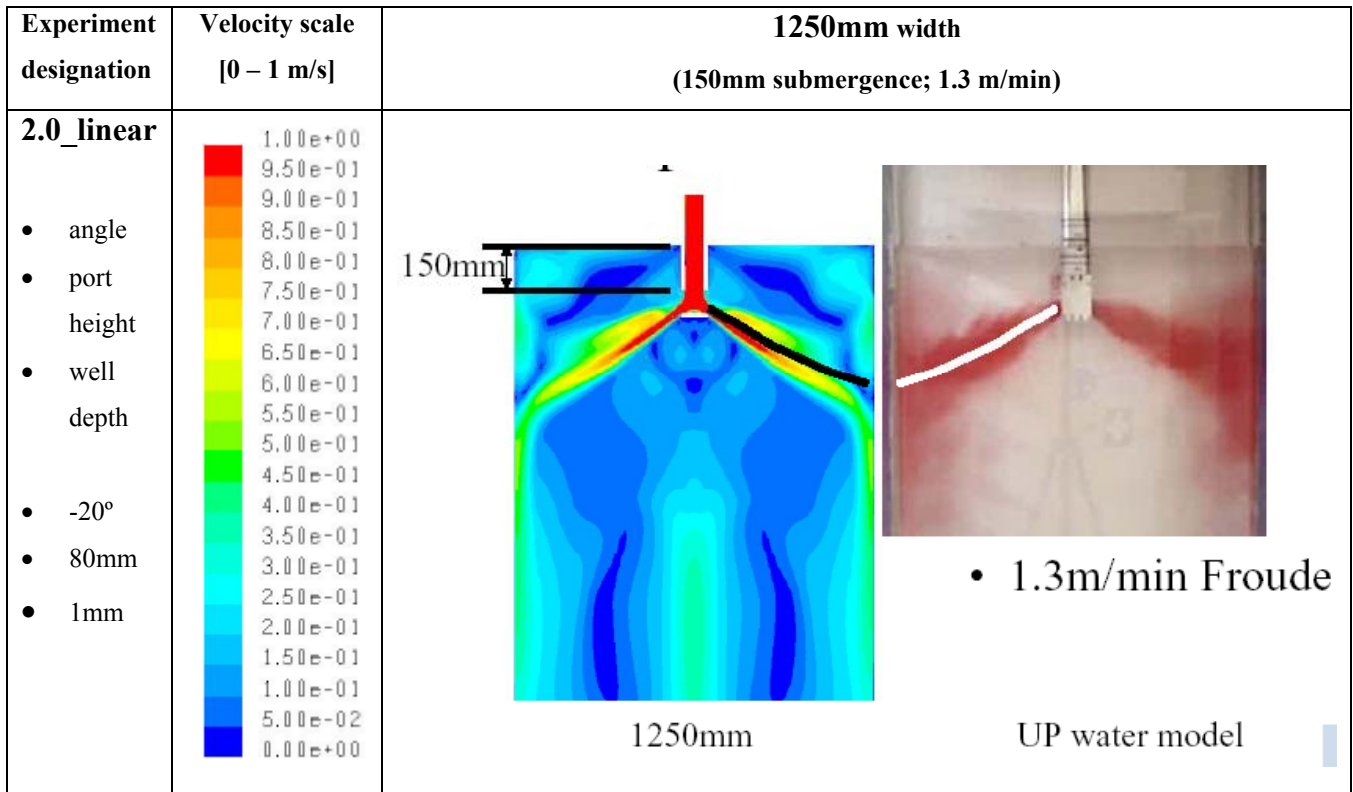


Figure Q.3: Validation of optimum SEN design at 150mm submergence depth, using contours of velocity (scale 0 – 1 m/s)

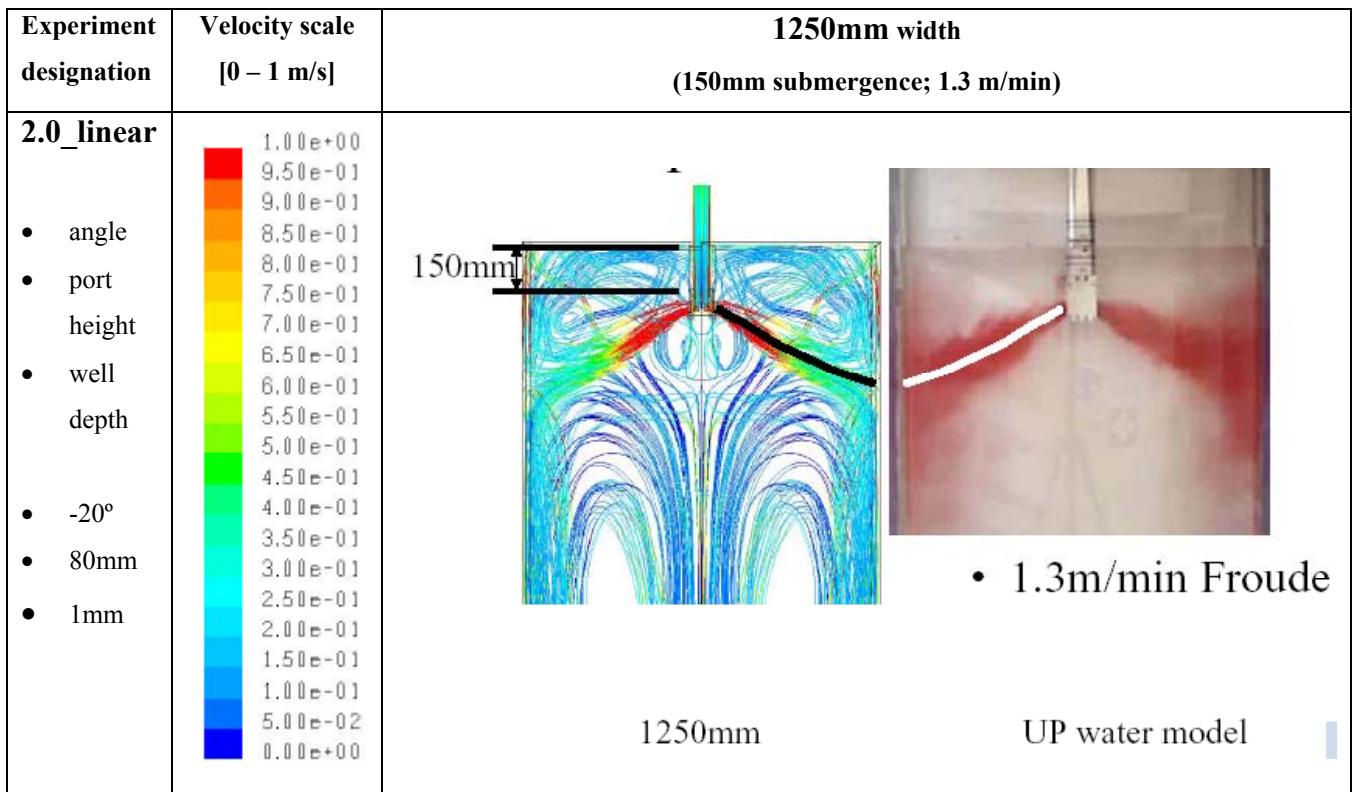


Figure Q.4: Validation of optimum SEN design at 150mm submergence depth, using path lines coloured by velocity magnitude (scale 0 – 1 m/s)